Critical Evaluation and Application of Position Sensorless Control Techniques for Reluctance Synchronous Machines

by

Wikus Theo Villet

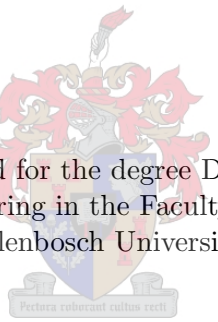

Dissertation presented for the degree Doctor of Philosophy
in Electrical Engineering in the Faculty of Engineering at
Stellenbosch University

Supervisor: Prof. Maarten J. Kamper

Aptil 2014

Declaration

By submitting this thesis electronically, I declare that the entirety of the work contained therein is my own, original work, that I am the sole author thereof (save to the extent explicitly otherwise stated), that reproduction and publication thereof by Stellenbosch University will not infringe any third party rights and that I have not previously in its entirety or in part submitted it for obtaining any qualification.

Date: December 2013

Abstract

The position sensorless controllability of the reluctance synchronous machine (RSM) is investigated in this thesis with the focus on industry applications where variable and dynamic torque is required from startup up to rated speed. Two low speed as well as one medium to high speed position sensorless control (PSC) method for RSMs are investigated. These methods are extended to operate in the entire rated speed region with a hybrid PSC structure that makes use of phase locked-loop synchronisation and a hysteresis changeover method.

It is shown in this thesis that PSC of the lateral rib rotor RSM is not possible from zero up to $\pm$ 0.2 $p.u$ current. It is shown through finite element (FE) simulations that PSC of the ideal rotor RSM however, is possible at zero reference current. A novel construction method is used to build two ideal rotor RSMs. Measured flux linkage curve results of the ideal rotor RSMs correlate well with simulation results and it is shown that the electrical angle of the machine can be tracked successfully at zero reference current.

The FE simulation package is used to compare the saliency of the RSM on a per-unit scale to three types of field intensified permanent magnet (FI-PM) synchronous machines and a field weakening interior permanent magnet synchronous machine. It is shown that the saliency of the RSM is larger than that of the investigated PM machines from zero up to rated load. It is thus concluded that the RSM is well suited to saliency-based PSC (SB-PSC) methods, which are used to control synchronous machines at startup and low speeds.

The hybrid PSC methods developed in this thesis, are tested and evaluated on three proposed industry applications. The first is a reluctance synchronous wind generator with an inverter output LC filter. The LC filter allows long cables to be used and reduces the voltage stress on the stator windings of the machine. The combination of the LC filter and hybrid PSC method allows the power electronics and controller to be stationed in the base of the turbine tower. A new stator quantity estimation method is derived to omit the need of current and voltage sensors on the machine side of the LC filter. Good maximum power point tracking laboratory results are shown with the high frequency injection-assisted hybrid PSC method.

The second application investigated is a position sensorless controlled variable gear electric vehicle (EV) RSM drive. Simulation and measured results show good torque capabilities of the position sensorless controlled EV RSM. It is shown through simulation results that the fundamental current harmonic is dominant in the demodulation scheme of the high frequency injection position sensorless control (HFI-PSC) method due to the high current rating of the proposed RSM. The HFI-PSC method is extended to reduce the effect of the fundamental current harmonic in the demodulation scheme without adding any additional filters.

The final investigated application is a novel mine scraper winch, which uses two position sensorless controlled RSMs to retrieve ore from the blast site underground. The new design improves on the safety, efficiency and durability of the current scraper winch design. Measured results show that the position sensorless controlled winch RSM is able to deliver rated startup torque with both investigated SB-PSC methods. Finally an automation method is implemented and tested to limited the applied force on the scraper and automatically free itself when stuck.

Uittreksel

Die posisie sensorlose beheer eienskappe van die reluktansie sinchroonmasjien (RSM) word in hierdie tesis ondersoek met die fokus op industriële toepassings waar varierende dinamiese draaimoment vereis word vanaf stilstand tot by ken spoed. Twee lae spoed- en een hoë spoed posisie sensorlose beheer (PSB) metodes vir RSMe is ondersoek. Hierdie metodes is uitgebrei om twee hibriede PSB metodes to skep wat die RSM van stilstand tot by kenspoed posisie sensorloos kan beheer. Die ontwikkelde hibriede metodes maak gebruik van 'n histerese oorskakelings skema en fase geslote lus sinchronisasie

Daar word in hierdie tesis bevestig dat die laterale rib RSM nie beheer kan word met die geondersoekte PSB metodes by nul stroom nie. Eindige element simulasie resultate wys egter daarop dat die ideale rotor RSM wel beheer kan word met die geondersoekte metodes by nul stroom. 'n Nuwe konstruksie metode is voorgestel om twee ideale rotor RSMe to bou. Gemete vloed omsluiting kurwes resultate korreleer baie goed met dié van die eindige element simulasies. Gemete resultate wys ook daarop dat PSB van die nuwe masjiene moontlik is by nul stroom.

'n Eindige element pakket is gebruik om die speek-koëffissiënt van die RSM te vergelyk met drie tipes veld-versterkte permanent magneet masjiene, asook een veld verswakte permanent magneet versinkte masjien. Die simulasie resultate wys dat die RSM se speek-koëffissiënt hoër is as die van die geondersoekte permanent magneet masjiene. Die RSM is dus geskik vir speek-koëffissiënt georienteerde PSB metodes, wat hoofsaaklik by stilstand en lae spoed gebruik word.

Die ontwikkelde hibried PSB metodes is getoets en geëvalueer met drie voorgestelde industriële toepassings. Die eerste is 'n reluktansie sinchroon wind generator met 'n omsetter uittree laagdeurlaat filter. Die laagdeurlaat filter laat toe dat langer kabels vanaf die omsetter na die generator gebruik kan word. Die kombinasie van die laagdeurlaat filter en die PSB metodes laat toe dat die drywingselektronika en die beheerders in die toring basis geplaas kan word. Dit kan die gewig van die nasel verminder. Goeie maksimum drywingspunt volging laboratorium resultate word getoon met die hoë frekwensie ondersteunde hibried PSB metode.

Die tweede geondersoekte toepassing is 'n posisie sensorlose beheerde, varierende ratkas elektriese voertuig RSM. Goeie simulasie en gemete draaimoment resultate van die RSM word getoon. Simulasie resultate toon dat die fundamentele q-as stroom harmoniek dominant is in die demodulasie skema van die hoë frekwensie PSB metode, as gevolg van die hoë ken stroom van die motor. Die hoë frekwensie PSB metode is uitgebrei om die fundamentele stroom harmoniek te onderdruk in die demodulasie skema sonder om enige filters by te voeg.

Die finale toepassing is 'n nuwe myn windas wat van twee posisie sensorlose beheerde RSMe gebruik maak om klippe ondergronds te verplaas vanaf die ontploffings area. Die voorgestelde ontwerp verbeter die huidige ontwerp ten opsigte van die veiligheid, energie effektiwiteit en robuustheid. Gemete resultate wys dat ken draaimoment moontlik is met altwee speek-koëffissiënt metodes. 'n Automasie metode, wat die maksimum draaimoment op die windas beperk en automaties homself bevry indien hy vasval, is voorgestel en geëvalueer.

Acknowledgements

I would like to express my sincere appreciation to:

- My Lord for helping me put down my own Ebenezer.
- Prof. Maarten Kamper, my supervisor, for all his advice and support.
- Oceantech for their support in my project, especially Michael Martin.
- Mr. Peter Landsmann, who influenced my work in so many ways in terms of advice, support and constant motivation.
- Dr. H.W de Kock, who always had time to answer my questions and to drive through to Stellenbosch.
- Prof. Ralph Kennel, without him my visit to Munich would not have been possible.
- JP du Plooy for the development of the Python script used to flux map machines from within JMAG.
- Chris Vorster and Albertu Prins for allowing me to use their JMAG models for my research and especially Chris for the design of the EV RSM.
- The international office of the University of Stellenbosch, for financial support.
- The international office of the Technical University of Munich, for their financial support.
- Daniela Dietmeier, who made my stay in Germany possible by organising funding and accommodation.
- The EEDSM bursary scheme, for their financial support.
- Marcia Ndala, who managed the funds from EEDSM.
- Andre Swart and Murry Jumat, without your practical knowledge and help none of this would have been possible.
- Fred Fourie, a true friend and a great colleague.
- Thank you to my parents who supported me in the decision to continue with my studies.
- Marelette de Wet, the one person without whom none of this would have been possible. Your love and support truly carried me throughout this last year, more than you would ever know. You truly are the love of my life.

I would lastly like to thank to Prof Ralph Kennel and Mr. Peter Landsmann of the Technical University of Munich. Thanks you for allowing me to visit your university for three months. I cannot describe in words how much I learned while under your academic supervision. Thank you to Peter for allowing me to use his setup in the laboratory and for always listening to my constant problems.

List of publications

Accepted conference proceedings:

- W.T. Villet, M.J. Kamper, P. Landsmann and R. Kennel. "Evaluation of a simplified high frequency injection position sensorless control method for reluctance synchronous machine drives". In Power Electronics, Machines and Drives (PEMD 2012), 6th IET International Conference on, pages 1-6, 2012.
- W.T. Villet, M.J. Kamper, P. Landsmann and R. Kennel. "Hybrid position sensorless vector control of a reluctance synchronous machine through the entire speed range". Power Electronics and Motion Control Conference (EPE/PEMC), 2012 15th International, pages LS4b-1.1-1-LS4b-1.1-7, 2012.
- M.J. Kamper and W.T Villet. "Design and Performance of Compensated Reluctance Synchronous Machine Drive with Extended Constant Power Speed Range". In Energy Conversion Congress and Exposition (ECCE), 2012 IEEE, pages 4330-4337, 2012.
- W.T. Villet and M.J. Kamper. "Design of a reluctance synchronous machine for saliency based position sensorless control at zero reference current". In Industrial Technology (ICIT), 2013 IEEE International Conference on, pages 301-306, 2013.
- W.T. Villet and M.J. Kamper. "Evaluation of reluctance synchronous machine rotor topologies for position sensorless control". In Post Southern African Universities power engineering conference (SAUPEC) paper, 2013.
- W.T. Villet, M.H.A. Prins, C.W. Vorster and M.J. Kamper. "Saliency performance investigation of Synchronous Machines for Position Sensorless Controlled EV drives". In Sensorless Control for Electrical Drives (SLED), 2013 Symposium on.

Accepted journal:

- W.T. Villet and M.J. Kamper. "Variable-gear EV Reluctance Synchronous Motor Drives - An Evaluation of Rotor Structures for Position Sensorless Control". In IEEE Transactions on Industrial Electronics.

Submitted journal under review:

- W.T. Villet and M.J. Kamper. "Position Sensorless Control of a Reluctance Synchronous Wind Generator with an inverter output LC Filter". In IET Electric Power Applications.

Opgedra aan:
Cornelia Petronella Villet
08-02-1963 tot 02-03-2013
Ek wens Ma was hier om die te lees, want sonder Ma sou niks van hierdie moontlik gewees het nie.

Nomenclature

Acronyms

$\alpha\beta$	Two axis stationary reference frame
ABC	Three phase stationary reference frame
AC	Alternating current
BPF	Band pass filter
CCAC	Constant current angle control
DC	Direct current
DFIG	Double fed induction generator
DTC	Direct torque control
dq	Direct quadrature - synchronously rotating reference frame
EV	Electrical vehicle
FE	Finite element
FG	Fixed gear
FI-IPM	Field intensified interior permanent magnet
FI-PM	Field intensified permanent magnet
FOC	Field oriented control
FW-IPM	Field weakening interior permanent magnet
HEV	Hybrid electrical vehicle
HF	High frequency
HFI-PSC	High frequency injection position sensorless control
IM	Induction machine
IPMSM	Interior permanent magnet synchronous machine
LPF	Low pass filter
LUT	Lookup table
MPPT	Maximum power point tracking
PI	Proportional integral
PLL	Phase-locked loop
PM	Permanent magnet
PMSG	Permanent magnet synchronous generator
PMSM	Permanent magnet synchronous machine
PSC	Position sensorless control
PWM	Pulse width modulation
RPS	Rapid prototyping system

RSG	Reluctance synchronous Generator
RSM	Reluctance synchronous machine
RTAI	Real-time application interface
SB-PSC	Saliency-based position sensorless control
SCIG	Squirrel cage induction generator
SM-FI-PM	Surface mounted field intensified permanent magnet
SPMSM	Surface mounted permanent magnet synchronous machine
SRM	Switched reluctance machine
SVPWM	Space vector pulse width modulation
UCG	Uncontrolled generator
UDDS	Urban dynamometer driving schedule
VG	Variable gear
VSD	Variable speed drive
VSI	Voltage source inverter
WEC	Wind energy conversion

Symbols

Symbol	Description
i	Current $[A]$
θ_r	Mechanical rotor angle $[rad]$
θ_e	Electrical rotor angle $[rad]$
ω_r	Mechanical rotor speed $[rad/s]$
ω_e	Electrical rotor speed $[rad/s]$
t	Time $[s]$
p	Pole pairs
$\boldsymbol{T}$	Reference frame transformation matrix
u	Voltage $[V]$
ψ	Magnetic flux-linkage $[Wb$-turns$]$
r_s	Phase resistance $[\Omega]$
L_d, L_q	d-and q-axis self-tangential inductances $[H]$
L_{ds}, L_{qs}	d- and q-axis secant inductances $[H]$
L_{dq}, L_{qd}	d- and q-axis mutual inductances $[H]$
T_m	Mechanical torque $[Nm]$
$\boldsymbol{J}$	Orthogonal rotation matrix
J_{eq}	Mechanical inertia $[kg.m^2]$
β_{eq}	Mechanical friction $[N]$
T_L	Load torque $[Nm]$
U_{dc}	DC bus voltage $[V]$
F_s	Switching frequency $[Hz]$
f_s	Sampling frequency $[Hz]$
T_s	Sampling time $[s]$
ϕ	Maximum torque per ampere current angle $[^\circ]$
U_{dAVG}	Average d-axis voltage $[V]$
M_L	Applied load $[Nm]$
ω_c	Carrier frequency $[rad/s]$
L_m	Mean inductance $[H]$
ΔL	Inductance Saliency $[H]$
u_c	Injection voltage $[V]$
k_p	Current proportional gain $[V/A]$
T_i	Current time constant $[s]$
k_{pPLL}	PLL proportional gain $[rad/s]$
T_{PLL}	PLL time constant $[s]$
$LPF_{\boldsymbol{i}}$	Current LPF $[rad/s$
LPF_{PLL}	PLL LPF $[rad/s]$
k_{ps}	Speed proportional gain $[Nms/rad]$
T_{is}	Speed time constant $[s]$
LPF_s	Speed LPF $[rad/s]$
$\acute{\boldsymbol{L}}_s^s$	Inductance derivative with respect to θ_e
ω_p	Speed changeover threshold $[rad/s]$
Y_Σ	Isotropic admittance $[S]$
Y_Δ	Salient admittance $[S]$
$\boldsymbol{u}_L^s$	Isotropic voltage vector $[V]$
$\Delta\boldsymbol{i}_{FM}^s$	Fundamental current circulation $[A]$
$\Delta\boldsymbol{i}_{HF}^s$	Saliency current circulation $[A]$

e^s_{prd}	Current prediction error $[A]$
u_{inj}	Arbitrary injection voltage $[V]$
θ_{CC}	Compensation curve [degrees]
ω_{h1}	Lower speed changeover threshold $[rad/s]$
ω_{h2}	Upper speed changeover threshold $[rad/s]$
θ_S	Electrical angle acquired from the SB-PSC method $[rad]$
θ_{FS}	Electrical angle acquired from the FS-PSC method $[rad]$
P_{in}	Input power $[kW]$
P_m	Shaft power $[kW]$
P_{Losses}	Power loss $[kW]$
η	Efficiency [%]
L_{dq}	Mutual inductance $[H]$
γ	Saliency shift$[^o]$
ζ	Saliency ratio
P_t	Turbine power $[kW]$
ρ_{air}	Air mass density [Kg/(m^3))]
r_b	Radius of the sweep are $[m]$
V_w	Wind Speed $[m/s]$
C_p	Turbine power coefficient
λ	Tip speed ratio
β	Blade pitch angle $[rad]$
w_m	Blade tip speed $[m/s]$
d_{abc}	Switching states
Z_c	Tower cable impedance [Ω]
P_{cu}	Copper losses $[W]$
P_{iron}	Iron losses $[W]$
R_f	Series filter resistance [Ω]
f_o	Cut-off frequency $[Hz]$
L_f	Filter inductance $[H]$
C_f	Filter capacitance $[F]$
$\boldsymbol{u}_i$	Inverter voltage vector $[V]$
$\boldsymbol{i}_i$	Inverter current vector $[V]$
d_{abc}	Inverter switching states
λ_{opt}	Optimal tip speed ratio
C_p^{max}	Maximum turbine power coefficient
T_{mopt}	Optimum generator shaft torque $[Nm]$
K_{opt}	Wind turbine constant
u_{ew}	End-winding inductance voltage drop $[V]$
L_{ew}	End-winding inductance $[H]$

Indices

s, r	Stator and rotor respectively
a, b, c	Stator phase axis
α, β	Stator fixed frame
d, q	Rotor fixed frame
$\wedge, *$	Estimated value and reference value respectively
δ	Injected direction
i	Inverter quantities

Contents

List of Tables

List of Figures

Chapter 1

Introduction

Fossil fuels are currently the primary source of energy across the globe, but are in limited supply and will one day be depleted. Carbon dioxide pollution is caused by the burning of fossil fuels. Carbon taxes are placing governments under pressure to reduce CO_2 emissions within their respective countries. Safer and environmentally cleaner ways of harvesting energy are thus required to provide electrical power and reduce the CO_2 emissions.

Renewable energy sources can be used to reduce the demand for fossil fuel energy. Wind and solar energy are both currently the most widely deployed and commercially used renewable energy sources. Renewable energy should not be the only area of focus in the campaign to reduce fossil fuel emissions. Energy efficiency is equally important. An estimated 60% of all electrical energy is consumed by electric motors and drives. Industrial electric motors such as pumps, fans etc. are proven to be more efficient when controlled with variable speed drives (VSDs). The power consumption of these VSD controlled pumps and fans can be reduced by half by dropping the flow rate by just 20% when full capacity is not needed.

The combination of renewable energy sources and energy efficient drives can contribute towards a sustainable clean energy usage cycle while reducing the carbon footprint.

1.1 The Reluctance Synchronous Machine

Permanent magnet synchronous machines (PMSMs) are widely used, especially in wind generator and electric vehicle (EV) research and applications. The PMSM is an attractive alternative to the induction machine (IM), which is currently the industry workhorse, due its high efficiency, good power factor and high torque density. Rare earth PM material is expensive due to a limited- and delayed supply chain. A new focus on non-PM machines for industry applications has led various researchers back to one of the most simple electrical machines, the reluctance synchronous machine (RSM).

The RSM consists of a standard, non-salient 3-phase stator and an unexcited salient rotor. The RSM has no rotor windings, hence is brushless. The RSM is advantageous from a manufacturing cost point of view due to it not having any rotor conductors or PMs. The RSM design is thus truly robust, affordable and well suited to harsh environments like mines.

The IM is still the industrial standard despite the advantages of the RSM. The RSM was never seriously considered as an alternative to the IM due to its poor performance when operated with open loop V/Hz control. The advances made in semi-conductor technology and VSDs have led to a rejuvenated investigation in the field of RSM technology. It is shown in [7] that a RSM delivers 50% more torque than an IM with the same stator volume. Investigations by Vagati [8, 9] and Kamper [10] on the performance of the VSD fed RSM with vector control followed. Both authors concluded that the RSM is more efficient than the IM, thus reopening discussions about the viability of the RSM drive for industry applications.

Soon more research followed on RSM designs, their efficiency and comparison to other AC machines [11–16]. It can be concluded from literature that the RSM has a 10%-15% higher torque density than the IM, which is a more modest conclusion than presented in [7], but still shows the value of the RSM.

The advantages of the RSM drive are summarised as follows:

- The reliability of the RSM is higher than that of PM machines due to it not suffering from demagnetisation.
- No high voltages occur under uncontrolled generator (UCG) operation as with PM machines. UCG voltage is important from a safety point of view.
- The excitation field of the machine can be adjusted, thus allowing for field weakening at high speeds.
- No possible arcing can occur in the rotor between broken rotor bars and the laminations as with IMs. This positive characteristic is important for certain mining applications.
- Constant current angle control and maximum torque per ampere curves, that are generated from finite element analysis, can be used to operate the RSM drive at optimum efficiency [17].
- High torque pulsations under short circuit inverter conditions are not a problem for RSMs, unlike with IMs.
- The RSM has a 10%-15% larger torque density than IMs
- The RSM efficiency is higher than that of the IM [12].
- The RSM does not have brushes or slip-rings.
- The RSM does not have any rotor conductors or PM material. This is important from a manufacturing costs point of view.

Some drawbacks of the RSM are summarised as:

- Accurate knowledge of the rotor position is required for optimum vector control as with all synchronous machines.
- The power factor of the RSM is lower than that of PM machines, hence a larger kVA rated drive is required.
- The power density of the RSM is smaller than that of PM machines.
- The performance of RSMs with large L_d/L_q ratios compares well to that of IMs in the extended constant power speed range [18]. The constant power speed range ratio of the RSM is however still much lower than that of interior PM machines.

It can thus be summarised that even though the RSM does not have the efficiency of the PMSM, it does have the advantage of not having any expensive rare earth PM material. Not only is it possible to manufacture the RSM more cheaply than the IM, but has been shown to have superior efficiency as well. For the RSM drive to be seen as a viable alternative to the IM however, certain criteria need to be met as identified by [17]:

1. Energy efficient performance in the entire speed range.

2. Position sensorless control.
3. Good dynamic response.
4. Robust design of machine.
5. Low audible noise.

1.2 Problem Statement

The item in the list of requirements, as listed above, that still needs to be addressed is number 2, namely position sensorless control (PSC) of the RSM. The topic of position sensorless controlled RSM drives is definitely not novel, dating back to 1991 [19]. The question raised in this thesis is, "has the research and development of PSC methods for RSM drives come far enough to be used in industry applications?" Various companies have started marketing and selling the RSM drive in the last few years as an alternative to the IM for fan and pump applications. Most of these products operate position sensorless. Implementing PSC on fans and pumps, which does not require high startup- or dynamic torque, is less challenging and can even be implemented with open loop V/Hz control. It it to be shown in this thesis however, that the RSM applications are not limited to fans and pumps, but that they can be used in applications where dynamically variable torque is required from startup up to rated speed.

A summary of PSC literature on synchronous machines is shown in Table A.1, in Appendix A. It is shown in Table A.1 that the majority of research concerning PSC methods for RSM drives is tested and evaluated on RSMs with power ratings of 5 kW or smaller. It is also shown in Table A.1 however, that this stems true for all types of synchronous machines. The average power rating of the literature summary, concerning RSM drives, is 2.2 kW. Also one should note that only a few of these publications are aimed at specific industry applications. Smaller rated machines provide a good platform to implement and evaluate PSC methods. These methods should however be tested on larger machines to asses their industry readiness especially for variable torque applications. It is thus proposed in this thesis that some of the PSC methods for RSM drives be evaluated with medium power range machines with industrial applications.

It is stated in the introduction of this chapter that it is necessary to reduce our carbon footprint to protect the earth. With this goal in mind, three areas of focus are chosen for this project namely:

- Renewable energy.
- Reduction of CO_2 at the point of use.
- Energy efficiency.

An industry application is chosen for each area of focus:

(i) **Position sensorless controlled reluctance synchronous wind generator with an inverter output LC filter:** The challenge with this application is implementing the PSC methods with the inverter LC filter. The purpose of the LC filter will be explained later in this thesis.

(ii) **Position sensorless controlled reluctance synchronous machine for a variable gear electric vehicle:** The challenge with this application is the startup torque required.

(iii) **Position sensorless controlled mine scraper winch:** The challenge with this application is the high startup torque required from the machine. Automating the entire scraping and retrieval process without a position sensor will also be challenging.

1.3 Thesis Layout

Chapter 2: A mathematical model is derived for the RSM. Some theory behind machine control with VSDs is briefly discussed.

Chapter 3: The non-linear aspects of the RSM are highlighted in this chapter. The finite element properties of the RSM are laid out and compared to the results of a measured analysis that is performed on the RSM. The simulation process is discussed. Finally an inventory summary of the machines investigated in this thesis is provided.

Chapter 4: The alternating high frequency injection PSC method is discussed and evaluated.

Chapter 5: The arbitrary injection PSC method is discussed and evaluated.

Chapter 6: The fundamental saliency PSC method is discussed and evaluated.

Chapter 7: Two hybrid PSC methods are derived and evaluated.

Chapter 8: Finite element software is used to investigate rotor modifications to improve the PSC performance of RSM drives. Two experimental machines are built and evaluated. The performance of these machines are evaluated under various different circumstances.

Chapter 9: Finite element software is used to compare the position sensorless controllability of different synchronous machine topologies on a per unit scale. Design improvements are proposed and investigated.

Chapter 10: A PSC method is derived for a reluctance synchronous wind generator with a LC inverter output filter.

Chapter 11: The investigated PSC methods are implemented and evaluated on a RSM for a variable gear electric vehicle drivetrain.

Chapter 12: The investigated PSC methods are implemented and evaluated on a position sensorless controlled mine scraper winch.

Chapter 2

Modelling and Control of the RSM Drive

A brief explanation of reference frame transformations, as used in drive systems, is given in this chapter followed by a mathematical derivation of the RSM in the discussed reference frames. This is followed by background knowledge regarding the control strategies implemented on the RSM drive in this thesis. Field oriented control is discussed first, followed by an overview of basic current- and speed controllers as implemented during this research.

2.1 Clarke Transformation

The Clarke transformation is used to transform three phase circuits to a stationary two-axis orthogonal reference frame [20]. The Clarke transformation is also known as the $\alpha\beta$ transformation and is written as:

$$\boldsymbol{i}_s^s = \begin{bmatrix} i_\alpha \\ i_\beta \\ i_o \end{bmatrix} = \frac{2}{3} \begin{bmatrix} 1 & -\frac{1}{2} & -\frac{1}{2} \\ 0 & \frac{\sqrt{3}}{2} & -\frac{\sqrt{3}}{2} \\ \frac{1}{2} & \frac{1}{2} & \frac{1}{2} \end{bmatrix} \begin{bmatrix} i_a \\ i_b \\ i_c \end{bmatrix} \tag{2.1}$$

where i_α and i_β are components in an orthogonal reference frame and i_o the homopolar component which is zero in a balanced system. This reference frame will be referred to as the stationary reference frame in this thesis. The subscript s, in (2.1) refers to stator quantities and the superscript s, denotes the quantity to the stationary reference frame. The transformation is shown in vector form in Fig. 2.1. The current vector $\boldsymbol{i}_s^s$ rotates with angular velocity ω.

2.2 Park Transformation

The park transformation is used to transform three phase AC circuits to two phase DC quantities in a synchronous rotor reference frame. In other words, all parameters are defined in a reference frame running synchronously to the rotor [21]. The park transformation, which is also known as the dq transformation, is derived as in (2.2).

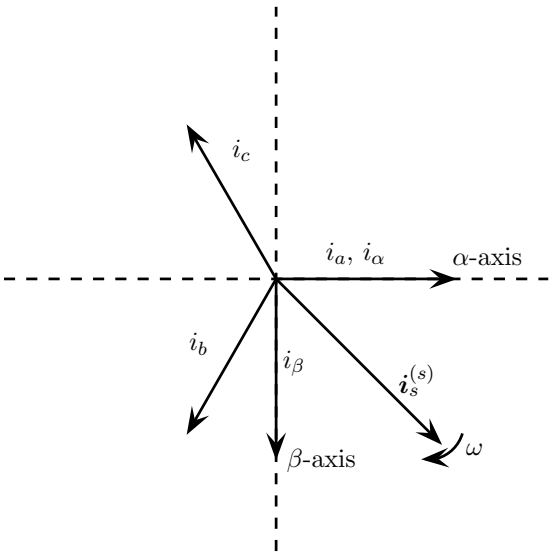

Figure 2.1: The Clarke Transformation.

$$\boldsymbol{i}_s^r = \begin{bmatrix} i_d \\ i_q \\ i_o \end{bmatrix} = \frac{2}{3} \begin{bmatrix} \cos(\theta_e) & \cos(\theta_e - 120^o) & \cos(\theta_e + 120^o) \\ -\sin(\theta_e) & -\sin(\theta_e - 120^o) & -\sin(\theta_e + 120^o) \\ \frac{1}{2} & \frac{1}{2} & \frac{1}{2} \end{bmatrix} \begin{bmatrix} i_a \\ i_b \\ i_c \end{bmatrix} \tag{2.2}$$

This reference frame is referred to as the rotary reference frame in this thesis. Superscript r, in (2.2) denotes the current in the rotary reference frame. The electrical rotor angle of the machine, θ_e, is calculated as in (2.3), where θ_r is the mechanical angle of the rotor, ω_e is the electrical rotor speed and p the number of pole pairs.

$$\theta_e = p\theta_r = \int \omega_e \, dt \tag{2.3}$$

The convention of the rotary reference frame as well as the *abc* reference frame are explained with a two pole RSM in Fig. 2.2. The direct axis is chosen in the direction with the most rotor steel and the quadrature axis is chosen in the direction with the least rotor steel, as seen in Fig. 2.2.

The rotary reference frame is more suitable for complex control systems of electrical machines than the *abc* reference frame [22]. The transformation to the rotary reference frame eliminates all the time varying inductances in the machine equations [22]. The signals of the control loops are *DC* quantities in steady state, making it easier to design the control system. The transformations above are not only used with the stator current, but also apply in general to other variables like voltage and flux linkage.

It is also handy to be able to transform current, voltage or flux linkage from the $\alpha\beta$ (stationary)- to the dq (rotary) reference frame and vice versa. This transformation is the one that is used during the course of this thesis to highlight various concepts. Transformation from the dq reference frame to the $\alpha\beta$ reference frame is done with $\boldsymbol{T}$ $(r \rightarrow s)$. For conversion from the $\alpha\beta$ reference frame to the dq reference frame, $\boldsymbol{T}^{-1}$ $(s \rightarrow r)$ is used. The two transformation matrices are defined as in (2.4) and (2.5).

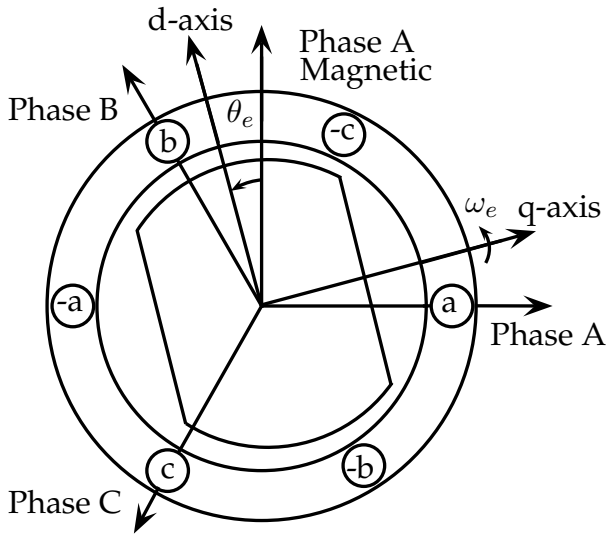

Figure 2.2: Rotary and *abc* reference frames of a 2-pole RSM.

$$\boldsymbol{T} = \begin{bmatrix} \cos(\theta_e) & -\sin(\theta_e) \\ \sin(\theta_e) & \cos(\theta_e) \end{bmatrix} \tag{2.4}$$

$$\boldsymbol{T}^{-1} = \begin{bmatrix} \cos(\theta_e) & \sin(\theta_e) \\ -\sin(\theta_e) & \cos(\theta_e) \end{bmatrix} \tag{2.5}$$

2.3 Mathematical Modelling of the RSM

System modelling is important to understand and control the RSM. The equations in the following subsections describe the RSM mathematically and are used to model and control the RSM drive.

2.3.1 Voltage equation

The RSM has a standard distributed winding 3-phase stator. The stator voltage vector is derived with Faraday and Ohm's law as:

$$\boldsymbol{u}_{abc} = \frac{d\boldsymbol{\psi}_{abc}}{dt} + r_s \boldsymbol{i}_{abc} \tag{2.6}$$

where r_s is the phase-resistance, $\boldsymbol{u}_{abc}$ the phase voltage vector and $\boldsymbol{\psi}_{abc}$ the flux linkage vector [23]. The RSM has no PM's or rotor windings, thus the only source of flux linkage is the stator coils as shown in (2.6). Equation (2.6) can be transformed to the rotary reference frame using (2.2) [23]:

$$u_d = r_s i_d + \frac{d\psi_d}{dt} - \omega_e \psi_q \tag{2.7}$$

$$u_q = r_s i_q + \frac{d\psi_q}{dt} + \omega_e \psi_d. \tag{2.8}$$

Assuming that the 3-phase system is balanced, u_o equals zero. Theoretically the transformation of the flux linkages to the rotary reference frame should remove all dependencies on θ_e [17]. The flux linkages however, still remains a function of θ_e due to stator slot openings as shown in Fig. 2.3 [17]. Furthermore,

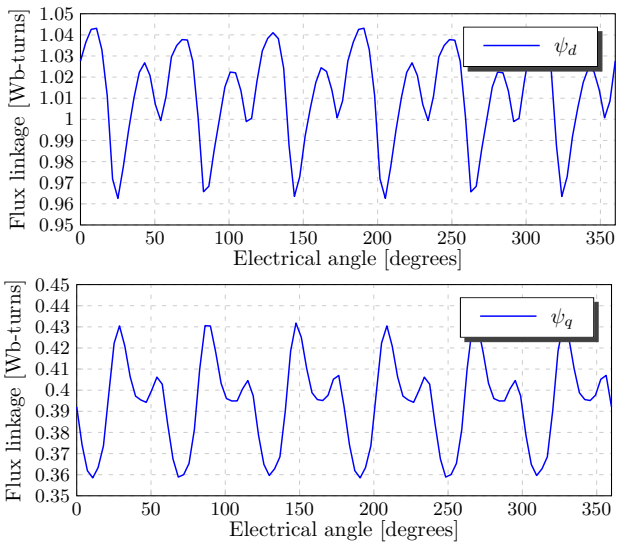

Figure 2.3: Flux linkage dependency on the electrical angle.

cross saturation and cross coupling is also present in the machine and needs to be taken into account when modelling the RSM [17]. Thus the d- and q-axis flux linkages are functions of i_d, i_q and θ_e, i.e.:

$$\psi_d = f(i_d, i_q, \theta_e) \qquad \psi_q = f(i_d, i_q, \theta_e). \tag{2.9}$$

The derivative of the d- and q-axis flux linkages can be expanded to partial derivatives as in (2.10) and (2.11) [24].

$$\begin{aligned} \frac{d\psi_d}{dt} &= \frac{\partial\psi_d}{\partial i_d}\frac{di_d}{dt} + \frac{\partial\psi_d}{\partial i_q}\frac{di_q}{dt} + \frac{\partial\psi_d}{\partial\theta_e}\frac{d\theta_e}{dt} \\ &= L_d\frac{di_d}{dt} + L_{dq}\frac{di_q}{dt} + \frac{\partial\psi_d}{\partial\theta_e}\omega_e \end{aligned} \tag{2.10}$$

and

$$\begin{aligned} \frac{d\psi_q}{dt} &= \frac{\partial\psi_q}{\partial i_q}\frac{di_q}{dt} + \frac{\partial\psi_q}{\partial i_d}\frac{di_d}{dt} + \frac{\partial\psi_q}{\partial\theta_e}\frac{d\theta_e}{dt} \\ &= L_q\frac{di_q}{dt} + L_{qd}\frac{di_d}{dt} + \frac{\partial\psi_q}{\partial\theta_e}\omega_e \end{aligned} \tag{2.11}$$

The partial derivatives of the flux linkages are represented by L_d and L_q, which are the self-tangential inductances [17]. Furthermore M'_d and M'_q are the d- and q-axis mutual-inductances [22, 23].

If the RSM rotor is skewed, the change in flux linkage due to rotor position is relatively small and can be omitted [22, 23]. The machine model therefore is simplified by not incorporating this component into the model. Thus, using equations (2.7), (2.8), (2.10) and (2.11) the RSM voltage equations are:

$$u_d = r_s i_d + L_d\frac{di_d}{dt} + L_{dq}\frac{di_q}{dt} - \omega_e\psi_q \tag{2.12}$$

$$u_q = r_s i_q + L_q\frac{di_q}{dt} + L_{qd}\frac{di_d}{dt} + \omega_e\psi_d \tag{2.13}$$

The tangential inductance is calculated with the slope of the flux linkage. The secant, or instantaneous inductance however, is the inductance at one flux linkage point and calculated as in (2.14). It is important to note that there is a difference between the tangential and secant inductances.

$$L_{ds} = \frac{\psi_d}{i_d} \quad and \quad L_{qs} = \frac{\psi_q}{i_q} \tag{2.14}$$

2.3.2 Torque equations

The torque produced by the RSM can be described mathematically by the vector product of the the current- and flux linkage vectors as in (2.15), which is in the stationary reference frame as indicated by superscripts s [17, 25]. The orthogonal rotation matrix $\boldsymbol{J}$ is defined as in (2.18) and is the equivalent of the complex operator j. Equation (2.16) describes the torque equation in the rotary reference frame as indicated by superscript r [20]. The factor 3/2 is a result of the non-power invariant transformation used. Equation (2.14) can be used to rewrite (2.16) with respect to the secant inductance as in (2.17).

$$\begin{aligned} T_m &= \frac{3p}{2}\boldsymbol{i}_s^{sT}\boldsymbol{J}\boldsymbol{\psi}_s^s = \frac{3p}{2}(\psi_\alpha i_\beta - \psi_\beta i_\alpha) && (2.15)\\ &= \frac{3p}{2}\boldsymbol{i}_s^{rT}\boldsymbol{J}\boldsymbol{\psi}_s^r = \frac{3p}{2}(\psi_d i_q - \psi_q i_d) && (2.16)\\ &= \frac{3p}{2}(L_{ds} - L_{qs}) i_d i_q && (2.17) \end{aligned}$$

$$\boldsymbol{J} = \boldsymbol{T}(\frac{\pi}{2}) = \begin{bmatrix} 0 & -1 \\ 1 & 0 \end{bmatrix} \tag{2.18}$$

2.3.3 Mechanical model

Combining the electrical model with a mechanical model creates a complete mathematical modelling of the RSM. The mechanical model of the RSM is derived in (2.19), where J_{eq} is the total system inertia and β_{eq} is the total system friction, both including the machine- and load instances. T_L is the applied load torque and ω_r is the mechanical rotor speed. The electrical speed is related to the mechanical speed by the number of pole pairs p, as shown in (2.20).

$$T_m = J_{eq}\frac{d\omega_r}{dt} + \beta_{eq}\omega_r + T_L \tag{2.19}$$

$$\omega_e = p\omega_r \tag{2.20}$$

2.4 Field oriented control of RSM drives

2.4.1 Variable speed drives for synchronous machines

The advance in power electronics allowed for the introduction of the variable speed drive (VSD). A very simple explanation of a VSD is shown in Fig. 2.4. A rectifier rectifies the 3-phase AC voltage to DC, after which an inverter inverts the DC voltages to AC voltages with variable frequency. With a VSD it is possible to vary the machine frequency and terminal voltage. This is very effective when used with asynchronous machines like the IM. Synchronous machines however, require the field to move synchronously to the rotor. This can be achieved with field oriented control (FOC). FOC, also known as vector control, allows the amplitude and phase voltages of synchronous machines to be varied.

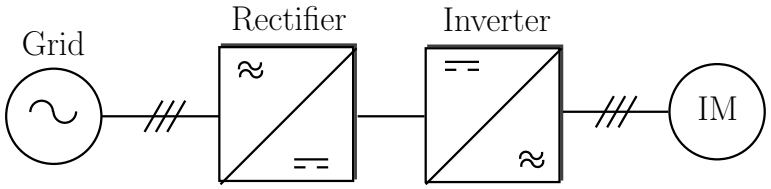

Figure 2.4: Power converter used for a variable speed drive.

The electrical angle of synchronous machines needs to be measured to implement FOC. This angle is used to transform the measured ABC currents to the rotary reference frame. The measured 3-phase currents are thus transformed to a DC current vector that allows standard control structures to be implemented [26]. By controlling the current it is not only possible to control the torque, but the speed and position of the rotor [26].

Stator voltages are usually not measured, implying open loop voltage vector control [26]. A voltage source inverter (VSI) is used to apply the 3-phase voltages to the electric machine. The switching states of the VSI are calculated by means of pulse width modulation (PWM). Space vector pulse width modulation (SVPWM) is the PWM scheme used in this project. The maximum applied voltage that may be obtained with basic PWM methods, like sub oscillation methods, is half of the DC bus voltage [27]. When using SVPWM, it is possible to apply voltages that are up to 15% higher than with normal PWM [27].

The VSI used in this thesis automatically adds deadtime to prevent the top and bottom switches conducting at the same time. The reference phase voltage in the stationary reference frame is limited to $0.866\,U_{dc}$, where U_{dc} is the DC bus voltage. If the magnitude of the reference voltage vector is higher than $0.866\,U_{dc}$, the reference voltage is limited while still retaining the reference voltage angle.

2.4.2 Current control of the RSM drive

Complex cascaded control structures can be implemented with synchronous machines for various applications. At the heart of these structures lies the current controller of the machine. Current control of RSM drives can be implemented with a PI controller. A PI controller will calculate reference voltages that will induce the reference current. It is thus necessary to derive a plant model for the RSM. Referring back to (2.12) and (2.13), there are two types of disturbances due to cross coupling and cross magnetization that can disturb the current controller [22]. The first are the speed voltage terms. These terms are a product of the electrical rotor speed and the flux linkage of the opposite axis. The speed voltages are dependent on the speed of the machine and according to [22], will affect the total voltage necessary to control the current during acceleration.

The second set of terms that can cause distortion are the cross magnetization terms. According to [22] equations (2.12) and (2.13) can be rewritten as in (2.21) and (2.22). The PI controller will only respond to the currents through the stator resistance and self-inductance if the speed voltage and mutual inductance terms are decoupled from the current control loop [22]. The d- and q-axis current control scheme with decoupled speed and mutual inductances terms are as shown in Figs. 2.5 and 2.6 [22].

$$u_d + \omega_e \psi_q - M'_d \frac{di_q}{dt} = r_s i_d + L_d \frac{di_d}{dt} \tag{2.21}$$

$$u_q - \omega_e \lambda_d - M'_q \frac{di_d}{dt} = r_s i_q + L_q \frac{di_q}{dt} \tag{2.22}$$

The continuous plant models $G_d(s)$ and $G_q(s)$ in the rotary reference frame are as in (2.23). Implementation of the controller is digital and the discrete transfer function of the plant is as in (2.24) [23]. Digital implementation is realised at a sampling frequency of $f_s = 12.2\ kHz$, and thus a sampling time of $T_s = 81.933\ \mu s$.

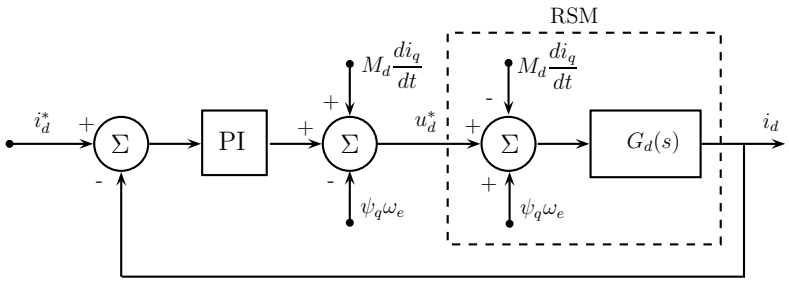

Figure 2.5: Decoupled d-axis current control.

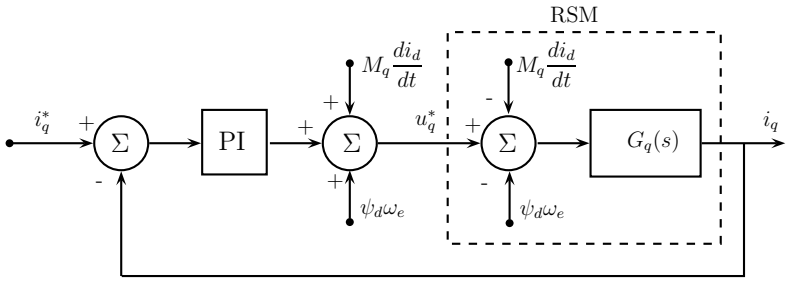

Figure 2.6: Decoupled q-axis current control.

$$G_{ds}(s) = \frac{1}{L_d s + r_s}, \qquad G_{qs}(s) = \frac{1}{L_q s + r_s} \tag{2.23}$$

$$G_{dz}(z) = \frac{1 - e^{-\frac{r_s T_s}{L_d}}}{r_s(z - e^{-\frac{r_s T_s}{L_d}})}, \qquad G_{qz}(z) = \frac{1 - e^{-\frac{r_s T_s}{L_q}}}{r_s(z - e^{-\frac{r_s T_s}{L_q}})} \tag{2.24}$$

Speed and mutual inductance decoupling requires lookup tables that accurately describe the non-linearity of the RSM. These measurements are not always available. It should be noted that the author decided not to use decoupling in this thesis. This was done in order to keep the control of the RSM simple and rather focus on the performance evaluation of the investigated position sensorless control (PSC) methods. Neglecting the decoupling terms opens up opportunities for further research. A block diagram of the current control as implemented in this thesis is shown in Fig. 2.7.

The reference current vector $\boldsymbol{i}_s^{r*}$ is divided into its x and y components: i_d^* and i_q^*. There are two ways of implementing this. The first is with constant d-axis current control. This method is outdated and inefficient as shown in [22]. The second method, which is proven to be the most efficient, is the constant current angel current control (CCAC) method [22, 23]. The maximum torque per ampere current angle, ϕ, is used as in (2.25) to calculate the appropriate reference currents. The CCAC angle can be acquired from finite element (FE) package simulations or through measurements.

$$\begin{aligned} i_d^* &= \boldsymbol{i}_s^{r*} cos(\phi) \\ i_q^* &= \boldsymbol{i}_s^{r*} sin(\phi) \end{aligned} \tag{2.25}$$

The current controller is protected against windup with a saturation flag that is set in the SVPWM function when the reference voltage vector exceeds the maximum voltage that can be applied. When this flag is set high the PI current controller stops its integration part, changing it to a proportional controller, until the reference voltage is within safety range. This is known as anti-integrator windup.

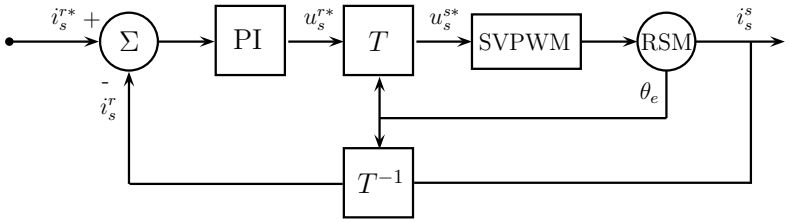

Figure 2.7: Space vector current control implementation.

The RSM torque is a function of current as well as the flux linkages, as seen in (2.16). Although the relationship between the machine current and the torque is not completely linear, current control can be used as a very simple method of torque control.

2.4.3 Speed control of the RSM drive

Cascaded control structures can be used to control the speed of the RSM drive. This cascaded control structure is as shown in Fig. 2.8. The inner control loop of the cascaded speed control structure is a current control loop as shown in Fig. 2.8. The outer control loop is the speed control loop. The speed controller is also implemented with a PI controller. The output of the speed controller is the reference current which is necessary to drive the speed error to zero.

The response time of the speed loop is chosen to be much slower than that of the current control loop [23]. With cascaded control structures the inner control loop should always have the fastest response time. In this case it can be assumed that the reference current is reached instantaneously.

2.4.4 Position sensorless vector control

It shown in this chapter that it is necessary to have knowledge of the electrical rotor angle of the RSM for FOC. This can be obtained from position sensors like resolvers, encoders and Hiperface encoders. Generally position sensors are expensive and fragile. Also control unit circuitry needs to be developed to read these sensors. It is thus clear that there are several cost and reliability advantages to having a position sensorless drive system. The PSC methods evaluated in this thesis are implemented with FOC and use the control structures discussed in this section.

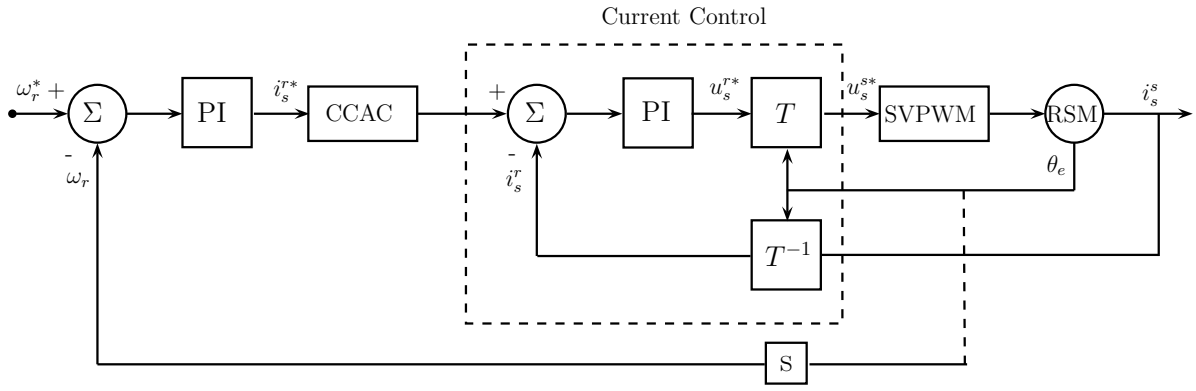

Figure 2.8: Space vector speed control implementation.

Chapter 3

Non-linear Mapping of Synchronous Machines

Equations are derived in Chapter 2 to model the RSM mathematically. It is crucial to have knowledge of the machine parameters to use the derived equations for modelling, simulations and lookup table creation. The d- and q-axis flux linkages and inductances of the RSM are not constant nor linear as a function of stator current, hence inaccurate results will be obtained from simulations, modelling etc. if these parameters are perceived as constant. Two methods of mapping the non-linearity of synchronous machines can be used. The first is by means of finite element (FE) software. The second method is by means measurements.

The two flux mapping methods used in this thesis are explained at the beginning of this chapter. This is followed by a brief explanation of the simulation software used as well as the practical setup used. Finally this chapter is concluded by summarising all the machines which are discussed in this thesis.

3.1 FE Software Aided Flux Mapping

Machine 1, as listed in Table 3.1, is used for evaluation in this section. The rest of Table 3.1 is discussed at the end of this chapter. The JMAG package is used for 2D FE simulations in this thesis. A quarter model mesh grid of Machine 1 is shown in Fig. 3.1a. Since this rotor has two pole pairs, only a quarter model is simulated. Laminated steel is used in the rotor and stator. The full stack length is taken into account during simulation.

The d-axis of the RSM is in the direction of the most steel and the q-axis in the direction of the flux barriers. Flux flows freely in the d-axis direction, but is limited in the q-axis direction. This results in a difference in inductance where $L_d > L_q$. The field plot of the quarter model of the RSM at rated conditions is shown in Fig. 3.1b. Saturation in the ribs of the RSM is visible in Fig. 3.1b.

A Python script which was developed at the Electrical Machines Laboratory, is used to communicate with JMAG to map ψ_d and ψ_q as a functions of i_d and i_q. It was shown in Fig. 2.3 that the flux linkage not only varies as a function of current but as a function of θ_e as well. The effect of θ_e on the flux linkages is not included in the flux map. The flux linkages are averaged over one electrical-, or ripple period. The Python script can run unskewed or skewed simulations. Skewing of the rotor is simulated in 5 sub-stacks. The flux mapping thus includes all the saturation and cross-coupling effects and can thus be used as a very accurate representation of the machine. JMAG does not include the effect of the end-winding inductance. The calculation of the end-winding inductance is not within the scope of this thesis and is thus not included in the FE modelling. It is recommended that this be addressed in future work. The two flux linkage maps obtained from the FE package are shown in Fig. 3.2. Figure 3.2 clearly shows that the flux linkage of the RSM is not constant nor is it linear as a function of current.

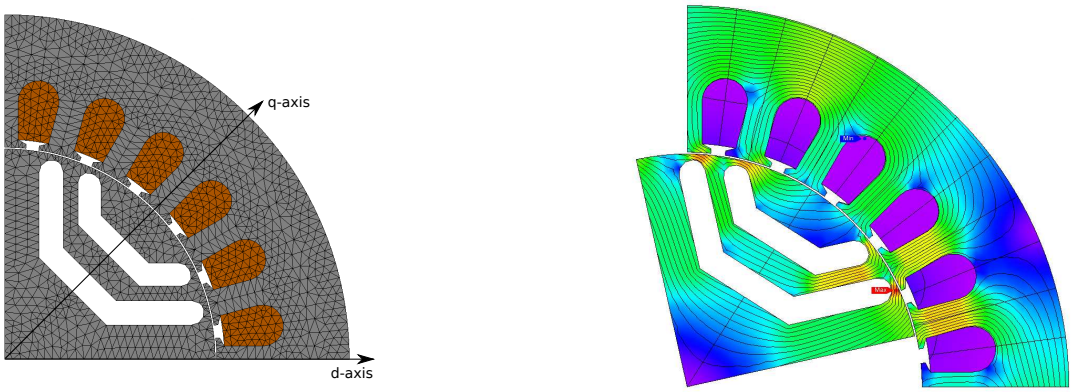

(a) Mesh grid of the RSM.

(b) Field plot of the RSM.

Figure 3.1: RSM modelling in the FE environment of Machine 1.

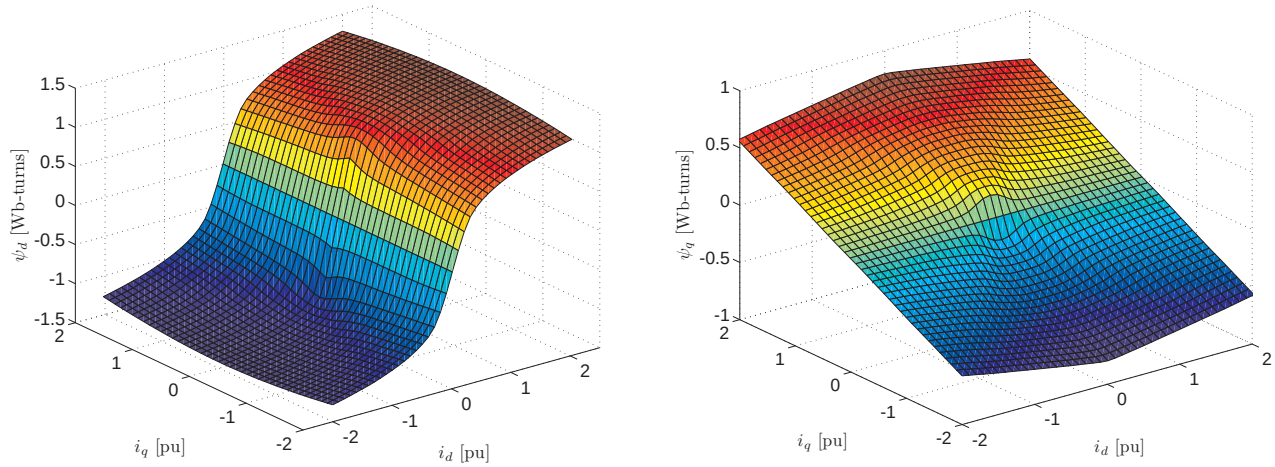

(a) FE simulated d-axis flux linkage map.

(b) FE simulated q-axis flux linkage.

Figure 3.2: FE simulated flux linkage maps of Machine 1.

The rotor of machine 1 is designed at Stellenbosch University. However, there is an uncertainty regarding the type of laminated steel used for the rotor. The stator is a standard off the shelf IM stator. The details of this stator steel are also not available due to the issue of intellectual property.

3.2 Measuring The Machine Flux Map

It is important to verify the FE software results by comparing it to measured results. Again machine 1 is used for evaluation in this section. The process of measuring the flux map of the RSM is developed by Mr. P. Landsmann from the Technical University of Munich. Although this method is not published the results obtained from this method are used in [2, 3] and [28]. The method of flux mapping is as follow.

If the stator current, $\boldsymbol{i}_s^r$, is kept constant with a current controller, the flux, $\boldsymbol{\psi}_s^r$ will also be constant in the rotor fixed frame. As a result (2.7) and (2.8) simplify to:

$$\boldsymbol{u}_s^r = r_s \boldsymbol{i}_s^r + \boldsymbol{J}\omega_e \boldsymbol{\psi}_s^r \tag{3.1}$$

If the RSM is driven at a constant speed ω while the current is controlled with a PI controller, the PI

controller will apply the voltage, $\boldsymbol{u}_s^r$, to keep the current constant at the driven speed. Assuming that the resistance r_s is known, it is possible to calculate $\boldsymbol{\psi}_s^r$ through:

$$\boldsymbol{\psi}_s^r = \boldsymbol{J}^{-1}\frac{\boldsymbol{u}_s^r - r_s\boldsymbol{i}_s^r}{\omega_e} \tag{3.2}$$

The stator resistance can be calculated during the measurements to account for temperature rise. Equation (2.7) can be used for this calculation if the voltage consists only out of a resistive term. This implies that the current vector has to be aligned with the flux linkage vector as in (3.3). According to P. Landsmann, this is only valid if the current vector alignment is in a general direction where the current doesn't produce torque. Usually this is in the d-axis direction. This measurement is achieved by turning the RSM at a high speed with a shaft connected IM while the current controller is set to rated current in the d-axis direction. The resistance is then calculated with (3.4) where u_{dAVG} is the average d-axis voltage over a predetermined period and i_d^* is the target d-axis current.

$$\boldsymbol{i}_s^{rT}\boldsymbol{T}\boldsymbol{\psi}_s^r = 0 \tag{3.3}$$

$$r_s = \frac{u_{dAVG}}{i_d^*} \tag{3.4}$$

The measured flux linkage maps of machine 1 consist of 29 different d-axis current values and 37 different q-axis current values, resulting in two 29x37 tables. The measured d- and q-axis flux linkage curves as obtained by P. Landsmann using equations (3.2) and (3.4), are shown in Figs 3.3a and 3.3b.

The uncoupled d- and q-axis flux linkages are used to compare the measured results of the RSM to the FE simulation results in Fig. 3.4a. These flux linkage curves are extracted from the measured flux map with (3.5). Some inconsistencies exists between the measured and FE results. It is the author's belief that this is due to the uncertainty regarding the stator- and rotor steel and the negligence of the end winding inductance in the FE model. The correlation between the simulated and measured results are still satisfactory.

The d- and q-axis tangential inductances are calculated from the uncoupled flux linkages as in (3.6) and (3.7). The measured- and FE simulation inductance curves are compared in Fig. 3.4b. The inconsistencies of the flux linkages affects the inductances as well. Also shown in Fig. 3.4b is the average difference inductance, ΔL. The significance of this machine parameter is explained in the next chapter.

$$\psi_d = \psi_d(i_d, 0); \qquad \psi_q = \psi_q(0, i_q) \tag{3.5}$$

$$L_d = \frac{\Delta\psi_d}{\Delta i_d}; iq = 0 \tag{3.6}$$

$$L_q = \frac{\Delta\psi_q}{\Delta i_q}; id = 0 \tag{3.7}$$

3.3 Simulation Tools

Simulations are valuable for testing of control algorithms. The simulation package used in this thesis is the MATLAB Simulink package from Mathworks. The synchronous machine Simulink block is shown in Fig. 3.5. This model allows the user to apply a voltage vector, $\boldsymbol{u}_s^s$, in the stationary reference frame as well as an applied load, T_L. The model then calculates the current vector in the stationary reference frame, torque, mechanical speed and rotor angle.

Figure 3.6 is a subset of the model in Fig. 3.5. This block diagram shows how the current vector and torque are calculated with (2.6) and lookup tables. The measured or simulated flux linkage maps

of the machine are used as lookup tables. The flux linkage vector, $\boldsymbol{\psi}_s^s$, is deliberately calculated in the stationary reference frame to ensure that all speed voltage and mutual inductance terms are included in the electrical model. The rest of the terms (speed and position) are calculated with standard machine equations.

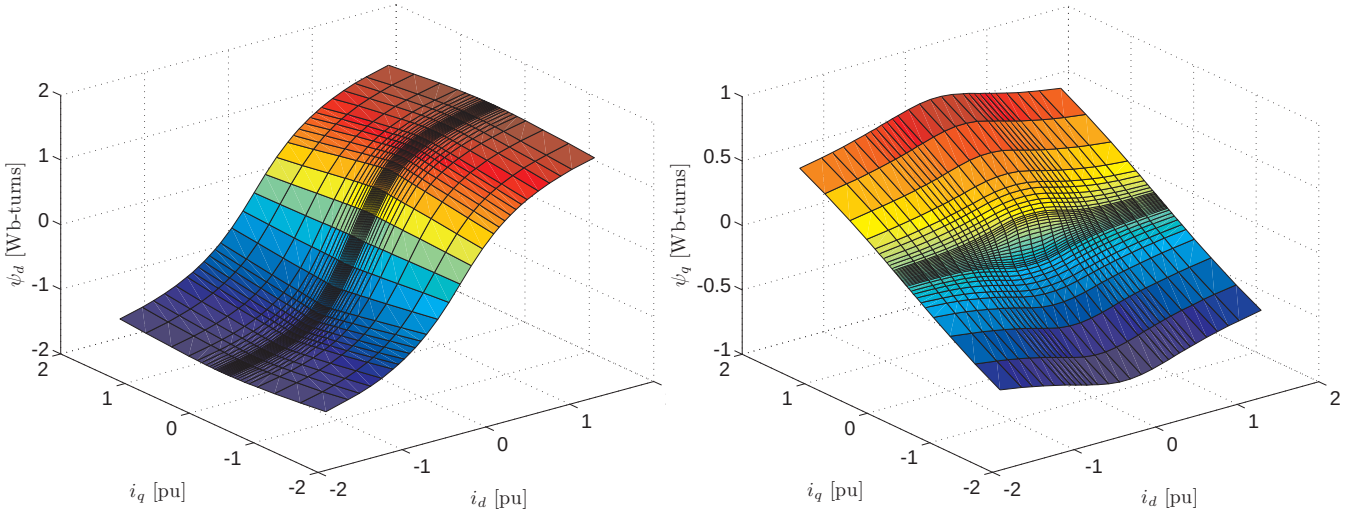

(a) Measured d-axis flux linkage map.

(b) Measured q-axis flux linkage map.

Figure 3.3: Measured flux linkage maps results of Machine 1.

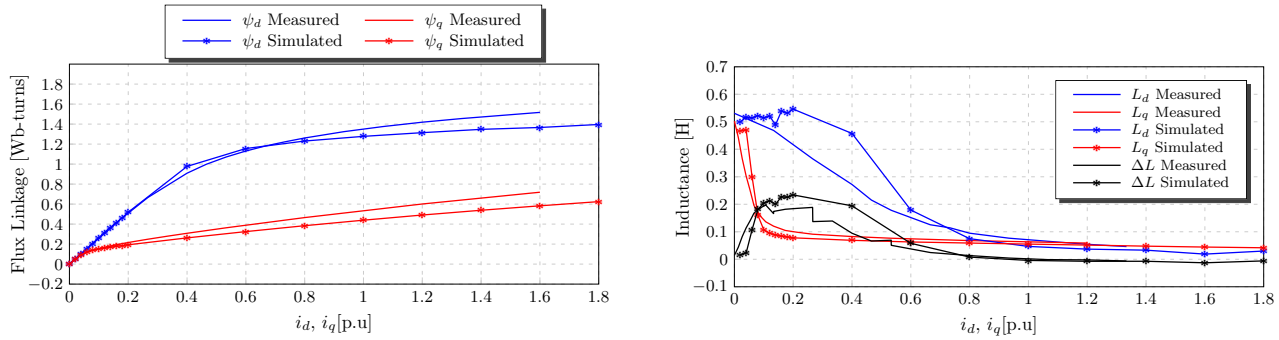

(a) Simulated and measured flux linkages.

(b) Simulated and measured inductances.

Figure 3.4: Uncoupled measured and simulated flux linkage and inductance curves of Machine 1.

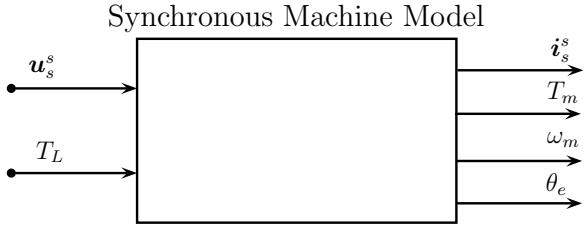

Figure 3.5: Synchronous machine model used in Simulink.

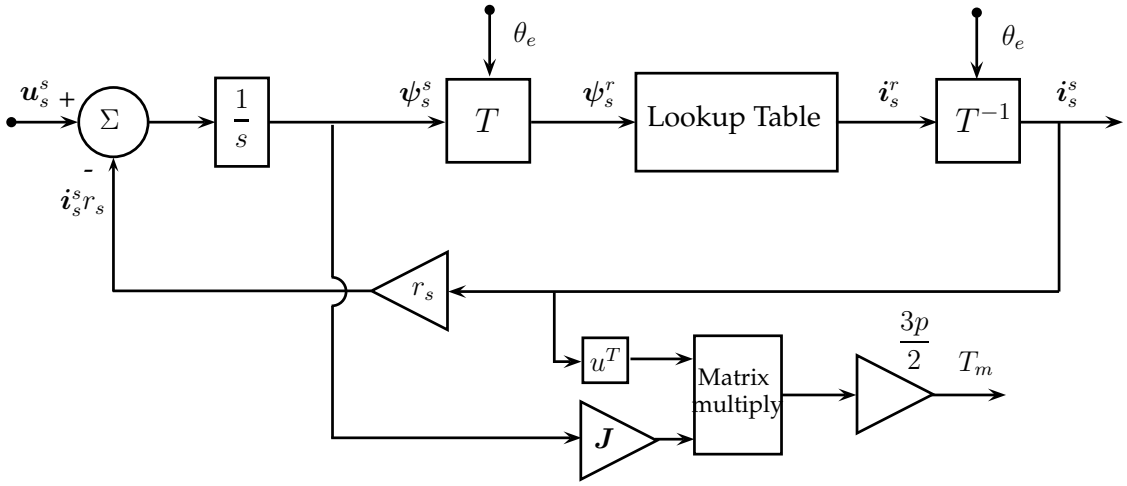

Figure 3.6: Simulink electrical model with lookup tables.

3.4 Test Bench Setup

The Pentium System is a rapid prototyping system (RPS) which was developed at the University of Wuppertal in Germany. The RPS is powered by a UNIX operating system and makes use of a real-time application interface (RTAI) to enable the implementation of real-time control systems. The RTAI allows the control system to be coded in ANSI-C. The RPS is used as a hardware in the loop system. This process allows for Simulink simulations to be directly tested by implementing them on the RPS.

Each RPS is used to control one of two DC link connected, SEW VSDs with PWM signals. The measured current and DC bus voltage are measured with the RPS on analog outputs on the inverter. The RPS measures the phase currents and the DC bus voltage with 12 bit analog to digital (A/D) converters. The rotor position is measured with an encoder which is connected to a 12 bit encoder card in the RPS.

An IM, also controlled with a VSD and RPS, is used to load the test machine unless stated otherwise. Two drive sizes are used in this thesis, two 5.5 kW drives and two 37 kW drives. A digital torque sensor is used to measure the torque. Figure 3.7 shows a diagrammatic representation of the test bench. A picture of the 5.5 kW test bench is shown in Fig. 3.8.

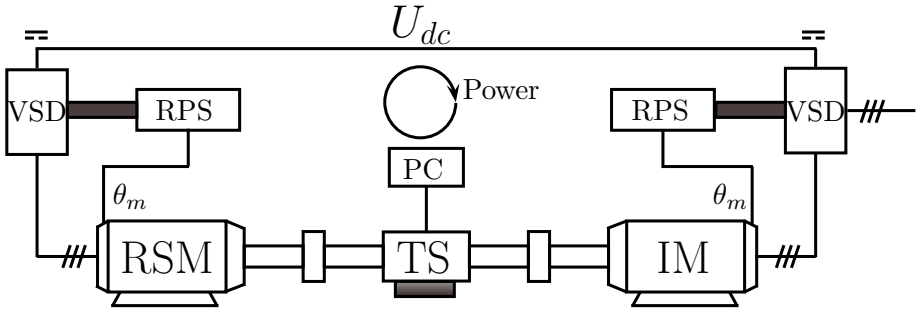

Figure 3.7: Diagrammatic representation of the test bench used in this research.

3.5 Inventory Of Investigated Machines

More than one synchronous machine is evaluated in this thesis. The evaluated machines are summarised in Table 3.1. Each machine's geometry, as set up in the FE environment, are shown in Fig. 3.9. Information regarding the rotor, winding factor, frequency etc. is shown in Table 3.1 Also shown in Table 3.1 is information regarding whether the machine is built (or just evaluated in FE) as well as in which chapters each machine is discussed in. Also, each machine is numbered. These machines will be referred to by their numbers in the remainder of this thesis.

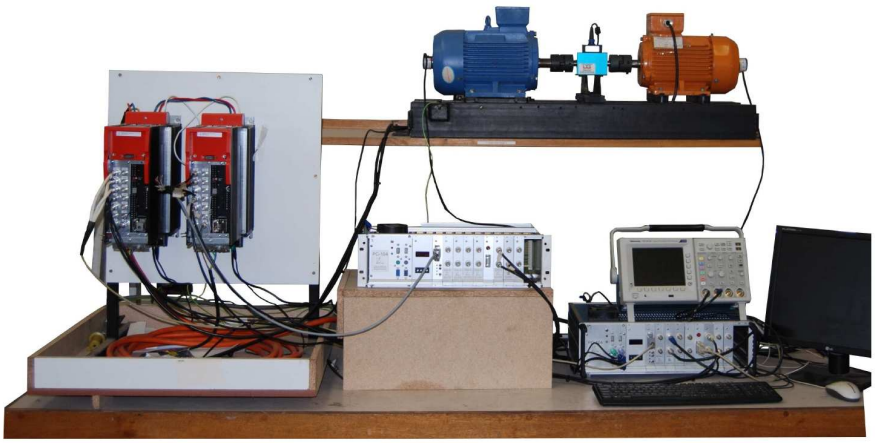

Figure 3.8: A picture of the 5.5 kW test bench used in this thesis.

Table 3.1: Inventory of the investigated synchronous machines.

Machine #	Type	Rotor	Windings	f [Hz]	I_{rms} [A]	p [kW]	ϕ [°]	Built	Chapter #
1	RSM	Unskewed	9/9	50	3.5	1.147	60	Yes	3,4,5,6,7,8
2	RSM	Unskewed	9/9	50	3.5	1.151	60	No	8
3	RSM	Unskewed	9/9	50	3.5	1.156	60	Yes	8
4	RSM	Skewed	9/9	50	3.5	1.153	60	Yes	8
5	RSM	Skewed	7/9	90	39.39	17.23	67	Yes	9,10
6	RSM	Skewed	7/9	160	139	35	67	No	9
7	RSM	Skewed	7/9	160	139	35	67	Yes	9,11
8	RSM	Skewed	7/9	160	139	35	67	No	9
9	FI-PM-Surface	Butterfly	8/9	160	143	41.3	71	Yes	9
10	FI-IPM	Butterfly	7/9	160	143	32.1	71	No	9
11	FI-IPM w/ barriers	Unskewed	8/9	160	143	34.1	86	No	9
12	FW-IPM	Skewed 2 Stacks	9/9	114.5	223	54	143	No	9
13	RSM	Unskewed	7/9	50	62.4	31.8	64	Yes	9,12

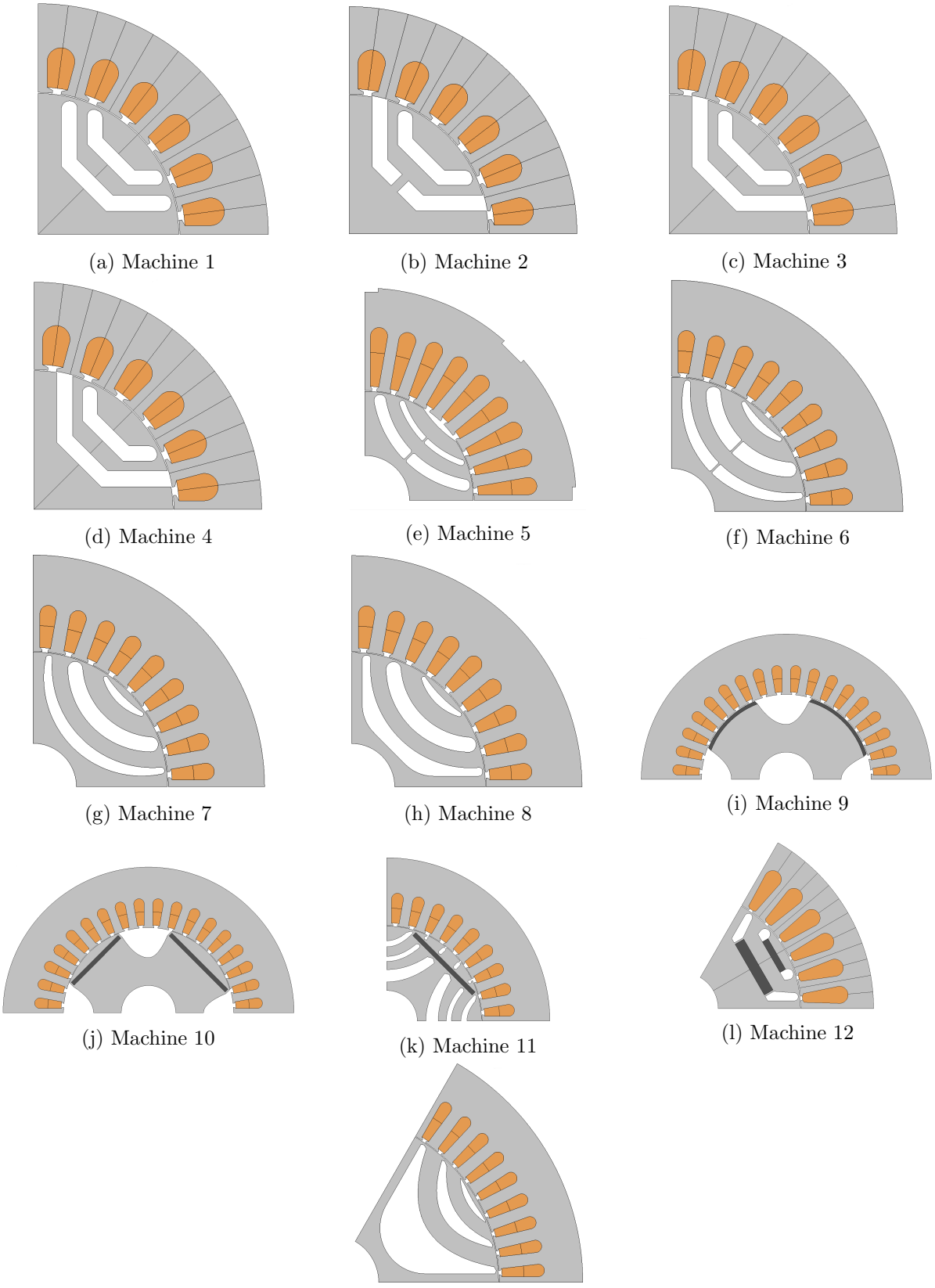

(a) Machine 1 (b) Machine 2 (c) Machine 3

(d) Machine 4 (e) Machine 5 (f) Machine 6

(g) Machine 7 (h) Machine 8 (i) Machine 9

(j) Machine 10 (k) Machine 11 (l) Machine 12

(m) Machine 13

Figure 3.9: FE geometries of the investigated synchronous machines.

Chapter 4

Alternating High Frequency Injection Position Sensorless Control

Various different position sensorless control (PSC) methods exist, where external excitation is used to exploit the machine geometry for PSC at standstill and low speeds. These methods are referred to as saliency-based PSC (SB-PSC) methods. The SB-PSC methods can be divided into three categories namely: 1.) continuous signal injection, 2.) transient signal injection and 3.) and PWM excitation without additional injection [29]. The hardware complexity of the continuous signal injection SB-PSC methods are the least complicated of the three categories [29]. In this thesis the focus is on continuous signal injection PSC methods.

Continuous signal injection SB-PSC methods can also be divided into different categories. The two continuous injection SB-PSC methods that are most common are the rotating high frequency- (HF) and the alternating HF injection methods. The alternating HF injection PSC (HFI-PSC) method causes less torque ripple and performs more dynamically than the rotating HF injection PSC method [29].

In this chapter the alternating HFI-PSC method is investigated and evaluated with machine 1. Various authors have researched the alternating HFI-PSC method for different types of synchronous machines [29–47]. At the beginning of this chapter the basic concept of the alternating HFI-PSC method will be explained, followed by the conventional implementation of this method. This will be followed by a derivation of a simplified way of implementation. This chapter will conclude by showing simulation- and measured results of machine 1 with the proposed HFI-PSC method.

4.1 The Alternating HFI-PSC Method

The alternating HFI-PSC method is implemented by superimposing a HF voltage vector onto the fundamental control voltage in the estimated rotary reference frame. An amplitude modulation scheme is used to track the saliency along the axis orthogonal to the injection axis [38]. This allows a demodulation scheme to track the anisotropy position of the rotor [32]. The anisotropy in a RSM rotates at the same angular frequency as the rotor. This implementation is based on the same principle as amplitude modulation used in radio transmission [48].

Conventional HF injection methods as explained in [30–35, 38, 39] and [44] amongst others, make use of a band pass filter (BPF) in the phase-locked loop (PLL) as shown in Fig. 4.1. The measured q-axis current, in the estimated rotary reference frame, is band pass filtered to extract a HF component that contains information regarding the position estimation error. This filtered current is then multiplied by $sin(\omega_c t)$ and low pass filtered (LPF) to extract an error signal. The working of this method will be explained in the rest of this chapter, for now it is only important to point out the structure of the conventional HFI-PSC method.

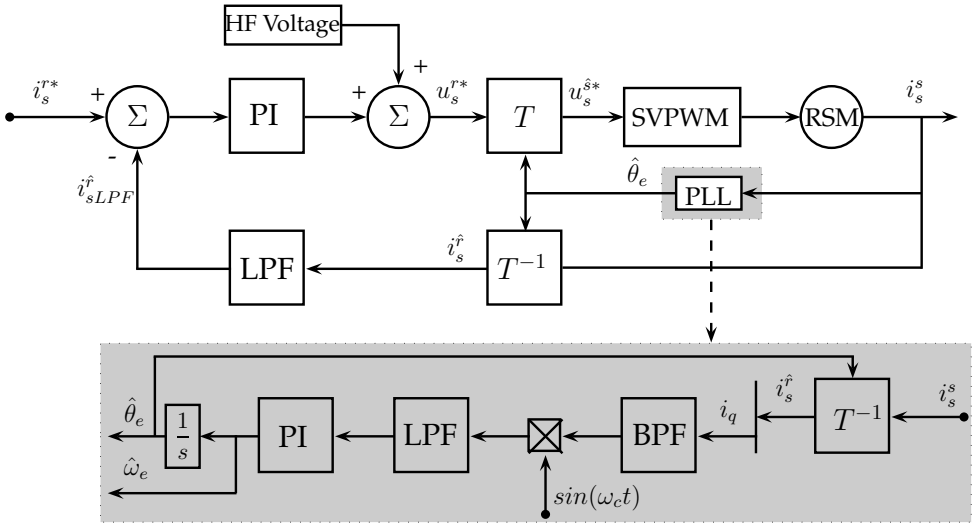

Figure 4.1: Conventional alternating high frequency injection position sensorless control scheme.

Investigations by [41] show the possibility of a simplified PLL scheme by omitting the conventional BPF from the PLL. In [41], the estimation capabilities of the simplified PLL scheme are analysed with and without the BPF on a 0.4 kW permanent magnet synchronous machine. Measured results in [41] show very good position estimation at a speed of 1.5 rev/min at no load. However, this simplified method has not yet been tested on a loaded machine or at higher speeds. The performance of this simplified method has not yet been evaluated on a RSM.

It is also suggested in [47] that the BPF can be omitted from the PLL. The implementation in [47] however, uses a 4^{th} order LPF instead of a 1^{st} order LPF in the PLL. The implementation proposed in [47], will be more computationally intensive than the proposed simplified method of [41]. The method proposed by [47] is only evaluated in simulation. It is this author's belief that the method proposed by [47] will suffer from too many time delays and computational complexity and will be unable to outperform the simplified method of [41]

The proposed alternating HFI-PSC method, as used in [41], is derived mathematically in this chapter. The proposed HFI-PSC method is then simulated, implemented and evaluated on machine 1.

4.2 High Frequency Machine Model

It is shown in Chapter 2 that the RSM can be modelled mathematically in the synchronous rotor reference frame (dq) with equations (2.12) and (2.13). To derive the HFI-PSC method, it is best to use the RSM voltage equations in vector form as in (4.1) and (4.2). The tangential inductance and mutual inductance matrices are defined as in (4.3).

$$\boldsymbol{u}_s^r = r_s \boldsymbol{i}_s^r + \boldsymbol{L}_s^r \frac{d\boldsymbol{i}_s^r}{dt} + \boldsymbol{M}_s^r \frac{d\boldsymbol{i}_s^r}{dt} - \omega_e \boldsymbol{J} \boldsymbol{L}_s^r \boldsymbol{i}_s^r \tag{4.1}$$

$$\boldsymbol{u}_s^r = \begin{bmatrix} u_d \\ u_q \end{bmatrix}, \qquad \boldsymbol{i}_s^r = \begin{bmatrix} i_d \\ i_q \end{bmatrix} \tag{4.2}$$

$$\boldsymbol{L}_s^r = \begin{bmatrix} L_d & 0 \\ 0 & L_q \end{bmatrix}, \qquad \boldsymbol{M}_s^r = \begin{bmatrix} L_{dq} & 0 \\ 0 & L_{qd} \end{bmatrix} \tag{4.3}$$

When evaluating the machine voltage as in (4.1) at HF excitation that is bounded as by (4.4), where f_s is the sampling frequency and ω_r is the maximum operating fundamental frequency, the resistive-, speed voltage- and mutual inductance terms fall away due to their small magnitudes compared to the tangential inductance terms [31,42]. Staying within the limit of (4.4) ensures that aliasing does not occur. Equation (4.1) thus simplifies to (4.5), where subscript c refers to the carrier- or high frequency component of each quantity. The model of the RSM under high frequency carrier-signal excitation is thus a pure inductive load [38].

$$2\omega_r < \omega_c < \frac{2\pi f_s - 2\omega_r}{2} \tag{4.4}$$

$$\boldsymbol{u}_{sc}^{r} = \boldsymbol{L}_{s}^{r}\frac{d\boldsymbol{i}_{c}^{r}}{dt} \tag{4.5}$$

4.3 Alternating Carrier Injection

The carrier voltage $\boldsymbol{u}_{sc}$ is applied to the estimated real axis (d-axis) in the rotary reference frame at a constant carrier frequency of ω_c, as in (4.6) [32,42,49,50]. The superscript $\hat{r}$ in (4.6), denotes the voltage in the estimated rotary reference frame. The frequency analysis function of MATLAB is used to illustrate the effect of the injected HF voltage on the fundamental voltage. The discrete Fourier transform of the injection voltage, $u_c cos(\omega_c t)$ at $f_c = 3\ kHz$, with a sampling frequency of $f_s = 10\ kHz$ is shown in Fig. 4.2a. The frequency spectrum of the applied voltage, $u_d + u_c cos(\omega_c t)$, is shown in Fig. 4.2b. The injection voltage is chosen to be significantly smaller than the applied voltage, as one would do during implementation of this PSC method.

$$\boldsymbol{u}_{sc}^{\hat{r}} = \begin{bmatrix} u_c cos(\omega_c t) \\ 0 \end{bmatrix} \tag{4.6}$$

Transforming the inductance matrix of (4.3) to the stationary reference frame yields (4.7) [38]. The mean inductance is represented by $L_m = (L_d + Lq)/2$ and $\Delta L = (Ld - Lq)/2$ the magnitude of the inductance saliency [37,42]. The HF voltage is injected and demodulated in an estimated rotary reference frame that is misaligned by an estimation error, $\Delta\theta_e = \theta - \hat{\theta}_e$. The inductance matrix of (4.3) thus transforms to the estimated rotor reference frame as in (4.8) [40].

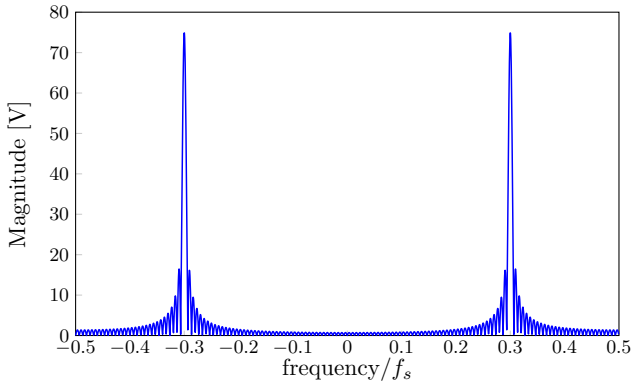

(a) FFT of HF injection voltage.

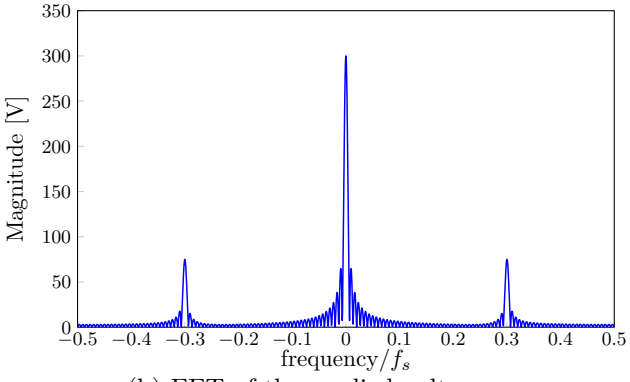

(b) FFT of the applied voltage.

Figure 4.2: Frequency analysis of the injected and applied voltage.

$$\begin{aligned} \boldsymbol{L}_s^s &= \begin{bmatrix} L_m + \Delta L cos(\theta_e) & -\Delta L sin(\theta_e) \\ -\Delta L sin(\theta_e) & L_m + \Delta L cos(\theta_e) \end{bmatrix} \\ &= L_m \boldsymbol{I} + \Delta L \begin{bmatrix} cos(2\theta_e) & sin(2\theta_e) \\ sin(2\theta_e) & -cos(2\theta_e) \end{bmatrix} \end{aligned} \tag{4.7}$$

$$\begin{aligned} \boldsymbol{L}_s^{\hat{r}} &= \begin{bmatrix} L_m + \Delta L cos(\Delta\theta_e) & -\Delta L sin(\Delta\theta_e) \\ -\Delta L sin(\Delta\theta_e) & L_m + \Delta L cos(\Delta\theta_e) \end{bmatrix} \\ &= L_m \boldsymbol{I} + \Delta L \begin{bmatrix} cos(2\Delta\theta_e) & sin(2\Delta\theta_e) \\ sin(2\Delta\theta_e) & -cos(2\Delta\theta_e) \end{bmatrix} \end{aligned} \tag{4.8}$$

The stator current is measured in the stationary reference frame and transformed to the estimated rotary reference frame. The HF current in the estimated rotor reference frame is derived as in (4.9). The superscript $\hat{r}$ denotes the current vector in the estimated rotor reference frame. It is thus necessary to derive the inverse inductance matrix as in (4.10) [40,42]. The current of the RSM in the estimated rotary reference frame can thus be modelled mathematically by (4.11) [37,42].

$$\begin{aligned} \boldsymbol{i}_s^{\hat{r}} &= \boldsymbol{L}_s^{\hat{r}-1} \int \boldsymbol{u}_{sc}^{\hat{r}} \\ &= \boldsymbol{L}_s^{\hat{r}-1} \begin{bmatrix} \frac{u_c}{\omega_c} sin(\omega_c t) \\ 0 \end{bmatrix} \end{aligned} \tag{4.9}$$

$$\boldsymbol{L}_s^{\hat{r}-1} = \frac{1}{L_d L_q} \left[L_m \boldsymbol{I} + \Delta L \begin{pmatrix} -cos(2\Delta\theta_e) & -sin(2\Delta\theta_e) \\ -sin(2\Delta\theta_e) & cos(2\Delta\theta_e) \end{pmatrix} \right] \tag{4.10}$$

$$\boldsymbol{i}_s^{\hat{r}} = \frac{u_c sin(\omega_c t)}{L_d L_q \omega_c} \left[L_m \begin{bmatrix} 1 \\ 0 \end{bmatrix} - \Delta L \begin{pmatrix} cos(2\Delta\theta_e) \\ sin(2\Delta\theta_e) \end{pmatrix} \right] \tag{4.11}$$

If $\Delta\theta_e$ is small enough, and if the closed loop system is in steady state, i.e. the estimated angle is tracking the actual angle, it is a reasonable assumption that $e^{-j\Delta\theta_e}$ is nearly time invariant [17]. If $e^{-j\Delta\theta_e}$ is indeed almost time invariant this will not result in a frequency shift and thus only scale the frequency components. This assumption can lead to simplifications of $\sin(\Delta\theta_e) \approx \Delta\theta_e$ and $\cos(\Delta\theta_e) \approx 1$ as applied in (4.12) [17].

$$\boldsymbol{i}_s^{\hat{r}} = \frac{u_c sin(\omega_c t)}{L_d L_q \omega_c} \left[L_m \begin{bmatrix} 1 \\ 0 \end{bmatrix} - \Delta L \begin{pmatrix} 1 \\ 2\Delta\theta_e \end{pmatrix} \right] \tag{4.12}$$

The first term on the right of (4.12), i.e. the d-axis component, does not contain any information about the electrical rotor angle. The second term on the right, i.e. the q-axis component, does have information regarding the estimation error and is scaled by the magnitude of the inductance saliency, ΔL.

Although the HF voltage is injected onto the d-axis in this section, it is also possible to inject the HF voltage on the q-axis with the same results. It is reported in [33] that injecting the HF voltage on the d-axis causes less torque ripple than injecting the HF voltage on the q-axis.

4.4 Sensorless Control Approach

The symmetrical spectrum in Fig 4.2b suggests that the pulsating vector can be interpreted as a superposition of two rotating vector carriers [38]. The carrier signal appears to lack spectral separation, which is essential for synchronous reference frame filtering [38]. As discussed earlier and shown in Fig. 4.1, conventional alternating HFI-PSC methods band pass filters i_q in the demodulation scheme to create proper spectral separation. This process then filters out one of the HF components displayed in Fig. 4.2b and rejects the DC- and the rest of the HF components. The filtered out HF component has information regarding the position estimation error, $\Delta\theta_e$.

According to [51], the spectrum of a signal $x(t)$ is shifted to the carrier frequency when multiplied by $cos(\omega_c t)$, as in (4.13). Multiplying the measured current in (4.11) with $sin(\omega_c t)$ leads to the trigonometry identity of (4.14)

$$x(t)cos(\omega_c t) \Longleftrightarrow \frac{1}{2}\big[X(\omega+\omega_c)+X(\omega-\omega_c)\big] \tag{4.13}$$

$$sin^2(\omega_c t) = \frac{1-cos(2\omega_c t)}{2} \tag{4.14}$$

The frequency domain of (4.14) shows one DC component and two HF components at twice the carrier frequency. This implies that if the q-axis component of (4.12) is multiplied by $sin(\omega_c t)$, before band pass filtering the signal, the resultant frequency spectrum will have one DC component and two HF components at twice the carrier frequency. Both the HF components and the DC component contains information about the position estimation error. The effect of the frequency shift, unscaled with respect to parameters and unfiltered (no BPF), can be seen in Fig. 4.3.

The DC component can be used to extract the position estimation error. It is clear that a simple LPF can separate this component from the other HF components. Separating the DC component from the components at twice the carrier frequency with a LPF is a lot easier than using a BPF at the carrier frequency before frequency shifting. Implementing a LPF in the demodulation scheme is easier than implementing the BPF, due to the passband of the BPF that has to be half the size of the LPFs passband. Since the conventional HFI-PSC methods implements the LPF as well, it is now clear that only this filter is necessary in the demodulation scheme.

Assuming that the remaining HF current components are rejected by a LPF after applying the trigonometry identity of (4.14), the low pass filtered current can be written as in (4.15). The current vector is separated into its d- and q-axis components in (4.16) and (4.17)

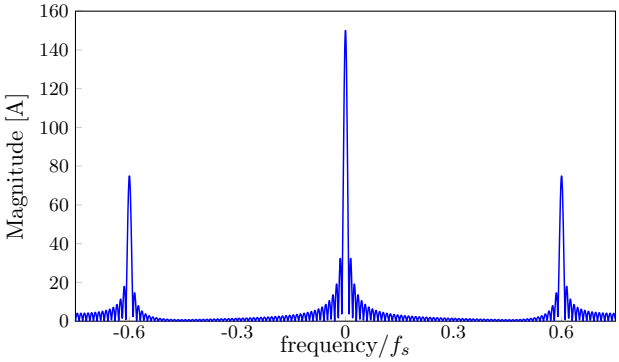

Figure 4.3: FFT of frequency shifted q-axis current.

$$\boldsymbol{i}^{\hat{r}}_{sLPF} = \frac{u_c}{L_d L_q \omega_c}\left[L_m \begin{bmatrix}1\\0\end{bmatrix} - \Delta L \begin{bmatrix}1\\2\Delta\theta_e\end{bmatrix}\right] \tag{4.15}$$

$$\boldsymbol{i}^{\hat{r}}_{dLPF} = \frac{u_c}{L_d L_q \omega_c}\left[L_m - \Delta L\right] \tag{4.16}$$

$$\boldsymbol{i}^{\hat{r}}_{qLPF} = -\frac{u_c \Delta L(2\Delta\theta_e)}{L_d L_q \omega_c} \tag{4.17}$$

It is shown in (4.17) that the q-axis current component in the estimated rotor reference frame is zero when the estimation error is zero [52]. Thus, only the q-axis current could be processed to acquire the rotor position. It is important to observe that the information of the position estimation error, $\Delta\theta_e$, will be too small for the PLL to track if $\Delta L \approx 0$. It is thus required that $L_d \neq L_q$ for this method to function properly.

4.5 Demodulation Of The Position Estimation Error

The q-axis component of the demodulated current response is proportional to the estimation error, $\Delta\theta_e$, as shown in (4.17). This is used to track the electrical rotor angle in a PLL system [32]. This estimator is in effect an amplitude null regulator [38]. A PI controller is used in the PLL structure to drive the error signal to zero.

The input to the PI controller is $\boldsymbol{i}^{\hat{r}}_{qLPF}$. The output of the PI controller is the estimated electrical rotor speed $\hat{\omega}_e$ as shown in (4.18). By integrating this value it is possible to extract the electrical rotor angle. If k_{iPLL} is the integral gain and k_{pPLL} is the proportional gain of the PI controller, the estimated electrical rotor angle, $\hat{\theta}_e$ can be calculated with (4.19). Estimated quantities are indicated with a ˆ upperscript.

$$\hat{\omega}_e = k_{iPLL} \int \boldsymbol{i}^{\hat{r}}_{qLPF} dt \tag{4.18}$$

$$\hat{\theta}_e = \int k_{pPLL} \boldsymbol{i}^{\hat{r}}_{qLPF} + \hat{\omega}_e dt \tag{4.19}$$

Tracking an error signal with a PI controller is robust against noise and measurement tolerances, for instance the limited resolution of analog to digital converters in drive controllers [32]. The proposed scheme for sensorless position detection is shown in Fig. 4.4. The only difference between the conventional scheme of Fig. 4.1 and the proposed scheme of Fig. 4.4 is the omission of the BPF in the PLL.

The design of the BPF in the conventional HFI-PSC method is critical to ensure that only the component around the carrier frequency is filtered out [53]. This requires a sharp roll-off frequency [53]. However, sharp roll-off frequency causes phase shift problems. Additional to the phase shift problem, filters also cause signal magnitude decrease as well as a time delay if implemented in ANSI-C. Filters can damp the dynamic response of the whole system and therefore impairs the PLL tuning capabilities. The proposed simplified HFI-PSC method should thus be more dynamic than the conventional method. The implementation of the LPF is done with a simple first order filter. First order filters are easy to implement and to configure. The implementation of the proposed PSC method is thus less complex than that of the conventional method.

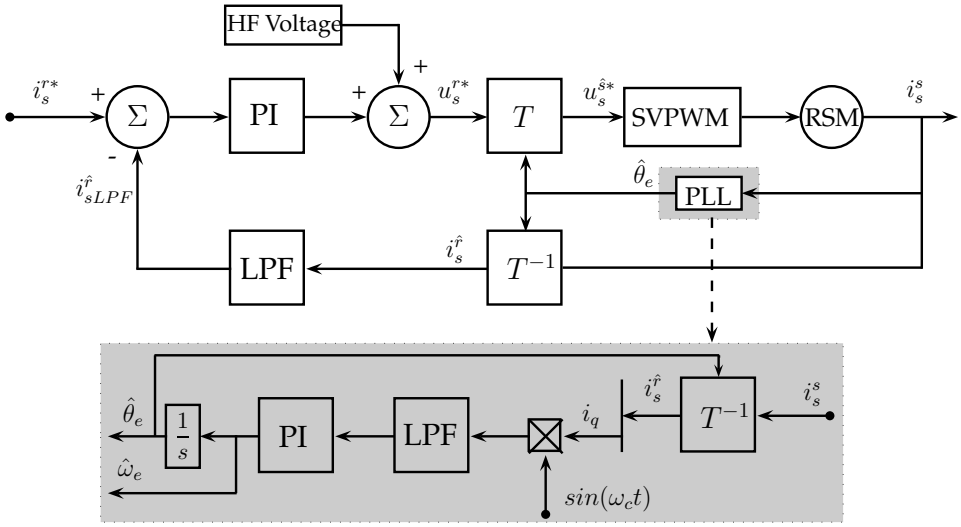

Figure 4.4: Proposed alternating high frequency injection position sensorless control scheme.

4.6 Simulation

The proposed HFI-PSC method is tested in the Simulink package. The measured flux maps of machine 1 are used in the simulation environment as described in Chapter 3. The simulation control parameters are as in Table 4.1. Rated current step simulation results of the position sensorless controlled RSM are shown in Fig. 4.5. The reference and simulated currents are as shown in Fig. 4.5a. It is shown in Fig. 4.5c that the current step results in a rated torque step being applied by the RSM. The machine speed is kept constant as if controlled by a larger shaft connected speed controlled machine (similar to test bench). The speed is increased up to rated and kept constant as shown in Fig. 4.5d. Another current step is applied at 6 s. The simulated position estimation error is shown in Fig. 4.5b. It is clear that there are large position estimation errors during current transients. If the transients are too large, this can cause desynchronisation of the PLL. Simulations show that the proposed HFI-PSC method is stable and viable.

Saturation of the flux linkage and cross-saturation between the magnetic d- and q-axis can cause the inductance saliency to misalign with the rotor. This is referred to as saliency shift. The saliency shift of the RSM can be measured as a function of current and used to compensate the angle offset in the control structure. The saliency shift is measured while the machine is controlled with a position sensor with the PSC method only observing the machine state. The saliency shift of machine 1, as acquired from the Simulink simulations, is shown in Fig. 4.6. The curve fit tool from MATLAB is used to derive (4.20), which can be used as a compensation curve. The simulated saliency shift and the curve fitted compensation curve are both shown in Fig. 4.6.

Table 4.1: Simulation controller parameters.

Current proportional gain	k_p	80	V/A
Current time constant	T_i	4	ms
PLL proportional gain	k_{pPLL}	290	rad/s
PLL time constant	T_{PLL}	13.7	ms
Current LPF	LPF_i	500	rad/s
PLL LPF	LPF_{PLL}	100	rad/s
Injection voltage	u_c	120	V
Injection frequency	ω_c	3.141 x 10^3	rad/s

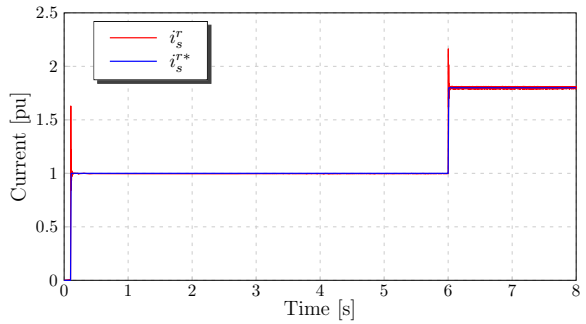

(a) Reference- and machine current.

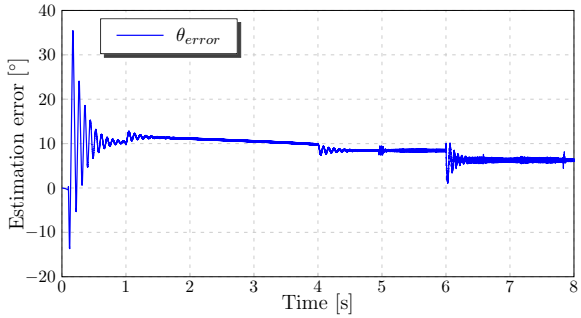

(b) Position estimation error.

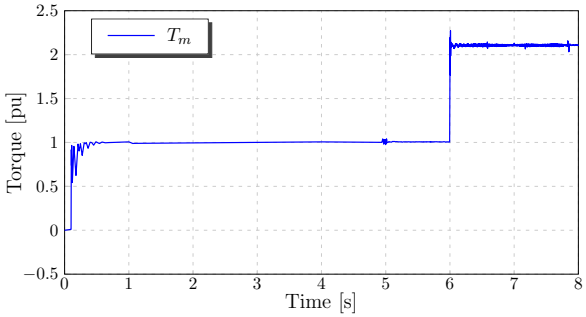

(c) Mechanical torque.

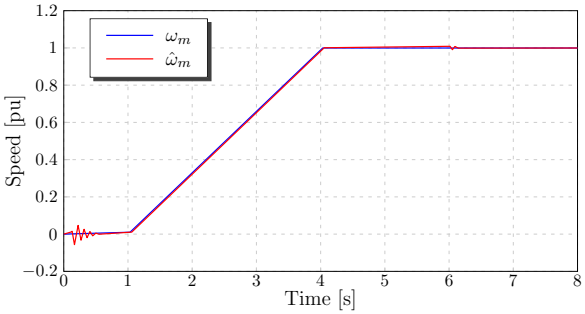

(d) Machine- and estimated speed.

Figure 4.5: HFI-PSC: Rated current step simulation of machine 1.

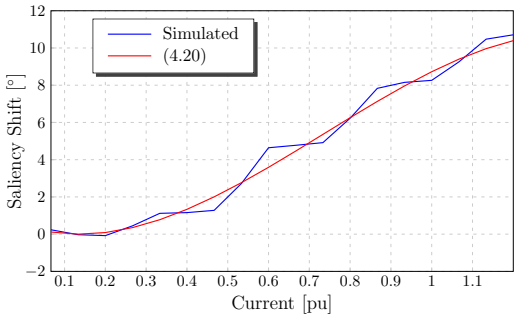

Figure 4.6: Simulated saliency shift of machine 1.

$$\theta_{CC} = -0.00052 * \boldsymbol{i}_s^{r3} + 0.0086 * \boldsymbol{i}_s^{r2} - 0.016 * \boldsymbol{i}_s^{r} + 0.0079; \tag{4.20}$$

4.7 Measured Results

The proposed method of PSC is implemented and evaluated at the Institute for Electrical Drive Systems and Power Electronics at the Technical University of Munich. A similar test bench as shown in Fig. 3.8 is used. Machine 1 is also used to test and evaluate the proposed PSC method.

It is shown in (4.15) that the position estimation error, which is used in the PLL scheme, is scaled by ΔL, thus it is necessary that $\Delta L \neq 0$ to ensure stable control with the HFI-PSC method. The measured flux map of machine 1 is used to map this machine's inductance saliency as a function of current. The measured uncoupled tangential inductances of machine 1 are shown in Fig. 4.7a. Also shown in Fig. 4.7a is the measured inductance saliency, ΔL. It is shown in Fig. 4.7a that the saliency of the RSM starts off

very small and increases as the machine current increases. The magnitude of inductance saliency of the RSM is not sufficient at small current vectors for stable HFI-PSC, especially at zero reference current. This is due to $L_d \approx L_q$.

This problem can be avoided by choosing the current vector in such a way as to ensure that there is always q-axis flux in the machine. This saturates the q-axis magnetic circuit creating a difference in inductance needed for the HFI-PSC method to function properly. To achieve saturation, i_q is always kept at a minimum of 1.2 A even at standstill under no load. The current vector approaches the MTPA current angle, ϕ, as its magnitude increase. This implies that the machine does not always operate at its maximum efficiency at small loads, but HFI-PSC is possible at these conditions. An example of how this is implemented is displayed graphically in Fig. 4.7b.

4.7.1 Current response

The inner loop of the cascaded vector controller is the current controller as explained in Chapter 2. It is required that this control loop be faster than the outer speed control loop. The performance of the current controller is thus evaluated first. The control parameters as implemented on the RPS are given in Table 4.2. A rated current step is applied to the position sensorless controlled RSM similar to the simulation test results shown in Fig. 4.5. The speed is kept constant by the IM at a speed of 0.25 pu. A digital oscilloscope is used to plot and save the reference- and measured current of the RSM. These results are shown in Fig. 4.8a.

The measured current vector in Fig. 4.8a (red line) is calculated with the real electrical angle θ_e. This vector is not used in the control loop and is only calculated to demonstrate the accuracy of the PSC method. That reference current is tracked almost instantaneously as shown in Fig. 4.8a. It is thus safe to assume that the position sensorless controlled RSM drive is able to deliver almost instantaneous rated torque.

The magnitude of ΔL decreases at high currents thus limiting the torque capabilities of the position sensorless controlled drive. The measured maximum torque that machine 1 can deliver with HFI-PSC as a function of machine speed is shown in Fig. 4.8b. This test is referred to as the limits of stable operation test. These results are compared to the measured results of [28], where a HFI-PSC method is used with time averages and a BPF in the PLL. Machine 1 is also used in [28]. It is shown in Fig. 4.8b that the startup torque (at $\omega_r = 0$) with the proposed simplified HFI-PSC method is lower than with the method used in [28]. The startup torque however, is still considerably high at 1.86 pu.

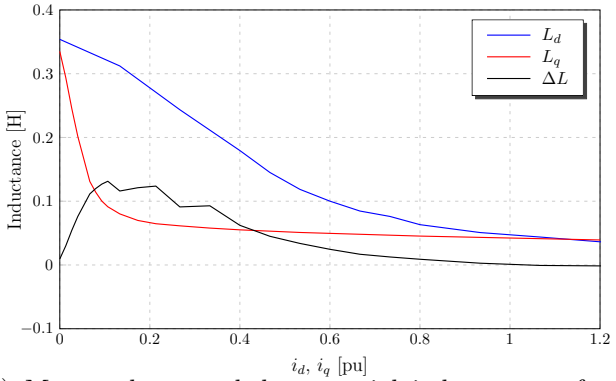

(a) Measured uncoupled tangential inductances of machine 1

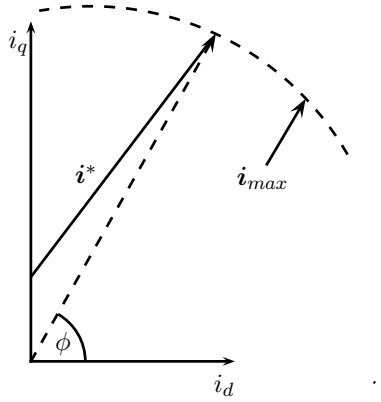

(b) Reference current as implemented with the HFI-PSC method to ensure q-axis flux saturation.

Figure 4.7: Inductance characteristics of machine 1.

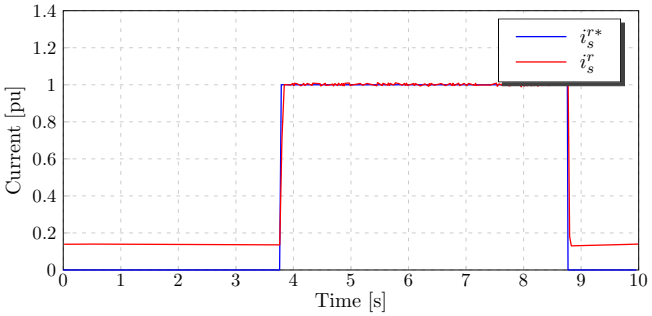

(a) Measured current step response with HFI-PSC on machine 1.

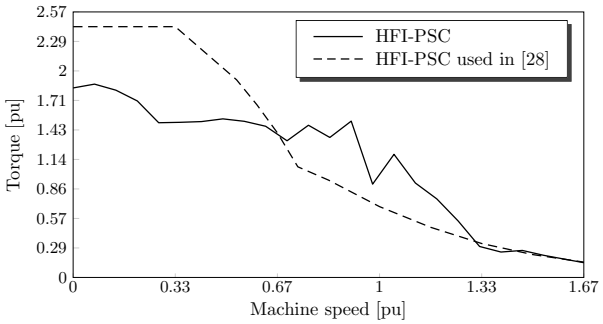

(b) Limits of stable operation.

Figure 4.8: HFI-PSC: Measured current response of machine 1.

Table 4.2: Rapid prototype system controller parameters for position sensorless current controlled machine 1.

Current proportional gain	k_p	100	V/A
Current time constant	T_i	2.73	ms
PLL proportional gain	k_{pPLL}	290	rad/s
PLL time constant	T_{PLL}	13.7	ms
Current LPF	LPF_i	2441	rad/s
PLL LPF	LPF_{PLL}	976.4	rad/s
Injection voltage	u_c	120	V
Injection frequency	ω_c	3 x 10^3	rad/s

The magnitudes of the speed voltage terms of the RSM increase proportionally to the machine speed, thus the voltage vector also increases in the rotary reference frame as a function of speed. It is thus possible for the voltage vector to reach the limit of the DC bus voltage of the VSD when controlled with HFI-PSC at higher speeds, due to the addition of the HF voltage. This also limits the maximum torque that the position sensorless controlled drive can produce at high speeds. This effect is evident in Fig. 4.8b where the available torque decreases as the machine speed increases. However, machine 1 can produce more torque with the proposed simplified HFI-PSC method at rated speed than with the method presented in [28]. SB-PSC methods are usually only used at standstill and low speeds, thus large torque at high speeds is not a requirement from the HFI-PSC method.

4.7.2 Speed response

The speed response of the position sensorless controlled RSM drive is investigated. The cascaded speed controller structure as discussed in Chapter 2 is used. The controller parameters, as implemented on the RPS, are shown in Table 4.3.

A speed step of 0.9 pu is applied by the position sensorless controlled RSM while a load of 0.6 pu is applied by the IM. These results are shown in Fig. 4.9. The reference- and measured speed, as obtained from a position sensor, are shown in Fig. 4.9a. The measured speed is not used in the feedback loop and is only used for performance investigative purposes. The estimated speed however, is used for feedback. The position sensorless controlled RSM drive is able to track speed steps effectively as shown in Fig. 4.9a. The position estimation error in Fig. 4.9b shows large position estimation errors during speed transients. The PLL however, does not desynchronise as a result of the large position estimation errors. Steady state position estimation errors do not exceed $|9^o|$.

The dynamic speed reversal of the position sensorless controlled RSM drive is also investigated. The machine is loaded by the IM at 0.3 pu torque. Speed reversal steps of $\pm$ 1.27 pu are performed by the

position sensorless controlled RSM drive. The results of this test are shown in Fig. 4.10. It is shown in Fig 4.10a that the position sensorless controlled RSM drive is able to perform speed reversal at speeds above rated, even when slightly loaded. Again, large position estimation errors are present during transients as shown in Fig 4.10b, but the PLL stays synchronised. Furthermore, it is shown in Fig. 4.10b that the sign of the position estimation error changes as the direction of the machine changes.

Table 4.3: Rapid prototype system controller parameters for position sensorless speed controlled machine 1.

Current proportional gain	k_p	100	V/A
Current time constant	T_i	2.73	ms
Speed proportional gain	k_{ps}	0.2	Nms/rad
Speed time constant	T_{is}	0.41	s
PLL proportional gain	k_{pPLL}	290	rad/s
PLL time constant	T_{PLL}	13.7	ms
Current LPF	LPF_i	2441	rad/s
Speed LPF	LPF_s	48.82	rad/s
PLL LPF	LPF_{PLL}	976.4	rad/s
Injection voltage	u_c	120	V
Injection frequency	ω_c	3 x 10^3	rad/s

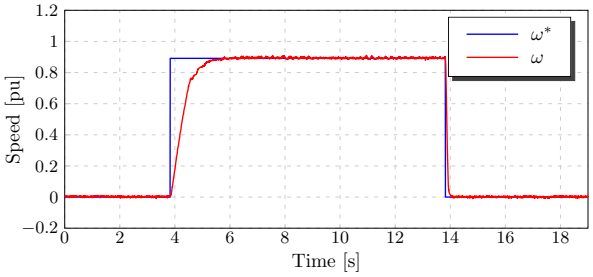

(a) Reference speed and measured speed.

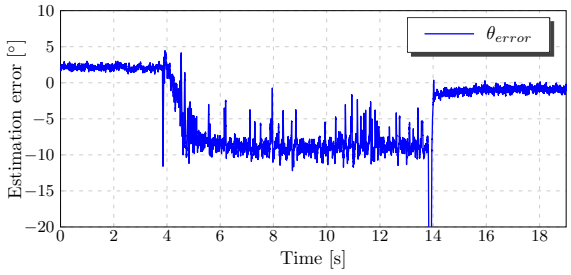

(b) Position estimation error.

Figure 4.9: HFI-PSC: Measured speed step response of machine 1 while loaded at 0.6 *pu*.

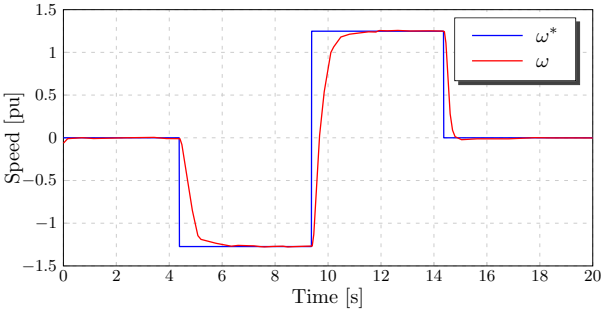

(a) Reference speed and measured speed.

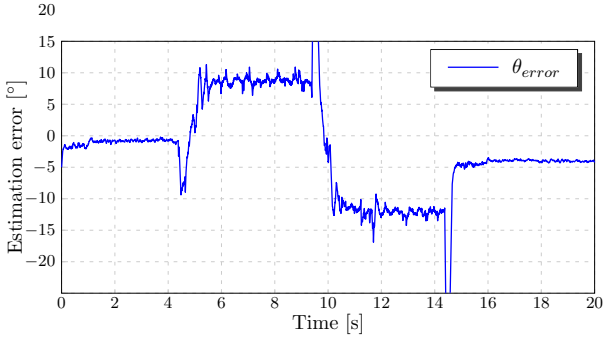

(b) Position estimation error.

Figure 4.10: HFI-PSC: Measured speed reversal response of machine 1.

4.8 Summary

A position sensorless control (PSC) method that exploits the saliency of the RSM, by injecting high frequency (HF) voltages, is investigated in this chapter, namely the alternating high frequency injection PSC (HFI-PSC) method. The conventional implementation of the alternating HFI-PSC method is discussed in this chapter. A simplified HFI-PSC method is proposed where the conventional band pass filter (BPF) is omitted from the phase-locked loop (PLL) structure. MATLAB is used to aid mathematical derivation to support validity of the proposed simplified PSC method. The advantages of having fewer filters in the control loop is that fewer parameter tuning is required, fewer time delays exist as a result of digital filtering and also less phase shift and decrease in signal magnitude. The simplified structure can also improve the dynamics of the control structure.

The proposed HFI-PSC method is simulated in the Simulink package with the flux map model of machine 1. Simulation results show that the proposed simplified HFI-PSC method is stable even during current transients. Furthermore, simulation results show that current controllers are stable with the HFI-PSC method allowing the RSM to deliver rated torque steps dynamically.

A test bench similar to the one described in Chapter 3 is used to implement, test and evaluate the proposed HFI-PSC method on machine 1. Flux map measurements of machine 1 reveal that there are certain constraints regarding the implementation of saliency-based PSC (SB-PSC) methods on the RSM. The inductance saliency of the RSM is too small for successful position estimation at small- and high current magnitudes. The control scheme is adapted at small current magnitudes to allow for stable PSC. Measured results show that the current controllers perform dynamically when rated current steps are applied while the RSM is controlled with the HFI-PSC method. It is shown that the position sensorless controlled RSM drive is able to deliver almost instantaneous rated torque. The PLL also stays synchronised during current transients.

The limits of stable operation test reveals that the position sensorless controlled RSM drive is able to deliver almost twice rated startup torque. These results also reveal that the maximum torque that can be produced by the RSM decreases as the speed increases while controlled with the HFI-PSC. This however, is not problematic as SB-PSC methods are usually only used at standstill and low speeds.

Speed control test results show that the RSM is able to apply dynamic speed steps while under HFI-PSC, even while loaded. A speed reversal test shows the capability of the position sensorless controlled RSM drive to do speed reversals at above rated speed.

Chapter 5

Arbitrary Injection Position Sensorless Control

The high frequency injection position sensorless control (HFI-PSC) method is presented in the previous chapter. The HFI-PSC method is classified as a continuous injection PSC method. A second continuous injection PSC method is introduced in this chapter, namely the arbitrary injection PSC (AI-PSC) method. The AI-PSC method is fairly "young" in comparison to the HFI-PSC method, which dates back to more than a decade. The AI-PSC method is also a saliency-based PSC (SB-PSC) method. The AI-PSC method however, takes a different approach in exploiting the machine saliency for PSC. The AI-PSC method is used at standstill and low speeds similar to the HFI-PSC method.

The evolution of the AI-PSC method is discussed in this chapter. This method starts off by being very machine parameter dependent, but is extended to be completely machine parameter independent. The end result is an algorithm that can be implemented on any synchronous machine for PSC at standstill and low speeds.

The AI-PSC method is evaluated in simulation with the measured flux maps of machine 1. Finally the AI-PSC method is implemented and evaluated on machine 1 in the laboratory environment.

5.1 Current Prediction

The flux linkage vector of the RSM, $\boldsymbol{\psi}_s^s$, in the stationary reference frame is assumed to have a linear dependency on the stator current vector, $\boldsymbol{i}_s^s$, in the linearised machine model equation [2,28]. This implies that $\boldsymbol{L}_s^s$ can be used to calculate the flux linkage as in (5.1).

$$\boldsymbol{\psi}_s^s = \boldsymbol{L}_s^s \boldsymbol{i}_s^s \tag{5.1}$$

The inductance matrix, (5.2) is constant in the rotary reference frame but time variant in the stationary reference frame [2, 3, 28]. The inductance matrix is thus derived in the stationary reference frame as in (5.4).

$$\boldsymbol{L}_s^r = \begin{bmatrix} L_d & 0 \\ 0 & L_q \end{bmatrix} \tag{5.2}$$

$$\begin{aligned} \boldsymbol{L}_s^s &= \boldsymbol{T}\boldsymbol{L}_s^r\boldsymbol{T}^{-1} && (5.3)\\ \boldsymbol{L}_s^s &= \begin{bmatrix} L_m + \Delta L cos(\theta_e) & -\Delta L sin(\theta_e) \\ -\Delta L sin(\theta_e) & L_m + \Delta L cos(\theta_e) \end{bmatrix} \\ &= L_m\boldsymbol{I} + \Delta L \begin{bmatrix} cos(2\theta_e) & sin(2\theta_e) \\ sin(2\theta_e) & -cos(2\theta_e) \end{bmatrix} && (5.4) \end{aligned}$$

The voltage equation of the RSM in the stationary reference frame is written as in (5.5). Equations (5.1) and (5.3) can be substituted in (5.5) as in (5.7) where $\acute{\boldsymbol{L}}_s^s$ is the inductance derivative with respect to θ_e [2, 54, 55].

$$\boldsymbol{u}_s^s = r_s\boldsymbol{i}_s^s + \dot{\boldsymbol{\psi}}_s^s \tag{5.5}$$

$$\begin{aligned} \boldsymbol{u}_s^s &= r_s\boldsymbol{i}_s^s + \frac{d}{dt}(\boldsymbol{T}\boldsymbol{L}_s^r\boldsymbol{T}^{-1}\boldsymbol{i}_s^s) && (5.6)\\ &= r_s\boldsymbol{i}_s^s + \boldsymbol{L}_s^s\frac{d}{dt}\boldsymbol{i}_s^s + \omega_e\acute{\boldsymbol{L}}_s^s\boldsymbol{i}_s^s && (5.7) \end{aligned}$$

Equation (5.7) can be rearranged to calculate the stator current derivative [2, 56]:

$$\frac{d}{dt}\boldsymbol{i}_s^s = \boldsymbol{L}_s^{s-1}(\boldsymbol{u}_s^s - r_s\boldsymbol{i}_s^s - \omega_e\acute{\boldsymbol{L}}_s^s\boldsymbol{i}_s^s) \tag{5.8}$$

The inverse matrix inductance in (5.8) is rewritten into its isotropic-, Y_Σ, and salient $Y_\Delta S(\theta_e)$ admittance terms in (5.9) [55]. The saliency and isotropic admittance are defined as in (5.10) and (5.11). The salient admittance term is a function of the electrical angle as shown in (5.12).

$$\frac{d}{dt}\boldsymbol{i}_s^s = (Y_\Sigma + Y_\Delta S(\theta_e))(\boldsymbol{u}_s^s - r_s\boldsymbol{i}_s^s - \omega_e\acute{\boldsymbol{L}}_s^s\boldsymbol{i}_s^s) \tag{5.9}$$

$$Y_\Sigma = \frac{Y_d + Y_q}{2} = \frac{1}{2}\left(\frac{1}{L_d} + \frac{1}{L_q}\right) \tag{5.10}$$

$$Y_\Delta = \frac{Y_d - Y_q}{2} = \frac{1}{2}\left(\frac{1}{L_d} - \frac{1}{L_q}\right) \tag{5.11}$$

$$S(\theta_e) = \begin{bmatrix} cos(2\theta_e) & sin(2\theta_e) \\ sin(2\theta_e) & -cos(2\theta_e) \end{bmatrix} \tag{5.12}$$

Usually it is wise to model the entire machine model mathematically when designing a control scheme. However, in this method the saliency admittance, Y_Δ of the RSM is consciously neglected from the machine equations [2, 28, 56]. The isotropic admittance, Y_Σ is a scalar with no dependency on the rotor angle, thus the inductance derivative with respect to the electrical angle, $\acute{\boldsymbol{L}}_s^s = 0$ [2]. Neglecting the saliency component, (5.8) is rewritten as in (5.14) [2, 28].

$$\begin{aligned} \frac{d}{dt}\hat{\boldsymbol{i}}_s^s &= Y_\Sigma(\boldsymbol{u}_s^s - r_s\boldsymbol{i}_s^s) && (5.13)\\ &= Y_\Sigma\boldsymbol{u}_L^s && (5.14) \end{aligned}$$

where

$$\boldsymbol{u}_L^s = \boldsymbol{u}_s^s - r_s \boldsymbol{i}_s^s \tag{5.15}$$

The hat above the current derivative in (5.14) points to the isotropic current derivative term. The vector $\boldsymbol{u}_L^s$ is the isotropic voltage term. The isotropic current vector of (5.14) will align with (5.15) if the machine is isotropic as shown graphically in Fig. 5.1 [56]. The RSM is not isotropic, in fact it is salient, and the salient part of the calculation was neglected, thus the current response will be that of a salient pole machine instead of an isotropic machine. This will result in an estimation error, $\Delta \boldsymbol{i}_s^s$, as shown in Fig 5.1. The current vector, $\boldsymbol{i}_s^s$, rotates at a frequency of ω_e on a circle around $\boldsymbol{u}_L^s$.

A discrete model of the RSM is used to predict the current response of an isotropic machine for one time step [56]. The discrete model of the isotropic voltage is derived in (5.16) [56]. Predictions are built with Euler approximations of (5.14) [28]. The forward euler integration is defined as in (5.17) and (5.18) [57]. The current prediction is thus written as in (5.19) [2, 28, 56].

$$\boldsymbol{u}_L^s[k] = \boldsymbol{u}_s^s[k] - r_s \boldsymbol{i}_s^s[k] \tag{5.16}$$

$$\dot{x}[k] = f(x[k], r[k]) \tag{5.17}$$

$$x[k+1] = x[k] + \int_{kT}^{([k+1])T} f(x[k], r[k]) dt \tag{5.18}$$

$$\hat{\boldsymbol{i}}_s^s[k+1] = \boldsymbol{i}_s^s[k] + Y_\Sigma \boldsymbol{u}_L^s[k] \Delta t \tag{5.19}$$

Equation (5.19) predicts the current response of a linear isotropic RSM for one time step Δt.

5.2 Saliency Tracking Approach

The measured current, $\boldsymbol{i}_s^s[k]$, is used in (5.19) to predict $\hat{\boldsymbol{i}}_s^s[k+1]$, which is the current that would be reached if the voltage $\boldsymbol{u}_s^s[k]$ is applied to an isotropic machine for one time step [2, 28]. The predicted current, $\hat{\boldsymbol{i}}_s^s[k+1]$ will have the same orientation as $\boldsymbol{u}_L^s$ in an isotropic machine [2, 28, 56]. When the voltage $\boldsymbol{u}_s^s[k]$ is applied to a salient machine, the measured current in the next time step will differ from the prediction due to the saliency of the machine [28]. The derivative of the measured current in (5.8) is expanded to (5.20) and rewritten as in (5.21) [2, 58].

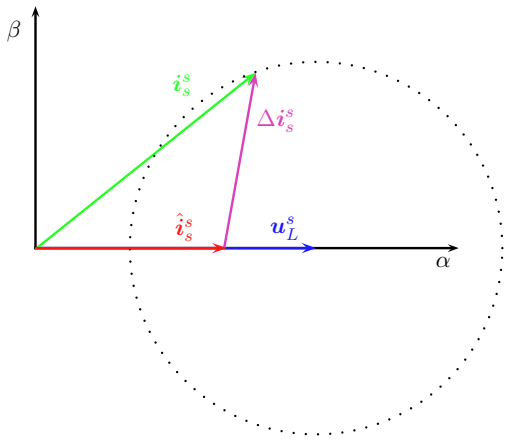

Figure 5.1: Current estimation error in vector form [2].

$$\frac{d}{dt}\boldsymbol{i}_s^s = \boldsymbol{L}_s^{s-1}(\boldsymbol{u}_s^s - r_s\boldsymbol{i}_s^s) - \boldsymbol{L}_s^{s-1}\acute{\boldsymbol{L}}_s^s\omega_e\boldsymbol{i}_s^s \tag{5.20}$$

$$\Delta\boldsymbol{i}_s^s = \boldsymbol{L}_s^{s-1}\boldsymbol{u}_L^s\Delta t + \Delta\boldsymbol{i}_{FM}^s \tag{5.21}$$

The current prediction error can be displayed graphically as in Fig. 5.2 where $\Delta\hat{\boldsymbol{i}}_s^s$ is the derivative of the current prediction of (5.14) [2]. It is shown in this graph that the difference caused by the neglect of the saliency results in two error components, $\Delta\boldsymbol{i}_{HF}^s$ and $\Delta\boldsymbol{i}_{FM}^s$ [28]. $\Delta\boldsymbol{i}_{FM}^s$ is the fundamental (EMF) circulation of the current vector at constant flux ($\boldsymbol{u}_L^s = 0$), induced by the movement of the salient rotor [28]. It scales with rotor speed and magnitude of the current $|\boldsymbol{i}_s^s|$ [28]. $\Delta\boldsymbol{i}_{HF}^s$ is caused by applying the voltage $\boldsymbol{u}_L^s$ to a salient machine instead of -isotropic [28]. It points in a circle around the predicted current and its orientation is determined by the rotor position θ_m.

By introducing $Y_\Sigma = \dfrac{Y_d + Y_q}{2}$, ΔY and the saliency matrix $\mathbf{S}(\theta_e)$, the inductance tensor can be separated in a scaling and rotating term and can be used to derive (5.23) [2, 28].

$$\Delta\boldsymbol{i}_s^s = Y_\Sigma\boldsymbol{u}_L^s + \Delta Y\boldsymbol{S}(\theta_e)\boldsymbol{u}_L^s\Delta t + \Delta\boldsymbol{i}_{FM}^s \tag{5.22}$$

$$= \Delta\hat{\boldsymbol{i}}_s^s + \Delta\boldsymbol{i}_{HF}^s + \Delta\boldsymbol{i}_{FM}^s \tag{5.23}$$

According to [56] both $\Delta\boldsymbol{i}_{HF}^s$ and $\Delta\boldsymbol{i}_{FM}^s$ rotate twice during one rotor turn, i.e have the same frequency as the electrical angle. Only $\Delta\boldsymbol{i}_{HF}^s$ scales with $\boldsymbol{u}_L^s$ which makes it more reliable to use for tracking. It is possible to measure $\Delta\boldsymbol{i}_{HF}^s$ by subtracting $\Delta\boldsymbol{i}_{FM}^s$ from the the current prediction error, $\boldsymbol{e}_{prd}^s$ as in (5.25) [28]. It is shown in (5.23) that $\Delta\boldsymbol{i}_{HF}^s$ can also be calculated as in (5.26) [2].

$$\Delta\boldsymbol{i}_{HF}^s = (\Delta\boldsymbol{i}_s^s - \Delta\hat{\boldsymbol{i}}_s^s) - \Delta\boldsymbol{i}_{FM}^s \tag{5.24}$$

$$= \boldsymbol{e}_{prd}^s - \Delta\boldsymbol{i}_{FM}^s \tag{5.25}$$

$$\Delta\acute{\boldsymbol{i}}_{HF}^s = Y_\Delta\boldsymbol{S}(\hat{\theta}_e)\boldsymbol{u}_L^s \tag{5.26}$$

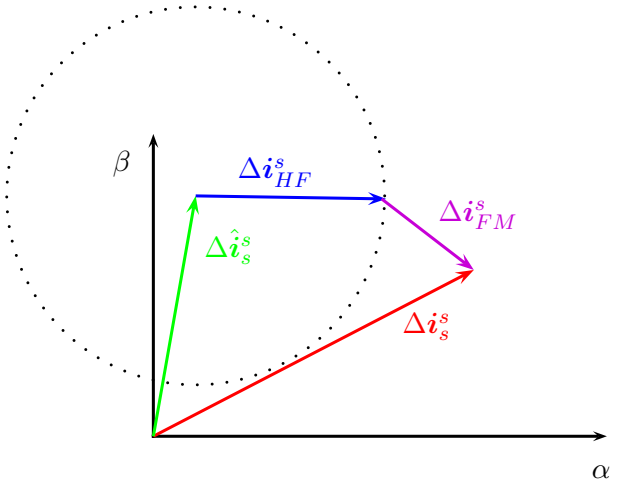

Figure 5.2: Current prediction error [2].

The difference in orientation between $\Delta \boldsymbol{i}^s_{HF}$ and $\Delta \acute{\boldsymbol{i}}^s_{HF}$ is the angle difference between the electrical angle and the estimated electrical angle. The difference in orientation is calculated with the vector product as in (5.27). The error signal, e_{pll}, can be fed through a PI controller which reacts in an almost similar way to the PLL of the HFI-PSC method [28]. The salient impedance, Y_Δ, just acts as a gain of the PI controller and is thus omitted from (5.27) [2].

$$e_{pll} = (\boldsymbol{i}^s_s - \hat{\boldsymbol{i}}^s_s - \Delta \boldsymbol{i}^s_{FM})^T \boldsymbol{J}\boldsymbol{S}(\theta_{pll})\boldsymbol{u}^s_L \tag{5.27}$$

5.3 Non-Linear Extension

The proposed AI-PSC method is thus far derived with a linear RSM machine model. The RSM behaviour however, is non-linear especially when the machine is saturated. Linearised assumptions will thus cause the proposed AI-PSC method to fail. The introduction of two non-linear extensions into the derivation of this method will ensure stability and satisfactory performance of this PSC method.

Mean inverse inductance

According to [2, 28], it is important to always point, $Y_\Sigma(i)$ into the middle of the circle in Fig. 5.2 when predicting $\Delta \hat{\boldsymbol{i}}^s_s$. The isotropic admittance is not constant and is calculated as in (5.28). The measured isotropic admittance of machine 1 is shown in Fig. 5.3.

$$Y_\Sigma(\boldsymbol{i}^r_s) = \frac{L_d^{-1}(i_d, 0) + L_q^{-1}(0, i_q)}{2} \tag{5.28}$$

where

$$L_d(i_d, i_q) = \frac{\partial \psi_d(i_d, i_q)}{\partial i_d} \tag{5.29}$$

$$L_q(i_d, i_q) = \frac{\partial \psi_q(i_d, i_q)}{\partial i_q} \tag{5.30}$$

To solve this problem, lookup tables are used to determine the mean admittance [28]. The lookup table can be obtained from FE simulations or measurements [28]. The PSC scheme is stabilised by adapting the non-linear isotropic admittance [2, 28].

Load angle compensation

Cross saturation between the d- and q-axis of synchronous machines can cause the magnetic axis to misalign with the rotor when the machine is loaded. The load dependent misalignment between the ori-

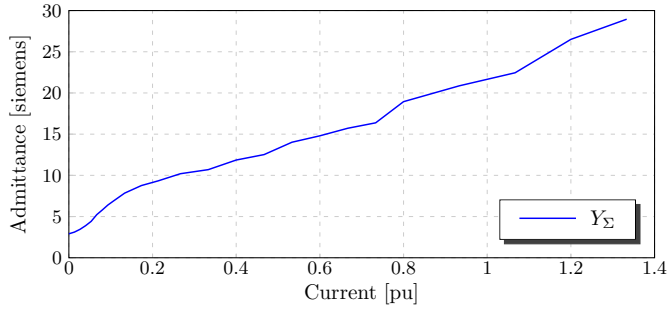

Figure 5.3: Measured isotropic admittance of machine 1.

entation of the inductance saliency and the rotor angle is well known from HF injection based approaches. The misalignment creates the problem that if the fundamental current is controlled according to the orientation for the saliency it takes less load for the saliency to vanish due to saturation than if the control is done using the actual rotor angle [2]. This problem is solved by adding a load dependent compensation angle to the PLL estimation before calculating $S(\theta_e)$. The load compensation curve of machine 1 is identified through measurements by [28] as (5.31). The compensation curve can be measured in the same way as described in Chapter 4. The compensation curve ensures satisfactory performance from the AI-PSC method.

$$C(T_m^*) = -0.038 * T_M^* \left[\frac{rad}{Nm}\right] \tag{5.31}$$

5.4 Injection Sequence

The method of PSC described in this chapter is originally developed in [56] as part of a predictive torque control scheme. With predictive torque control, $\boldsymbol{u}_L^s$ is always sufficiently large to be able to predict the current with (5.19). Migrating this method to FOC requires some form of signal excitation to induce a current that can be predicted.

A rotating HF voltage can be superimposed onto the fundamental control voltage in the stationary reference frame similar to conventional HF injection methods to ensure that the voltage excitation is large enough. A pulse injection sequence is suggested in [54]. A current response can be ensured for every setpoint by adding a pulse injection sequence signal to the reference voltage vector [54]. According to [54] an increased injection frequency produces more position information per time unit, larger distance to the bandwidth of the current controller and lower audible noise. Taking these considerations into account, [54] suggests that a rectangular signal with half the PWM frequency be used. Furthermore, it is stated in [54] that additional voltage injection limits the excitation range for the fundamental current control, as with conventional HF injection methods. A trade off thus exists between signal frequency and signal amplitude.

The injection signal is rotated with fractions of 2π. The injection sequence in the stationary reference frame is as follows:

$[1\ ;\ 0] \rightarrow$ Aligned with the a-phase,
$[\cos(120^o)\ ;\ \sin(120^o)] \rightarrow$ Aligned with the b-phase
$[\cos(240^o)\ ;\ \sin(240^o)] \rightarrow$ Aligned with the c-phase

Not only does this injection sequence allow current excitation for position estimation, it also allows estimation of the resistance and the mean admittance, Y_Σ, as will be shown in the next section.

5.5 Reduced Machine Parameter Dependency

The AI-PSC method as derived thus far requires knowledge of the stator resistance, rotor speed, inductance and the mean admittance. Suggestions are made in [54] and [58] about how to extend the AI-PSC method to be completely parameter insensitive.

Current circulation

The circulation of the the current, caused by the rotating saliency at constant flux, is described by $\Delta \boldsymbol{i}_{FM}^s$ [28]. This component needs to be compensated for due to the large saliency of the RSM, but this requires accurate machine parameter knowledge that is almost impossible to reproduce [28]. In case of

small or medium saliencies e.g for surface mounted PMSMs, the neglect of this term has only a small effect on the position estimation [56]. For machines with a strong inductance saliency like RSMs the magnitude of this term will become comparable to the other terms in (5.25) if large currents are applied at high rotor speeds [56].

According to [2] and [28], $\Delta \boldsymbol{i}^s_{FM}$ rotates with a frequency around rotor speed and is nearly constant in the rotor reference frame. It is suggested by [2] and [28] that $\Delta \boldsymbol{i}^s_{FM}$ be calculated by low pass filtering the prediction error in rotor reference frame. It is important to implement the digital filter in the rotor reference frame [2]. According to [2], the low pass filtered fundamental current circulation, $\Delta \boldsymbol{i}^s_{FM}$, can be used in (5.25) to calculate $\Delta \boldsymbol{i}^s_{HF}$. Furthermore, it is stated by [2] that the subtraction of (5.25) results in a high pass filtered prediction error e^s_{prd}. It is thus suggested by [28] that a digital high pass filter be used on e^s_{prd} to reduce the effects of $\Delta \boldsymbol{i}^s_{FM}$ in machines with strong saliencies which operate at high speeds.

Mean inverse inductance

To realise complete parameter insensitivity a few assumptions are necessary. The first assumption made by [54] is that none of the terms in (5.20) will change within two PWM cycles except for $\boldsymbol{u}^s_L$. The resistive voltage is very small compared to the other terms and its variation within two cycles is certainly negligible [54]. An assumption can thus be made that the EMF vector, $\Delta \boldsymbol{i}^s_{FM}$, can only be considered if the switching frequency is much larger than the rotor frequency. It is stated in [54] that if these terms in (5.20) are considered to be constant, the difference between two current progressions can be forecast by using the stator voltage instead of the inductance voltage [54]. Now the isotropic term in (5.21) can be approximated by:

$$\Delta \hat{\boldsymbol{i}}^s_s = Y_\Sigma(\boldsymbol{u}^s_L[k] - \boldsymbol{u}^s_L[k-1])t_s \tag{5.32}$$

$$= Y_\Sigma(\boldsymbol{u}^s_s[k] - \boldsymbol{u}^s_s[k-1])t_s \tag{5.33}$$

The influence of the resistive and induced voltage is cancelled out in the model in (5.33) by always considering the difference between two consecutive steps as in (5.34) [54]. The difference in current response of the isotropic machine can be measured with (5.35) [54, 55].

$$\Delta(\Delta \hat{\boldsymbol{i}}^s_s) = Y_\Sigma \Delta \boldsymbol{u}^s_s t_s \tag{5.34}$$

$$\Delta(\Delta \boldsymbol{i}^s_s) = \boldsymbol{i}^s_s[k] - 2\boldsymbol{i}^s_s[k-1] + \boldsymbol{i}^s_s[k-2] \tag{5.35}$$

Now e^s_{prd} can be calculated by:

$$e^s_{prd} = \Delta(\Delta \boldsymbol{i}^s_s) - \Delta(\Delta \hat{\boldsymbol{i}}^s_s)) \tag{5.36}$$

The final remaining machine parameter that needs to be estimated is the mean admittance, Y_Σ. According to [54], Y_Σ describes the average current slope for HF voltage excitation at the actual setpoint. The injection sequence presented by [54] and implemented in this chapter allows for fast updates of the average inductance. The current slope, after the application of a voltage vector, represents the actual machine admittance for this small signal excitation [54].

Assuming that the rotor position is unknown and the machine is at standstill, the mean admittance Y_Σ can be obtained by rotating the injection direction and integrating the current response in the injection frame for half a rotation as follows:

$$Y_\Sigma = \frac{1}{\pi} \int_0^\pi \frac{\frac{d}{dt} i_\delta}{u_\delta} d\theta_e, \tag{5.37}$$

where δ denotes the component in the injection direction [54]. It is shown in [58], that the mean admittance can be approximated in the discrete case by:

$$Y_\Sigma = \frac{1}{6}\sum_{k=1}^{6}\frac{\Delta \boldsymbol{i}_{HF}^{T}\boldsymbol{u}_s^s}{\boldsymbol{u}_s^{sT}\boldsymbol{u}_s^s 2t_s} \tag{5.38}$$

Even though the integral is approximated by a sum, the result will be exact since the sum of the sinusoidal values that are equally distributed within 2π, equals zero [54].

Figures 5.4 - 5.7 show the schematic implementation of the proposed AI-PSC method. The schematic of the current prediction scheme is shown in Fig. 5.4. The mean inverse inductance is calculated as in Fig. 5.5. The low frequency saliency component is separated from the current prediction error as in Fig. 5.6. The saliency tracking scheme is implemented graphically as in Fig. 5.7.

5.6 Simulation

Simulations are done in the Simulink package with the measured flux maps of machine 1. The simulation control parameters are as in Table 5.1. The performance of the PSC method is improved in the simulation environment by high pass filtering $\boldsymbol{e}_{prd}^s$ in the estimated rotor reference frame as explained earlier in this chapter. It is found however, that assumptions made in the derivation of the PSC method still affect the PSC performance at high speeds even with the filtering.

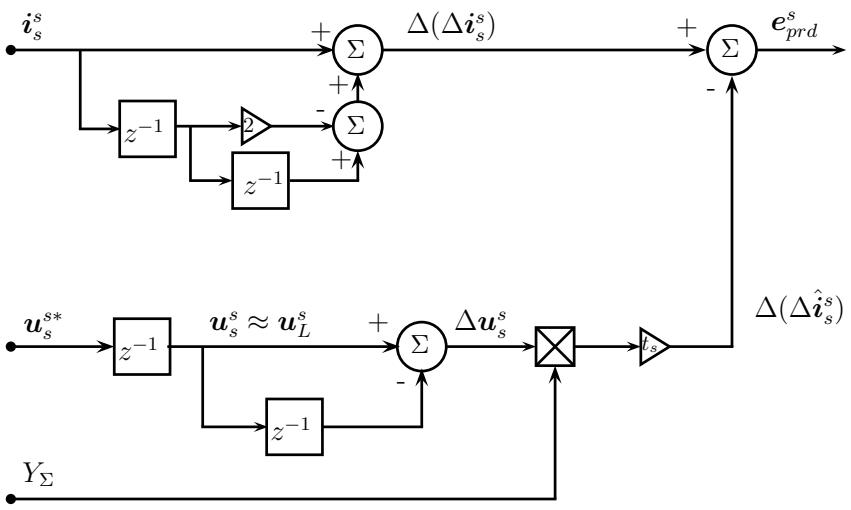

Figure 5.4: Current prediction scheme.

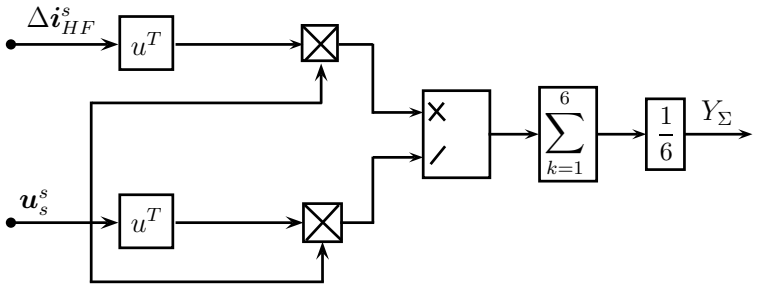

Figure 5.5: Mean inverse inductance.

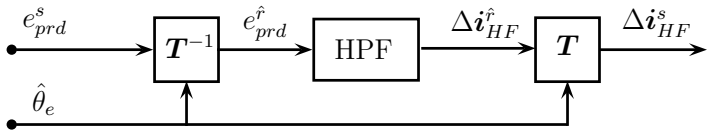

Figure 5.6: Separation of high frequency prediction error and fundamental circulation current.

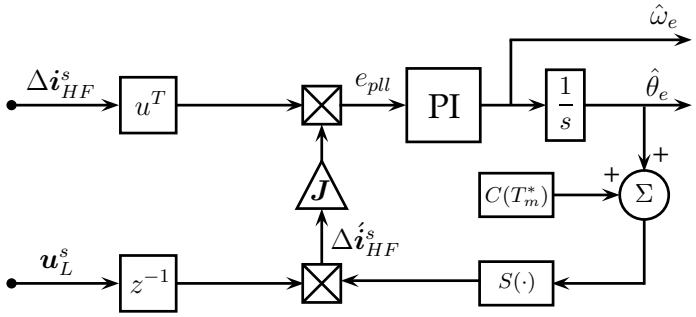

Figure 5.7: Saliency tracking scheme.

Table 5.1: Simulation controller parameters

Current proportional gain	k_p	270	V/A
Current time constant	T_i	2.73	ms
PLL proportional gain	k_{pPLL}	1.5	rad/s
PLL time constant	T_{PLL}	2.5	ms
Current LPF	LPF_i	900	rad/s
Injection voltage	u_{inj}	160	V

Simulation results of machine 1 with the AI-PSC method are shown in Fig. 5.8. A rated current step is applied as shown in Fig. 5.8a while the speed is kept constant as if controlled by a larger shaft connected machine. It is clear that the reference current is reached almost instantaneously. It is shown in Fig. 5.8c that the rated current step results in a rated torque step. Another current step is applied at $6s$. The speed is slightly ramped up, however it is kept in the low speed region as shown in Fig. 5.8d due to the limitation of the AI-PSC method. Large position estimation errors are shown in Fig. 5.8b at startup. This is due to the delays required for current prediction and eventually synchronisation of the PLL once the AI-PSC method is activated. Furthermore, it is shown in Fig. 5.8b that the position estimation error increases past 10° when the machine is overloaded.

Simulations results show that the AI-PSC method works effectively with the RSM even though machine 1 has a very large saliency, limiting its performance at high speeds. This method is usually only used at standstill and low speeds, thus the limitations of this method in the medium to high speed region should not be a problem.

5.7 Measured Results

The AI-PSC method is tested on machine 1 in the laboratory environment. It is shown in Chapter 4 that the magnitude of this RSM's inductance saliency is too small at zero and small current vectors for the alternating HFI-PSC method to track the electrical angle of the machine. The reference current vector is altered to implement HFI-PSC at zero reference current as explained in Chapter 4. This same methodology is also necessary when implementing the AI-PSC on the RSM.

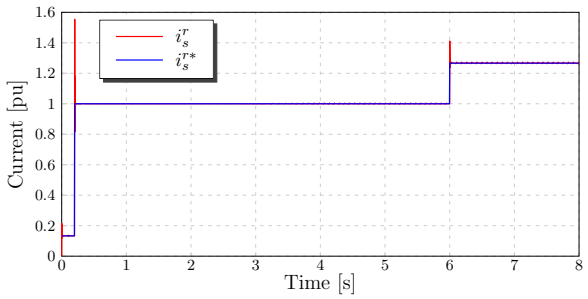

(a) Reference- and machine current.

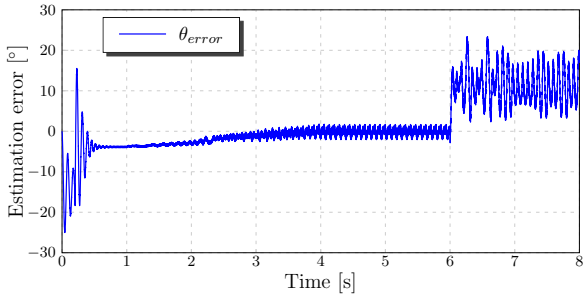

(b) Position estimation error.

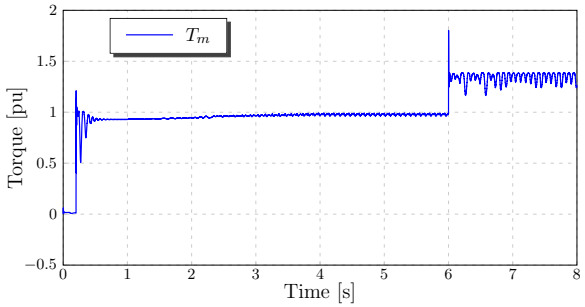

(c) Mechanical torque.

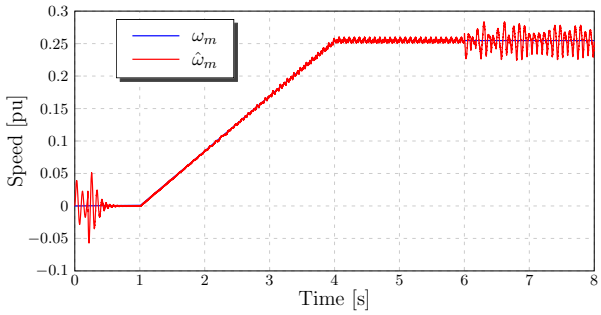

(d) Machine- and estimated speed.

Figure 5.8: AI-PSC: Rated current step simulation of machine 1.

5.7.1 Current response

The current controller, which is the inner loop of the control structure, is evaluated first. The parameters as implemented on the RPS are given in Table 5.2. A rated current step is applied to the position sensorless controlled RSM, similar to the simulation result, in Fig. 5.9a. The speed is kept constant by the IM at a speed of 0.25 *p.u.* A digital oscilloscope is used to plot and save the reference- and measured current of the RSM. These results are shown in Fig. 5.9a.

The measured current vector in Fig. 5.9a (red line) is calculated with the real electrical angle θ_e as in the measured results of Chapter 4. The measured current vector gives a good indication of the quality of the PSC method. The results in Fig. 5.9a show that the position sensorless controlled RSM can apply rated torque steps when controlled with the AI-PSC method.

The maximum torque, that machine 1 can deliver when controlled with the AI-PSC method as a function of rotor speed, is shown in Fig. 5.9b. These results are compared to those of the HFI-PSC method. It is clear that the startup torque of the position sensorless controlled RSM at zero speed, is very high at 3.3 *p.u.* This is much higher than what is possible with the HFI-PSC method. The torque curve of the AI-PSC method however, drops quite steeply as the speed increases. This is due to the large saliency of the RSM and the assumptions made regarding the fundamental component in the derivation

Table 5.2: Rapid prototype system controller parameters for position sensorless current controlled machine 1.

Current proportional gain	k_p	220	V/A
Current time constant	T_i	2.73	ms
PLL proportional gain	k_{pPLL}	1.8	rad/s
PLL time constant	T_{PLL}	2.73	μs
Current LPF	LPF_i	-	rad/s
Injection voltage	u_{inj}	160	V

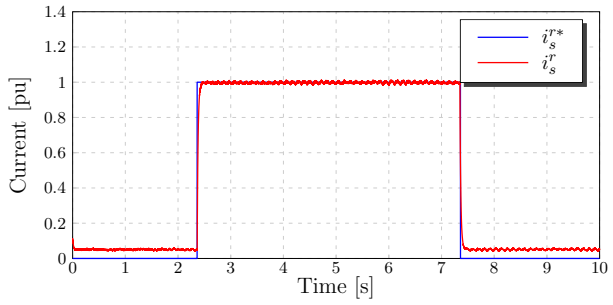

(a) Measured current step response on machine 1.

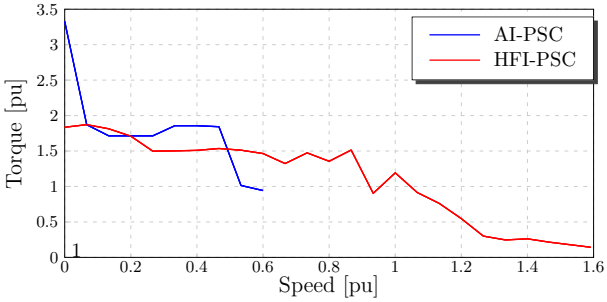

(b) Limits of stable operation.

Figure 5.9: AI-PSC: Measured current response of machine 1.

of the method. Unity torque is possible with the AI-PSC method up to a speed of 0.6 *p.u.* SB-PSC methods however, only operate in the low speed region and at standstill. The results in Fig. 5.9b are thus satisfactory.

5.7.2 Speed response

Speed control is implemented with the AI-PSC method on machine 1. The controller parameters, as implemented on the RPS, are shown in Table 5.3. The IM is used to load to the position sensorless controlled RSM at rated torque while at standstill. A speed step is applied by the RSM while still loaded, as shown in Fig. 5.10a. It is shown in Fig. 5.10a that the measured speed is very noisy and thus requires low pass filtering in the speed controller feedback. The measured speed however is not used in the speed controller feedback, but rather the estimated speed acquired from the PSC method.

It is shown in Fig. 5.10a that the speed controller reaches its reference speed even when rated load is applied. The position estimation error in Fig. 5.10b shows large position estimation errors when the machine is loaded. The increased error under load is due to the saliency shift of the machine. The load angle compensation equation, (5.31), is used compensate for the saliency shift.

The dynamic speed response of the position sensorless controlled RSM is investigated with the AI-PSC method. These results are shown in Fig. 5.11. Again, the RSM is loaded at rated torque by the IM at standstill. A positive speed step is applied by the RSM followed by a negative speed step as shown in Fig. 5.11a. It is shown in Fig. 5.11a that it is possible for the RSM to do speed reversal at rated load while controlled with the AI-PSC method. The position estimation error results in Fig. 5.11b show that the position estimation error changes sign when the machine direction changes, but does not cause the PLL to desynchronise.

Table 5.3: Rapid prototype system controller parameters for position sensorless speed controlled machine 1.

Current proportional gain	k_p	220	V/A
Current time constant	T_i	2.73	ms
Speed proportional gain	k_{ps}	0.09	Nms/rad
Speed time constant	T_{is}	0.41	s
PLL proportional gain	k_{pPLL}	1.8	rad/s
PLL time constant	T_{PLL}	2.73	μs
Current LPF	LPF_i	-	rad/s
Speed LPF	LPF_s	24.41	rad/s
Injection voltage	u_{inj}	160	V

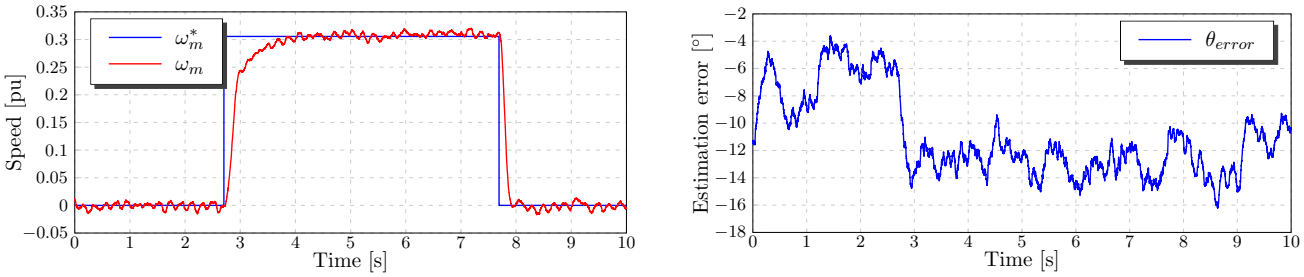

(a) Reference speed and measured speed.

(b) Position estimation error.

Figure 5.10: AI-PSC: Measured speed step response of machine 1 at rated load.

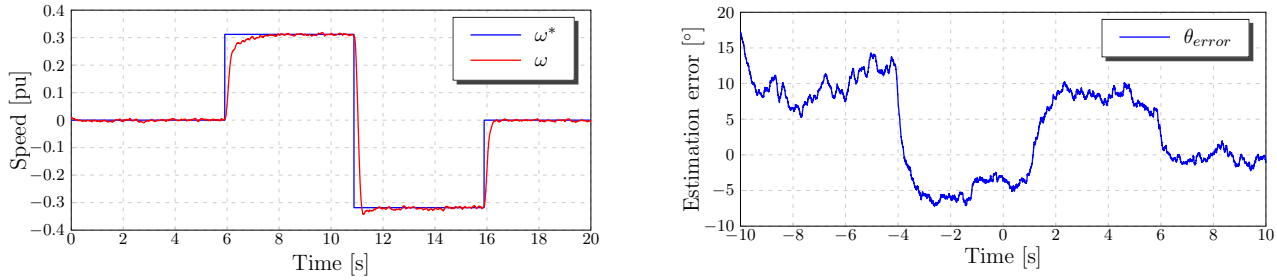

(a) Reference speed and measured speed.

(b) Position estimation error.

Figure 5.11: AI-PSC: Measured speed reversal response of machine 1 at rated load.

5.8 Summary

A fairly new saliency-based position sensorless control (SB-PSC) method is introduced and investigated in this chapter. The arbitrary injection position sensorless control (AI-PSC) method exploits the machine saliency with pulse injected HF voltages in the stationary reference frame at half of the PWM frequency. The euler method is used to predict the current response of an isotropic machine. The current response however, is that of a salient pole machine. The measured and predicted current vectors are used to estimate the electrical angle of the machine.

The drawback of the investigated method is its limited torque capabilities at high speeds when used with machines with large inductance saliencies. SB-PSC methods however, are only used at standstill and low speeds. The advantage of the AI-PSC method is that the position estimation is done in the stationary reference frame instead of the estimated rotary reference frame as with the high frequency injection position sensorless control (HFI-PSC) method. The PLL is more stable when position estimation is done in the stationary reference frame due to fewer uncertainties. Furthermore, no current low pass filters are necessary due to the very high injection frequency. The biggest advantage of the AI-PSC method is its parameter insensitivity. The AI-PSC method is a general algorithm that can be implemented on any synchronous machine due to its online parameter estimation.

The proposed AI-PSC method is simulated in the Simulink package with the flux map model of machine 1. Simulations results show that current controllers are stable with PSC allowing the RSM to deliver rated torque dynamically.

The proposed AI-PSC method is implemented and evaluated on machine 1. Measured results show that the position sensorless controlled RSM can deliver rated torque steps. Limits of stable operation test results reveal that the AI-PSC method is able to deliver higher startup torque than the HFI-PSC method. The torque that the position sensorless controlled RSM can deliver however, decreases sharply as the machine speed increases. Speed control tests results show that the RSM can apply dynamic speed steps at rated load when controlled with the AI-PSC method. Speed reversal at rated load is also possible.

Chapter 6

Fundamental Saliency Position Sensorless Control

Position sensorless control (PSC) methods for synchronous machines can be divided into two main categories. The first is the saliency-based PSC (SB-PSC) methods. Two continuous injection SB-PSC methods are discussed and evaluated in Chapters 4 and 5. The second category of PSC methods is the fundamental- and model-based methods. This includes back emf-, flux linkage- and observer-based methods [29]. Fundamental- and model based techniques are only used to control synchronous machines from minimum to high speeds as they are not able to estimate the electrical angle at standstill and low speeds.

Back EMF PSC methods are used with PM synchronous machines to estimate the electrical angle at minimum to high speeds [59]. These methods observe the back EMF of the machine to estimate the direction of the rotor flux, which is the same as the rotor position. The back EMF is a product of the flux linkage and speed as shown by the synchronous machine voltage equations [17]. Thus, both the rotor speed and back EMF need to be sufficiently large for proper estimation, limiting successful PSC to the medium to high speed range of the machine [17].

The conventional back EMF method of position detection cannot be used to control the RSM due to the only source of flux being the stator currents. The active flux method is a unified AC machine fundamental model PSC method [60]. This method is not considered in this thesis but the author acknowledges that this is a well-developed PSC method. Other methods include stator flux estimation methods [61, 62] and direct estimator methods [63]. A flux linkage-based fundamental model method for RSMs is introduced in [3]. This method is the fundamental saliency position sensorless control (FS-PSC) method. This method takes into account the non-linear relationship between the isotropic flux and current, allowing the position sensorless controlled RSM to produce high torque with good dynamics. However, this method, like the other fundamental model-based methods, is unable to estimate the rotor position at low speeds and standstill.

The FS-PSC method, as described by [3], is discussed in this chapter. The performance of this method is then investigated with simulations and implemented on a test bench to evaluate its performance.

6.1 Linear Position Estimation

The flux linkage vector, $\boldsymbol{\psi}_s^r$, in the rotary reference frame is a function of the stator current in the rotor reference frame, $\boldsymbol{i}_s^r$. Although this relationship can be linear or nonlinear it has to be anisotropic for a RSM [28]. An assumption is made in [3], that the flux linkage vector in the rotor fixed frame, $\boldsymbol{\psi}_s^r$, has a linear dependency on the current vector in the rotor fixed frame, $\boldsymbol{i}_s^r$. This implies that $\boldsymbol{\psi}_s^r$ can be calculated using the secant inductance vector, $\boldsymbol{L}_{ss}^r$ as in (6.1).

$$\boldsymbol{\psi}_s^r = \boldsymbol{L}_{ss}^r \boldsymbol{i}_s^r \tag{6.1}$$

Similarly to the tangential inductance vector derived in Chapter 4, the secant inductance vector can be derived in the stationary reference frame as in (6.2) [3]. Equation (6.2) is simplified to (6.3).

$$\boldsymbol{L}_{ss}^s = \begin{bmatrix} L_{ds}cos^2(\theta_e) + L_{qs}sin^2(\theta_e) & (L_{ds} - L_{qs})sin(\theta_e)cos(\theta_e) \\ (L_{ds} - L_{qs})sin(\theta_e)cos(\theta_e) & L_{ds}sin^2(\theta_e) + L_{qs}cos^2(\theta_e) \end{bmatrix} \tag{6.2}$$

$$\boldsymbol{L}_{ss}^s = L_\Sigma \boldsymbol{I} + L_\Delta \begin{bmatrix} cos(2\theta) & sin(2\theta) \\ sin(2\theta) & -cos(2\theta) \end{bmatrix} \tag{6.3}$$

In (6.3), $L_\Sigma = (L_{ds} + L_{qs})/2$ is the isotropic- and $L_\Delta = (L_{ds} - L_{qs})/2$ the rotating terms [37, 42]. It is possible to express the secant inductance matrix in the stationary reference frame and thus it is possible to derive $\boldsymbol{\psi}_s^s$ in terms of (6.3) as in (6.4). The flux linkage equation is simplified by substituting ψ_Σ^s and $\boldsymbol{\psi}_\Delta^s$ as in (6.5) [3]. The vector $\boldsymbol{\psi}_\Delta^s$ is defined by [3] as the fundamental saliency and ψ_Σ^s the isotropic flux linkage. Both these vectors can be derived from d- and q-axis flux linkages as in (6.6)

$$\begin{aligned} \boldsymbol{\psi}_s^s &= L_\Sigma \boldsymbol{i}_s^s + L_\Delta \begin{pmatrix} cos(2\theta) & sin(2\theta) \\ sin(2\theta) & -cos(2\theta) \end{pmatrix} \boldsymbol{i}_s^s & (6.4) \\ &= \psi_\Sigma^s + \boldsymbol{\psi}_\Delta^s & (6.5) \end{aligned}$$

$$\psi_\Sigma^s = \frac{\psi_d + \psi_q}{2}, \qquad \boldsymbol{\psi}_\Delta^s = \frac{\psi_d - \psi_q}{2} \tag{6.6}$$

It is shown in Fig. 6.1, as drawn by [3], that ψ_Σ^s is parallel to the stator current and $\boldsymbol{\psi}_\Delta^s$ rotates with double the rotor speed while having a constant magnitude equal to the current angle, ϕ [3]. Assuming that the values of L_{ds} and L_{qs} are constant and obtainable, it is possible to calculate $\boldsymbol{\psi}_\Delta^s$ and in doing so shift the circle to the origin [3]. By combining (6.7) with (6.8) it is possible to achieve this through online measurements as in (6.9).

$$\boldsymbol{u}_s^s = r_s \boldsymbol{i}_s^{(s)} + \dot{\boldsymbol{\psi}}_s^s \tag{6.7}$$

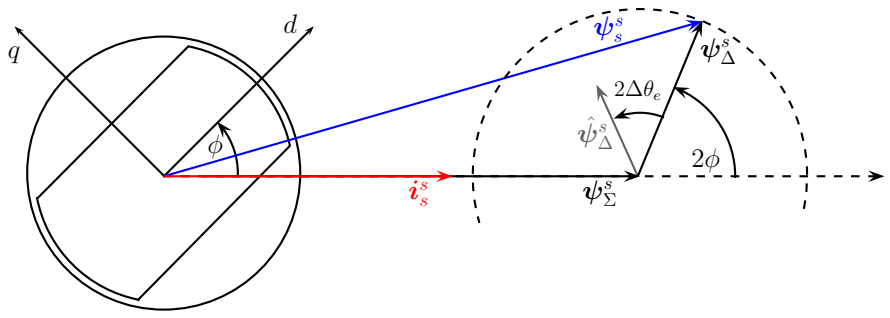

Figure 6.1: Flux linkage orientation due to saliency [3].

$$\boldsymbol{\psi}_{\Delta}^{s} = \boldsymbol{\psi}_{s}^{s} - L_{\Sigma}\boldsymbol{i}_{s}^{s} \tag{6.8}$$

$$= \int \boldsymbol{u}_{s}^{s} - r_{s}\boldsymbol{i}_{s}^{s}dt - L_{\Sigma}\boldsymbol{i}_{s}^{s} \tag{6.9}$$

The isotropic inductance, L_{Σ}, as shown in (6.9) can be measured or obtained from FE simulations to calculate the rotating fundamental saliency vector, $\boldsymbol{\psi}_{\Delta}^{s}$ [3]. Equation (6.10) can be used to reconstruct $\hat{\boldsymbol{\psi}}_{\Delta}^{s}$ in the estimated rotary reference frame with the estimated electrical angle. Essentially the vectors $\boldsymbol{\psi}_{\Delta}^{s}$ and $\hat{\boldsymbol{\psi}}_{\Delta}^{s}$ will be aligned if $\hat{\theta}_{e} = \theta_{e}$. Thus, the angle difference between these two vectors is the electrical position estimation error, $\Delta\theta_{e}$. This angle can be calculated with the vector product of these two vectors as in (6.11) [3]. The position estimation error, $\Delta\theta_{e}$ is used as the input of a PI controller which is similar to the the PLL used in the previous two chapters, hence the notation θ_{pll}.

$$\hat{\boldsymbol{\psi}}_{\Delta}^{s} = L_{\Delta}\begin{bmatrix} cos(2\hat{\theta}_{e}) & sin(2\hat{\theta}_{e}) \\ sin(2\hat{\theta}_{e}) & -cos(2\hat{\theta}_{e}) \end{bmatrix}\boldsymbol{i}_{s}^{s} \tag{6.10}$$

$$\Delta\theta_{e} = \theta_{pll} = \boldsymbol{\psi}_{\Delta}^{s}\boldsymbol{J}\hat{\boldsymbol{\psi}}_{\Delta}^{s} \tag{6.11}$$

It is shown in Fig. 6.1 that the length of $\boldsymbol{\psi}_{\Delta}^{s}$ and $\hat{\boldsymbol{\psi}}_{\Delta}^{s}$ will differ if L_{Δ} is omitted from (6.10). The parameter, L_{Δ}, is constant with no angle offset and thus only acts as a gain to the PLL. L_{Δ} is thus omitted during the calculation of the position estimation error. Integrator drift occurs as a result of the voltage integration in (6.9). The length of $\boldsymbol{\psi}_{\Delta}^{s}$ does not matter either, thus it is possible to drag $\boldsymbol{\psi}_{s}^{s}$ towards ψ_{Σ}^{s} smoothly by subtracting $k_{d}\boldsymbol{\psi}_{\Delta}^{s}$ within the integration of (6.9) as in (6.12) to prevent integrator drift [3].

$$\boldsymbol{\psi}_{\Delta}^{s} = \int \boldsymbol{u}_{s}^{s} - r_{s}\boldsymbol{i}_{s}^{s} - k_{d}\boldsymbol{\psi}_{\Delta}^{s}dt - L_{\Sigma}\boldsymbol{i}_{s}^{s} \tag{6.12}$$

The drift compensation will have a small effect on the magnitude of $\boldsymbol{\psi}_{\Delta}^{s}$ but no effect on its orientation even at low rotor speeds [3]. The linear position estimation scheme as discussed in this chapter, is shown in Figure 6.2.

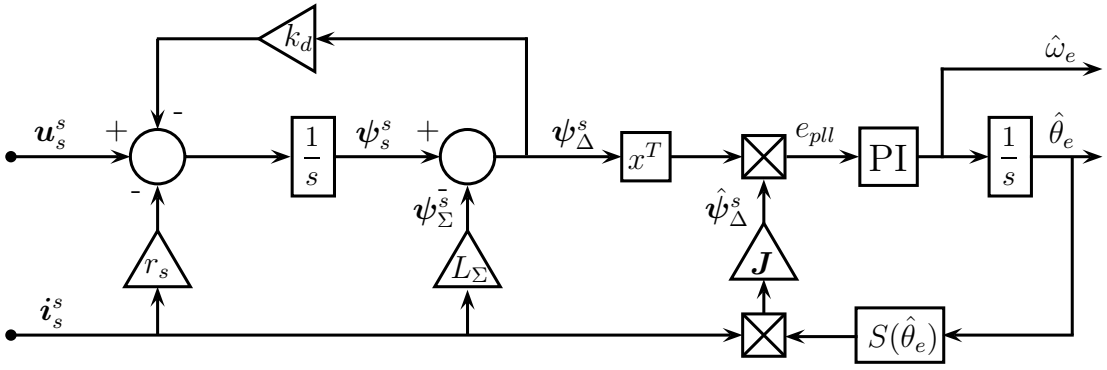

Figure 6.2: Linear fundamental saliency position estimation scheme.

6.2 Nonlinear Position Estimation Method

6.2.1 Nonlinear position estimation technique

The FS-PSC method is derived thus far with the assumption that the relationship between the flux linkage- and current vector is linear. However, as shown in the flux linkage maps in Fig. 3.3, there are strong effects of saturation and cross saturation in the RSM. This of course will affect the performance of a linear position estimation scheme. This problem can be fixed by always finding the centre of the flux circle in Fig. 6.1, by accurate estimations of ψ_Σ^s [3]. The isotropic flux, ψ_Σ^s, should be seen as a non linear function of the stator current and can be represented by lookup tables. By using lookup tables to estimate ψ_d and ψ_q as functions of d- and q-axis current respectively, it is possible to derive ψ_Σ as done in equations (6.13) and (6.14) [3].

$$\psi_\Sigma^s(\boldsymbol{i}_s^s) = \frac{\psi_d(|\boldsymbol{i}_s^s|,0)+\psi_q(0,|\boldsymbol{i}_s^s|)}{2}\frac{\boldsymbol{i}_s^s}{|\boldsymbol{i}_s^s|} \tag{6.13}$$

$$= \psi_\Sigma(|\boldsymbol{i}_s^s|)\frac{\boldsymbol{i}_s^s}{|\boldsymbol{i}_s^s|} \tag{6.14}$$

6.2.2 Angle compensation

When the isotropic flux component, ψ_Σ^s, is pointing to the centre of the circle, the circulating fundamental salient component, $\boldsymbol{\psi}_\Delta^s$, can be calculated by subtracting ψ_Σ^s from $\boldsymbol{\psi}_s^s$ [3]. In [3], it is shown as in Fig. 6.3 that in the non-linear case, $\boldsymbol{\psi}_\Delta^s$ does not run on a circle any more [3]. The magnitude varies during circulation leading to a wrong reconstruction of $\hat{\boldsymbol{\psi}}_\Delta^s$ when using (6.10) due to the wrong angle being used [3]. This will lead to large position estimation errors.

It is stated in [3] that the position estimation error is a function of the current, and the current reference signal is a one dimensional signal. In, [3] a machine specific one dimensional compensation curve is created to add to the estimated angle before calculating (6.10). The non-linear position estimation scheme with angle compensation, $C(i_s)$ is shown in Fig. 6.4.

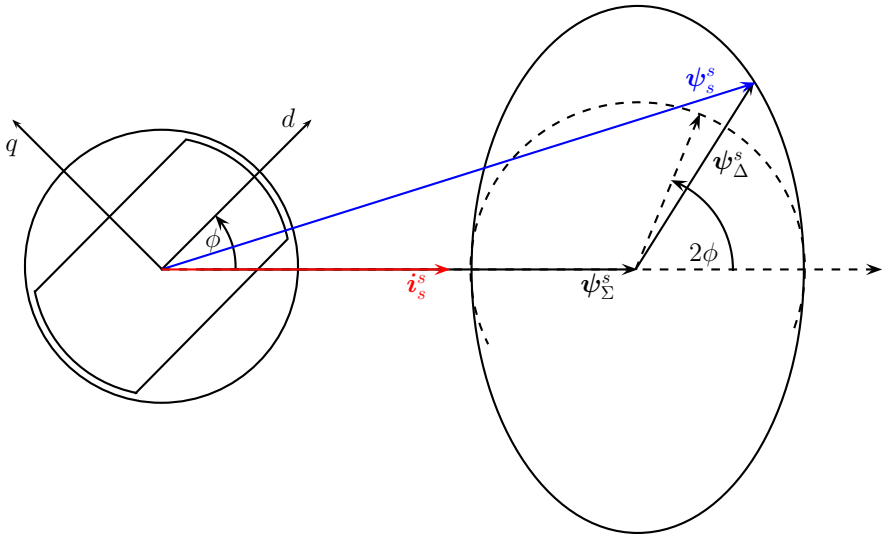

Figure 6.3: Nonlinear circulation of the flux linkage. [3].

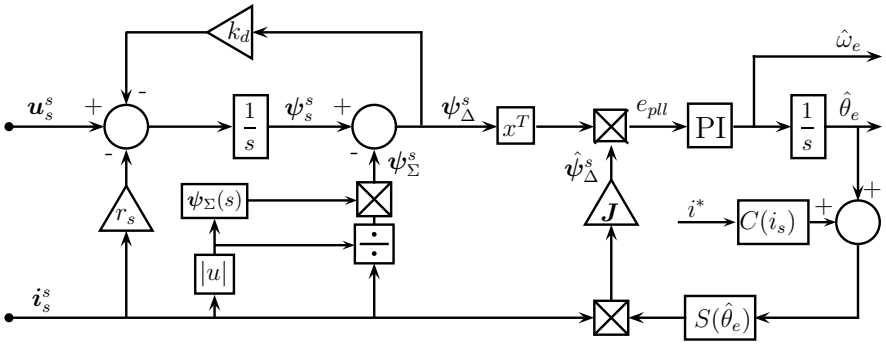

Figure 6.4: Non-linear funamental saliency estimation scheme.

6.3 Simulation

The FS-PSC method, as discussed in this chapter, is evaluated in simulation with the Simulink package and the measured flux maps of machine 1. The lookup table of ψ_Σ^s is generated from the measured flux linkages curves. The measured d- and q-axis flux linkage curves of machine 1, as a function of current, are shown in Fig. 6.5. Also shown in Fig. 6.5 is the isotropic flux linkage (ψ_Σ^s) and the fundamental saliency ($\boldsymbol{\psi}_\Delta^s$) derived from ψ_d and ψ_q.

It is shown in Fig. 6.5 that the magnitude of the fundamental saliency, $\boldsymbol{\psi}_\Delta^s$, does not decrease as the current in the machine increases, unlike the inductance saliency used with the HFI-PSC and AI-PSC methods. It can thus be concluded that the FS-PSC method does not have the torque limitations of the SB-PSC methods as it will not step out when loaded.

The simulation control parameters are as in Table 6.1. Simulation results of the FS-PSC method with machine 1 are shown in Fig. 6.6. A rated current step is applied as shown in Fig. 6.6a. It is shown in Fig. 6.6a that the reference current is reached almost instantaneously. The position estimation error in Fig. 6.6b shows large errors at startup and during the current step. This is due to the machine speed being

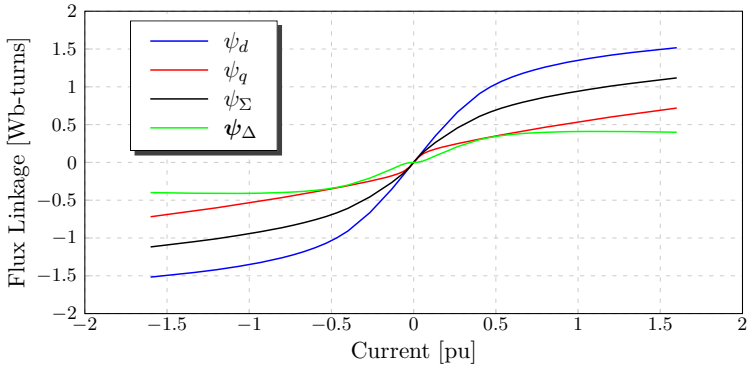

Figure 6.5: Measured flux linkage curves of machine 1.

Table 6.1: Simulation controller parameters

Current proportional gain	k_p	80	V/A
Current time constant	T_i	28	ms
PLL proportional gain	k_{pPLL}	5	rad/s
PLL time constant	T_{PLL}	2.86	ms

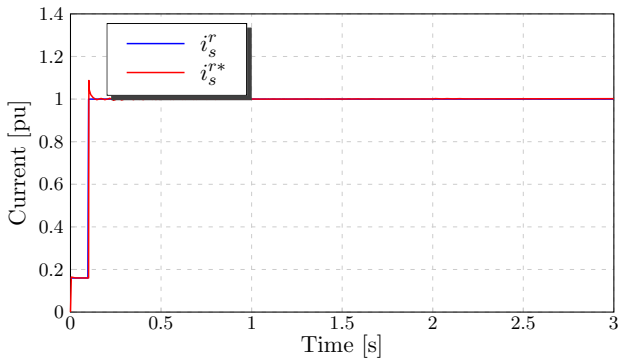

(a) Reference- and machine current.

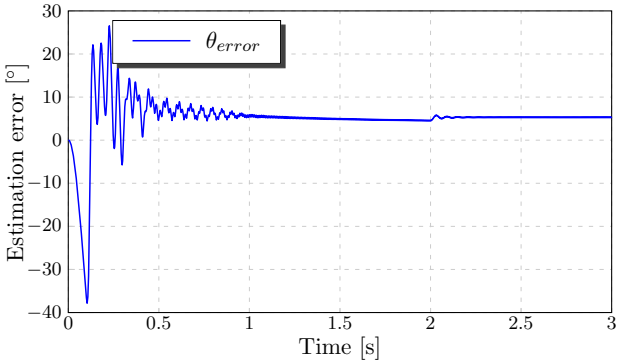

(b) Position estimation error.

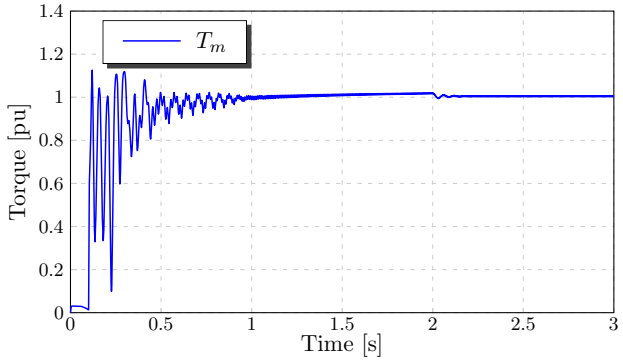

(c) Mechanical torque.

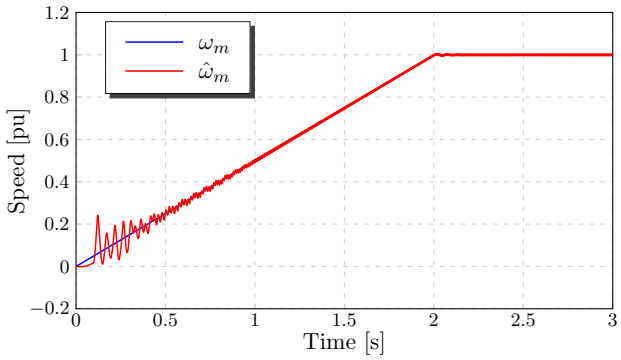

(d) Simulated speed and estimated speed.

Figure 6.6: FS-PSC: Rated current step simulation of machine 1.

very low as shown in Fig. 6.6d. The large position estimation errors in the low speed region affects the torque applied by the machine as shown in Fig. 6.6c. Finally, it is shown in Figs. 6.6b and 6.6d that the position estimation error decreases as the machine speed increases and the PLL stabilises. This response is to be expected of model-based PSC methods. It is thus shown in the simulation environment that the FS-PSC method is unstable in the low speed region, but exhibits good results in the medium to rated speed region.

6.4 Measured Results

The FS-PSC method is implemented and evaluated at the Institute for Electrical Drive Systems and Power Electronics at the Technical University of Munich. A similar test bench as shown in Fig. 3.8 is used. Machine 1 is also used to test and evaluate the proposed PSC method. The same lookup table as used in the simulation is used for laboratory tests on the test bench.

During the implementation of the FS-PSC method, it is found that the estimation scheme is stable at a speed of 0.27 $p.u$ and higher. The FS-PSC method is unstable at speeds below 0.27 $p.u$ due to parameter errors and drift effects. The FS-PSC method is only evaluated in the medium to high speed region.

6.4.1 Current response

The current control parameters as implemented on the RPS are given in Table 6.2. The measured maximum torque that the RSM can produce with the FS-PSC method as a function of speed is shown in

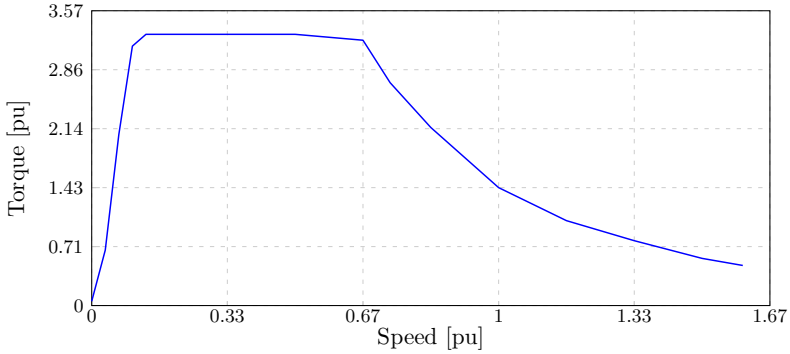

Figure 6.7: FS-PSC: Limits of stable operation.

Table 6.2: Rapid prototype system controller parameters for position sensorless current controlled machine 1.

Current proportional gain	k_p	200	V/A
Current time constant	T_i	27.3	ms
PLL proportional gain	k_{pPLL}	220	rad/s
PLL time constant	T_{PLL}	40.97	ms

Fig. 6.7. The position sensorless controlled RSM is not able to deliver startup torque with the FS-PSC method, as expected. The RSM can however deliver high torque in the medium to high speed region, as shown in Fig. 6.7. The only limitation to the torque that can be delivered by the position sensorless controlled RSM is the limited DC bus voltage and the current rating of the VSD. These limitations are also applicable when implementing FOC with a position sensor, thus the RSM is able to produce the same torque in the medium to high speed region with the FS-PSC method as with FOC with a position sensor.

6.4.2 Speed response

The speed control parameters as implemented on the RPS are given in Table 6.3. The results of a speed step applied by the RSM with the FS-PSC method are shown in Fig. 6.8. The RSM is loaded at 0.6 $p.u$ by the IM at a speed of 0.25 $p.u$. It is shown in Fig. 6.8a that a speed step is applied by the RSM from 0.25 $p.u$ to 1 $p.u$. The position estimation error never exceeds 5^o, as shown in Fig. 6.8b, which is satisfactory.

The results of a slight speed step applied by the position sensorless controlled RSM with the FS-PSC method while at full load are shown in Fig. 6.9 . The measured- and reference speeds are shown in Fig. 6.9a. It is shown in Fig. 6.9b that the current of the position sensorless controlled RSM is above rated during the speed step. Finally, it is shown in Fig. 6.9c that even though the position estimation

Table 6.3: Rapid prototype system controller parameters for position sensorless speed controlled machine 1.

Current proportional gain	k_p	200	V/A
Current time constant	T_i	27.3	ms
Speed proportional gain	k_{ps}	0.2	Nms/rad
Speed time constant	T_{is}	0.41	s
PLL proportional gain	k_{pPLL}	220	rad/s
PLL time constant	T_{PLL}	40.97	ms
Speed LPF	LPF_s	48.82	rad/s

error exceeds 15^o during transients, the PLL stays synchronised. It can thus be concluded that the RSM performs well when controlled with the FS-PSC method and a cascaded speed controller.

6.5 Summary

A relatively new model-based position sensorless control (PSC) method for RSMs is investigated in this chapter. The fundamental saliency PSC (FS-PSC) method utilises the fundamental saliency of the machine to estimate the electrical angle. The working of the FS-PSC method is validated with simulated and measured results. Simulations and measurements results show that the FS-PSC method, like back EMF PSC methods, is unstable at standstill and low speeds, but estimation performance improves with increasing speed.

Simulation and measured results show that the FS-PSC method delivers satisfactory performance and that the RSM can deliver speed steps at rated load when controlled with the FS-PSC method. Limits of stable operation test results show that the the FS-PSC method does not step out at high loads as with the saliency-based PSC methods. They also show that the achievable torque in current control is limited purely by the current rating of the VSD and the maximum DC bus voltage.

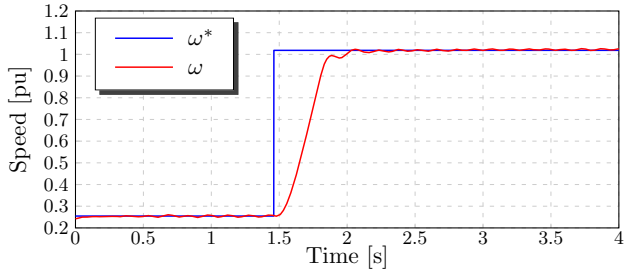

(a) Reference speed and measured speed.

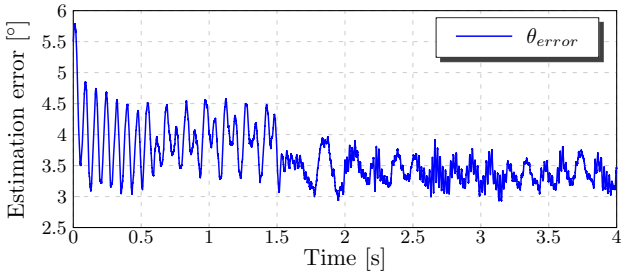

(b) Position estimation error.

Figure 6.8: FS-PSC: Measured speed step response of machine 1.

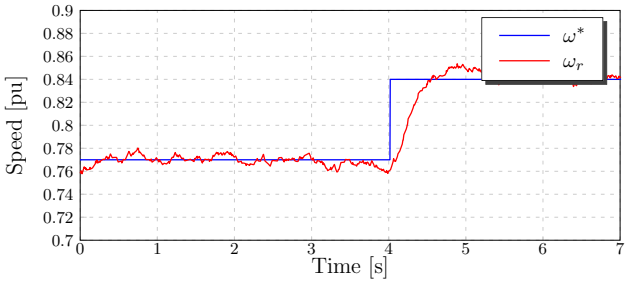

(a) Measured speed.

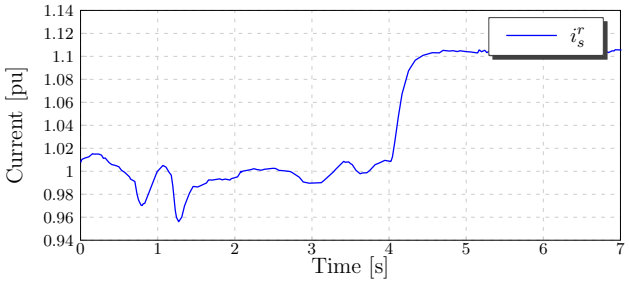

(b) Measured current.

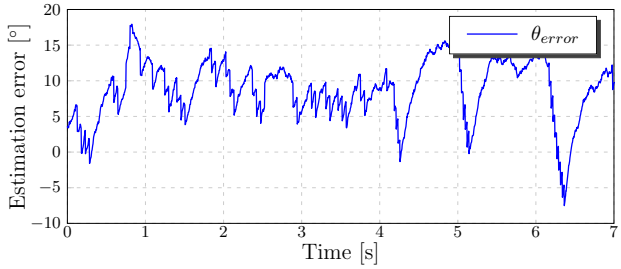

(c) Position estimation error.

Figure 6.9: FS-PSC: Measured speed step response of machine 1.

Chapter 7

Hybrid Position Sensorless Control

Several authors have investigated different variations of hybrid position sensorless control (PSC) methods to overcome the shortcoming of model-based- and back EMF methods to implement PSC of PM synchronous machines (PMSMs) throughout the entire rated speed range [64–75]. The conventional high frequency injection position sensorless control (HFI-PSC) method, with a band pass filter (BPF) in the demodulation scheme, is used in conjunction with a model-based method to control a PMSM in the entire rated speed region in [64,66,76,77]. This is achieved by using the HFI-PSC method at standstill and low speeds and the model-based method from minimum to high speeds.

Various methods of changeover between the low- and high speed PSC methods are presented and evaluated in literature. Changeover between the estimation methods in [64,66,76], are done with weighted speed gains. Both methods are always active with this implementation and one set of control parameters is used for both estimation methods. A voltage model method is combined with a conventional HFI-PSC method in [78] to control a PMSM in the entire rated speed region. In [78], the estimated electrical angle of both the low speed and high speed estimation schemes are summed and driven through a PLL, thus both methods stay active during the entire operation irrespective of the machine speed.

7.0.1 Hybrid PSC Methods for RSM drives

A current-frequency method is used with an active flux-based PSC method to control a small axial laminated RSM in [79]. The axial laminated RSM has the advantage of having a larger inductance saliency than conventional transverse laminated RSMs. The stator current frequency is ramped up while the d- and q-axis current references are kept constant in the proposed method of [79]. This method is i.e. an open loop control method that cannot predict the rotor position at standstill and low speeds, which can be problematic during direction change. Also startup torque capabilities are limited. The hybrid method described in [79], is extended in [80] to replace the current frequency method with the conventional HFI-PSC method at standstill. A fusion structure is implemented in [80] by taking the difference between the estimated electrical angles of the HFI-PSC method and the active flux method and feeding it through a PLL.

A RSM hybrid PSC method that utilises the indirect flux detection by on-line reactance measurement (INFORM) model at low speeds and standstill, and an EMF model at high speeds is proposed in [81]. Changeover between PSC methods is done at fixed speed points in [81]. A hybrid method combining high frequency injection with flux estimation is proposed for the RSM in [61]. This method is stabilised by a speed observer. Changeover between estimation schemes is done gradually with speed dependant gains. One set of controller gains is used due to the nature of the changeover between the two schemes,

Two types of hybrid PSC methods are derived and evaluated in this chapter. A different approach is taken with regard to the changeover between position estimation methods. Both hybrid PSC methods use the fundamental saliency position sensorless control (FS-PSC) method at minimum to high speeds.

The first hybrid method uses the simplified HFI-PSC method at standstill and low speeds and the second the AI-PSC method. The HFI assisted hybrid PSC method is published by this author in [82]. After publication of [82], a similar method is introduced in [83], where the simplified HFI-PSC method described in Chapter 3 is used with the active flux method for PSC of an axial laminated RSM in the entire rated speed range.

7.1 Hybrid Estimation Method

The two types of PSC methods are evaluated in the previous chapters; both have their advantages and disadvantages. The saliency-based PSC (SB-PSC) methods (HFI-PSC and AI-PSC) have the advantage of accurate position estimation at standstill and very low speeds. The drawback of these methods is the additional injected voltages which take up a large portion of the available DC bus voltage, limiting the voltage that can be applied by the inverter to control the RSM at high speeds. Furthermore, the injected voltage can cause additional torque ripple, additional noise and high frequency losses. SB-PSC methods also have limited torque capabilities due to the decrease in inductance saliency magnitude when the RSM is loaded.

The FS-PSC method makes use of the full DC link bus voltage. The RSM can thus produce the same torque at medium to high speeds when controlled with the FS-PSC method as with FOC and a position sensor. This method is also more dynamic than the SB-PSC methods at medium to high speeds. The FS-PSC method tracks the fundamental saliency of the RSM for position estimation. Unlike the inductance saliency, which is used with SB-PSC methods, the fundamental saliency does not decrease in size at high loads, making the FS-PSC method effective at high load conditions. The drawback of the FS-PSC method however, is it instability at very low speeds and standstill due to parameter errors and drift effects.

Combining one of the SB-PSC methods with the FS-PSC method will thus eliminate some of the individual drawbacks like position estimation at standstill and limited torque capabilities.

7.1.1 Changeover between position estimation methods

Changeover between the position estimation methods needs to be seamless and effective. The method of changeover used in this project is based on a hysteresis effect. During acceleration from standstill, a changeover occurs from the SB-PSC method to the FS-PSC method at a speed threshold of ω_{h2}. During deceleration, changeover from the FS-PSC method to the SB-PSC method occurs at a speed threshold of ω_{h1}, where $\omega_{h1} < \omega_{h2}$.

Using two different speed points for changeover, instead of one single speed threshold, has the drawback that ω_{h2} is slightly higher than minimum operation speed of the FS-PSC method. It does however, have the advantage that a speed ripple around the changeover thresholds will not result in an unnecessary back and forth switching between position estimation methods.

Due to the different nature of the two types of position estimation methods, it is found that the control and PLL parameters for each individual method are different. With the proposed hysteresis changeover scheme it is possible to drive each position estimation method with its own optimised current controller and PLL gains, ensuring optimum performance from each individual method. The state space diagram in Fig. 7.1 shows the procedure that is implemented to change between the two position estimation methods. The estimated electrical angle acquired from the SB-PSC method is represented by θ_S and the angle from the FS-PSC method by θ_{FS}.

To ensure seamless changeover between the two position estimation methods, the PLLs are synchronised by feeding the position estimation error from the active PLL to the inactive PLL right before changeover. During changeover from the SB-PSC method to the FS-PSC method, both estimation methods will have different position estimation errors, but the SB-PSC method will have a more accurate

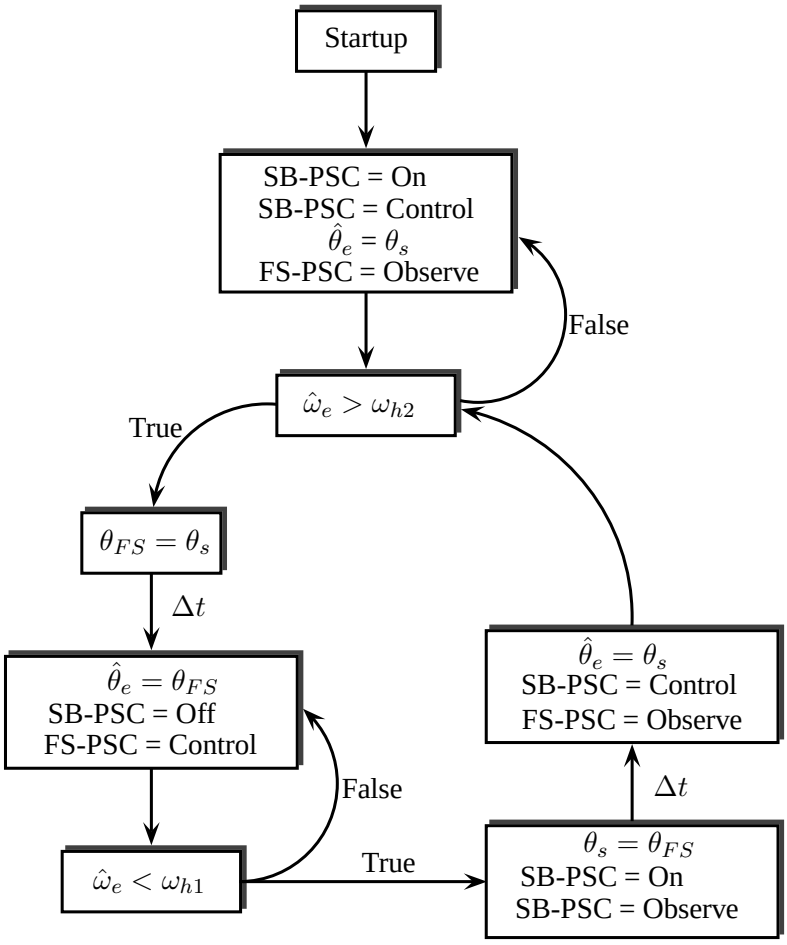

Figure 7.1: State space diagram of the Hybrid PSC method.

position estimation. By forcing the FS-PSC PLL to track the position estimation error of the SB-PSC method, it immediately synchronises the FS-PSC PLL with a more accurate position estimation. This synchronising of the two PLLs is represented in Fig. 7.1 by $\theta_{FS} = \theta_S$.

When changing from the FS-PSC method to the SB-PSC method, the PLL of the SB-PSC method is directly synchronised with the active FS-PSC method. This synchronising of the PLLs is represented in Fig. 7.1 by $\theta_S = \theta_{FS}$. Using PLL synchronisation allows the SB-PSC method to be "switched off" when the FS-PSC method is active. This frees up the entire DC bus as no more voltage injection required. The low pass filters used in the feedback current with the SB-PSC method can also be omitted from the control structure. In this implementation of the hybrid PSC method, the FS-PSC method is always active, although not always in control, but the SB-PSC method is "switched off" when not in control.

7.2 Measured Results

Testing and evaluation of the HFI assisted hybrid PSC method were performed at the Institute for Electrical Drive Systems and Power Electronics at the Technical University of Munich. The AI assisted hybrid PSC method was tested and evaluated at the Electrical Machines Laboratory at the University of Stellenbosch. Machine 1 is used for testing and evaluation of both methods.

7.2.1 Current response

The measured maximum torque that the RSM can deliver while controlled with the two hybrid PSC methods as a function of speed are displayed in Fig. 7.2. The results of the HFI assisted hybrid PSC method are shown in Fig. 7.2a and that of the AI assisted hybrid PSC method in Fig. 7.2b. The hysteresis effect is clearly visible in both figures due to the two changeover threshold speed values ω_{h1} and ω_{h2}. The upper part of the hysteresis band is the FS-PSC method and the lower part is the SB-PSC method.

Saturation of the flux linkage at low speed under very high load causes the SB-PSC methods to lose track due to the disappearing inductance saliency. Although limited by the SB-PSC methods, the startup torque that the RSM can produce when controlled with the hybrid PSC methods is between two and three times the rated torque, thus overcoming the problems perceived by [65]. The results in Fig. 7.2 show that despite very high loads, the proposed hybrid PSC method is able to track the rotor position in the entire rated speed region.

7.2.2 Speed response

The performance of the speed controlled RSM with the proposed hybrid PSC methods is evaluated. The results in Fig. 7.3 show a large speed step applied by the RSM while controlled with the AI assisted hybrid PSC method. The measured speed response in Fig. 7.3a shows no noticeable evidence of changeover between the position estimation schemes. It is also shown in Fig. 7.3b, that the changeover between the two position estimation schemes has little to no effect on the position estimation error. It is shown in Fig. 7.3b however, that there is a transient in the position estimation error for a brief moment during deceleration. The AI-PSC method requires a few cycles to start accurately estimating the mean admittance of the RSM thus resulting in a brief transient of the position estimation error.

The results of a speed reversal test at $|1.27|$ $p.u$ with the HFI assisted hybrid PSC method are shown in Fig. 7.4. No effect of the changeover between the two position estimation schemes are visible. During this specific experiment, changeover between the two position estimation schemes occurs four times. These results thus show that it is even possible to apply speed steps at above rated speed with the proposed hybrid PSC method.

7.2.3 Hysteresis Changeover Analysis

The purpose of the hysteresis changeover method is, amongst others, to avoid unnecessary switching between the two position estimation methods during a speed ripple. To investigate the feasibility of this argument, the RSM speed is increased while controlled with the hybrid PSC method to activate the FS-PSC method and then lowered to the middle of the hysteresis region ensuring that the FS-PSC method is still active. A series of tests are performed in this region.

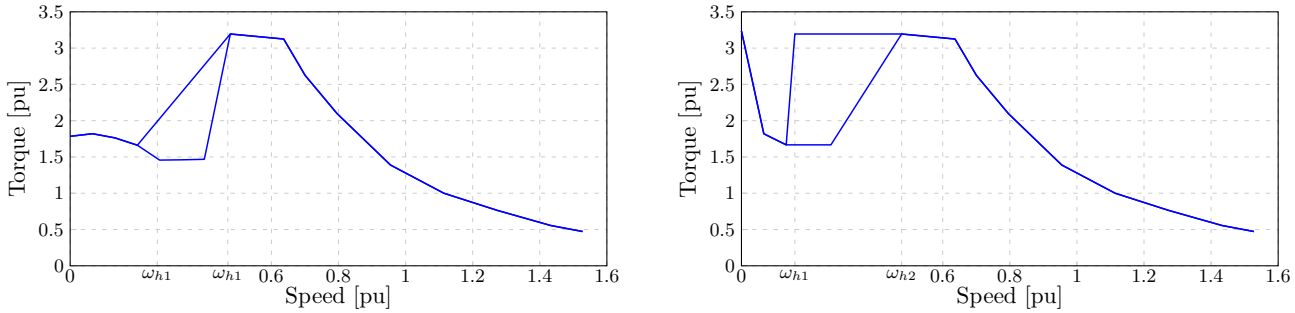

(a) HFI assisted hybrid PSC method. (b) AI assisted hybrid PSC method.

Figure 7.2: Limits of stable operation of machine 1.

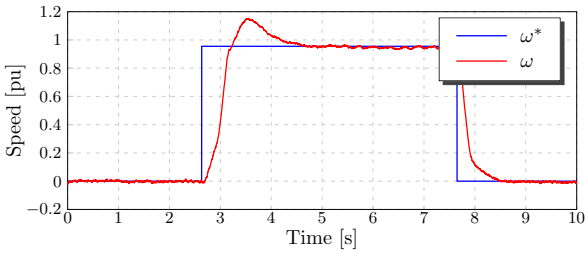

(a) Reference and measured speed.

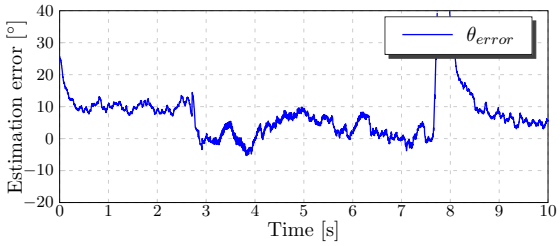

(b) Position estimation error.

Figure 7.3: AI assisted hybrid PSC: Measured speed step response of machine 1.

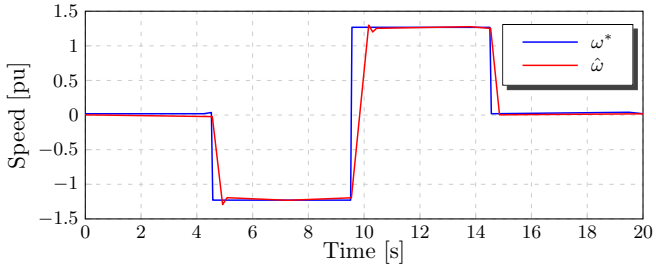

Figure 7.4: HFI assisted hybrid PSC: Measured speed reversal of machine 1.

The measured results of a torque step, applied by the IM, in this region are shown in Fig. 7.5. The torque step is shown in Fig. 7.5a. An analog signal is written out through the D/A converter which indicates which PSC method is in control throughout this test. This measured signal is shown in Fig. 7.5b. One changeover occurs due to speed undershoot as a result of the applied load as shown in Fig. 7.5b. Another changeover occurs at the removal of the load due to the speed overshoot as shown in Fig. 7.5b. It is clear that there is no unnecessary back and forth switching between the two estimation methods and changeover only occurs once due to over- or undershoot.

The effect of variable torque switching on the hybrid PSC method is investigated in Fig. 7.6. While operating in the middle of the hysteresis region, the load from the IM is applied and removed several times with impulse-like characteristics. Again, it is shown in Fig. 7.6b that there is no unnecessary back and forth switching between the two position estimation methods except when the load causes speed under- or overshoot. These results suggest that the implementation of the hysteresis changeover is indeed successful. Sacrificing changeover speed threshold for stability is a valid trade-off.

7.3 Summary

Two hybrid position sensorless control (PSC) methods that make use of a saliency-based position sensorless control (SB-PSC) method at standstill and a fundamental saliency position sensorless control (FS-PSC) method at minimum to high speeds are introduced. The two SB-PSC methods used are the simplified high frequency injection- (HFI-PSC) and the arbitrary injection position sensorless control (AI-PSC) methods.

A hysteresis method is used for changeover between the two position estimation methods, which is in contrast to popular methods introduced in literature. The hysteresis changeover method sacrifices a portion of the speed region where the FS-PSC method is active for stability. One advantage is that the RSM can be controlled with different controller- and PLL gains for each PSC method ensuring optimum performance from each method. Another advantage is that a torque ripple in the medium speed region will not result in an unnecessary back and forth switching between estimation methods.
Furthermore, seamless changeover between estimation methods is ensured by synchronising the inactive

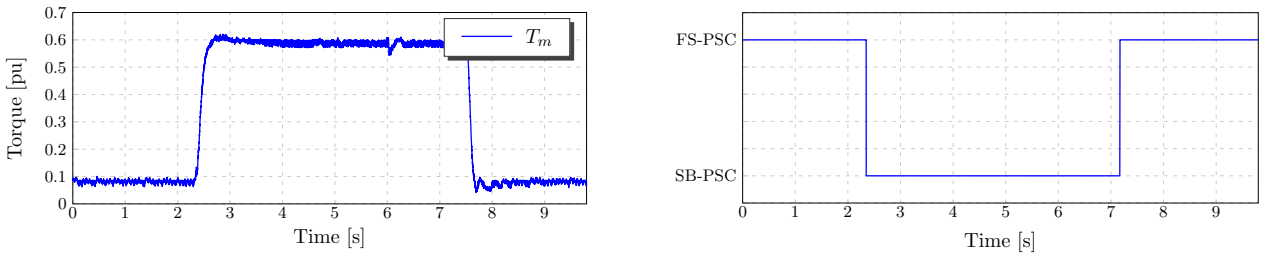

(a) Applied load. (b) Active position estimation method.

Figure 7.5: Hysteresis changeover stability investigation 1.

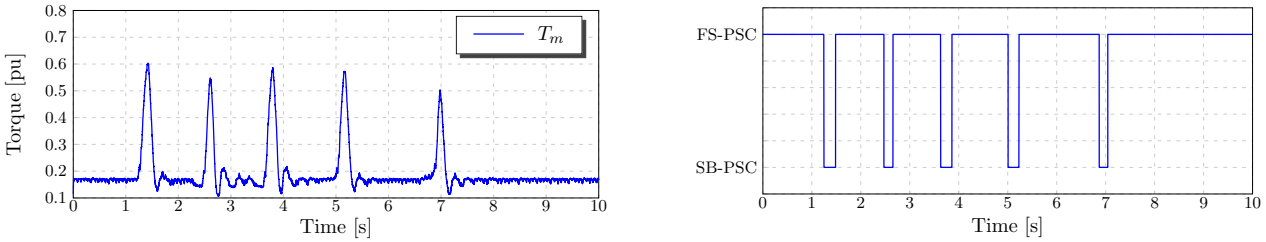

(a) Applied load. (b) Position estimation error.

Figure 7.6: Hysteresis changeover stability investigation 2.

PLL with the active PLL one cycle before changeover. This ensures that the inactive PLL directly synchronises with the estimated electrical angle. This also allows the injection voltages of the SB-PSC methods to be switched off when the FS-PSC method is in control. The entire DC bus voltage can be used for space vector pulse width modulation when the injection voltage is switched off. It is also advantageous due to a reduction in system noise, torque ripple and audible noise.

Measured results show that both hybrid methods are able to produce rated torque from startup up to rated speed. This overcomes the problems perceived by [65]. Speed response tests are successful and results show that there are no noticeable effects in machine response when changeover occurs. Speed reversal results show that accurate PSC is possible during direction change even when speed steps of above rated speed are applied, improving on previous work done by [79].

Chapter 8

Design and Evaluation of a RSM for Saliency-Based Position Sensorless Control at Zero Reference Current

Various authors have investigated the correlation between the design of synchronous machines and the performance saliency-based position sensorless control (SB-PSC) methods [49, 50, 52, 84–105].

Genetic algorithms are used in [94] with a finite element (FE) software package to optimise surface mounted permanent magnet synchronous (SMPMS) machines. Firstly, a SMPMS machine is optimised in [94] for maximum torque with minimum torque ripple. A second SMPMS machine is optimised in [94] for maximum saliency and finally a third machine is optimised for maximum saliency and torque with a minimum torque ripple. The split ratio is defined in [94] as the ratio of the inner stator radius to the outer stator radius. Results in [94] show that the split ratio is the most sensitive parameter in terms of saliency. The split ratio should be increased to increase the saliency, but this results in an increased inductance ripple [94]. Furthermore, it is found that to increase the saliency, the stator tooth width should be decreased and the slot opening width should be increased. Finally, it is shown that the slot geometry is also an effective saliency optimisation parameter.

The effects of flux linkage saturation and mutual inductances on the SB-PSC performance of interior permanent magnet machines (IPM) are investigated in [89] and [95]. It is shown in [89] that the saliency of the IPM improves when the stator saturates instead of the rotor. It is shown in [95] however, that a critical point exists where the saliency shift of the IPM grows exponentially beyond the bandwidth of the PLL. Results in [95], show that this critical point can be moved higher up the maximum torque per ampere curve by rather saturating the rotor instead of the stator. A trade-off thus exists between saliency shift and inductance saliency.

Machine 1 is used in this chapter to identify and investigate certain design aspects that negatively affect the SB-PSC capabilities of RSM drives. Rotor design modification are proposed and two improved RSM designs are constructed to verify simulation results. The efficiency of the modified RSMs are evaluated and compared to that of machine 1. Bandwidth, thermal and frequency harmonic evaluations are also performed to further evaluate the new modified RSMs.

8.1 Degradation of saliency-based position sensorless control performance

According to [49, 52, 84–86], there are two effects that can distort the PSC capability of PM machines, namely, flux linkage saturation and cross-coupling between the magnetic d- and q-axis. The magnitude

of the inductance saliency, ΔL, decreases as the flux linkages saturate within the machine until PSC is not possible any more. This saturation effect occurs when the machine is loaded.

It is found that cross-coupling between the d- and q-axes is caused by the asymmetrical saturation of flux in the rotor [84, 85]. To investigate the distortion caused by the cross coupling effect in RSMs, three rotor structures, as shown in Fig. 8.1, are simulated in the JMAG FE package. The rotor structures of machines 1-3 are referred to by [49] as the lateral- (Fig 8.1a), central rib- (Fig. 8.1b), and ideal, (Fig. 8.1c), rotors.

The flux density maps of Figs. 8.1a and 8.1c at rated conditions are similar and symmetrical, as also identified by [49, 84]. However, high distortion is present in Fig. 8.1b where the flux lines concentrate in the central rib. The flux lines are forced to concentrated in the middle of the rotor due to the central rib [84]. The interaction of the q-axis flux lines with the d-axis are high and thus increases the cross coupling between the d- and q-axes. If the concentration of flux on the central rib is high enough it can cause the PSC method to misalign with the d-axis of the rotor. This phenomenon is referred to as saliency shift in [86] and [87]. The saliency shift effect is thus not unique to PM machines but is also present in certain RSM designs at specific operating conditions.

It is suggested in [85] that a high number of flux barriers per pole constraint the d- and q-axis flux linkages to more definite paths. One solution to the saliency shift problem might thus be to increase the number of flux barriers and in doing so reduce the cross-coupling between the two axes and thus reduce the saliency shift of the machine.

8.2 Evaluation of the lateral rib rotor RSM (Machine 1)

Machine 1 is a RSM with an unskewed lateral rib rotor configuration, as in Fig. 8.1a. Machine 1 is used as a benchmark to further evaluate the SB-PSC capabilities of RSMs. It is shown in Chapter 2 that the partial derivatives of the d- and q-axis flux linkages are used to calculate the tangential inductances as in (2.10). Both the d- and q-axis flux linkages are functions of both i_d and i_q [49]. However, if the tangential inductances are calculated with (8.1) it is possible to investigate the inductance saliency of the RSM with regard to the geometry of the design, minimising the cross coupling effects. The uncoupled d- and q-axis flux linkages are thus used in (8.1) to calculate the tangential inductance. This will be referred to in the rest of this chapter as the uncoupled machine evaluation.

$$L_d = \frac{\Delta\psi_d}{\Delta i_d}; \psi_d(i_d, 0) \qquad L_q = \frac{\Delta\psi_q}{\Delta i_q}; \psi_q(0, i_q) \tag{8.1}$$

The measured and simulated uncoupled results of machine 1 are shown in Fig. 8.2. The uncoupled flux linkages, as a function of current, are shown in Fig. 8.2a and tangential inductances Fig. 8.2b. It is clear

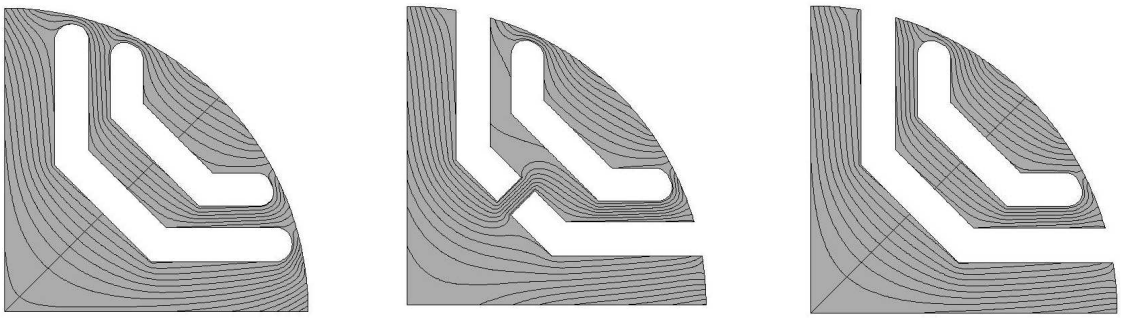

(a) Machine 1. (b) Machine 2. (c) Machine 3.

Figure 8.1: Cross coupling effects of machines 1-3.

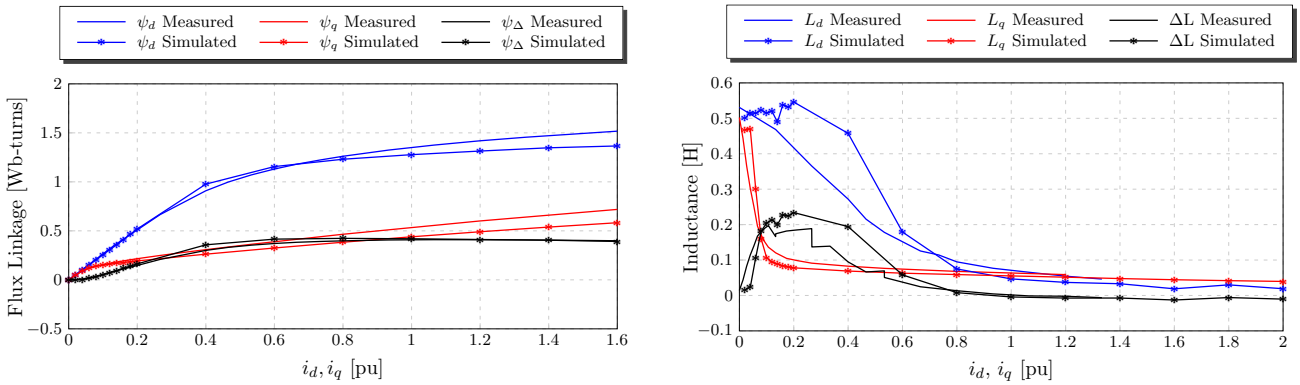

(a) Flux linkage.

(b) Inductance.

Figure 8.2: Measured and simulated uncoupled results of machine 1.

that there are some irregularities between the measured and the simulated results. As stated in Chapter 3 these irregularities might be due to an uncertainty regarding the rotor- and stator steel and the neglection of the end-winding inductance. The important aspect regarding this comparison is that the shape of the flux linkages of the measured and simulated results are satisfactorily similar.

The measured and simulated fundamental saliency, ψ_Δ, of machine 1 are shown in Fig. 8.2a. This vector is used with the FS-PSC method to control the RSM at medium to high speeds. It is shown in Fig. 8.2a that the magnitude of fundamental saliency does not decrease as the load of the machine increases. This then ensures good torque capabilities from the FS-PSC method. Machine design modifications with regard to the fundamental saliency will thus not be considered in this chapter. Two important results are observed in the measured and simulated inductance saliency, ΔL, shown Fig. 8.2b.

1. The magnitude of ΔL decrease as the load increases until PSC is not possible. This is due to the saturation of the flux within the machine as identified by [49, 52, 84, 85].

2. $L_d \approx L_q$ at small current magnitudes. This results in ΔL being too small for SB-PSC.

The effect of the two identified problem areas play a large role in the performance of the saliency-based position sensorless controlled RSM. The maximum torque that the RSM can produce when controlled with a SB-PSC method is limited due to the saturation of the flux linkages at large currents.

The limited inductance saliency at zero and small current magnitudes also prevents the SB-PSC methods from tracking the electrical angle of the RSM. It is possible however, to avoid this specific problem area by choosing the current vector in such a way that $i_q \neq 0$, to saturate the q-axis magnetic circuit. It is found that the minimum q-axis current necessary for machine 1 is 0.2 pu. This method of flux linkage saturation is used with the two SB-PSC methods evaluated in chapters 4 and 5. Although effective, this method is not energy efficient due to the current vector not always following the maximum torque per ampere locus. This method of course also implies that there is always current in the machine even at standstill under no load.

This method of flux linkage saturation will not be suitable for certain applications which require high efficiency. One such example application is electric vehicles (EV's) where battery life is crucial. The urban dynamometer driving schedule (UDDS) is a dynamometer test on fuel economy in urban driving conditions and is used to better understand performance expectations of an EV on urban roads. The test simulates an urban route of 12.07 km in Fig. 8.3 [4]. Various instances are shown in Fig. 8.3 where the vehicle is at constant speed or accelerating, as expected. Surprisingly however, the UDDS also reveals that there are various instances where the vehicle stands still or coasts where no torque is required. It is important that all driving conditions, including standstill and coasting, are investigated to improve the

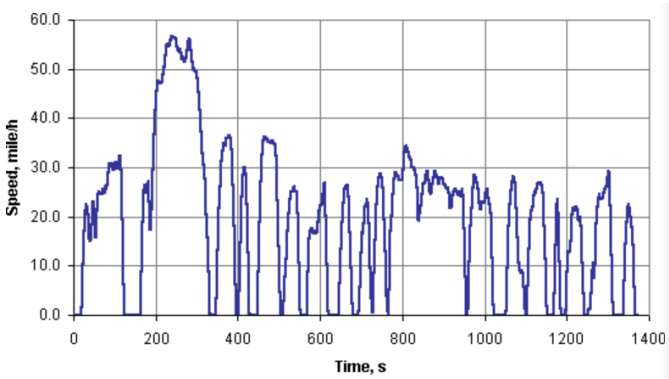

Figure 8.3: Urban dynamometer driving schedule (UDDS) for 12.07 km [4].

performance of EVs. It is thus clear that the saliency-based position sensorless controlled lateral rib RSM will not operate at maximum efficiency if implemented in an EV.

8.3 Evaluation of the central rib rotor RSM (Machine 2)

The problems of flux linkage saturation and saliency shift, with regard to SB-PSC, have already been addressed for PM machines with proposed machine design solutions in [49, 52, 85–89, 95, 106] and [107] amongst others. The problem of limited inductance saliency of the RSM at very small current vectors are also identified by [108] but no solution to this problem exists as yet.

Although, as identified in the previous section, the central rib rotor RSM can potentially suffer from saliency shift, this rotor structure is investigated as an alternative to the lateral rib rotor for high inductance saliency at zero reference current. Machine 2 (central rib RSM) has an unskewed central rib rotor RSM configuration and is used in this investigation. The uncoupled FE simulation results of machines 1 and 2 are compared in Fig. 8.4. Machines 1 and 2 are indicated in the figure label by M1 and M2. It is shown in Fig. 8.4b that machine 2 also suffers from a lack of inductance saliency at small current vectors. The central rib rotor RSM is thus not a viable alternative to the lateral rib rotor RSM.

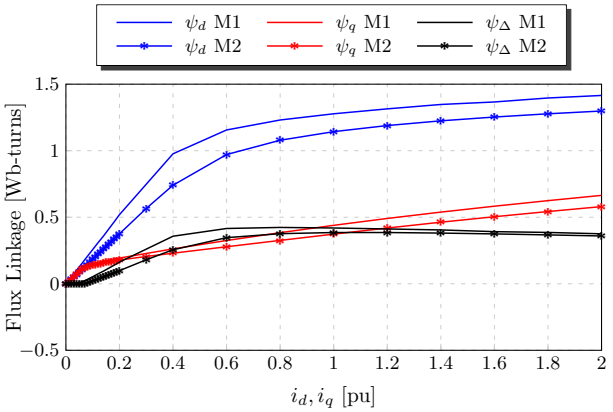

(a) Flux linkage.

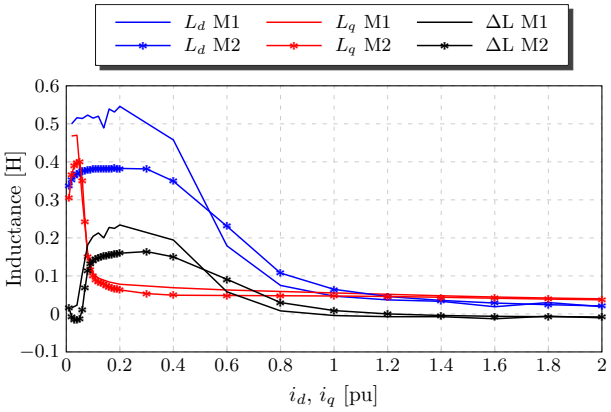

(b) Inductance.

Figure 8.4: Simulated uncoupled results comparison of machines 1 and 2.

8.4 Evaluation of the ideal rotor RSM (Machine 3)

Machine 3 is used to evaluate the inductance saliency of the ideal rotor RSM. This machine has an unskewed rotor. The FE simulation results of the uncoupled flux linkages and inductances of machine 3 are compared to the simulation results of machine 1 in Fig. 8.5. Again machines 1 and 3 are represented in the figure label by M1 and M3. It is shown in Fig. 8.5a that $\psi_d(i_d, 0)$ and $\psi_q(0, i_q)$ have different gradients at already very small current magnitudes, resulting in a high inductance saliency at very low currents. Not only does this configuration have a large inductance saliency magnitude at zero current, it also has a more constant saliency magnitude up to 0.4 *p.u* and slightly better than machine 1 up to 1.2 *p.u*. These results suggest that the geometry of the ideal rotor configuration has, as expected, a higher inductance saliency at very small currents than that of the other two configurations.

8.5 Skewing of the RSM rotor

It is not unusual to skew the RSM rotor one stator slot pitch to reduce its torque ripple. The effect of rotor skewing of a PM machine on its SB-PSC capability is investigated in [88]. The rotor is skewed a quarter of a slot pitch in [88], and the findings are that skewing has little or no effect on the PSC capability of the machine. It is stated in [88], that the results are inconclusive and do not confirm that a full slot pitch skew has no effect on the inductance saliency of the machine.

Machines 1 and 3 are simulated in JMAG with a full slot pitch skew to investigate the effect on the inductance saliency of the RSM. Both machines 1 and 3 are simulated in five skewed sub-machines to simulate a full slot pitch skewed rotor. The FE simulated inductance saliency results are shown in Fig. 8.6. These results show that there is very little deviation of the inductance saliency when a RSM rotor is skewed one stator slot pitch, and that it possesses all the necessary characteristics for successful SB-PSC.

8.6 Ideal Rotor RSM Configuration

FE simulation results, as shown in the previous sections, show that the ideal rotor RSM (machine 3) will perform well with a SB-PSC method at zero reference current. It is thus decided to build and evaluate machine 3, which has an unskewed ideal RSM rotor. Furthermore, it is also shown in the previous section that skewing of the RSM rotor has little or no effect on the SB-PSC capability of the RSM. To confirm this machine 4, which has a skewed ideal RSM rotor, is also built and evaluated.

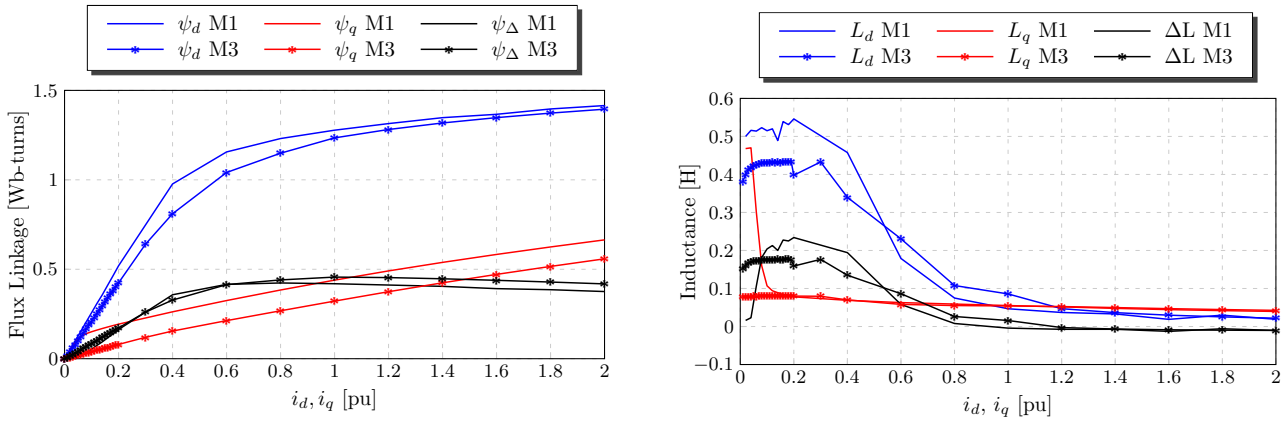

(a) Flux linkage.

(b) Inductance.

Figure 8.5: Simulated uncoupled results comparison of machines 1 and 3.

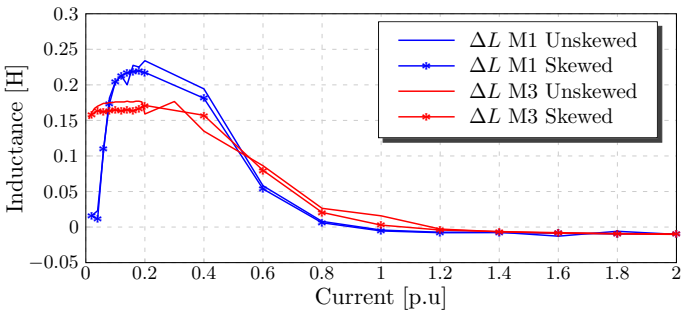

Figure 8.6: Simulation results of a comparison between skewed and unskewed RSM rotors.

8.6.1 Construction of machines 3 and 4

One obvious construction problem is that the removal of the lateral ribs of the flux barrier also removes the structural support iron. This implies that the piece of q-axis steel "floats" without any structural support. To overcome this problem, a novel solution is implemented. Two rotors are constructed, both with the lateral rib rotor configuration of Fig. 8.1a. One rotor is skewed and one unskewed. Slots that match the flux barriers of the rotor laminations are cut into one of the end-caps of the rotor. This makes it possible to fill the axial length of the rotor with epoxy-resin to form an epoxy-cast.

Epoxy is very strong, but is not recognised as an adhesive substance, thus it will not be able to hold the floating piece of iron in place. To take advantage of the strength of the epoxy-cast, small cut outs and iron snags are laser cut into the laminations as shown on the CAD design of the rotor laminations in Fig. 8.7a.

The cut outs shown in Fig. 8.7a help the epoxy to grip the floating piece of iron and prevent it from moving away. After allowing the epoxy to harden, a lathe is used to cut out the lateral ribs. The rotor of machine 3 without its lateral ribs is shown in Fig. 8.7b. The end-cap which is used to fill the rotor of machine 3 with epoxy is shown in Fig. 8.8a. The floating q-axis is also visible in Fig. 8.8a. The top view of the rotor of machine 4 is shown in Fig. 8.8b. It is clear that the epoxy line is not straight due to the skewed rotor.

8.6.2 Measured evaluation of machine 3

The flux mapping method described in Chapter 3 is used to measure and characterise machine 3. The flux mapping results of machine 3 are shown in Fig. 8.9. The measured d- and q-axis flux linkages as a function of i_d and i_q are shown in Figs. 8.9a and 8.9b. The calculated torque is shown in Fig. 8.9c.

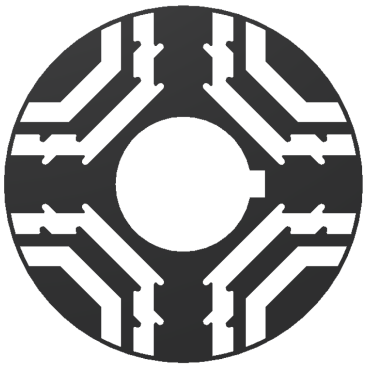

(a) CAD sketch of the rotor laminations.

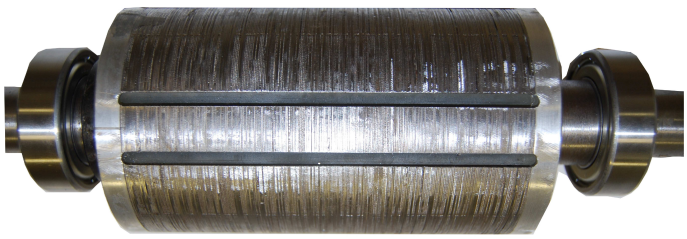

(b) Epoxy filled rotor of machine 3 with the ribs removed.

Figure 8.7: Construction of the ideal RSM rotor.

The flux linkage maps in Figs. 8.9a and 8.9b can be used for Simulink simulations and to create lookup tables which are necessary for the FS-PSC method. The flux linkage maps can also be used to compare measured uncoupled results to the FE results.

The uncoupled d- and q-axis flux linkages of machine 3 are acquired from the flux mapping results to compare to the FE simulated results as in Fig. 8.10. It shown in Fig. 8.10, that the measured results correlate well with the FE simulated results. More importantly, it is shown in Fig. 8.10b that the measured inductance saliency at small and zero current is not zero as the design requirement.

The measured uncoupled results of machine 1 are compared to that of machine 3 in Fig. 8.11. It is shown in Fig. 8.11a that the gradients of ψ_d and ψ_q of machine 3 are different at small current magnitudes unlike that of machine 1. This results in machine 3 having a higher inductance saliency than machine 1 at small current magnitudes as shown in Fig. 8.11b. It is also important to note that the fundamental saliency, ψ_Δ, curve of machine 3 is almost identical to that of machine 1 as shown in Fig. 8.11a. The modification made to the rotor should thus not affect the performance of the FS-PSC method.

8.6.3 SB-PSC of machine 3

A simple test is derived to investigate if the SB-PSC performance of machine 3 is indeed superior to that of machine 1 at small current magnitudes. The test bench described in Chapter 3 is used in this test. The alternating HFI-PSC method is used to control the current of machine 3, with the reference current set to 0 A, while the IM is used to drive machine 3 at a constant speed. SB-PSC is not possible with machine 1 under these conditions due to ΔL being too small when $i_s^{r*} = 0$, resulting in an unstable PLL.

The results of the HFI-PSC test on machine 3 are shown in Fig. 8.12. It is shown in Fig. 8.12a that

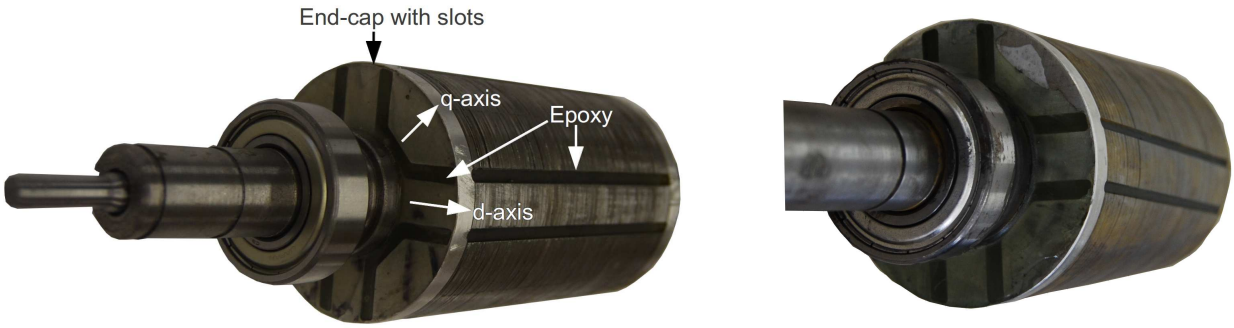

(a) Machine 3. (b) Machine 4.

Figure 8.8: Top view of machines 3 and 4.

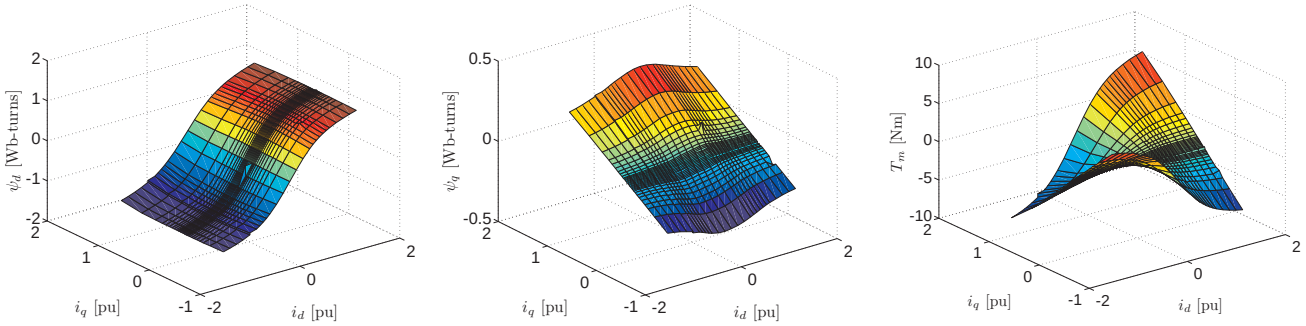

(a) D-axis flux linkage. (b) Q-axis flux linkage. (c) Calculated torque.

Figure 8.9: Measured flux mapping results of machine 3.

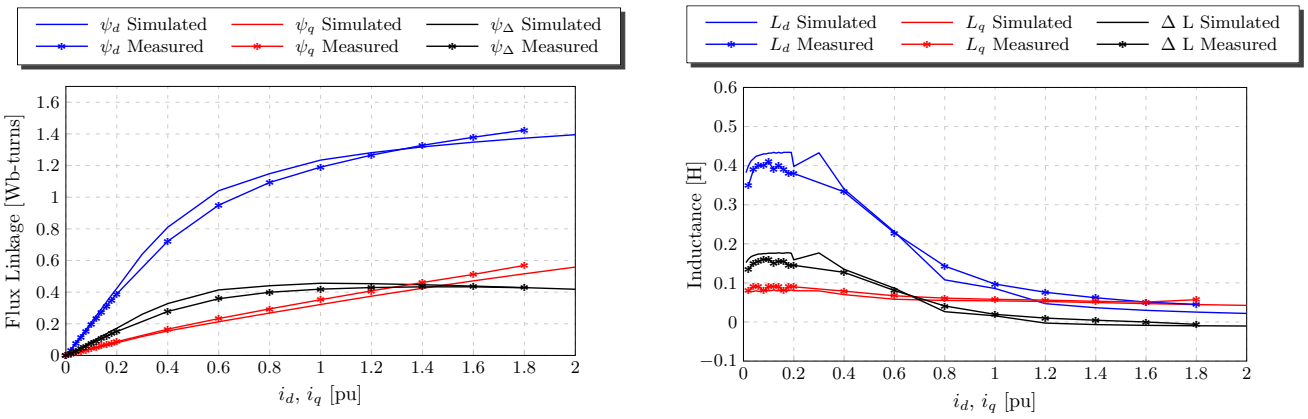

(a) Flux linkage.

(b) Inductance.

Figure 8.10: Uncoupled simulated vs. measured results of machine 3.

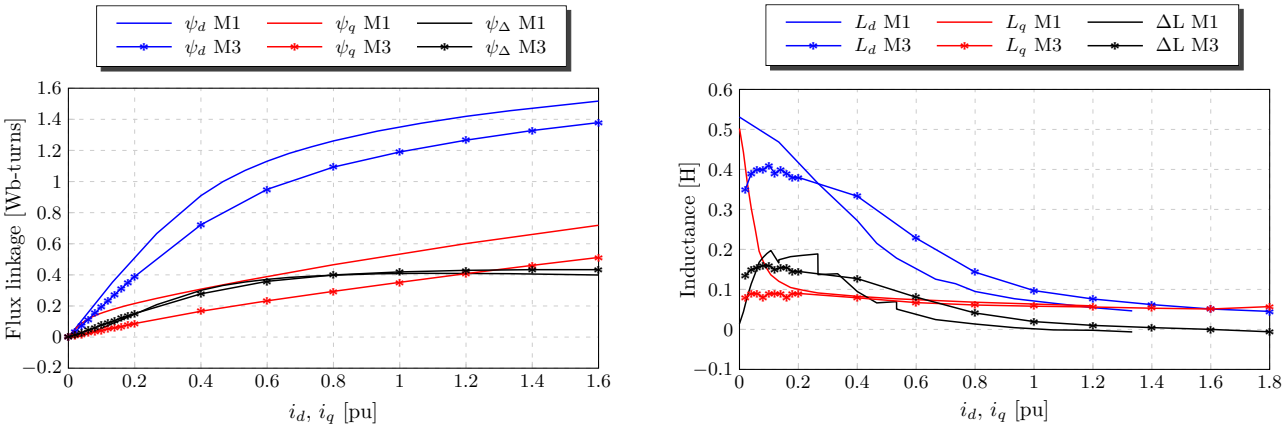

(a) Flux linkage.

(b) Inductance.

Figure 8.11: Comparison of measured uncoupled results of machines 1 and 3.

the electrical angle of the RSM is tracked accurately. The position estimation error in Fig. 8.12b shows a small position estimation error of $\pm 4^o$. A very small q-axis current of 0.04 $p.u$ is present in the machine, as shown in Fig. 8.12c, as a result of the HF voltage excitation. It is thus shown that no additional q-axis current is required to saturate the q-axis flux linkage for stable SB-PSC.

8.6.4 Measured evaluation of machine 4

Measured flux maps are not made of machine 4. The uncoupled d-and q-axis flux linkages are measured however, to compare to the FE simulation results. The uncoupled simulated and measured results of machine 4 are shown in Fig. 8.13. Again the measured results correlate well with the FE simulation results. The results in Fig. 8.13b show that this configuration has a large enough inductance saliency to perform SB-PSC at zero reference current.

The measured inductance saliency of machines 1, 3 and 4 are compared on one graph in Fig. 8.14. This graph clearly shows that machines 3 and 4 have larger inductance saliencies than machine 1 at small and zero current magnitudes as well as a higher inductance saliencies at larger currents. Also one can conclude from the graph in Fig. 8.14 that the unskewed (machine 3) and skewed (machine 4) ideal rotors have more or less the same inductance saliency.

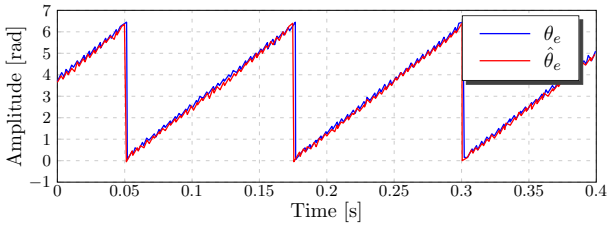

(a) Electrical angle.

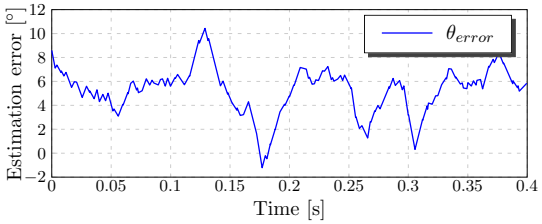

(b) Position estimation error.

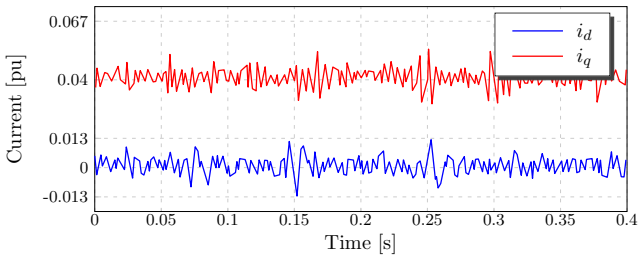

(c) Measured current.

Figure 8.12: HFI-PSC test of machine 3 at zero reference current.

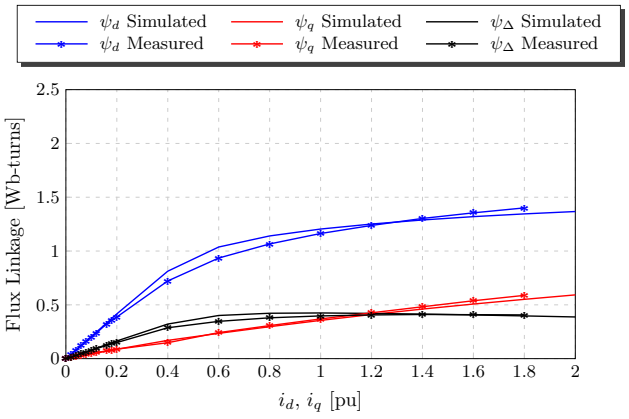

(a) Flux linkage.

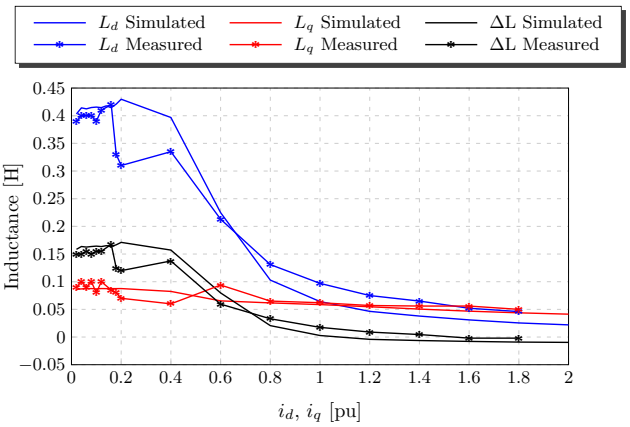

(b) Inductance.

Figure 8.13: Uncoupled simulated vs. measured results of machine 4.

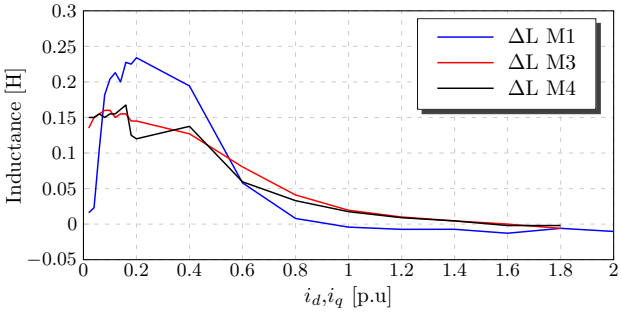

Figure 8.14: Measured inductance saliency comparison.

8.6.5 SB-PSC of machine 4

The SB-PSC test performed on machine 3 is duplicated on machine 4, again with the HFI-PSC method. The reference current is again kept at 0 A. These results are shown in Fig. 8.15. It is shown in Figs. 8.15a and 8.15b that the electrical angle of machine 4 is tracked accurately. It is shown in Fig. 8.15c that

there is only a small q-axis current response as a result of the HF excitation voltage. These results thus show that, as with machine 3, SB-PSC is possible at zero reference current.

8.7 Efficiency Evaluation

Machines 3 and 4 are designed to improve the efficiency of the position sensorless controlled RSM drive at zero reference current. It is shown in the UDDS of Fig. 8.3 that there are various instances where no torque is required from the machine and where the efficiency of machines 3 and 4 will be superior to that of machine 1. Also shown in Fig. 8.3 are various instances where the vehicle speed is more or less constant. It is thus important that an EV should also perform efficiently at constant speed. The efficiency of machines 1, 3 and 4 are measured with a position sensor and position sensorless. Two important questions are to be answered by the efficiency evaluation:

- Does the removal of the lateral ribs in order to create the ideal rotor RSM, influence the overall efficiency of the machine?
- Is there a performance loss when the RSM is controlled position sensorless instead of with FOC with a position sensor?

Measured results of the efficiency evaluation are summarised in Table 8.1. All tests are performed at the rated frequency of 50 Hz. The FS-PSC method is used in the PSC tests as this is a test at rated speed. The rated shaft power of machine 1 is 1.14 kW. This is chosen as the 1.0 $p.u$ output power for comparison purposes. The current of machines 3 and 4 are varied to also produce shaft powers of $\pm$ 1.14 kW. This ensures sensible efficiency evaluation between the three machines. The current rating of machine 1 is taken as the 1.0 $p.u$ current.

It is shown in Table 8.1 that the losses, when controlled with a position sensor, compare well to the losses of each machine respectively when controlled position sensorless. These results then suggest that the losses of the RSM are the same when controlled with a position sensor as with PSC. Furthermore, these results show that machines 3 and 4 have a higher torque per ampere rating than machine 1. It can

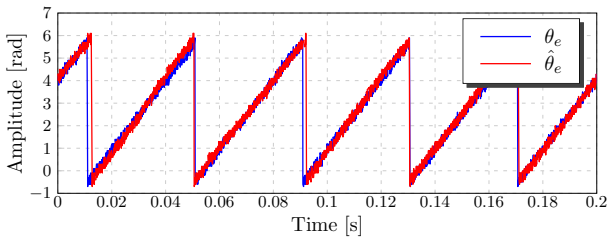

(a) Electrical angle.

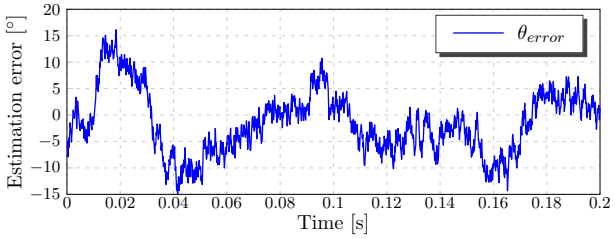

(b) Position estimation error.

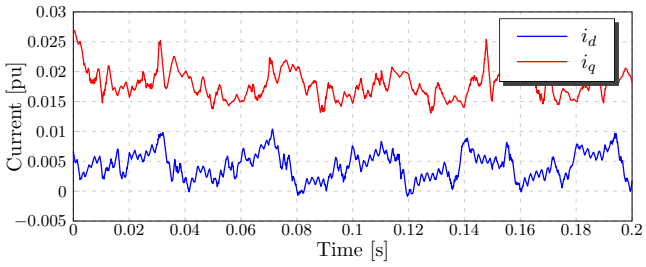

(c) Measured current.

Figure 8.15: HFI-PSC test of machine 4 at zero reference current.

thus be concluded that the ideal rotor RSM has a higher torque per ampere rating than the lateral rib rotor RSM. Finally Table 8.1 shows that the efficiency of machines 3 and 4 are slightly higher than that of machine 1. This might be due to machines 3 and 4 having less copper losses than machine 1.

It might be that the removal of the ribs of the lateral rib rotor RSM causes high frequency flux pulsations in the iron segments of the rotor. However, no additional losses in the two ideal rib rotor RSMs (machines 3 and 4) have been measured. This aspect must be further investigated, specifically for larger size RSMs.

8.8 Bandwidth Evaluation

The dynamics of a RSM drive are determined by its maximum bandwidth. Position sensorless controlled machines can suffer from sluggish behaviour due to a limited bandwidth. The extent of this limitation however, is still under question. The bandwidth difference between the lateral rib rotor and the ideal rotor RSM drive is also unknown. Machines 1, 3 and 4 are used for this investigation. In these tests sinusoidal speed reference signals are applied to the machine at no load while in speed control. The speed reference signal is as shown in Fig. 8.16. The frequency of the sinusoidal speed reference signal is increased until the machine is unable to track the reference speed. This is followed by a decrease in the sinusoidal speed reference amplitude until the machine is able to completely track the reference speed. It should be noted that the results of these tests are very much limited to the test bench used due to inertia, backlash, switching frequency of the drive etc. All the tests are done on the same test bench however, thus test results will still give valuable insight.

The speed bandwidth of the three machines when controlled with a position sensor are compared in Fig. 8.17a and their measured bandwidths with the HFI assisted hybrid PSC method are compared in Fig. 8.17b. It is shown in Fig. 8.17a that the speed bandwidths of all three machines are very similar when controlled with a position sensor. The measured speed bandwidth, when controlled position sensorless, in Fig. 8.17b show that although the machines 3 and 4 have a limited bandwidth at high frequencies, it can deliver unity response at higher speed reference frequencies than that of machine 1.

It is shown that the bandwidth of the position sensorless controlled machine 3 is more or less the same as when controlled with a position sensor, up until 1.8 Hz. The results in Fig. 8.17b show that machine 4

Table 8.1: Measurements of machines 1,3 and 4.

Machine #	Control	i [pu]	P_{in}	P_m	P_{loss}	η
1	Position sensor	1.0	1.35 kW	1.14 kW	0.21 kW	84.4%
	Position sensorless	1.0	1.35 kW	1.14 kW	0.21 kW	84.4%
3	Position sensor	0.91	1.35 kW	1.16 kW	0.19 kW	85.9%
	Position sensorless	0.91	1.36 kW	1.16 kW	0.20 kW	85.2%
4	Position sensor	0.93	1.35 kW	1.15 kW	0.20 kW	85.2%
	Position sensorless	0.93	1.36 kW	1.15 kW	0.21 kW	84.6%

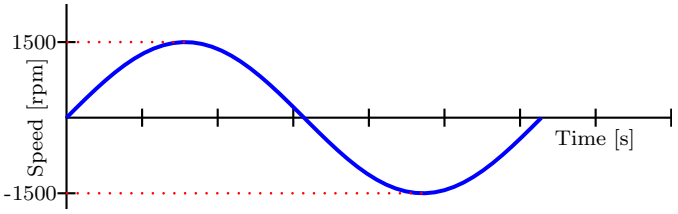

Figure 8.16: Speed reference for speed bandwidth evaluation of the three RSMs.

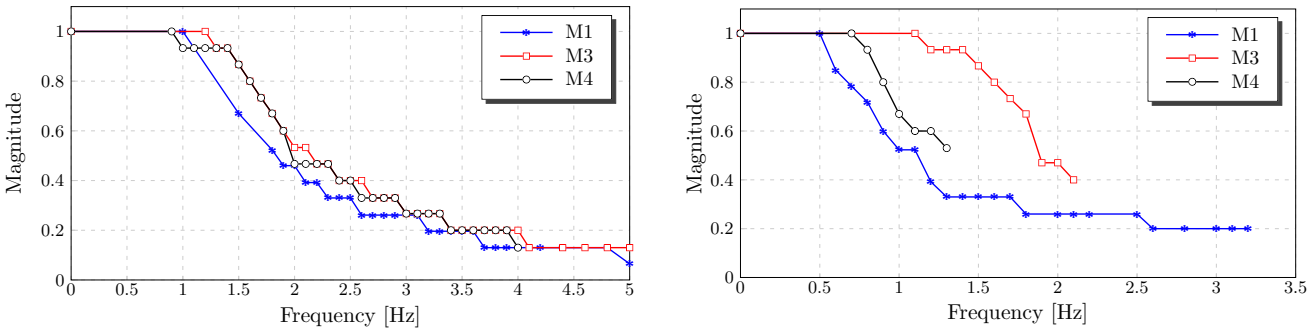

(a) FOC with a position sensor.

(b) PSC.

Figure 8.17: Measured speed bandwidth of machines 1,3 and 4.

has a smaller speed bandwidth when controlled position sensorless than its unskewed counterpart machine 3. It can thus be concluded that some of the bandwidth of the position sensorless controlled drive is sacrificed when the rotor is skewed.

8.9 Thermal Evaluation

Machines 1,3 and 4 are subjected to thermal tests while controlled with a position sensor and position sensorless. All three machines are subjected to rated conditions for an hour. The main objective of these tests is to determine if there is a noticeable difference in temperature when the drive is operated position sensorless, compared to operation with a position sensor. The second objective is to determine if the epoxy-resin and removal of the ribs, to create the ideal rotor RSM, results in a noticeable difference in rotor heat. It might be that the removal of the ribs influences the way that heat is transferred within the machine.

The casing of all three machines are enclosed, thus the closest point to measure the rotor temperature is at the drive end of the shaft. The temperature differences of the rotor shaft are shown in Fig. 8.18a. The abbreviations in Fig. 8.18a are: SC = Sensored control and PSC = position sensorless control. The measured temperature difference of the stator casing over time are shown in Fig. 8.18b. Measured results in Fig. 8.18a indicate that the shaft of the position sensorless controlled machines are slightly hotter than when controlled with a position sensor. The difference in temperature however, is very small. The results in Fig. 8.18a also show that the shaft of machine 3 is slightly cooler. Again the difference in temperature when compared to the other two machines is very small. The measured results in Fig. 8.18b show that the temperature rise on the casings is almost identical during all 6 cases.

It can thus be concluded that there is no major difference in temperature rise of the lateral rib rotor RSM without the epoxy-resin cast and the ideal rotor RSM with the epoxy-resin cast. It can also be concluded that there is no major difference in the temperature rise of the RSM when controlled with a position sensor or position sensorless.

8.10 Frequency Harmonics of the Fundamental Saliency Position Estimation Error

The purpose of this test is to evaluate if the RSM's FS-PSC capability is affected when the ribs of the lateral rib rotor RSM are removed. Machines 1,3 and 4 are evaluated with speed control at 50 Hz at full load. The FFT of the FS-PSC position estimation error, θ_{error}, of all three machines under these conditions are displayed in Fig. 8.19. It is shown in [3] that the position estimation error of the FS-PSC

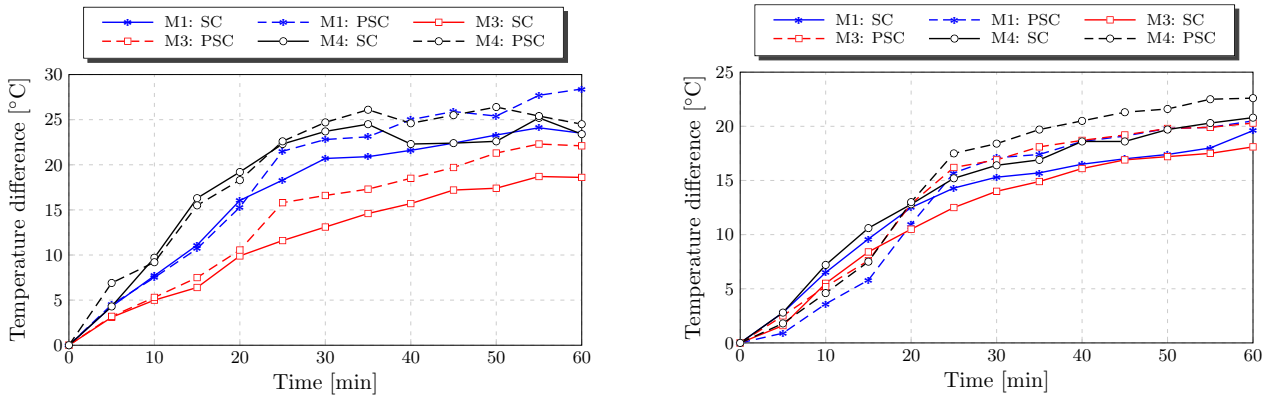

(a) Temperature difference on the rotor.

(b) Temperature difference on the casing.

Figure 8.18: Measured thermal evaluation of machines 1,3 and 4.

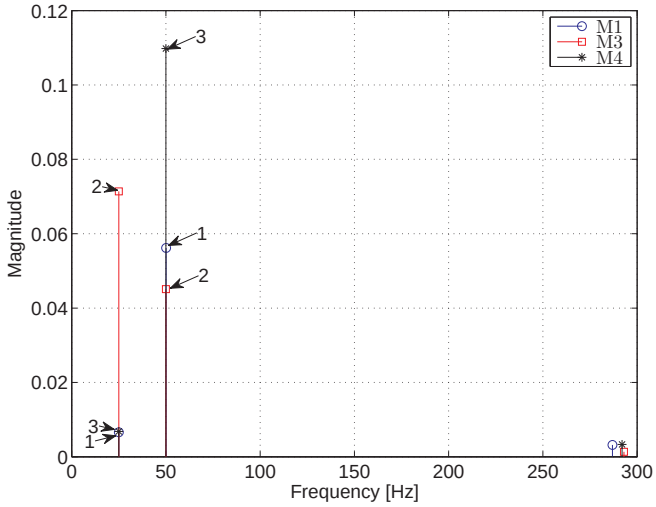

Figure 8.19: FFT of θ_{error} of the FS-PSC method.

method is related to the electrical frequency of the machine. The effect of this phenomenon can be seen in Fig. 8.19. It is clear that there are large 50 Hz harmonics present in the position estimation error of all three machines in Fig. 8.19.

In effect the PLL of the FS-PSC method is fed θ_{error}, which is speed dependent. It is shown in Fig. 8.19 that there are two main harmonics present in θ_{error}, namely 25 Hz and 50 Hz. The PLL tracks the 50 Hz harmonic, which is the dominant harmonic for position estimation. Furthermore, it is shown in Fig. 8.19 that machine 4 has the largest 50 Hz harmonic and the smallest 25 Hz one. This might be due to the skewing of the rotor which reduces harmonics in the flux linkage of the machine. This graph suggests that it is easier for the FS-PSC method to track the electrical angle of the skewed ideal rotor RSM due to the reduction of the 25 Hz harmonic in θ_{error}. This was also the experience of the author during implementation and testing.

8.11 Summary

Two effects that distort the saliency-based position sensorless control (SB-PSC) capabilities of PM synchronous machines (PMSMs) are identified in literature. It is shown in this chapter that these two phenomena are not unique to PM machines, but affect RSMs as well. A measured and simulated evaluation of machine 1 in this chapter reveals that the RSM suffers from a third problem area where SB-PSC is inhibited. This occurs at zero reference current where $L_d \approx L_q$. It is shown in the previous chapters that this problem area can be avoided by saturating the q-axis circuit. This method however, is not energy efficient.

The central rib rotor RSM is simulated in the JMAG finite element (FE) package to investigate if this machine is a viable alternative to the lateral rib rotor RSM. FE simulation results show that the inductance saliency of the central rib rotor RSM is, as with the lateral rib rotor RSM, too small at small current vectors for SB-PSC. The ideal rotor RSM is also evaluated in the JMAG FE package and it is shown that the inductance saliency of this machine is large enough at small current vectors for SB-PSC. The JMAG FE package is also used to investigate the effect of rotor skewing on the SB-PSC capabilities of the RSM. Simulation results show that there is very little deviation in the inductance saliency when a RSM rotor is skewed one stator slot pitch.

Machines 3 and 4 are constructed to confirm FE simulation results. Machine 3 has a unskewed ideal RSM rotor and machine 4 a skewed ideal RSM rotor. A novel construction method is developed to create the ideal rotor RSM. An epoxy-cast is formed in a lateral rib RSM rotor where after the lateral iron ribs is removed with a lathe. The epoxy-cast provides structural stability to the now detached piece of q-axis steel. The measured uncoupled flux linkage results of machines 3 and 4 compare well to the FE simulation results. The measured inductance saliency of both machines 3 and 4 are larger than that of machine 1 at small current magnitudes. Measured results prove that that SB-PSC of machines 3 and 4 is successful at zero reference current. Machines 3 and 4 are thus both an improvement on machine 1. It is also shown that the measured inductance saliencies of the unskewed and skewed rotor RSMs (machines 3 and 4) are almost identical.

It is shown in the efficiency evaluation that the ideal rib rotor does not only have a higher efficiency than the lateral rib rotor RSM, but also has a higher torque per ampere rating. It is also revealed that the losses of neither of the three evaluated machines increase when controlled with the FS-PSC method. The speed bandwidth evaluation revealed that machine 3 has the largest PSC bandwidth. It is also concluded that some of the position sensorless controlled machine's bandwidth is sacrificed when the rotor is skewed.

Thermal evaluation results show no significant difference in temperature between the lateral rib rotor RSM and the ideal rotor RSM with the epoxy-cast. Results also show that PSC does not result in any significant temperature increase when compared to FOC with a position sensor. The FFT of the FS-PSC position estimation error showed dominant speed dependent harmonics. It is concluded from this test that the harmonics in the position estimation error is reduced when the rotor of the RSM is skewed, and thus the FS-PSC capabilities of the drive are improved.

Chapter 9

Saliency Performance Comparison of Synchronous Machines

The field-intensified permanent magnet (FI-PM) synchronous machine is proposed in [109] to improve on the extended constant power speed range performance of the field weakening interior permanent magnet (FW-IPM) synchronous machine. It is also shown in [110] that the FI-PM machine outperforms the FW-IPM machine in the extended constant power speed range. Not only does the FI-PM machine have good constant power speed range performance, but it is also reported in [111] that the magnet volume of the FI-PM machine is 70% less than that of a FW-IPM machine. It is shown in [112] and [113] that even low coercive force magnets can be used with the FI-PM machine when designed properly.

The magnet of the FI-IPM machine is aligned with the rotor d-axis, thus positive d-axis current intensifies the magnet flux [111]. The FI-PM machine thus has the unique feature where L_d increases under saturation [111]. This holds advantages for saliency-based position sensorless control (SB-PSC) methods due to $L_d > L_q$ when the machine is loaded. It is stated in [111] and [114] that the FI-PM machine suffers from less saturation induced saliency decrease, lower cross-coupling effects and also has a reduction in secondary saliencies when compared to the FW-IPM. Good SB-PSC performance is recorded in [115] with a FI-PM machine.

Electric machine rotors are usually skewed to reduce the torque ripple. The rotor of the RSM consists of laminated steel only, thus the process of skewing its rotor is no more complex than that of an induction machine rotor. Skewing of PM machine rotors, like the FW-IPM- and FI-PM machines, on the other hand increases manufacturing complexity. An alternative method of torque ripple reduction is proposed in [116–118] and [119] where the rotor of a RSM, a PM assisted RSM and an IPM machine are designed with asymmetric rotor poles. This rotor design is referred to as a butterfly rotor in [116]. Two of the evaluated FI-PM machines have asymmetric rotor structures for reduced torque ripple.

Finite element (FE) simulation software is used in the previous chapter to modify the rotor of a RSM to improve its SB-PSC performance. The inductance saliency, ΔL, is used in the previous chapter to determine the quality of the machine's SB-PSC capability. The inductance saliency however, is not an accurate indicator of a machine's SB-PSC capability when different sizes and types of synchronous machines are to be compared. The number of turns per-phase, current density, geometry etc. are all factors which contribute to the SB-PSC capability of synchronous machines.

A per-unit machine parameter which allows comparison between different synchronous machine types and sizes in terms of their SB-PSC capabilities is investigated in this chapter. This per-unit scale is used to predict the SB-PSC performance of a range of synchronous machines by means of FE simulations before the manufacturing process. Similar evaluations are performed in [120] and [121], but without comparing the individual machine to other machine types and sizes. The types of machines compared in this chapter include a 4- and 6 pole RSM, three different types of FI-PM machines and a FW-IPM machine.

9.1 Saliency Ratio and Saliency Shift

The incremental inductances of the RSM are as defined in (9.1). These inductances are different to the absolute inductances and vary as a function of i_d and i_q [99]. According to [101], it can be assumed that the mutual inductances, which are caused by cross-saturation, are the same. Hence the mutual inductances are as in (9.2).

$$\begin{cases} \psi_d = \psi_d(i_d, i_q), \\ \psi_q = \psi_q(i_d, i_q), \end{cases} \qquad L_d = \frac{\partial \psi_d}{\partial i_d} \quad ; \quad L_q = \frac{\partial \psi_q}{\partial i_q} \tag{9.1}$$

$$\frac{\partial \psi_d}{\partial i_q} = \frac{\partial \psi_q}{\partial i_d} = L_{dq} = L_{qd} \tag{9.2}$$

It is shown in [101] that the small signal (HF) linear relationship between inductance, flux linkage- and current derivatives for the RSM can be represented by:

$$\delta \boldsymbol{\psi}_s^r = \begin{bmatrix} L_d & L_{dq} \\ L_{qd} & L_q \end{bmatrix} \delta \boldsymbol{i}_s^r \tag{9.3}$$

The small-signal current- and flux column matrices are represented by $\delta \boldsymbol{i}_s^r$ and $\delta \boldsymbol{\psi}_s^r$ in (9.3) respectively. The small signal currents are thus described as in (9.4) and (9.5) [95].

$$\delta i_d = \frac{L_q \delta \psi_d + L_{dq} \delta \psi_q}{L_d L_q - L_{dq}^2} \tag{9.4}$$

$$\delta i_q = \frac{L_d \delta \psi_q - L_{dq} \delta \psi_d}{L_d L_q - L_{dq}^2} \tag{9.5}$$

When the alternating HFI-PSC method is considered, the RSM can be described electrically by (9.6). Equation (9.6) is only valid when the injection frequency is high enough. The HF voltage is as in (9.7).

$$\boldsymbol{u}_s^r = \boldsymbol{L}^r \frac{d}{dt} \boldsymbol{i}_s^r \tag{9.6}$$

$$\boldsymbol{u}_s^r = \begin{bmatrix} u_c cos(\omega_c t) \\ 0 \end{bmatrix} \tag{9.7}$$

The resulting flux linkage can be written as in (9.8) according to [95] and [101]. The small signal current response can thus be rewritten as in (9.9) [101].

$$\delta \psi_d = \frac{u_c}{\omega_c} sin(\omega_c t) \tag{9.8}$$

$$\delta i_s^r = \frac{u_c sin(\omega_c t)}{\omega_c} \left[\frac{\Sigma L}{L_d L_q - L_{dq}^s} - \left(\sqrt{\left(\frac{\Delta L}{L_d L_q - L_{dq}^s} \right)^2 + \left(\frac{L_{dq}}{L_d L_q - L_{dq}^s} \right)^2} \right) e^{-j2\Delta\theta_e} \right] \tag{9.9}$$

It is stated by [95,99,101] that the negative sequence component of (9.9) (which is used in the demodulation process) is rotated by an angle γ due to the mutual inductance, L_{dq}. This angular offset is known as the saliency shift and can be calculated as in (9.10) [95, 99, 101].

$$\gamma = -0.5 \arctan\left(\frac{L_{dq}}{\Delta L} \right) \tag{9.10}$$

As stated by [99], the saliency shift will be zero at no load or if the geometric saliency is dominant enough to mask the effect of the saturation saliency. This then prevents the magnetic axis from moving away

from the rotor d-axis [99]. It is possible to compensate for the saliency shift within the control structure, if the saliency shift of the machine is known.

Although the mutual inductance causes a shift of the magnetic axis, it also contributes to the magnitude of the saliency [99]. This term should thus be taken into account when calculating the saliency of the machine. The saliency ratio is defined in [101] as the ratio of the negative sequence amplitude over the positive sequence amplitude. The saliency ratio equation is as in (9.11) [99, 101]. The saliency ratio is thus a parameter greater than zero and smaller than 1 that allows the machine saliency to be characterised on a per unit scale. Larger saliency ratio values are considered better for SB-PSC, but the effectiveness of the SB-PSC also depends on the saliency shift.

$$\zeta = \frac{\sqrt{(L_d - L_q)^2 + 4L_{dq}^2}}{L_d + L_q} \tag{9.11}$$

9.2 Saliency performance of a HEV RSM

A 17 kW RSM which is used in an experimental HEV in [122], is evaluated in the JMAG FE simulation package. This machine is listed in Table 3.1 as machine 5. The saliency ratio and saliency shift of machine 5 are calculated at various operating points on the maximum torque per ampere current angle curve with equations (9.10) and (9.11). The saliency ratio and saliency shift are also measured to verify the FE results. These results are shown in Fig. 9.1. There is a constant saliency ratio measurement error of ±6% as shown in Fig. 9.1a, which is acceptable. The saliency shift as shown in Fig. 9.1b however, does not correlate well. This is due to the small mutual inductance term which is difficult to measure.

It is shown in Fig. 9.1a that the saliency ratio of the RSM climbs quite steeply as the current increases and then steadily declines as the machine approaches full load while the saliency shift increases non-linearly. The results in this chapter show that the FE simulation results can be used to predict the saliency parameters of a machine even though there is a small error tolerance between the measured and simulated saliency ratio.

9.3 Saliency Performance Investigation by means of FE Simulation

Eight different synchronous machines are compared in terms of their saliency ratio and -shift. These machines are listed in Table 3.1 as machines 6-13. Machines 6-11 are designed to fit the specifications of the Opel Corsa used for the EV project in this thesis and operate with its stock gearbox in a variable gear drivetrain. More details regarding the Corsa will be provided in Chapter 11. Machines 6-13 are optimised

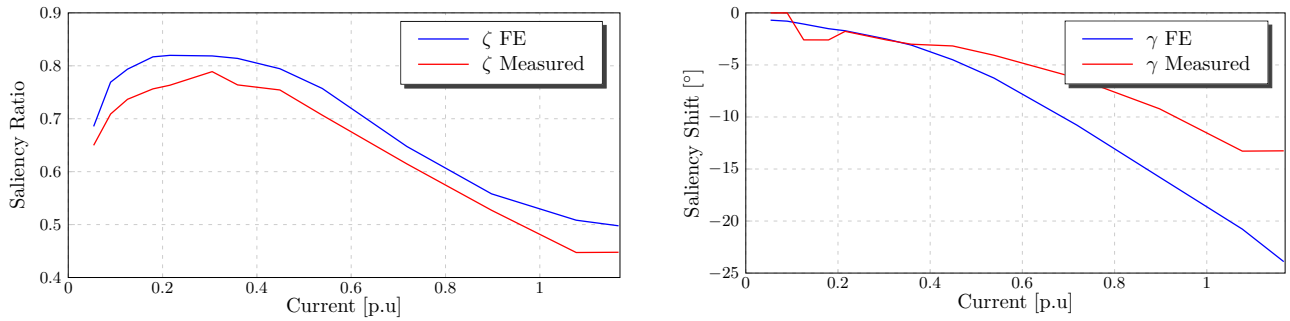

(a) Saliency ratio.

(b) Saliency shift.

Figure 9.1: Measured and simulated saliency ratio and -shift of machine 5 on the constant current angle curve.

for optimal torque and efficiency performance, but not for optimal PSC performance [123] Machines 6-8 are RSMs. Machines 6-8 have skewed rotors and chorded stator windings to reduce their torque ripple. The configuration of these machines are shown in Figs. 3.9f-3.9h.

Machines 9-11 are FI-PM machines. The FI-PM machines are also designed to fit the specifications of the Opel Corse with a variable gear drivetrain. The FI-PM machine has good constant power speed range performance, as mentioned above, thus this machine will perform well with a fixed gear drivetrain as well. Having a variable gear drivetrain however, brings down the size of the machine as less torque is required on the drive side.

Machine 9 is a surface mounted field intensified permanent magnet (SM-FI-PM) machine. The configuration of machine 9 is shown in Fig. 3.9i. Machine 10 is a field intensified interior permanent magnet (FI-IPM) machine with its magnet buried in the rotor. This machine is shown in Fig. 3.9j. Finally machine 11 is also a FI-IPM machine, but with flux barriers on the q-axis as shown in Fig. 3.9k. All of the FI-PM machines have chorded stator winding configurations to reduce the torque ripple. The rotors of the SM-FI-PM and FI-IPM machine without barriers also have asymmetrical butterfly rotors to reduce the torque ripple even further. These FI-PM machines are simulated as half models instead of quarter models due to the asymmetrical butterfly rotors.

For comparison purposes, a FW-IPM machine which is designed for a fixed gear drivetrain EV, is included as machine 12. This machine is shown in Fig. 3.9l. The final machine evaluated is machine 13 which is a 6 pole RSM which is to be evaluated in Chapter 12. This machine, which is shown in Fig. 3.9m, is used for a traction mining application with high startup torque, thus SB-PSC is very important.

All eight machines are simulated in the JMAG FE package in order to investigate and compare each machine's saliency ratio and -shift performance at its maximum torque per ampere current angle. These results are shown in Fig. 9.2. The saliency ratios of the four RSM designs (ζ 6-8 & ζ 13) are quite large throughout their rated region as seen in Fig. 9.2a. The saliency ratios of the FI-PM machines (ζ 9-11) are all very small in the low current region, but increase almost linearly with current. However, the saliency ratios of all three FI-PM machines are still lower at rated conditions than that of the RSMs.

The saliency ratio of the SM-FI-PM machine (ζ 9) is very small up until $\pm 50\%$ rated current. Inverter non-linearities, system noise, limited measurement bandwidth etc. might prevent this small saliency ratio from being exploited for SB-PSC. The saliency ratio of the FI-IPM machines (ζ 10, ζ 11) however, are both larger than that of the SM-FI-PM machine throughout the entire rated current region. In contrast to the increasing saliency ratio of the FI-PM machine, the FW-IPM machines' (ζ 12) saliency ratio decreases almost linearly to current. SB-PSC of this machine will not be possible at rated current. It has to be noted however, that the FW-IPM machine is a water cooled machine, thus it has a much larger current rating. Nevertheless it is shown that characteristics of the FW-IPM machine are still highlighted.

It is shown in Fig. 9.2b that the saliency shift of the two asymmetric rotor FI-PM machines (γ 9, γ 10) is fairly constant but large. The saliency shift of the FI-IPM machine (γ 11) with flux barriers however, is much smaller and coincides more or less with that of the RSMs. The addition of the flux barriers to the design of the FI-PM machine constraints the flux within definite paths in the rotor, limiting the cross coupling between the d- and q-axis. This then reduces the saliency shift significantly. It is also shown that the sign of the saliency shift of the FW-IPM (γ 12) changes direction when the gradient of the saliency ratio (ζ 12) changes its sign at 0.9 *p.u.* Furthermore Fig. 9.2b shows that all four RSMs have minimal saliency shift.

9.4 Measured Saliency Performance of the EV RSM (Machine 7)

Machine 7 is chosen for the Opel Corsa variable gear EV drivetrain, built and evaluated as explained in [123]. The saliency ratio of machine 7 is measured to compare to the FE simulation results shown in the previous section. Due to this machine's very high current rating no drive was available to test this

machine up to rated load, but measured results up to 0.6 $p.u$ correlate well with the FE results, and thus it can be assumed that the FE results are accurate up to rated load. The measured and simulated results are compared in Fig. 9.3.

9.5 Improving the Saliency Ratio and Saliency Shift.

It is shown in the previous sections that it is possible to accurately predict the saliency ratio and -shift of synchronous machines by means of FE simulations. It thus makes sense to exploit the flexibility and comfort of FE software to determine how to increase the saliency ratio and decrease the saliency shift of synchronous machines. It is found in [94] that to increase the saliency ratio of PM machines the tooth width of the stator should be decreased and the slot opening width should be increased. It is also shown in [94] that the slot geometry is an effective saliency parameter. The author in [85] states that the d-

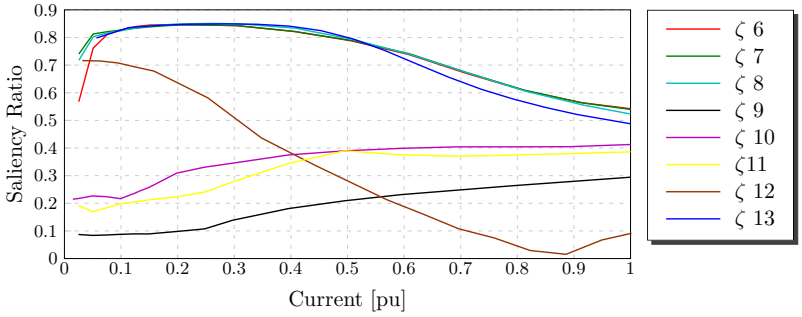

(a) Saliency ratio.

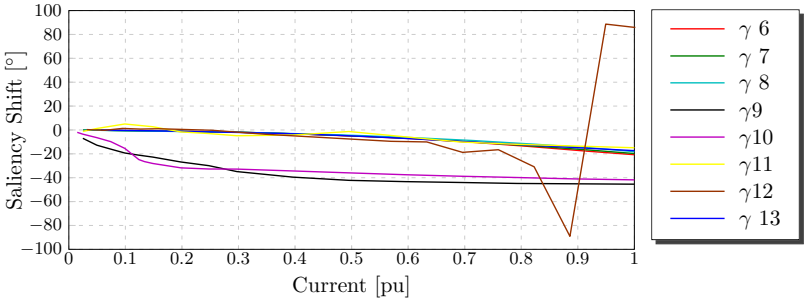

(b) Saliency shift.

Figure 9.2: Simulated saliency ratio and -shift comparison on the constant current angle curve.

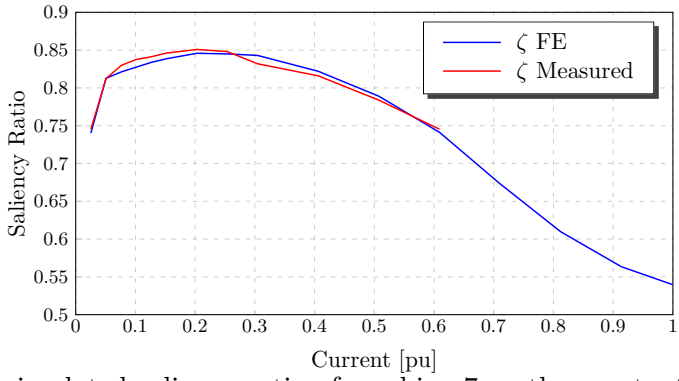

Figure 9.3: Measured and simulated saliency ratio of machine 7 on the constant current angle curve..

and q-axis flux linkages are constrained in more definite paths when the rotor has a high number of flux barriers per pole, thus reducing the cross-coupling effect. The saliency shift is thus reduced when the cross-coupling between the magnetic d- and q-axis is reduced. Machine 7 is used as a base model to investigate these effects. Three different modifications are investigated on machine 7:

1. Increasing the number of rotor flux barriers from 3 to 8.
2. Increasing slot opening width from 2.53° to 4.23°.
3. Increasing the number rotor flux barriers from 3 to 8 and increase the slot opening width from 2.53° to 4.23°.

The geometries of the base model (machine 7) and the modified designs are shown in Fig. 9.4. The FE simulation results of the three described experimental modifications are summarised in Table 9.1. The aim of the machine modifications are to increase the saliency ratio, ζ, and to minimise the magnitude of the saliency shift, $|\gamma|$. The torque ripple is also evaluated to determine how the modifications affect the power quality of the machine. None of these machines, including the base machine, are simulated with skewed rotors to increase the speed of the investigation. It should be noted, however, that the base model (machine 7) is optimised for maximum torque and minimum torque ripple and the optimisation process is not applied to the three modified designs. The torque of the based model is chosen as the 1 $p.u$ to compare to the modified designs.

The results summary of modification 1 in Table 9.1 clearly shows that the magnitude of the saliency shift decreases when the number of flux barriers per pole are increased. This coincides with the results shown in [85]. The saliency ratio, however also decreases by 6.94%. The results of modification 2 show that both the saliency ratio and the saliency shift improve when the slot opening width is increased. These results also coincide with the results shown in [94]. The saliency shift improvement of modification 2 is more than double than that of machine 1.

The simulation results of modification 3 show that the saliency shift improves even further when the number of flux barriers per pole is increased as well as the slot opening width increased. This saliency shift improvement of modification 3 however, is slightly more than that of modification 2 with a reduction in size of the saliency ratio. The increase in torque ripple of modification 3 is also significantly larger than the other two modifications. The simulated saliency ratio and -shift curves of the base model and modifications as a function of current are as shown in Fig. 9.5.

It is important to investigate if and how the machine modifications affect the shaft power quality of the machine. It is shown in Table 9.1 that the torque ripple of all three modified machine designs are large. Proper optimisation might however reduce the torque ripple. Another aspect that is to be investigated is how the losses in the machine are affected. The losses of the base model are compared to those of the modified designs in Table 9.2. The rotor- and stator losses of the base model are chosen as the 1 $p.u$ value in this investigation. It is shown in Table 9.2 that iron losses in the stator of all three modified designs are lower than that of the base model. The iron losses in the rotor of the modified designs however, are higher. The rotor iron losses of modification 3 are more than twice that of the the base model. It is thus

Table 9.1: Summarised simulated results of experimental modifications made to machine 7.

	ζ	$\lvert\gamma\rvert$	TR
Base	53.66%	18.56°	13.92 %
Modification 1	↓ 6.94%	↓ 2.01°	↑ 3.97%
Modification 2	↑ 4.68%	↓ 4.61°	↑ 3.66%
Modification 3	↓ 2.93%	↓ 4.9°	↑ 8.78%

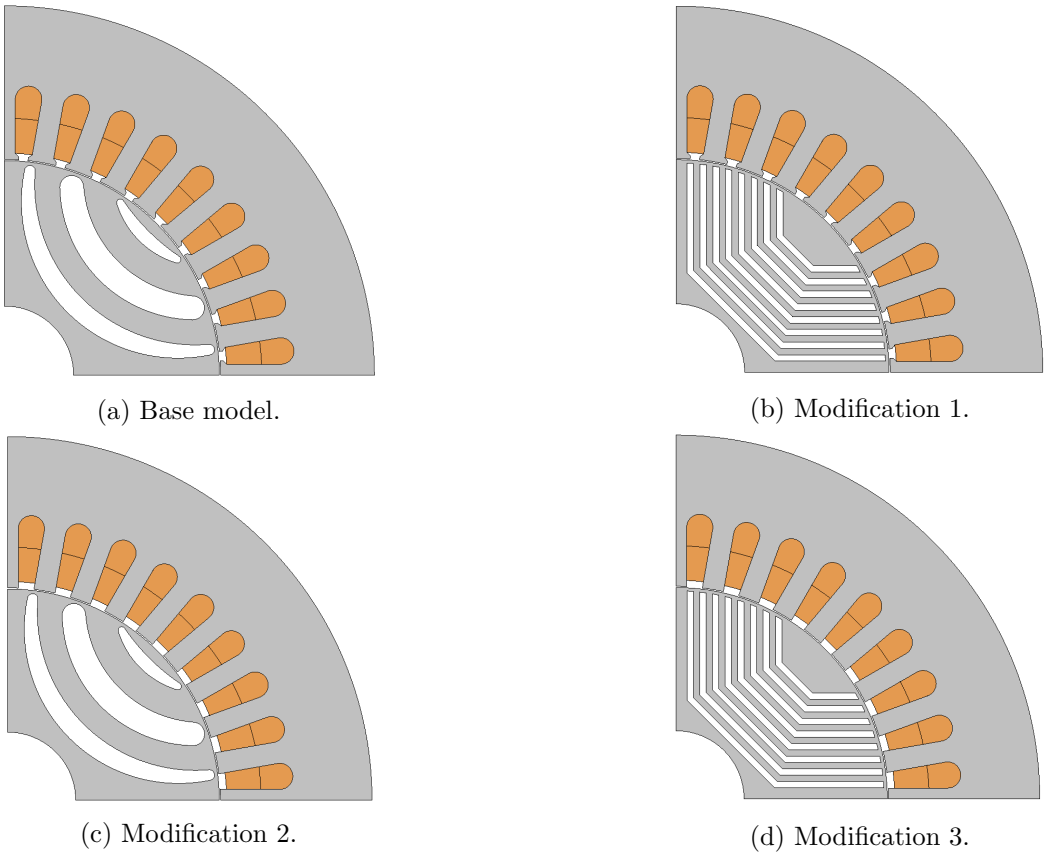

(a) Base model. (b) Modification 1.

(c) Modification 2. (d) Modification 3.

Figure 9.4: Geometry of the base- and modified RSMs.

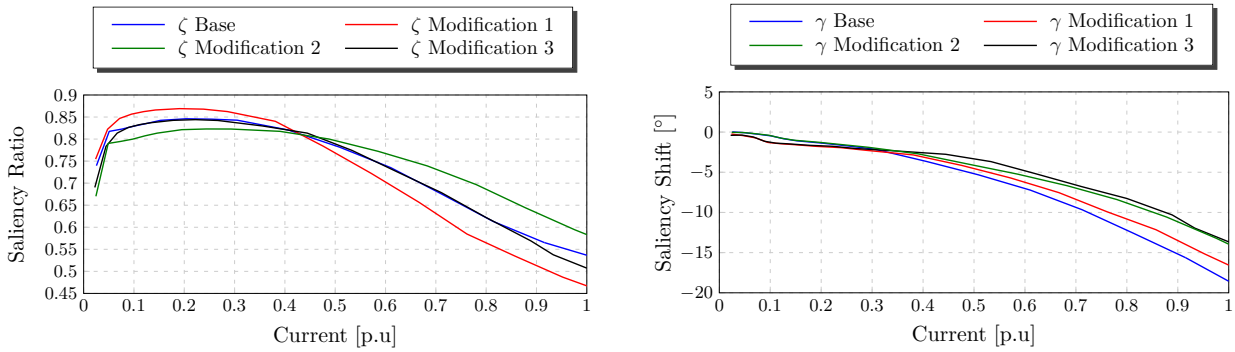

Figure 9.5: FE simulated saliency ratio and saliency shift of the base model and modified designs on the constant current angle curve.

important from a efficiency point of view that proper optimisation methods be used to reduce the rotor losses if any of these modifications are to be considered.

9.6 Summary

Saliency ratio- and saliency shift equations are used to calculate the saliency performance of different synchronous machines types and sizes on a per-unit scale. These equations give an indication of the saliency-based position sensorless control (SB-PSC) capability of the machine. Measurements of a HEV

Table 9.2: Comparison of losses obtained from FE.

	Rotor core [pu]	Stator core [pu]
Base	1	1
Modification 1	1.4	0.82
Modification 2	1.53	0.85
Modification 3	2.16	0.75

RSM are used to confirm that it is possible to accurately predict the saliency ratio of a machine with finite element (FE) simulations. The saliency ratio and -shift of the investigated RSMs show that the RSM has favourable characteristics for SB-PSC.

The saliency ratio simulation results of three field intensified permanent magnet (FI-PM) machines and a field weakening interior permanent magnet (FW-IPM) machine are compared to those of the RSMs. It is found that the saliency ratio of the RSM is higher than that of the FI-PM machines throughout the entire rated current region. It is also shown that the saliency ratio of the FW-IPM machine declines steeply as the current increases.

Simulation results show that the saliency ratio of all three FI-PM machines increase with current, as expected. It is found however, that the FI-PM machine configuration with the magnet on the surface (SM-FI-PM) has a large region at small currents where SB-PSC might not be possible. It is found that the saliency ratio of the two field intensified interior permanent magnet machines (FI-IPM) are larger than that of the SM-FI-PM machine in the entire rated current region.

FE simulation results show that the saliency shift of the two FI-PM machines without flux barriers are significantly larger than that of the FI-IPM machine with flux barriers. The saliency shift of the FI-IPM machine with flux barriers correlates well with that of the investigated RSMs.

Furthermore it is shown with simulation results that the saliency ratio of the RSM is reduced when the number of flux barriers per pole are increased. The saliency shift however, improves. It is also shown that both the saliency ratio and -shift improve when the width of the stator slot opening is increased. It is found that it is unwise to increase the number of flux barriers per pole as well as the stator slot opening due to a large increase in torque ripple.

FE simulations are used to investigate the effect of the machine modifications on the iron losses in the machine. It is found that the stator iron losses are reduced with all three modifications, but there is a increase in rotor losses. It is thus concluded that proper optimisation methods should be used to reduce the losses in the machine if these modifications are considered to improve the SB-PSC performance of the machine.

Chapter 10

Position Sensorless Controlled Reluctance Synchronous Wind Generator with a LC Inverter Output Filter

A brief literature study is provided in this section regarding variable speed wind turbines, reluctance synchronous generators (RSGs) and position sensorless control (PSC) of wind turbines. A RSG setup is proposed and laboratory measured results are provided in the final section.

10.0.1 Variable Speed Wind Turbines

The generator side of a wind turbine must have the ability to vary its speed to match the aerodynamic behaviour of the turbine rotor for maximum power conversion [124]. It is well known that the power captured from the wind turbine can be modelled with (10.1) [125].

$$P_t = \frac{1}{2}\rho_{air}\pi r_b^2 v_w^3 C_p(\lambda,\beta) \tag{10.1}$$

$$\lambda = \frac{w_m r_b}{v_w} \tag{10.2}$$

In (10.1), ρ_{air} is the air mass density, r_b the radius of the rotor sweep area, v_w the wind speed and finally C_p is the turbine power coefficient [125]. The turbine power coefficient is a function of the blade pitch angle β, and the tip speed ratio, λ defined as in (10.2) [125]. In (10.2), w_m is the blade tip speed. Maximum power coefficient is achieved by having a constant tip speed ratio, thus maximum turbine power is achieved by varying the turbine speed [124].

The standard squirrel-cage induction generator (SCIG) with a multi-stage gearbox is a fixed speed wind turbine configuration as the SCIG is directly connected to the grid. Two variable speed wind turbine concepts are favoured in the industry. The first is the most widely used generator, the doubly fed induction generator (DFIG) with a multi-stage gearbox and a small scale converter [126]. The power rating of the converter is approximately 25% of the rated power of the generator [124]. Speed variation of $\pm$ 30% synchronous speed is achieved by varying the frequency and the current in the rotor windings [126]. This turbine setup is attractive from a costs point of view due to the partial size converter [127]. The drawbacks of this system however, are the use of slip rings and controllability issues during grid faults [127].

The second industry favoured variable speed wind turbine configuration has a full scale converter. The generator is electrically decoupled from the grid by the DC bus of the converter. Topologies

vary from SCIG's, wound rotor synchronous generators and permanent magnet synchronous generators (PMSGs) [127]. Also, drivetrains vary from multi-stage gearboxes, reduced stage gearboxes and direct drive topologies with multi-pole PM generators. It is reported in [127] that the advantages of the full scale converter setup over the partial converter DFIG setup are the possible elimination of slip rings, full speed- and power controllability, better grid support and better grid code compliance. All the power is controlled by the converter, thus the full scale converter will add extra losses to the wind energy conversion (WEC) system. The full speed controllability might however mitigate the added drive losses [128]. It is suggested in [126] that variable speed wind turbines with full scale converters will dominate in large wind farm topologies in the future.

10.0.2 Control Of Converter-Fed Wind Turbines

The control structure for a general wind turbine system, as presented in [127, 129–131], is shown in Fig. 10.1. The current is controlled on the generator side to control the torque and thus the rotor speed for maximum power generation [127]. The grid side converter has the advantage of controlling the active and reactive power to and from the grid [128]. Wind turbine specific control include maximum power point tracking (MPPT), pitch control, low voltage ride through and providing grid support [127]. The DC link is equipped with a chopper to prevent over voltage [127]. External energy storage units can also be connected to the DC bus to manage active power flow into the grid [127].

It is still not clear whether direct torque control (DTC) or field oriented control (FOC) are best suited for control of wind turbines. Some large wind turbine manufactures have completely adopted DTC in their position sensorless wind turbine converters [132]. A FOC method for industrial wind turbines is presented in [133] where the voltage phases and fundamental model methods are used to extract a rotor angle. In [134], simulation tools are used to compare the performance of a DTC and FOC controlled direct drive variable speed PMSG for large wind turbines. It is shown in [134] that very similar results are obtained with both control strategies.

FOC exhibits good torque response, accurate speed control and achieves full torque at zero speed [134]. FOC, however needs to be extended to be position sensorless so as to avoid using fragile position sensors.

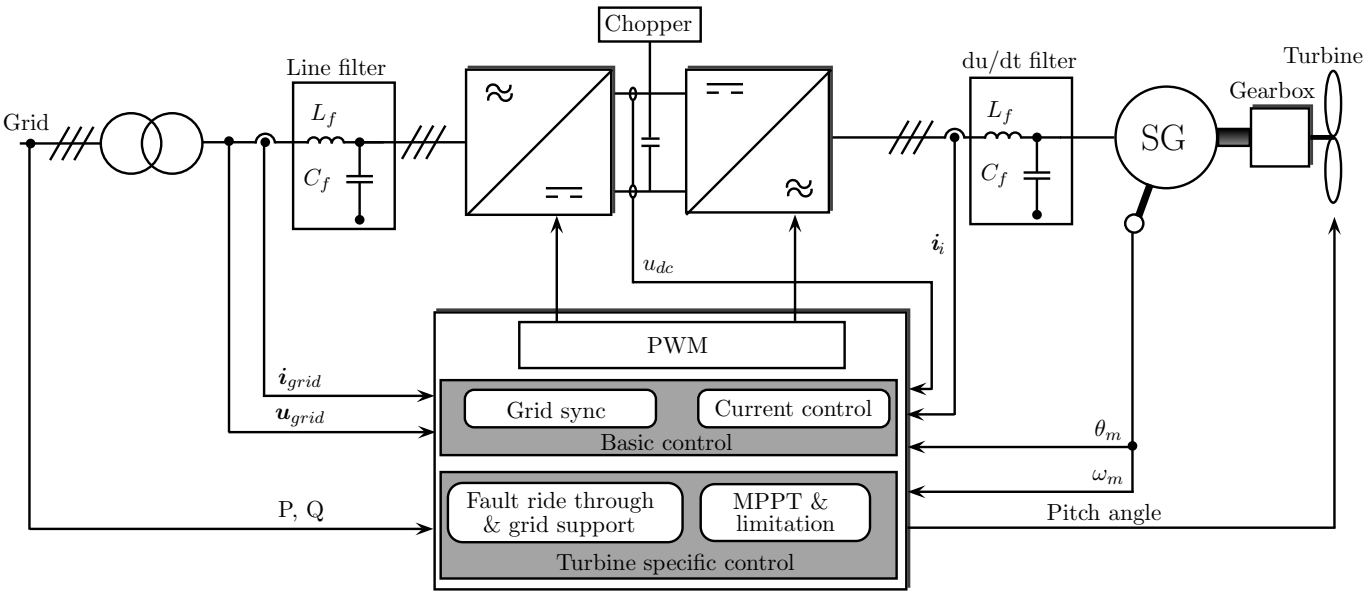

Figure 10.1: General control structure for a variable speed wind turbine system.

The advantages of DTC is its dynamic behaviour and that it is inherently position sensorless. The main disadvantages of DTC are the variable switching frequency, high torque pulsations and fast sampling time requirements [134]. The DTC method can be extended with space vector modulation (SVM). The DTC-SVM method has the advantage of a constant switching frequency and reduced torque ripple compared to DTC [135]. The electrical rotor position is also a requirement for DTC-SVM methods, however thus also needs to be extended to be position sensorless [136].

10.0.3 Inverter Output Low Pass Filter

In [137] and [138] it is stated that the rectangular waveform created by PWM inverters can cause several problems on the machine cables and at the machine terminals. It is therefore suggested that a LC filter be inserted between the inverter and the machine to ensure sinusoidal machine voltages and to reduce the overvoltage peaks caused by the fast voltage rise time and switching frequency. This filter is referred to as a du/dt filter and is used in various industry converters [130, 131, 139]. This also allows for the usage of standard machines without additional stress designs and helps to avoid motor de-rating [137].

LC filters on long cables also prevent voltage reflections which may cause voltages spikes of twice the DC bus voltage at the motor terminals damaging the machine insulation [137, 138, 140, 141]. The rate of voltage rise can also cause bearing currents to circulate in the machine and electromagnetic interference which can be prevented with an inverter output LC filter [138, 141]. Various commercial industry retailers of du/dt filters for wind turbines are available [142, 143].

10.0.4 The Inverter-Fed Reluctance Synchronous Generator

Not much literature exists on the subject of inverter-fed RSGs. In [144], a finite element (FE) package is used to simulate a 6 pole reluctance synchronous wind generator system. The simulation results in [144] however, are not verified by measured results. A voltage source inverter fed RSG is proposed in [145] and [146]. The proposed super high speed reluctance generator application is aimed at aircraft carriers, space shuttles and deep sea marine engines. The implementation in [145] and [146] requires an encoder and has no inverter output LC filter. An axial laminated RSG is proposed in [147] where it is shown that the iron losses in the machine contribute to the power factor of the reluctance motor, but reduce the power factor of the reluctance generator [147]. The author in [147] showed that for high efficiency and power factor the inductance ratio, L_d/L_q, of the RSG needs to be high.

In [126], PMs are added to a reluctance rotor to improve operating performance. This is referred to as a PM assisted RSG. Optimal current control is derived from the torque equation and used for maximum power control [126]. This generator is controlled with positive d-axis current and negative q-axis current. Fast dynamic response is obtained in [126]. A position sensor is used for vector control in [126] and no LC filter is used. A conceptional PM-assisted RSG for mild hybrid vehicles with a large constant speed range is proposed in [148]. A position sensor is used for vector control and no LC filter is used [148].

10.0.5 Position Sensorless Controlled Variable Speed Generators

The axial laminated RSG presented in [147], is controlled position sensorless with a model based DTC implementation in [149]. The method proposed in [149] is only able to control the generator in the medium to high speed region. Simulation and measured results are thus all at high speed. No LC filter is used with this implementation. A few DTC methods are proposed for control of PMSGs without a LC filters [136, 150]. It can be stated however, that the efficiency measurements obtained in [150] are sub par compared to what has come to be expected of PM machines. This might be due to the DTC implementation not being extended to incorporated SVM.

A wide variety of vector position sensorless control (PSC) methods for variable speed PMSGs without LC filters are presented in literature [151–154]. Most of these proposed methods rely on fundamental

or model based methods only and thus only control the generator in the medium to high speed region [152–154].

According to [155] an inverter output LC filter can cause many well known PSC methods to fail at standstill. A saliency based PWM injection method, which is able to estimate the electrical angle of a PMSM, with an inverter output filter is proposed in [155]. The drawback of this method is the need to measure the stator current on the machine side of the LC filter. The stator and inverter current can differ due to the effect of the filter, thus the inverter current needs to be measured as well to prevent damage to the drive. A similar method is presented in [156] for an undersea propulsion system.

In [157], a PMSM is controlled position sensorless with an output LC filter. A model based scheme is used for PSC in the medium to high speed range [157]. The observer matrix is deactivated at startup and low speeds, allowing the controller to run without correctional feedback. This is due to the model based scheme's inability to function at standstill and low speeds. Large position estimation errors are exhibited in the low speed range in [157]. This implementation however, measures the stator currents and voltages on the machine side of the filter. It is found in [157] that the position estimation degrades proportional to increasing angular velocity due to the low pass filtering of the phase voltages and sampling delays.

A high frequency injection PSC (HFI-PSC) method is used in [68] to control a PMSM with an inverter output LC filter. In this implementation the only measured quantities are the inverter phase current and the DC bus voltage. A mathematical model of the machine and the filter is used to estimate the stator quantities by deriving linear machine equations in [68].

10.0.6 Literature Study Summary

Literature regarding inverter fed RSGs is very limited. No literature could be found on a RSGs controlled with FOC PSC methods. Literature regarding reluctance synchronous machines (RSMs) with LC inverter output filters, with or without a position sensor, is also very limited. The closest match that could be found is in [158], where a LC filter is used with a solid rotor RSM to reduce the rotor losses. A common problem with position sensorless controlled synchronous machines with inverter output filters is limited controllability through the entire rated speed range. Another common problem is that current and voltage probes are either used on the inverter- or machine side of the LC filter. Inverter current needs to be measured to protect the drive. Stator current and voltages on the machine side of the inverter are necessary for accurate MPPT and PSC. Linearised mathematical models of the generator are often used to estimate stator quantities. Other literature also considered in this study includes [159–163].

10.1 Proposed Reluctance Synchronous Generator Setup

It is pointed out in [124] that a wind turbine system with a lower efficiency that delivers energy at a lower cost is a better solution than a high efficiency, high cost system. It is thus important to minimise the cost of energy delivered [124]. A converter-fed RSG is proposed as an alternative to conventional variable speed concepts. The RSG is cheaper to manufacture than SCIGs, DFIGs, wound rotor synchronous generators and PMSGs. Not only is manufacturing of the RSG cheap, but research has also shown that the efficiency of the RSM compares well to that of the induction machine, if not better [12, 13].

The RSG is brushless and is able to perform variable speed operation through the entire speed range unlike the DFIG which has brushes. As discussed in the introduction, a variable speed wind generator, as the proposed turbine setup, will allow maximum power transfer from the turbine. The RSG is a high speed machine and will thus use a similar multi-stage gearbox as the SCIG and the DFIG. The high efficiency and single stage, or no gearbox, setup of the PMSG seems more attractive than the multi-stage gearbox RSG setup. The disadvantage of the PMSG turbine setup however, are the large quantities of expensive PM material that is used and the increased nacelle mass. Manufacturing complexity is also

high for large power PMSGs. The RSG can thus be seen as an attractive alternative to the conventional fixed speed and variable speed wind turbine setups.

The aim is to propose and implement a RSG WEC system that is robust, reliable and requires minimum maintenance. It is well known that the RSG is robust and reliable. The proposed turbine setup will thus not make sense if some other part of the WEC system is unreliable. It is reported in [164] that ±14% of turbine failures per year are as a result of frequency converter failure contributing to 18% of the yearly turbine downtime. Converter failure results in the second longest turbine downtime accumulated hours per year after pitch control failure [164].

Recently some companies have started installing the converter in the tower base instead of the nacelle [5, 131]. Some of the benefits listed in [5] are: "reduced nacelle weight and size, vibrations sensitive components are stationary, more efficient maintenance and easier to replace components if necessary." The power converter location of the AREVA M5000-116 wind turbines, situated in the Alpha Ventus offshore wind farm off the coast of Germany, are also located in the tower base [165]. A diagram of the tower layout from the WinWind3 catalogue is shown in Fig. 10.2 [5].

The proposed RSG setup is as shown in Fig. 10.3. This implementation allows all the power electronics and controllers to be stationed on the ground. Although this will not necessarily improve the reliability of the converter it might reduce the downtime of the turbine during maintenance of the converter. The weight of the nacelle is thus also reduced. An inverter LC filter is a necessity especially if the cables from the converter to the machine are quite long as in this case. The LC inverter output filter will ensure sinusoidal machine voltages to reduce insulation deterioration, bearing currents and EMI. The LC filter also allows unshielded cables to be used.

The only measurable quantities in the proposed setup are the DC bus voltage and the inverter current. No additional measuring probes are necessary, thus reducing the risk of device failure. The most important feature of this setup is the omission of the position sensor. It is close to impossible to connect a high resolution position sensor to the machine and to locate the control unit in the tower base. By omitting this sensor the robustness of the entire turbine setup is increased. Only the generator side of the converter, which is highlighted in blue in Fig. 10.3, is considered in this thesis. Subscript i in Fig 10.3 identifies inverter quantities, i.e. the voltage or current on the inverter side of the filter. Subscript s identifies the stator quantities. The symbol $\boldsymbol{d}_{abc}$ represents the inverter switching states.

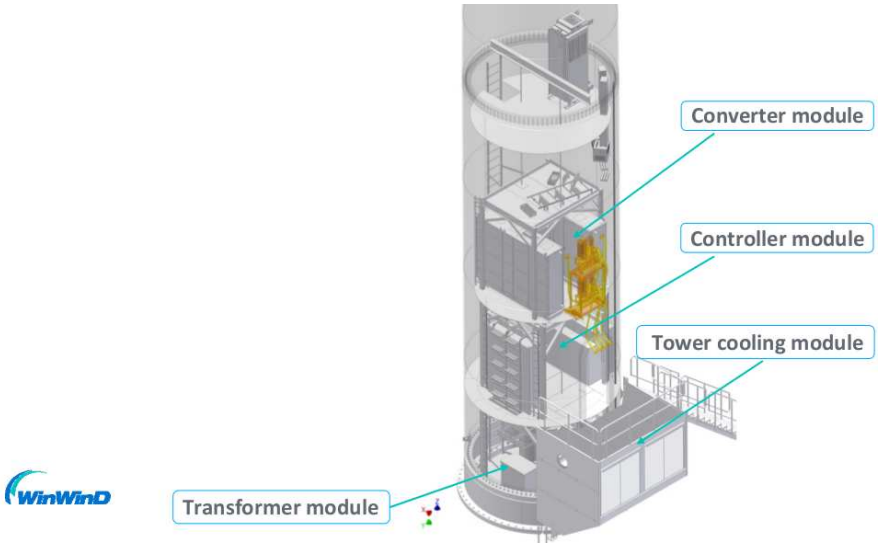

Figure 10.2: Tower layout of the WinWind3 wind turbine [5].

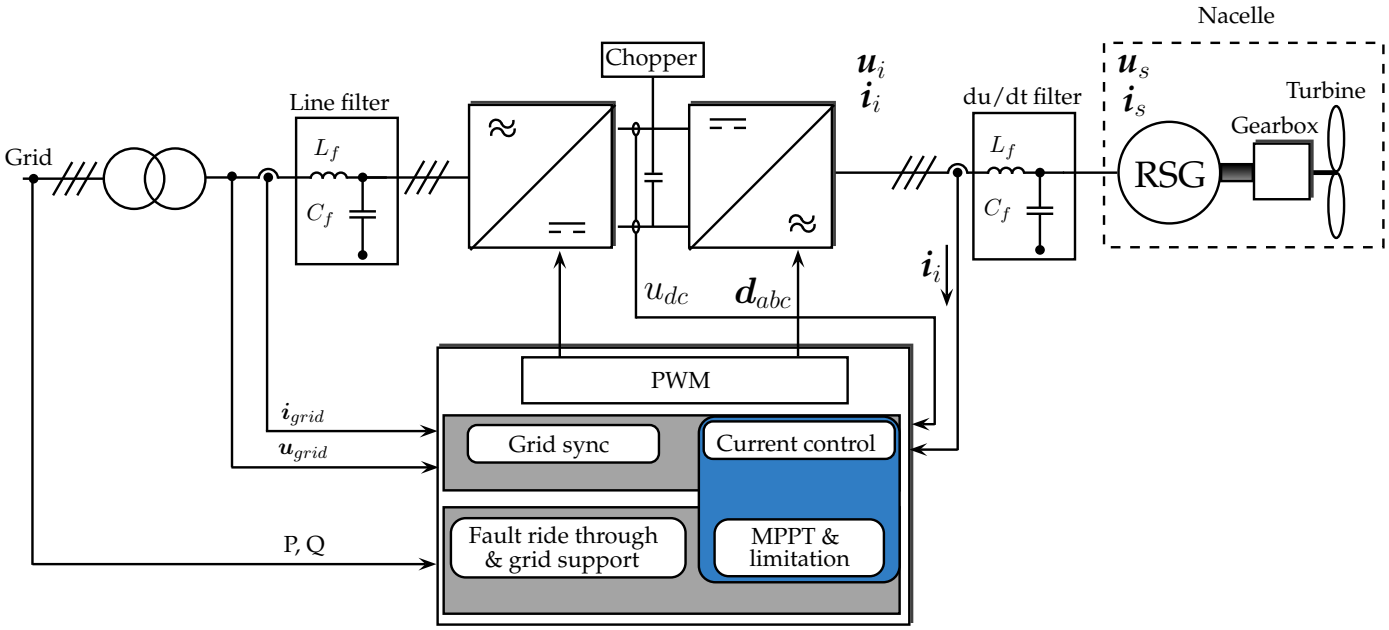

Figure 10.3: Proposed reluctance synchronous generator wind turbine setup.

10.2 The Reluctance Synchronous Generator

Machine 5 is used as the RSG and is listed in Table 3.1 as a 17.25 kW machine at 90 Hz. High speed operation will not be required, thus this machine is rated as a 9.6 kW RSG at 50 Hz. The RSM has four operating regions as shown in Fig. 10.4a. Quadrants 1 and 3 are motoring regions and 2 and 4 generator regions. The RSG is controlled in quadrant 4 (shaded quadrant) within this investigation.

Derived equations in [147] show that the RSG operates at maximum efficiency if the copper and iron losses of the d-axis current equal the the copper and iron losses of the q-axis current. Iron losses are developed mainly due to the d-axis current and copper losses mainly due to the q-axis current [147]. The RSG thus operates at maximum efficiency when $P_{cu} = P_{iron}$ [147]. Finally, [147] states that the maximum efficiency and power factor of the reluctance generator decrease as the number of pole pairs increase. It can thus be concluded from the work done in [147], that different design rules should exist for designing reluctance synchronous generators than for reluctance synchronous motors. It is thus important to point out that the RSG used in this investigation is designed for optimal motor performance, but it will still be possible to investigate the validity of RSG drives with this machine.

The measured efficiency and power of the evaluated RSG, as a function of current, are shown in Fig. 10.4b. The efficiency is quite satisfactory for a non PM machine. The generator torque and power of a variable speed wind turbine are usually varied during MPPT for maximum power transfer. It is shown in Fig. 10.4b that the efficiency of this RSG increases slightly below its rated power rating. This machine will thus perform well with MPPT.

10.3 Inverter Output LC Filter and Stator Quantities Estimations

The addition of the LC filter complicates the control structure of the RSG, especially with PSC methods as will be explained in this section. The cut-off frequency of the LC inverter output filter needs to be designed to be well below the switching frequency of the drive, but higher than the fundamental frequency of the machine. The transfer function of the LC filter is as shown in (10.3). In (10.3), L_f, C_f and R_f

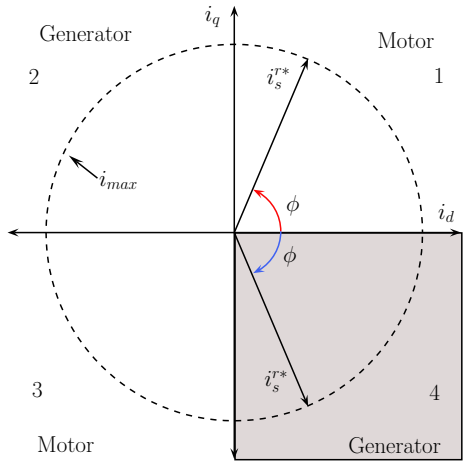

(a) Four quadrant control of the reluctance synchronous machine.

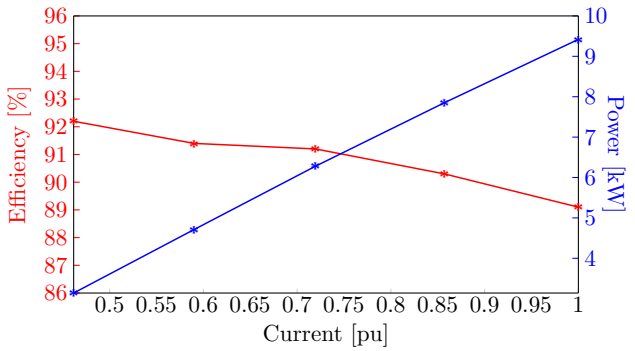

(b) Measured efficiency of the RSG at rated speed.

Figure 10.4: The 9.6 kW RSG.

are the filter inductance, capacitance and series resistance respectively. The cut-off frequency can be calculated with (10.4) [166].

$$H_d(s) = H_q(s) = \frac{\dfrac{1}{L_f C_f}}{s^2 + s\dfrac{R_f}{L_f} + \dfrac{1}{L_f C_f}} \tag{10.3}$$

$$f_o = \frac{\omega_o}{2\pi} = \frac{1}{2\pi\sqrt{L_f C_f}} \tag{10.4}$$

By neglecting the speed voltage terms of the machine equations in (2.7) and (2.8), the machine transfer function can be derived as an inductive and resistive load as shown by (10.5) and (10.6).

$$\frac{i_d(s)}{u_d(s)} = \frac{1}{L_d s + R_s} \tag{10.5}$$

$$\frac{i_q(s)}{u_q(s)} = \frac{1}{L_q s + R_s} \tag{10.6}$$

The machine and filter parameters are summarised in Table 10.1. To evaluate the effect of the LC filter on the plant it is necessary to evaluate the combination of the LC filter and plant transfer function. The bode plot of the d- and q-axis transfer functions at rated conditions are displayed in Figs. 10.5a and 10.5b. The combination of the plant transfer functions and LC filter are also plotted in Figs. 10.5a and 10.5b. These graphs clearly show that the filter adds a resonance frequency to the plant and cuts off after f_o. The importance of this resonance frequency with respect to the PSC of the generator will be explained later.

It is shown in Fig. 10.3 that the only measurable quantities in the proposed WEC system are the DC bus voltage and the inverter current. The inverter- and the stator currents however, are not the same, due to the current flow in the capacitor. The inverter or reference control voltages are also not equal to the stator voltage during transients.

Table 10.1: Machine and LC filter parameters.

Machine Parameters	
Stator resistance R_s	0.15 Ω
Direct-axis inductance L_d	23.8 mH
Quadrature-axis inductance L_q	4.41 mH
Pole pairs N_p	2
Rated speed	1500 rev/min
Rated current (rms)	40 A
Rated torque	61 Nm
Rated power	9.6 kW
Constant current angle ϕ	67°
Rated saliency ratio γ	0.53
Rated saliency shift ζ	18.63^o
Drive Parameters	
Switching frequency F_s	6.1 kHz
Sampling frequency f_s	12.2 kHz
DC bus voltage u_{dc}	540 V
LC Filter Parameters	
Inductance L_f	1.33 mH
Capacitance C_f	25 μF
Series resistance R_f	0.2 Ω
Cut-off frequency f_o	872.82 Hz

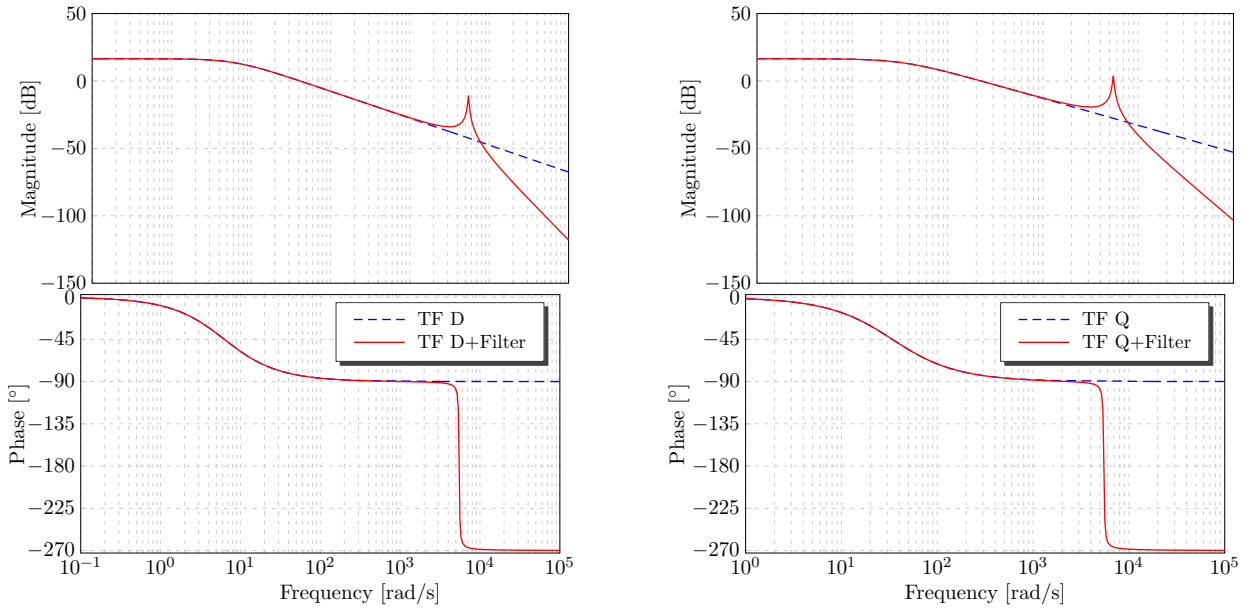

(a) Bode plot of the D-axis transfer function.

(b) Bode plot of the Q-axis transfer function.

Figure 10.5: Bode plots of the RSG with and without the inverter output filter.

The effect of the difference in inverter and stator quantities on the RSG control structure can be summarised as:

- $\boldsymbol{i}_i^s = \boldsymbol{i}_s^{s*} \neq \boldsymbol{i}_s^s$: The reference currents in the control structure and the stator current are not equal, therefore affecting the MPPT of the generator.
- $\boldsymbol{i}_i^s \neq \boldsymbol{i}_s^s$ & $\boldsymbol{u}_s^{s*} \neq \boldsymbol{u}_s^s$: Flux linkage estimations which are used with the fundamental saliency position sensorless control (FS-PSC) method will be inaccurate and can thus cause this method to fail.

Adding stator current and -voltage measurement probes is possible, but it is preferable not to add any additional measuring probes to the WEC system. The stator currents and -voltages are measured in [155, 167], however the inverter currents should also be measured to prevent damage to the inverter. In [68] and [168] the author used a linear mathematical derivation of the machine as well as the LC filter model to calculate the stator voltages and -currents. The machine used in [68] and [168] however, has nearly constant d- and q-axis inductances. The d- and q-axis inductance of the RSG is non-linear as a function of current, and lookup tables will be necessary if this method is to be used with the RSG. It is thus proposed to use only the mathematical model of the filter to estimate the stator currents and -voltages. The combined RSG and LC filter voltage equation in vector format in the $\alpha\beta$ reference frame is as in (10.7).

$$\boldsymbol{u}_i^s = L_f \frac{d\boldsymbol{i}_i^s}{dt} + \boldsymbol{u}_s^s + R_f \boldsymbol{i}_i^s \tag{10.7}$$

The machine's stator voltage is equal to the voltage across the filter capacitor, i.e.

$$\boldsymbol{u}_s^s = \frac{1}{C_f} \int \boldsymbol{i}_c \, dt \tag{10.8}$$

Now substitute (10.8) into (10.7) and rewrite into its Laplace equivalent equation:

$$\boldsymbol{u}_i^s(s) = sL_f \boldsymbol{i}_i^s(s) + \frac{1}{sC_f} \boldsymbol{i}_c(s) + R_f \boldsymbol{i}_i^s(s) \tag{10.9}$$

It is assumed that the rate of change of the current in the machine is much lower than that of the capacitor during transients. This assumption validates (10.10) and is used to derive (10.12)

$$\boldsymbol{i}_i^s(s) = \boldsymbol{i}_c(s) = sC_f \boldsymbol{u}_s^s(s) \tag{10.10}$$

$$\begin{aligned} \boldsymbol{u}_i^s(s) &= s^2 L_f C_f \boldsymbol{u}_s^s(s) + \frac{1}{sC_f} sC_f \boldsymbol{u}_s^s(s) + sR_f C_f \boldsymbol{u}_s^s(s) && (10.11) \\ &= \left(s^2 L_f C_f + sR_f C_f + 1\right) \boldsymbol{u}_s^s(s) && (10.12) \end{aligned}$$

Reshuffling yields

$$\boldsymbol{u}_s^s(s) = \left(\frac{\boldsymbol{u}_i^s(s) - sR_f C_f \boldsymbol{u}_s^s(s) - \boldsymbol{u}_s^s(s)}{s^2 L_f C_f} \right) \tag{10.13}$$

Equations (10.13) and (10.8) can be used to estimate the stator voltage and the capacitor current. The capacitor current can be used to calculate the actual machine current. This estimation scheme is displayed in Fig. 10.6.

10.4 Position Sensorless Control Implementation

The LC filter is designed to remove the switching frequency harmonics of the drive. It is shown in Chapter 5 that the arbitrary injection PSC (AI-PSC) method injects voltage pulses at half the switching frequency to exploit the machine saliency for PSC. The injection voltages will thus be filtered out if this method is used with an inverter output filter with a low cut-off frequency, as in this case. The AI assisted hybrid PSC method is thus not a plausible PSC method for this application.

The PSC method used is the HFI assisted hybrid PSC method. The stator quantities that are estimated with the method displayed in Fig. 10.6 are used for PSC. The estimated stator current is also used as feedback for the current controller instead of the inverter current. The working of this setup is

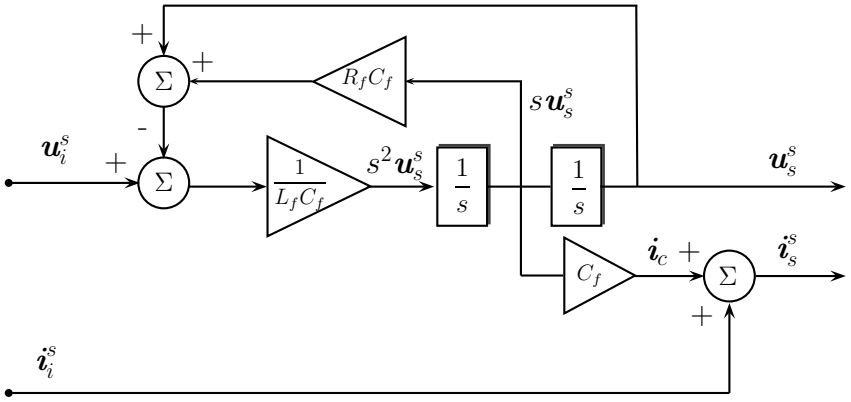

Figure 10.6: Schematic of stator quantity estimation method.

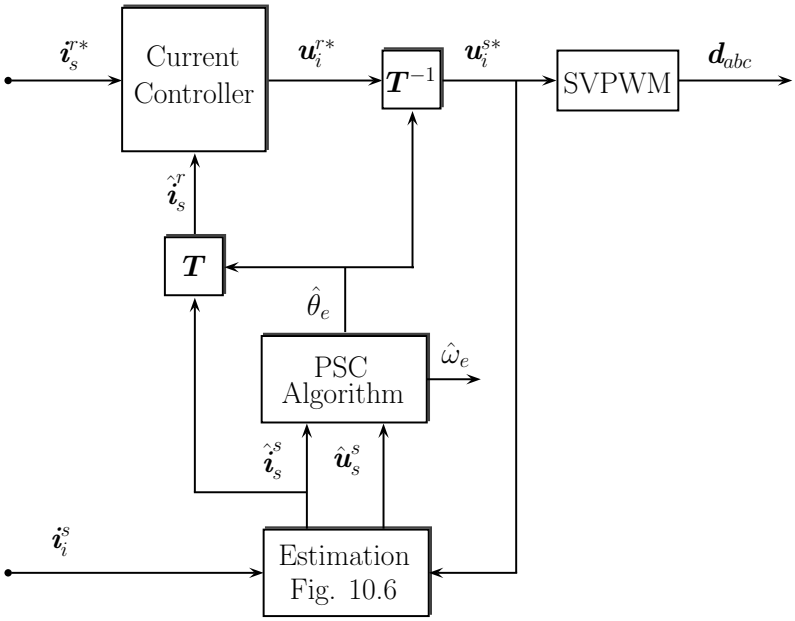

Figure 10.7: Position sensorless controller.

shown in Fig. 10.7. Transformation between reference frames is done with transformation matrices $\boldsymbol{T}$ and $\boldsymbol{T}^{-1}$.

The machine and filter transfer function frequency response in Fig. 10.5 shows that a peak resonance frequency is created by the filter. This peak needs to be above the fundamental frequency but low enough to ensure sinusoidal phase voltages. This resonance peak can be used to design the control parameters for the HFI-PSC method. The injected voltage will be amplified if its frequency is chosen in the vicinity of the resonance frequency allowing the injection voltage magnitude to be reduced. However, if the injection frequency is too close to the resonance frequency, the HF stator voltages and -currents might be dangerously high [68].

As stated by [68] it is advisable to choose the injection frequency just below the resonance frequency to prevent dangerously high stator quantities, but high enough to allow the filter to boost the HF current response. The filter thus aids the HFI-PSC with this methodology instead of damping HF response. The injection frequency for this system is thus chosen at 716 Hz by experimental implementation. The

injection voltage is reduced from 66 V to 33 V by using the LC filter to boost the HF current response.

The FS-PSC method is used to control the generator in the medium to high speed regions as part of the hybrid PSC methodology. This method makes use of lookup tables for position estimation. The FS-PSC lookup tables of machine 5 are generated from FE simulated flux maps. It is found that the performance of the FS-PSC method is unstable if the inverter quantities are used instead of the estimated stator quantities. The derived stator quantities estimation method thus stabilises the FS-PSC method. Also, this method makes use of a load dependent compensation curve to compensate for non-linearities within the machine. It is also found that this curve should be calculated through measurements with the LC filter and the estimated stator quantities for the best performance.

10.5 Measured Results

A laboratory test bench is used to test and evaluate the 9.6 kW RSG drive system. A diagram of the test bench is as shown in Fig. 10.8. Two of the rapid prototyping systems (RPSs) are each connected to a VSD. The one VSD has a 3-phase LC filter connected between its output terminals and the 9.6 kW RSG. The rotor position, θ_m, of the RSG is measured with a rotary encoder and fed back to the RPS. This measured position and speed are however not used in the control of the RSG, but only to determine the quality of the PSC method.

The RSG is connected via a torque sensor (TS) to a 45 kW induction machine (IM) that emulates the turbine and gearbox system. A personal computer (PC) is connected to the TS and is used to measure and record the shaft torque, power and speed. The IM is controlled with a simple open loop V/Hz method. The RPS allows the user to program and implement specific speed and/or torque steps via the IM to the RSG drive system. The DC buses of the two VSDs are connected allowing the power to circulate within the system. The controller parameters, as implemented on the RPS, are shown in Table 10.2.

10.5.1 Evaluation of the LC filter and stator quantities estimation method

High voltage differential probes are used to measure the line-line voltage on both sides of the LC filter to investigate its effectiveness. Rated load is applied by the position sensorless controlled RSG while the IM keeps the frequency fixed at 50 Hz. The results are as shown in Fig. 10.9. It is shown in Fig. 10.9a that the inverter voltage, u_{iab} is rectangular. The rectangular shape is caused by the switching of the semi-conductors. The machine terminal voltage, u_{sab}, is also shown in Fig. 10.9a. This voltage is sinusoidal as a result of the LC inverter output filter. The FFT of the inverter voltage, u_{iab}, is as shown in Fig. 10.9b. It is clear that the inverter voltage is very noisy. The FFT of the stator voltage, u_{sab}, in Fig. 10.9c shows that almost all of the switching harmonics are filtered out by the LC filter and only the fundamental 50 Hz harmonic remains.

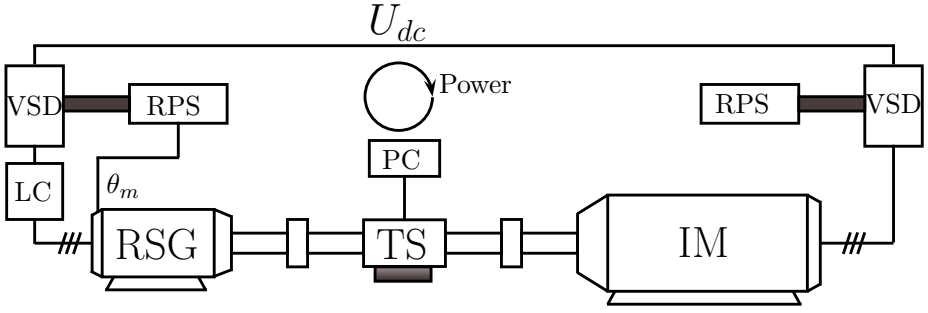

Figure 10.8: Diagram of laboratory setup used to test the RSG drive system.

Table 10.2: Rapid prototype system controller parameters for position sensorless speed controlled machine 5.

HFI			
Current proportional gain	k_p	0.6	V/A
Current time constant	T_i	9.764	ms
PLL proportional gain	k_{pPLL}	40	rad/s
PLL time constant	T_{PLL}	24.41	ms
Current LPF	LPF_i	2441	rad/s
Speed LPF	LPF_s	48.82	rad/s
PLL LPF	LPF_{PLL}	976.4	rad/s
Injection voltage	u_c	33.3	V
Injection frequency	ω_c	4500	rad/s
FS			
Current proportional gain	k_p	3	V/A
Current time constant	T_i	36.615	ms
PLL proportional gain	k_{pPLL}	220	rad/s
PLL time constant	T_{PLL}	24.41	ms
Speed LPF	LPF_s	19.53	rad/s

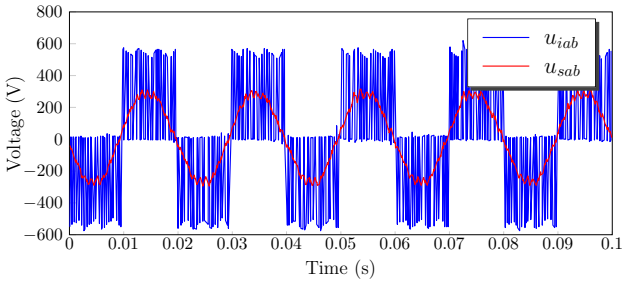

(a) Measured line-line inverter and stator voltage.

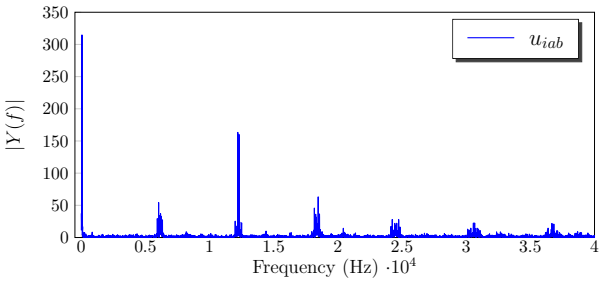

(b) FFT of line-line measured inverter voltage.

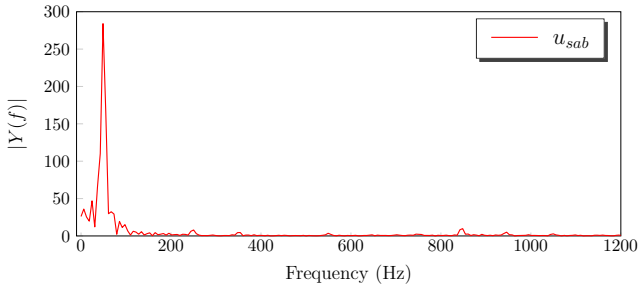

(c) FFT of measured line-line stator voltage.

Figure 10.9: Measured line-line voltage on the inverter and machine side of the LC inverter output filter.

High voltage differential probes are used in a second test to measure the a-phase voltages while generating rated power with the hybrid PSC method. The measured inverter phase voltage, u_{ia}, is shown in Fig. 10.10a. The measured stator phase voltage, u_{sa}, applied to the machine terminals as well as the estimated phase voltage, $\hat{u}_{sa}$, are also shown in Fig. 10.10a. These results show that the phase voltage applied to the machine is sinusoidal due to the LC low pass filter. It is also shown in Fig. 10.10a that the estimation scheme (Fig. 10.6) is successful in estimating the stator phase voltage. There is however a slight phase difference between the measured- and estimated stator voltage. The FFT of the a-phase inverter voltage, as shown in Fig. 10.10b, shows that this voltage signal is very noisy. The FFT of the stator phase voltage and the estimated stator phase voltage correlate well as shown in in Fig. 10.10c where only one distinct

fundamental harmonic is shown.

Finally, a current measuring probe is used to measure the a-phase stator current, i_{sa} while generating rate power. This measured current is shown in Fig. 10.11a as well as the measured inverter current, i_{ia} and the estimated stator current $\hat{i}_{sa}$. Figure 10.11b is a zoomed in window of Fig. 10.11a and shows that the inverter- and stator current differ during the negative peak of the sine wave. It is shown in Fig. 10.11 that the stator quantity estimation scheme (Fig. 10.6) is able to estimate the stator current during the negative peak of the sine wave within a satisfactory degree of accuracy.

The measured results of this section show that sinusoidal voltages are supplied to the terminals of the RSG via the LC filter. It is also shown that the performance of the derived voltage and current estimation method is satisfactory.

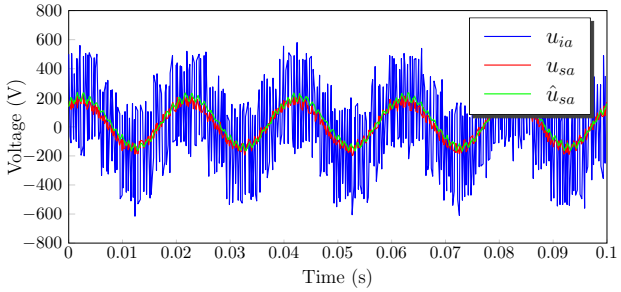

(a) Measured and estimated phase inverter and stator voltages.

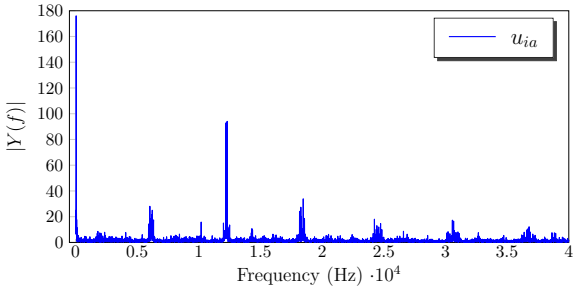

(b) FFT of measured inverter phase voltage.

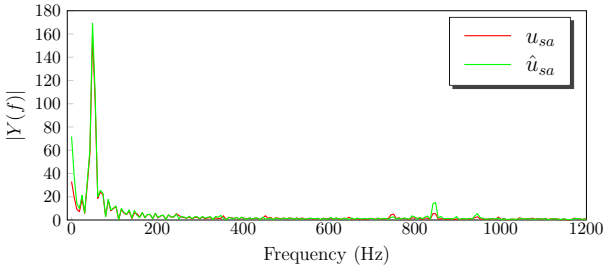

(c) FFT of measured and estimated stator phase voltages.

Figure 10.10: Measured and estimated phase voltage on the inverter and machine side of the LC inverter output filter.

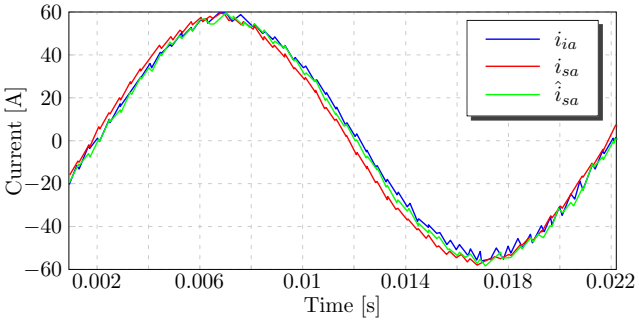

(a) Measured and estimated phase current

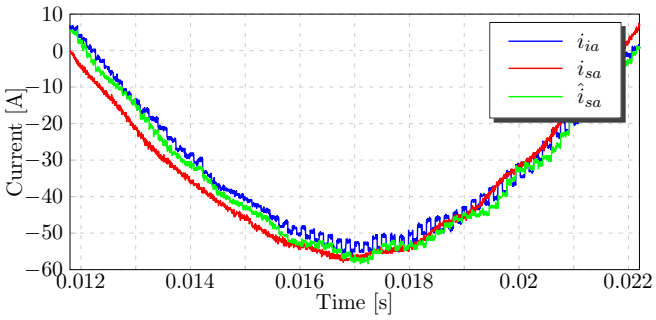

(b) Zoomed in measurement of Fig. 10.11a

Figure 10.11: Measured and estimated phase current at full load.

10.5.2 Torque reference-based maximum power point tracking

The objective of MPPT is to adjust the tip speed of the turbine blades to operate on the maximum power point curve of the turbine as the wind speed varies [136]. The optimal tip speed ratio, λ_{opt}, will maximise the turbine power coefficient, C_p^{max}. The optimal tip speed ratio is constant and defined as in (10.14) [136]. The wind speed is rewritten in (10.15) as a function of the optimal tip speed and tip speed ratio.

$$\lambda_{opt} = \frac{w_{mopt} r_b}{v_w}; \qquad C_p^{max}(\lambda_{opt}) \tag{10.14}$$

$$v_w = \frac{w_{mopt} r_b}{\lambda_{opt}} \tag{10.15}$$

The generator torque is written as in (10.16). Equations, (10.1) and (10.15) can be substituted in (10.16) to calculate the optimum shaft torque as in (10.17) [6,136,169]. K_{opt} is the wind turbine constant. Equation (10.17) can be used in the control structure as the reference torque with the estimated mechanical speed of the generator as in (10.18) [136]. It is thus clear that the wind speed is not needed to implement torque reference-base MPPT.

$$T_m = \frac{P_m}{w_m} \tag{10.16}$$

$$T_{mopt} = K_{opt} w_{mopt}^2 \tag{10.17}$$

$$T_m^* = K_{opt} \hat{\omega}_m^2 \tag{10.18}$$

The maximum torque curve equation can be calculated by determining K_{opt}. Alternatively, the maximum torque curve can be measured as a function of machine speed [169]. An example of such a maximum power- and torque curve, as presented in [6], is shown in Fig 10.12. The reference torque trajectory can be derived mathematically as a function of rotor speed [169,170]. Alternatively lookup tables can be used with an interpolation function to determine the reference generator torque. The relation between the RSM torque and current can be used to calculate the reference current needed to fit the optimal torque curve. Torque reference-based MPPT is thus implemented in this project as in Fig. 10.13.

The optimal torque curves of wind turbines are usually propriety information of the manufacturer. An optimal torque curve is thus created for this project for laboratory testing. Equation (10.19) is the

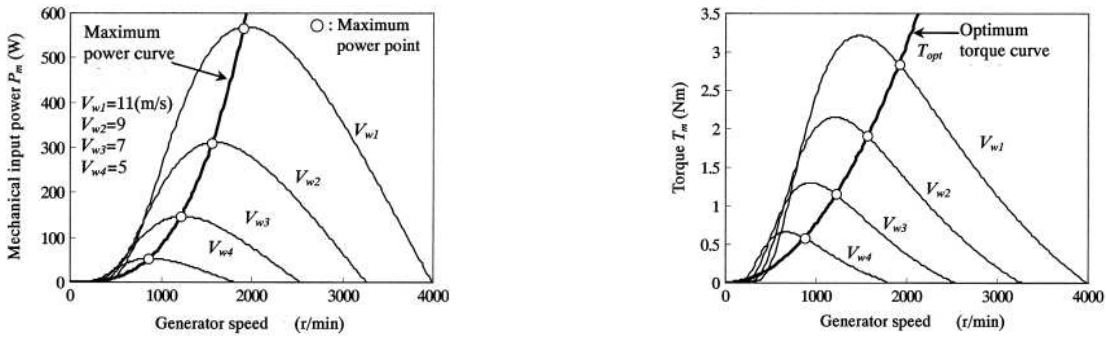

(a) Power versus speed characteristics.

(b) Torque versus speed characteristics.

Figure 10.12: Wind turbine characteristics [6].

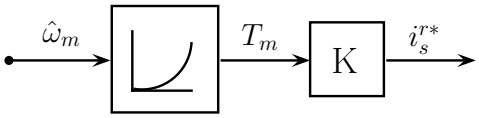

Figure 10.13: Torque reference-based MPPT implementation.

assumed MPPT function used for laboratory testing. This function is derived to allow rated power generation at rated generator speed.

$$\boldsymbol{i}_s^{r*} = \frac{i_{rated}}{\omega_{rated}} * \hat{\omega}_m \tag{10.19}$$

The reference current, as calculated from (10.19), is low pass filtered with a digital low pass filter in the control structure. This ensures that smooth torque is always applied by the generator even during wind spikes

10.5.3 Evaluation of the position sensorless controlled RSG

The next step is to verify the combined effectiveness of the, MPPT, hybrid PSC and stator quantity estimation method. The generator speed and torque is measured and stored during testing with the torque and speed sensor device. The MPPT equation, (10.19), is used offline in MATLAB with the measured speed to calculate reference generator current, $\boldsymbol{i}_s^{r*}$. The calculated reference current is interpolated in MATLAB on the three dimensional torque map of the machine to calculate the MPPT reference torque as shown in (10.20). The three dimensional torque map, as shown in Fig. 10.14, is acquired from the JMAG flux mappings procedure.

$$T_m(FE) = LUT(\boldsymbol{i}_s^{r*}) \tag{10.20}$$

$T_m(FE)$ is thus the MPPT reference torque. The MPPT reference torque is compared to the measured generator torque. Figure 10.15 is a schematic representation of how this procedure is implemented.

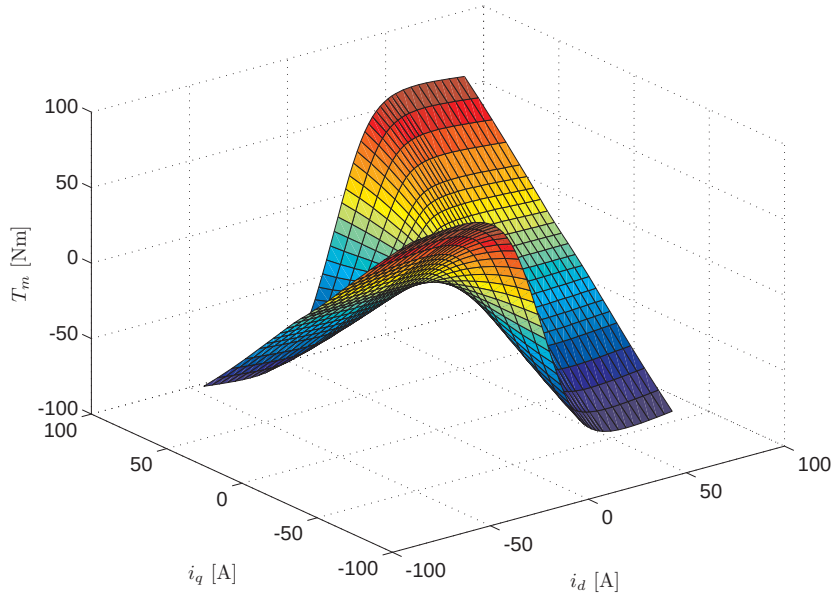

Figure 10.14: 3D torque lookup table of the RSG generated from FE software .

The results of a speed ramp test are shown in Fig. 10.16. In this test the IM ramps its speed up from standstill to rated frequency. The measured speed sensor speed is shown in Fig. 10.16a, the measured torque sensor torque ($T_m(T)$) and MPPT FE torque ($T_m(FE)$) in Fig. 10.16b, and finally the measured shaft power ($P_m(TS)$) and the MPPT FE calculated power ($P_m(FE)$) are shown in Fig. 10.16c. It is clear that the torque and power of the position sensorless controlled RSG drive correlates well with the MPPT torque and -power. In a second test a speed step is applied by the IM from 0.9 $p.u$ to 1.022 $p.u$ as shown in Fig. 10.17. Again the measured results in Fig. 10.17 correlate well with the MPPT reference values.

It is well known that the addition of a LC inverter output filter can damp the dynamic response of the inverter-fed electrical machine. The filter can also affect the machine's PSC performance. The dynamic

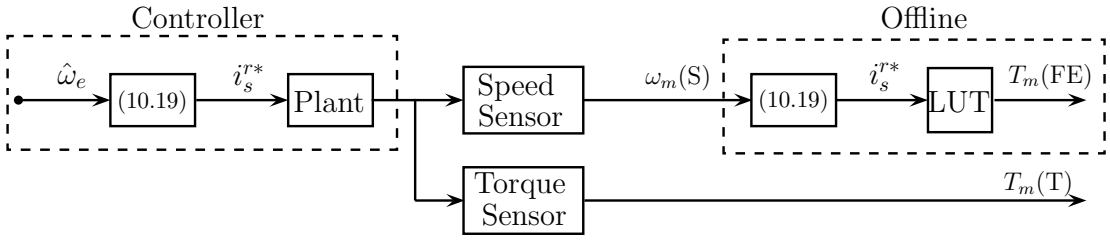

Figure 10.15: Method of comparing measured torque of the RSG with the MPPT reference torque obtained from FE.

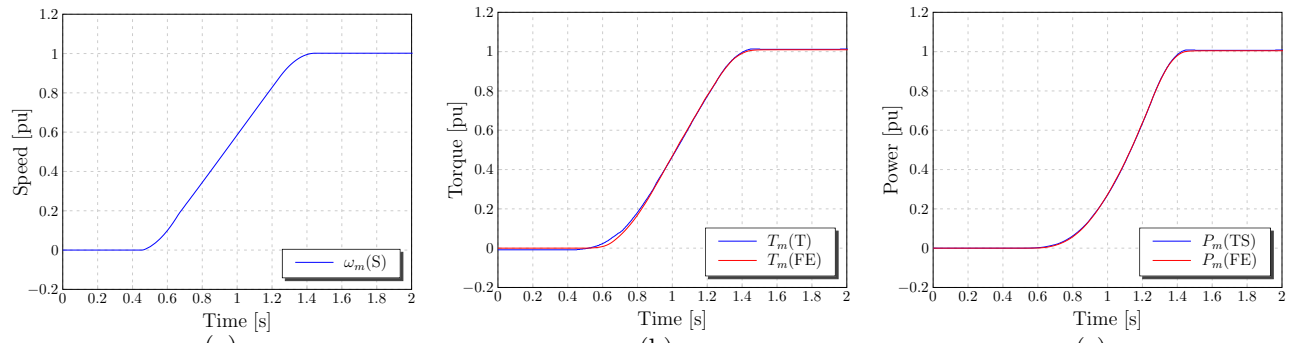

Figure 10.16: Measured speed ramp test of the position sensorless controlled RSG drive.

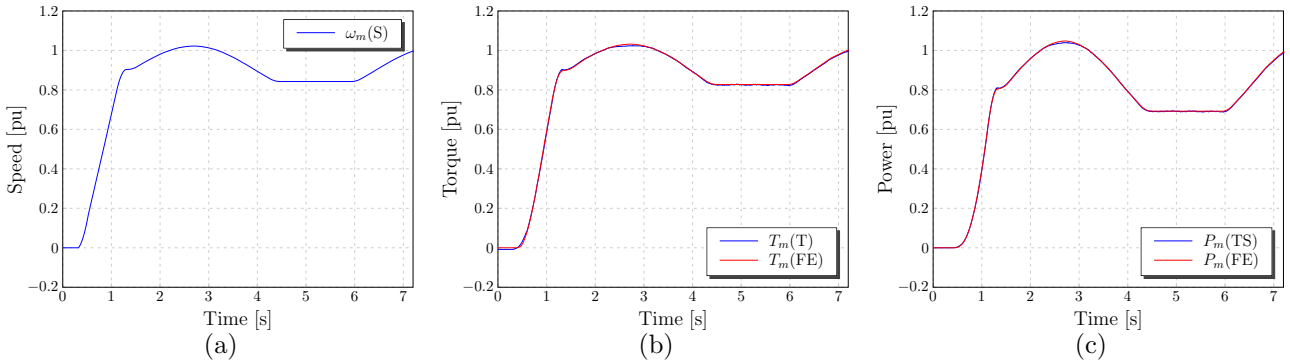

Figure 10.17: Measured speed step in the mid speed region of the position sensorless controlled RSG drive.

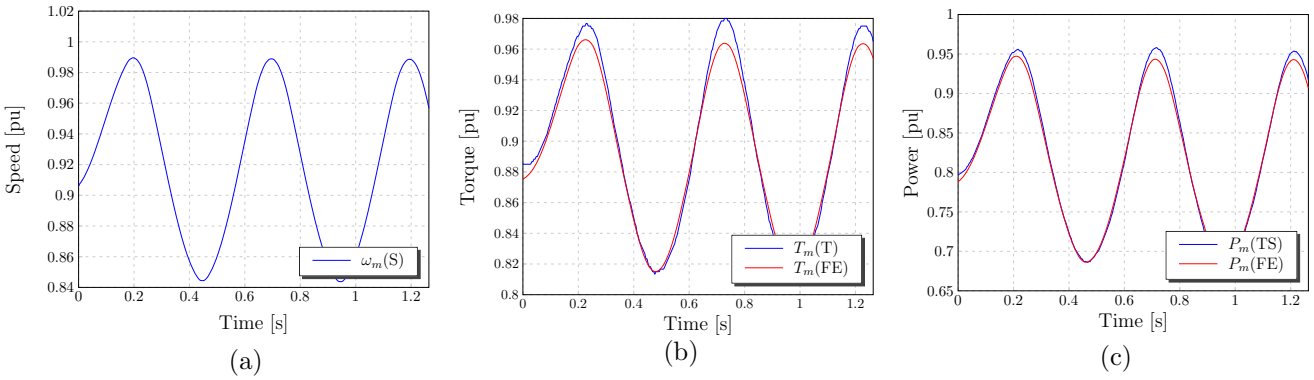

Figure 10.18: Measured dynamic test of the position sensorless controlled RSG drive.

behaviour of the position sensorless controlled RSG with the inverter ouput filter is investigated by varying generator speed sinusoidally with the IM as shown in Fig. 10.18a. The MPPT reference torque should also vary sinusoidally as a function of speed according to (10.19). The machine response at different frequencies and amplitudes is investigated. The results of one of these tests are displayed in Fig. 10.18. The results in Fig. 10.18 show that the HFI assisted hybrid PSC method is able to control the RSG dynamically, even though the conditions are more dynamic than what is expected of a wind generator. It is shown in Fig. 10.18b however, that there are instances where the measured torque ($T_m(T)$) does not correlate with the MPPT torque ($T_m(FE)$). This as result of the digital low pass filter in the control structure, implemented to smooth out the generator torque. The low pass filter of the estimated speed, which is used in (10.19), also affects the MPPT. The dynamic performance, however is still satisfactory.

10.6 Summary

A position sensorless controlled reluctance synchronous generator (RSG) with a LC inverter output filter for high speed wind generators is proposed and evaluated. The proposed generator configuration allows the converter to be stationed in the turbine tower instead of the nacelle. This configuration has weight advantages and possible converter maintenance advantages. It is shown that an estimation scheme is derived to estimate stator quantities to avoid the need for additional sensors on the machine side of the LC filter. The derived estimation method only uses the filter parameters to calculate the stator current and -voltage.

Experimental evaluation shows that the LC filter ensures sinusoidal stator voltages. It is also shown that the derived estimation method is successful in estimating the stator quantities, hence eliminating the need for additional measuring probes.

The high frequency injection (HFI) assisted hybrid position sensorless control (PSC) method is proposed to control the RSG. The arbitrary injection (AI) assisted hybrid PSC method is not considered due to its incompatibility with the LC filter. The injection frequency of the HFI-PSC method is chosen just below the resonance frequency of the filter to boost the HF current response. By carefully choosing the injection frequency it was possible to halve the size of the injection voltage. Care was taken to measure the compensation curve of the fundamental saliency position sensorless control (FS-PSC) method with the LC filter connected.

Laboratory tests show that it is possible to control the RSG position sensorless with a LC inverter output filter and the proposed stator quantity estimation method. Results show good correlation between the reference MPPT torque and the measured torque. Measured results shows good dynamic response of the RSG.

Chapter 11

Position Sensorless Controlled Reluctance Synchronous Machine for a Variable Gear Electric Vehicle Drivetrain

A summary of commercially available electric vehicles (EV's) and selected hybrid electric vehicles (HEVs) is shown in Table B.1 in Appendix B. Most commercially available electric vehicles (EVs) make use of a single induction-(IM) or permanent magnet (PM) machine drivetrain as shown in Table B.1 [171]. The Renault EV models have wound rotor synchronous machines. Some of the older and smaller EV's still use DC machines.

The DC machine consists of a wound rotor with a brush commutator and a stationary field excitation [21, 171]. Excitation in the stator can either be done with coils or PMs. The DC machine is a well established technology and easy to control [172]. DC machines have a low power density and lower efficiency than the three phase machines considered for EV applications [171, 173]. The wound rotor synchronous machine also makes use of brushes for rotor field excitation [21]. The magnetic flux linkage can be regulated allowing this machine to operate in a large constant power speed range without flux weakening [171,174]. Joule losses however, put the efficiency of this machine lower than other synchronous machines without rotor currents [171,175]. One advantage of the IM is its simple method of construction [171]. Torque is induced in this machine by the rotor slip [21]. The IM technology is well developed, inexpensive and reliable. The efficiency of the IM compares to that of the RSM [12, 13]. The IM does however sacrifice efficiency in the extended constant power speed range [171, 172].

PM machines are very attractive for HEV and EV applications due to their high efficiency, good power factor, high torque density and compact design [171, 176, 177]. The surface mounted permanent magnet synchronous machine (SPMSM) is commonly used in HEVs [176]. This machine however, has a very limited constant power speed range [178]. The interior permanent magnet synchronous machine (IPMSM) is favoured for newer generations EV and HEVs [175, 176]. The IPMSM has a higher torque density than the SPMSM and has very good field weakening performance, hence has a large constant power speed range [175,176,178]. The torque ripple and cogging torque of the IPMSM is also lower than that of the SPMSM [178]. A four wheel electric sports car is presented in [175] where four direct drive IPMSMs are used to reach a top speed of 244 km/h.

A small amount of PM material can be added to the RSM to increase its power factor and performance [179]. This is referred to as the PM assisted RSM and this machine has been proposed over the years by a few authors for EV and HEV applications [148, 180–182]. Efficiencies of 90% at 6000 rev/min are reported in [148]. The efficiency of this machine however, drops to 73% at 500 rev/min. A position

sensorless control (PSC) method is proposed in [183] for PM assisted RSMs for automotive applications. Both the alternating high frequency injection (HFI) and the rotating HFI-PSC method are used in [183], no measured full load tests are however presented.

Research done by the authors of [171] indicate that a shift to EVs and HEVs by industrialised countries can lead to a shortage and price increase of rare earth PM material. Research in PM-less EV drives thus makes sense. Two PM-less machines are presented in [184] as alternatives to IPMSM of the hybrid Toyota Prius namely an IM and a switched reluctance machine (SRM). Neither machine could really compete with the efficiency of the IPMSM, especially in the field weakening region where the iron losses of the SRM climbed to more than 13 times the size of the copper losses. It is shown in [184] however, that the material cost of the IM and SRM are much less than that of the IPMSM. Another PM-less motor is proposed in [122] for a parallel HEV application namely the RSM. Very good measured performance and acceleration results are reported in [122].

It is not yet clear if completely position sensorless EV and HEV drives will be adopted by the industry. At the very least, PSC methods will be used as backup with a position sensor [185]. Fault detection methods can be implemented to detect position sensor faults and activate PSC. One such method is presented in [185] where an extended back emf method is used with a HFI-PSC method to control an IPMSM intended for a HEV application. A similar hybrid PSC method for EV's and HEV's is presented in [186,187]. These methods use a HFI-PSC method at low speeds and standstill with a back EMF method at minimum to high speed to control an IPMSM position sensorless. A PWM injection, saliency-based PSC (SB-PSC) method, is proposed in [188] for an IPMSM intended for EV applications. This method is tested and evaluated on a Nissan Prairie. Direct torque control is also investigated by some authors for EV and HEV control due to its inherent position sensorless capabilities [189, 190].

11.1 The EV Drivetrain

The drivetrain configuration of conventional EVs is different to that of the internal combustion engine vehicle. A typical internal combustion vehicle drivetrain is as shown in Fig. 11.1 [172]. This is also known as a variable gear (VG) drivetrain. The torque characteristics of the internal combustion engine and the electric motor are not the same, hence the drivetrains of commercially available EV's are different to the one shown in Fig. 11.1.

The most common EV drivetrain replaces the variable gear differential gearbox with a single differential gear as shown in Fig. 11.2a. This is referred to as the transmission-less or fixed gear (FG) drivetrain [172]. Another popular EV drivetrain is known as the direct drive. One or two motors are connected directly to the front or back wheels of the vehicle without a differential gear. This drivetrain topology is shown in Fig. 11.2b. The electric sports car presented in [175] has 4 direct drive motors.

The final two drivetrain configurations are the in-wheel configurations. The first in-wheel configuration, as shown in Fig. 11.2c, has a single reduction gear and the second, as shown in Fig. 11.2d, is an in-wheel direct drive configuration.

Variable gear drivetrain

A simulation package is used in [1] with a generic model of a 40 kW electric motor to simulate three different types of drivetrains. The investigated drivetrains are a direct drive-, a four speed VG- and a

Figure 11.1: Internal combustion engine vehicle drivetrain.

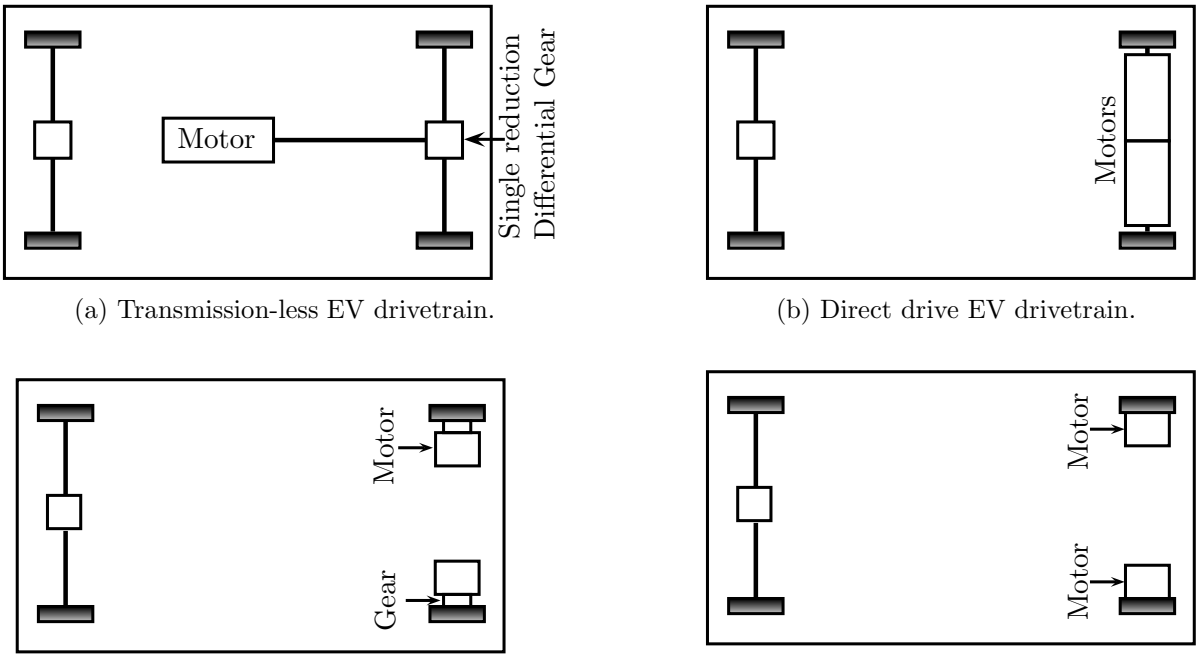

(a) Transmission-less EV drivetrain.

(b) Direct drive EV drivetrain.

(c) In-wheel direct drive EV drivetrain with single reduction gear.

(d) In-wheel direct drive EV drivetrain.

Figure 11.2: EV drivetrains.

continuously VG drivetrain which is a fictional gearbox with an infinite number of gears. Simulations results in [1] show that a VG drivetrain allows the electric motor to operate on a nominal line of maximum efficiency.

Six different drive cycles are used in [1] to simulate the motor efficiency with the three investigated drivetrains. The simulation results are summarised in Table 11.1 [1]. It is shown in Table 11.1 that an energy consumption improvement is possible with a 4 speed gearbox. Similar results are also presented in [191]. It is possible however, that the gain in efficiency will be cancelled out by the losses in the gearbox.

There are various advantages associated with a VG EV drivetrain:

1. Higher motor efficiency [1, 191–193]. A VG drivetrain allows the motor to operate on a nominal line of maximum efficiency as stated above.

2. Increased acceleration [1, 194]. It is shown in [1] that a vehicle acceleration from 0-100 km/h is

Table 11.1: Simulated improvement of energy consumption of a generic EV motor over 6 different drive cycles [1].

Drive cycle	Single gear	4 Speed gearbox		Continuously variable gearbox	
	kWh/100km	kWh/100km	Improvement %	kWh/100km	Improvement %
Europe NEDC	8.33	7.96	4.5	7.89	5.3
Europe City	6.87	6.22	9.7	6.12	11.0
USA FTP-75	8.45	7.77	8.0	7.53	10.9
USA City I	9.06	8.43	7.0	8.19	9.6
Japan 11 mode	6.93	6.61	4.6	6.55	5.4
Japan 10 mode	7.20	6.41	11.0	6.31	12.4

reduced by 5.9 s with a two speed VG gearbox drivetrain as opposed to a FG drivetrain.

3. Less torque is required from the electric machine thus opening up the possibility of a downsized motor [1, 194].

4. Field weakening performance is not required. Machines with inadequate field weakening performance for FG EV drivetrains can thus be considered.

5. Increased pull-away torque [194]. A VG gearbox can increase the road gradient at which an EV can ascend. It is shown in [194] that the gradient at which an EV can pull away from standstill is increased by 11.9° when the same motor is used with a 2 speed VG drivetrain instead of a FG drivetrain.

6. Increased regenerative energy during braking is also possible [191].

11.2 Proposed Variable Gear Electric Vehicle

It is shown in [195] that RSMs with high L_d/L_q ratios, like the axial laminated RSM, have good constant power speed range performance. RSMs with lower L_d/L_q ratios, as with the transverse laminated RSM however, have limited constant power speed range performance [18]. Constant power speed range performance is not as critical with a VG EV drivetrain allowing the transverse laminated RSM to be a viable option for EV applications.

The transverse laminated RSM is proposed for a VG EV drivetrain as shown in Fig. 11.3. Some information regarding the machine is provided even though the analysis and design are not within the scope of this thesis. An Opel Corsa is converted to an electric vehicle as part of an ongoing EV project at the University of Stellenbosch. A photo of the converted Corsa is shown in Fig. 11.4. The specifications of the RSM are thus modelled on the internal combustion engine of the Opel Corsa. The internal combustion engine of the Opel Corsa delivers 35 kW at 4800 rev/min in fifth gear with a wheel speed of 120 km/h. The peak power of the internal combustion engine of the Opel Corsa is 55.3 kW at 4800 rev/min.

Three RSM designs are considered for the Opel Corsa conversion project namely machines 6,7 and 8 as shown in Fig. 3.9. Machine 7 is chosen for the EV drive. The process of the design optimisation and performance evaluation of this machine is discussed in [123]. The EV machine and drive parameters are listed in Table 11.2. In this chapter the possibility of controlling the EV RSM without a position sensor is investigated. Limited literature exists regarding PSC of EV's. It is this author's belief that this will change as EV's become even more important. The two hybrid PSC methods developed in this thesis thus far are to be evaluated with the proposed RSM VG EV drive.

Pull-away torque is critical in EV applications especially with a FG EV drivetrain. Pull-away torque is even more critical at larger road gradients. SB-PSC methods are generally used at standstill and low speeds for PSC of synchronous machines. It is shown in previous chapters that the performance of the SB-PSC methods are limited when the machine is loaded due to the disappearing inductance saliency at flux linkage saturation. The pull-away torque required from an electric motor in a VG EV drivetrain is less than what is required from an electric motor with a FG EV drivetrain. The aim is to deliver rated continuous startup torque position sensorless even though it is possible that rated continuous torque will not be a requirement at startup with the VG drivetrain setup.

Figure 11.3: Proposed RSM VG EV drivetrain.

Figure 11.4: Converted EV Opel Corsa.

Table 11.2: RSM EV drive parameters.

Machine Parameters	
Stator resistance R_s	0.28 Ω
Direct-axis inductance L_d	1.97 mH
Quadrature-axis inductance L_q	0.304 mH
Pole pairs N_p	2
Rated speed	4800 rev/min
Continues current (rms)	140 A
Continues torque	69.63 Nm
Continues power	35 kW
Peak current (rms)	212 A
Peak torque	110 Nm
Peak power	55.3 kW
Constant current angle ϕ	67^o
Continues saliency ratio γ	0.54
Continues saliency shift ζ	19.75^o
Drive Parameters	
Switching frequency F_s	6.1 kHz
Sampling frequency f_s	12.2 kHz
DC bus battery voltage u_{dc}	337.5 V
Battery power	40.5 kW

Another interesting aspect that is investigated in this chapter is the effect of the low battery voltage on the performance of the two SB-PSC methods. HF voltage excitation is used by both methods to exploit the inductance saliency for PSC. The DC bus voltage limit will thus be reached easily if the injection voltage and machine speed is too large when the machine is loaded. The fundamental saliency position sensorless control (FS-PSC) method is still fairly new, hence no evaluation of this method exists at speeds above 1500 rev/min. It is shown in [3] and in Chapter 8 that the position estimation error of the FS-PSC method has frequency components which relate to the rotor frequency. Even though no problems are predicted it is still important to evaluate this method at 160 Hz which is the fundamental frequency of the proposed EV RSM.

11.3 Simulation

Simulink is used to design and verify the control parameters of machine 7. It is also used to verify that stable PSC is possible with the proposed RSM. Three dimensional flux maps are created of machine 7 with a Python script and the JMAG FE package. These flux maps are used in the Simulink package for simulations as described in Chapter 3. The FS-PSC lookup table is also derived from the flux maps of

machine 7.

11.3.1 HFI-PSC

Current control of machine 7 is simulated with the HFI-PSC method. The simulation machine control parameters are listed in Table 11.3. It is shown in Table 11.3 that the DC bus voltage is limited in the simulation environment to that of the battery voltage of the Corsa.

Initial design and simulations of the HFI-PSC method proved challenging. More light was shed on the problem by analysing the frequency spectrum of the q-axis current, which is used in the demodulation process. It was found through simulations that the fundamental DC harmonic is 1518 times larger than the HF carrier harmonic, preventing successful spectral separation. This is due to the larger current rating of machine 7. This could explain why this problem was not picked up with the smaller evaluated RSMs. Also, the larger maximum torque per ampere current angle of machine 7 contributes even further towards the amplitude of the fundamental q-axis current harmonic. The HFI-PSC method is simplified by omitting the band pass filter (BPF) in the demodulation scheme as explained in Chapter 4. The BPF will be beneficial in this case to remove the fundamental q-axis current harmonic.

A simple solution is derived to decouple the fundamental q-axis current harmonic. It is shown in Fig. 11.5 that the HFI-PSC method has conventional low pass filters (LPFs) in the current feedback loop. The low pass filtered q-axis current should thus only consist of a fundamental DC component. This low pass filtered current is simply subtracted from the unfiltered q-axis current in the demodulation scheme to remove the fundamental component as shown in red in Fig. 11.5. This is, in effect, a band stop filter. The advantages of the simplified HFI-PSC method is thus retained as no additional filters are added to the control or demodulation scheme. Simulation results reveal that the ratio of fundamental- to HF current component is reduced to 125.

Proper spectral separation is achieved with the modified fundamental current harmonic decoupling demodulation process. A rated current and torque step is applied in simulation as shown in Figs. 11.6a and 11.6c. The position estimation error is satisfactorily small at steady state as shown in Fig. 11.6b. The PLL stays synchronised even when large position estimation errors occur during the transient current step. The effect of the momentarily large position estimation error also reflects in the estimated machine speed as shown in Fig. 11.6d. The machine speed is ramped up to the minimum necessary operating speed, after rated current is applied. The applied voltage does not exceed the limit of the DC bus in the simulation, hence control is stable. It is shown in Fig. 11.6 that the machine current is not zero before the current step to ensure that the q-axis flux linkage saturates for SB-PSC, as with machine 1.

The HFI position estimation error curve, as a function of current, is extracted from Simulink by simulating the position estimation error at different current setpoints as shown in Fig. 11.7a. This is of course partially influenced by the saliency shift of the machine. It is interesting to note the resemblance

Table 11.3: HFI-PSC: Simulation controller parameters for position sensorless speed controlled machine 7.

Current proportional gain	k_p	6.283	V/A
Current time constant	T_i	0.1	ms
PLL proportional gain	k_{pPLL}	20	rad/s
PLL time constant	T_{PLL}	0.7	ms
Current LPF	LPF_i	1000	rad/s
PLL LPF	LPF_{PLL}	500	rad/s
Injection voltage	u_c	60	V
Injection frequency	ω_c	6 x 10^3	rad/s
DC bus voltage	U_{dc}	337.5	V

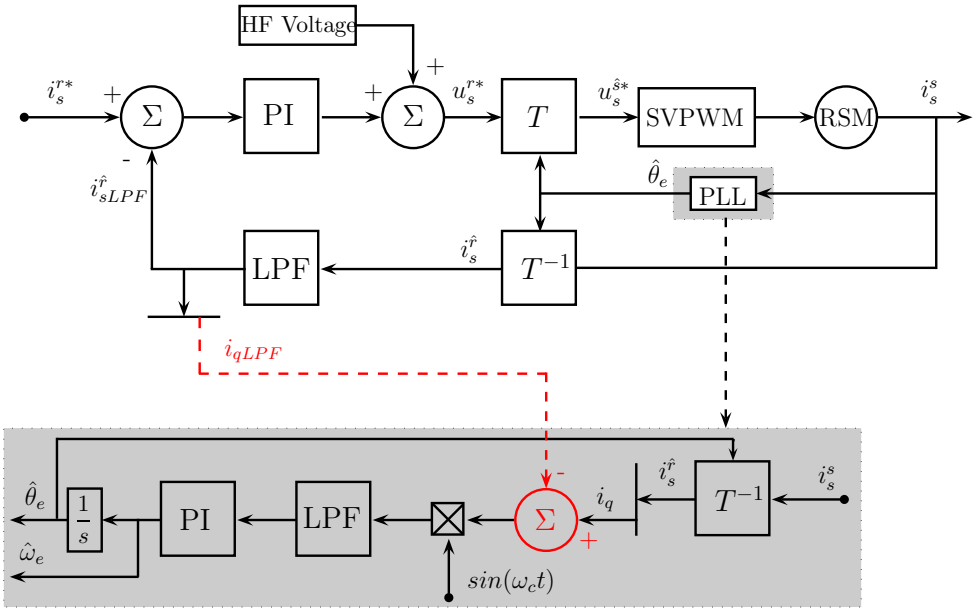

Figure 11.5: Modified HFI-PSC scheme with fundamental current harmonic decoupling.

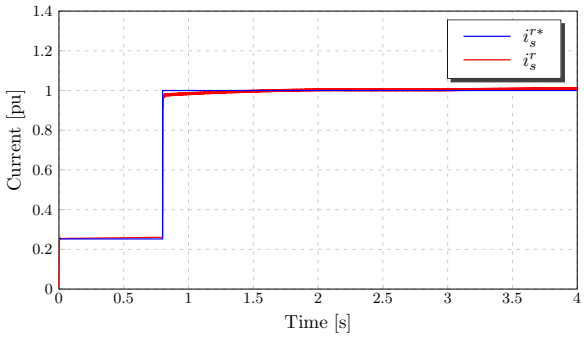

(a) Reference- and machine current.

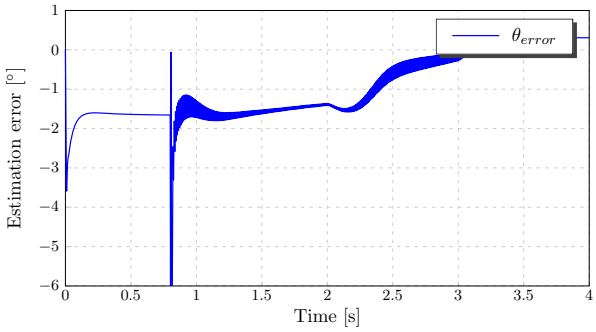

(b) Position estimation error.

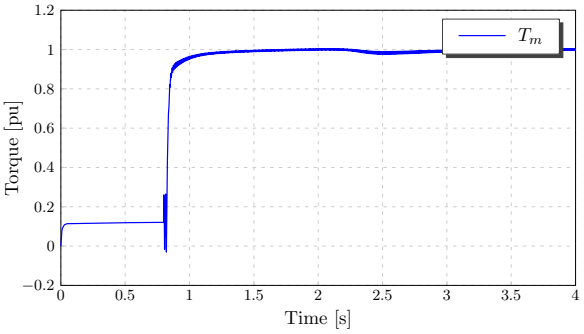

(c) Mechanical torque.

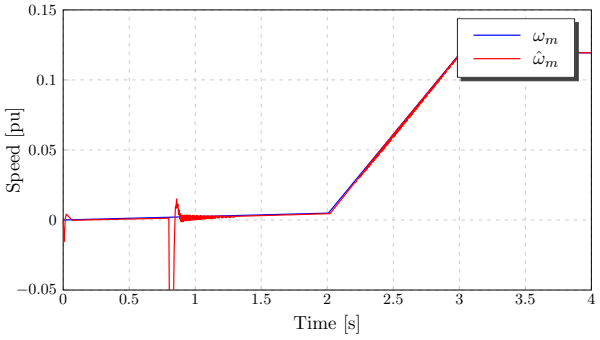

(d) Simulated- and estimated speed.

Figure 11.6: HFI-PSC: Simulated rated current step.

in shape of the position estimation error and the FE simulated mutual inductance in Fig. 11.7b. This correlation makes sense as it is shown in (9.10) that the saliency shift is caused by the mutual inductance term. Both graphs change gradient signs at ± 0.6 $p.u$ current. This observation again highlights the influence of the machine geometry on the SB-PSC capability of RSMs.

The simulation results of this subsection show that it is possible for the RSM to deliver rated continuous

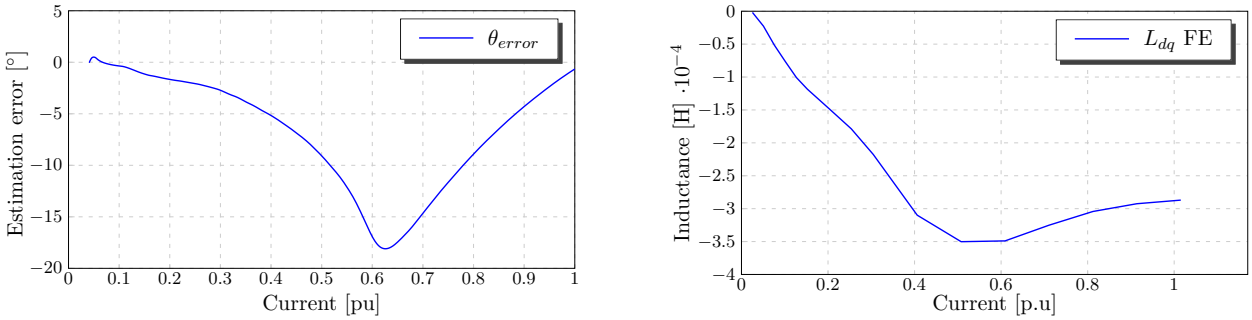

(a) Simulated position estimation error.

(b) Simulated mutual inductance.

Figure 11.7: HFI-PSC: Simulated mutual inductance and position estimation error.

torque at standstill and low speeds with the HFI-PSC method if proper spectral separation is secured by decoupling of the fundamental current component.

11.3.2 AI-PSC

The next SB-PSC method to be evaluated in the simulation environment is the arbitrary injection position sensorless control (AI-PSC) method. The simulation machine control parameters are listed in Table 11.4. Again the DC bus voltage is limited to that of the EV battery package voltage. It is found that the AI-PSC method is not as dynamic in the simulation environment as the HFI-PSC method. The machine response is still however satisfactory.

A 300 ms current ramp command from almost zero- to rated current is applied to the RSM while in current control. The simulation results of the current ramp are shown in Fig. 11.8. It is shown in Fig. 11.8a that the reference current is tracked quite accurately without any overshoot. A small amount of current is in the machine before the current ramp is applied, as with the HFI-PSC simulations, to saturate the q-axis flux linkage for SB-PSC. The accurate current control reflects in the simulated torque results of Fig. 11.8c. It is shown in Fig. 11.8b that the position estimation deteriorates as a function of speed. This is due to a combination of the high inductance saliency of the RSM and the assumptions made in the derivation of the AI-PSC method at high rotor speeds, as described in Chapter 5. Creating a compensation curve for the position estimation error however, is still possible.

The simulation results of this subsection show that it is possible to deliver rated torque at standstill and in the low speed region with the EV RSM when controlled with the AI-PSC method.

11.3.3 FS-PSC

Finally the FS-PSC method is evaluated in the simulation environment. The simulation control parameters are listed in Table 11.5. The DC bus voltage is limited to that of the battery pack voltage as with

Table 11.4: AI-PSC: Simulation controller parameters for position sensorless speed controlled machine 7.

Current proportional gain	k_p	6.28	V/A
Current time constant	T_i	10	ms
PLL proportional gain	k_{pPLL}	0.8	rad/s
PLL time constant	T_{PLL}	0.492	ms
Current LPF	LPF_i	500	rad/s
Injection voltage	u_{inj}	30	V
DC bus voltage	U_{dc}	337.5	V

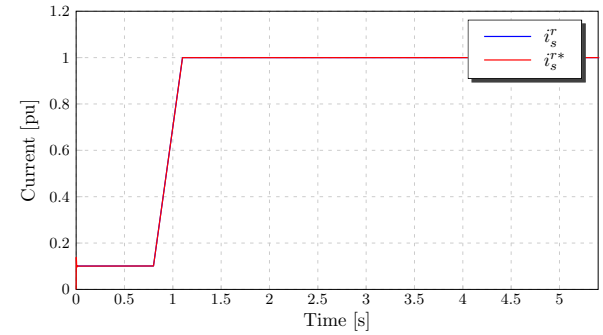

(a) Reference- and machine current.

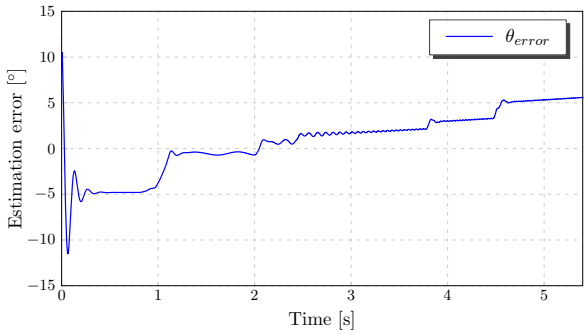

(b) Position estimation error.

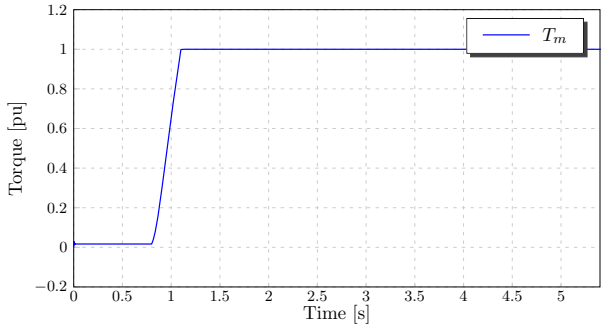

(c) Mechanical torque.

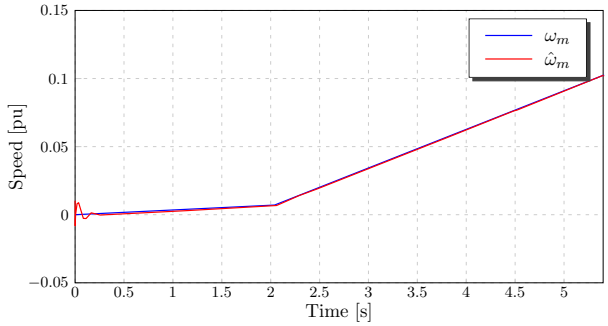

(d) Simulated and estimated speed.

Figure 11.8: AI-PSC: Simulated rated current ramp.

the previous two simulations. A rated current step is applied by the position sensorless controlled RSM in Fig. 11.9 while the speed is ramped up. The position estimation error in Fig. 11.9b shows that the FS-PSC method is unstable in the low speed region, as expected. The FS-PSC method is stable in the high speed region however, and it is possible to control the RSM under full load at rated speed, even with the low DC bus voltage.

The simulation results of this subsection suggest that there should be no concern regarding the effectiveness of the FS-PSC method at the high rated speed of the EV RSM, even at full load.

11.4 Measured Results

Testing and evaluation of the position sensorless controlled EV RSM are confined to the laboratory environment. The laboratory setup is as shown in Fig. 11.10. It is shown in Fig. 11.10 that the VG gearbox is not used in the test platform. Measured efficiency results of the evaluated EV RSM with the VG drivetrain are shown in [123] however. Two identical EV RSMs are connected via a torque sensor. Each RSM is controlled with a variable speed drive (VSD) and a rapid prototyping system (RPS). The DC buses of the two VSDs are connected allowing power to circulate. Unfortunately, there are certain

Table 11.5: FS-PSC: Simulation controller parameters for position sensorless speed controlled machine 7.

Current proportional gain	k_p	4.723	V/A
Current time constant	T_i	7.37	ms
PLL proportional gain	k_{pPLL}	5	rad/s
PLL time constant	T_{PLL}	2.86	ms
DC bus voltage	U_{dc}	337.5	V

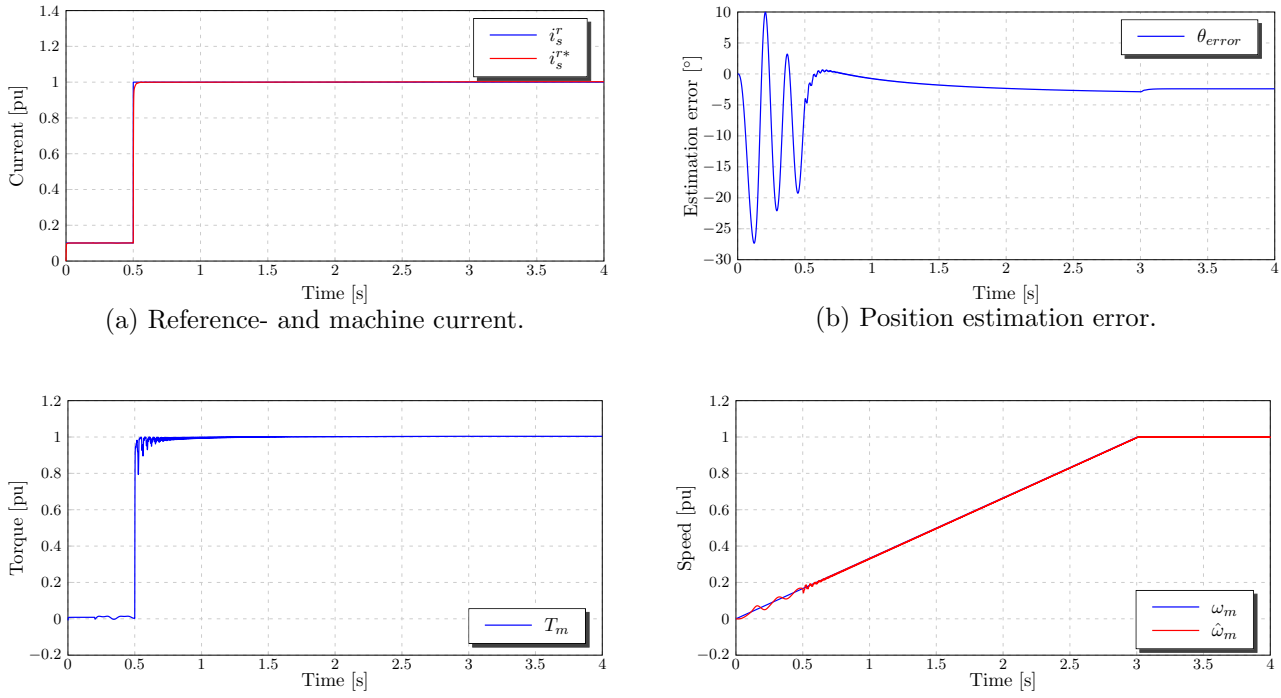

(a) Reference- and machine current.

(b) Position estimation error.

(c) Mechanical torque.

(d) Simulated and estimated speed.

Figure 11.9: FS-PSC: Simulated rated current step.

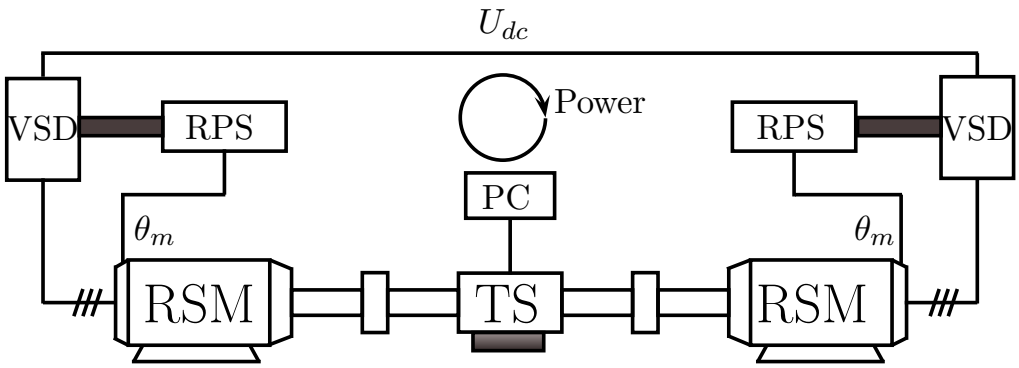

Figure 11.10: Diagram of laboratory setup used to test the EV drive system.

constraints to this test environment. A list of these constraints follow:

1. The rated current of each VSD is limited to 73 A. The continuous current rating of the RSM is 140 A, thus full load tests are not possible. It is shown thus far in this thesis that the simulation environment can be used quite accurately to investigate PSC methods and their performance on RSMs. Measured results at 73 A can thus be used with the simulation results to show the PSC capabilities of the evaluated RSM. Very valuable investigations are performed in the next chapter to investigate the PSC startup torque capabilities of a traction RSM, thus filling the gap left by the test bench constraints in this chapter.

2. The mechanical constraints of this test bench do not allow a load test at rated speed. The high speeds of the evaluated RSM introduced troublesome mechanical vibrations. Some recommendations are made in the final chapter regarding this problem. Load tests are limited to the low speed region in this thesis. No-load tests are however performed at rated speed.

The supply voltage of the VSDs is 400 V L-L. The available DC bus voltage is thus higher than that of the Corsa battery pack. The magnitude of the reference voltage is however limited in the control algorithm, to only use 337.5 V of the available DC bus voltage. This is accomplished by limiting the reference voltage as to not exceed the relation in (11.1). The maximum phase voltage that can be applied with the space vector modulation method is 57.5% of the DC bus voltage [196].

$$\sqrt{((u_d^*)^2 + (u_q^*)^2)} \leq 0.866 * 337.5 \tag{11.1}$$

11.4.1 HFI-PSC

The control parameters as implemented on the RPS are listed in Table 11.6. The machine speed is kept constant at 0.13 $p.u$ by one of the speed controlled RSMs. Load is applied by the second position sensorless controlled RSM by controlling its current. The HFI-PSC method is implemented and evaluated on the current controlled RSM. The current of the position sensorless controlled RSM is limited to 70 A, although the maximum current rating of the VSD drive is 73 A. This current limitation allows the speed controlled RSM to keep the speed fixed at 0.13 $p.u$ even when load is applied.

The current is ramped up in the current controlled RSM as seen in the measured torque in Fig. 11.11a. The torque is ramped up slowly to comply with the mechanical and electrical constraints of the test bench and to ensure that the speed is kept constant by the speed controlled RSM. Two measurements are made, one with an encoder (SC) and one with the HFI-PSC method (PSC). It is shown in Fig. 11.11a that the torque of the position sensorless controlled RSM correlates well with that of the RSM when controlled with an encoder. The reference- and measured current of the position sensorless controlled RSM, during the current ramp, are shown in Fig. 11.11b. The measured current vector is transformed to the rotary reference frame with the measured electrical angle instead of the estimated electrical angle. This current vector is not however used in the control structure. It is shown in Fig. 11.11b that the reference current is tracked satisfactorily. The position estimation error is satisfactory small as shown in Fig. 11.11b.

The next test is a locked rotor test. Again it is shown in Fig. 11.12a that the torque delivered by the position sensorless controlled RSM (PSC) correlates well with that of the RSM when controlled with an encoder (SC). Finally a position sensorless controlled speed reversal test with a cascaded speed controller at no load is implemented. It is shown in Fig. 11.12b, in blue, that a positive speed step is applied by the RSM followed by a negative speed step. The reference current is shown in Fig. 11.12b in red. Very small position estimation errors occur even during transient steps as shown in Fig. 11.12b

It is shown in this subsection that the EV RSM performs well with the HFI-PSC method with good torque capabilities.

Table 11.6: HFI-PSC: RPS controller parameters for position sensorless speed controlled machine 7.

Current proportional gain	k_p	1.5708	V/A
Current time constant	T_i	0.1	ms
PLL proportional gain	k_{pPLL}	60	rad/s
PLL time constant	T_{PLL}	0.7	ms
Current LPF	LPF_i	1000	rad/s
PLL LPF	LPF_{PLL}	500	rad/s
Injection voltage	u_c	66	V
Injection frequency	ω_c	6 x 10^3	rad/s
DC bus voltage	U_{dc}	337.5	V

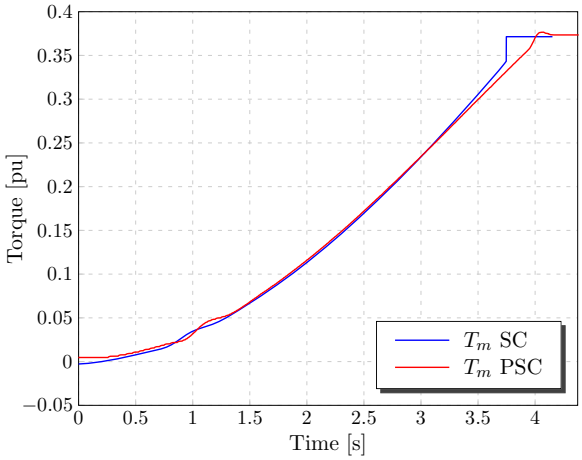

(a) Measured torque.

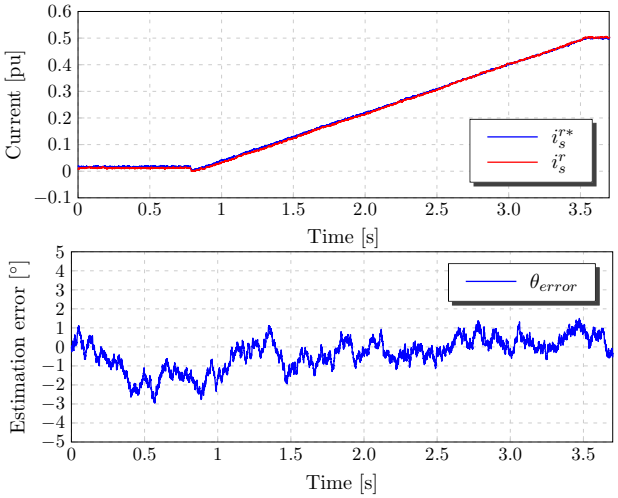

(b) Reference-, measured current and position estimation error of position sensorless controlled RSM.

Figure 11.11: HFI-PSC: Measured results of a current ramp at a constant speed of 0.13 *p.u.*

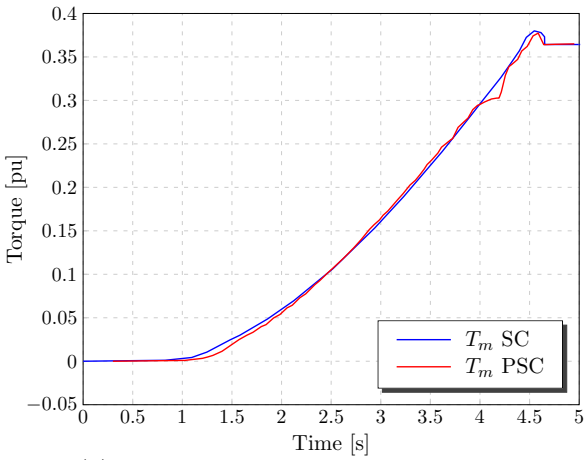

(a) Measured locked rotor torque.

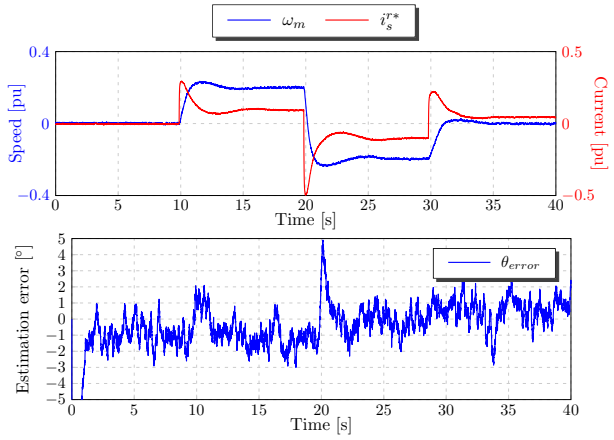

(b) Measured speed, reference current and position estimation error of the speed reversal test.

Figure 11.12: HFI-PSC: Measured results.

11.4.2 AI-PSC

The next SB-PSC method evaluated in the laboratory environment is the AI-PSC method. The control parameters as implemented on the RPS are listed in Table 11.7. The current of the RSM is ramped up to 70 A while the speed is kept steady at 0.13 *p.u* by the speed controlled RSM. The measured torque delivered by the RSM when controlled with an encoder (SC) and with the AI-PSC method (PSC) are compared in Fig. 11.13a. Again the torque of the position sensorless controlled RSM compares well with that of the of the torque delivered by the RSM when controlled with a position sensor. The reference- and measured current of the position sensorless controlled RSM during the current ramp are shown in Fig. 11.13b. The reference current is tracked well by the current controller. It is also shown in Fig. 11.13b that the position estimation error is satisfactorily small.

The results of the locked rotor test are shown in Fig. 11.14a. The torque delivered by the RSM, when controlled with the AI-PSC method (PSC), compares well with that of the RSM when controlled with

an encoder as shown in Fig. 11.14a. Finally a position sensorless controlled speed reversal test with a cascaded speed controller at no load is implemented. A positive speed step is followed by a negative speed step as shown in blue in Fig. 11.14b. The reference current is shown in red in Fig. 11.14b. The measured position estimation error is satisfactorily small even during transients as shown in Fig. 11.14b.

Table 11.7: AI-PSC: RPS controller parameters for position sensorless speed controlled machine 7.

Current proportional gain	k_p	1.5708	V/A
Current time constant	T_i	10	ms
PLL proportional gain	k_{pPLL}	0.8	rad/s
PLL time constant	T_{PLL}	0.255	ms
Current LPF	LPF_i	550	rad/s
Injection voltage	u_{inj}	30	V
DC bus voltage	U_{dc}	337.5	V

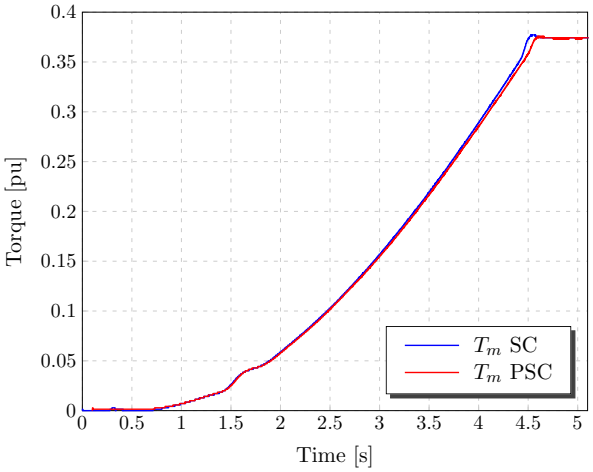

(a) Measured torque.

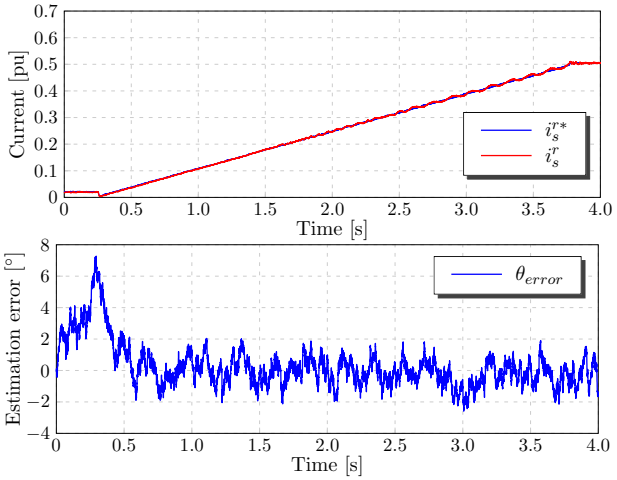

(b) Reference-, measured current and position estimation error of position sensorless controlled RSM.

Figure 11.13: AI-PSC: Measured results of a current ramp at a constant speed of 0.13 $p.u.$

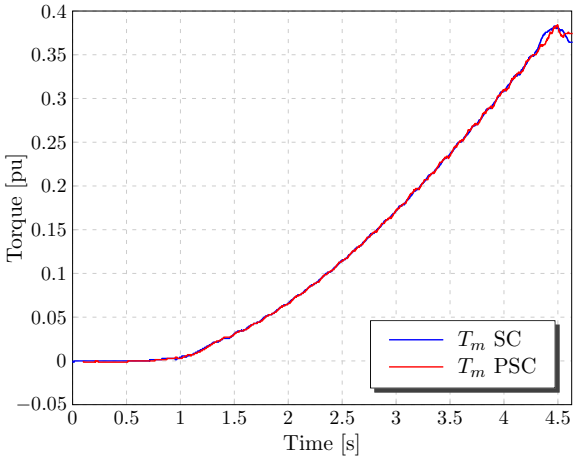

(a) Measured locked rotor torque.

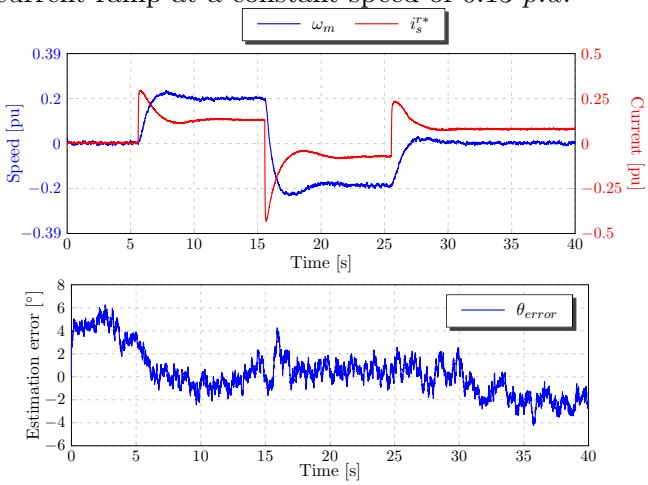

(b) Measured speed, reference current and position estimation error of the speed reversal test.

Figure 11.14: AI-PSC: Measured results.

It is shown in this subsection that the EV RSM has good torque capabilities when controlled with the AI-PSC method.

11.4.3 FS-PSC

The final stand alone PSC method evaluated in the laboratory environment is the FS-PSC method. The RPS controller parameters are listed in Table 11.8. Measured steady state torque results at a constant speed of 0.28 $p.u$ are shown in Fig. 11.15a. The two torque measurements of the RSM with an encoder (SC) and with the FS-PSC (PSC) method compare well. The steady state measured- and estimated speeds of the position sensorless controlled RSM, of the test performed in Fig. 11.15a, are shown in Fig. 11.15b. The corresponding position estimation error is also shown in Fig. 11.15b. There are some dominant speed related oscillations present in θ_{error}, as expected. The average position estimation error however, is $\pm 0°$.

Finally a no load test is performed at the rated speed of the RSM with the FS-PSC method. The results of this test are shown in Fig. 11.16. The estimated- and the measured speeds are a very close match, as shown in Fig. 11.16a. The position estimation error, shown in Fig. 11.16b is satisfactorily small. It is thus shown in this subsection that accurate position sensorless control of the EV RSM is possible with the FS-PSC method. It is also shown that the method is able to estimate the electrical angle of the machine at the high rated speed of the EV RSM.

11.4.4 HFI assisted hybrid PSC method.

The first of two evaluated hybrid PSC methods is the HFI assisted hybrid PSC method. Load tests of the stand alone methods have already been investigated, hence are not repeated for the hybrid methods. The

Table 11.8: FS-PSC: RPS controller parameters for position sensorless speed controlled machine 7.

Current proportional gain	k_p	1.57	V/A
Current time constant	T_i	30	ms
PLL proportional gain	k_{pPLL}	120	rad/s
PLL time constant	T_{PLL}	2	ms
DC bus voltage	U_{dc}	337.5	V

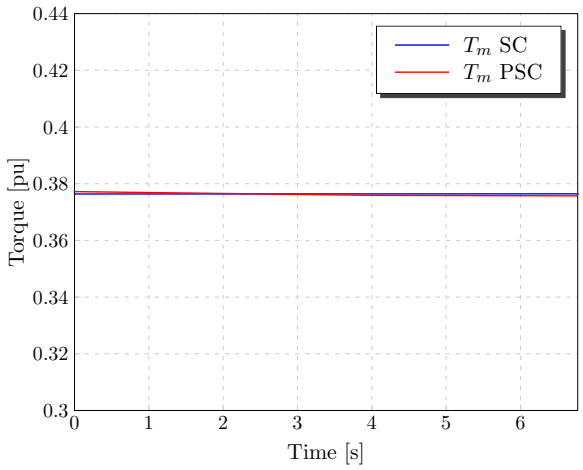

(a) Measured torque at a constant speed of 0.28 $p.u$.

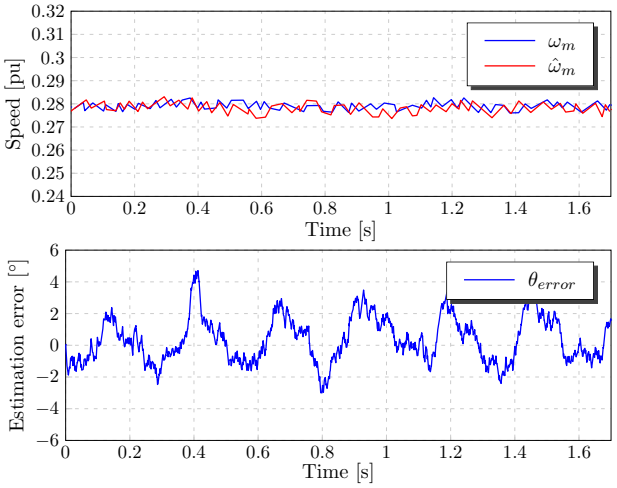

(b) Measured-, estimated speed and position estimation error.

Figure 11.15: FS-PSC: Measured steady state results.

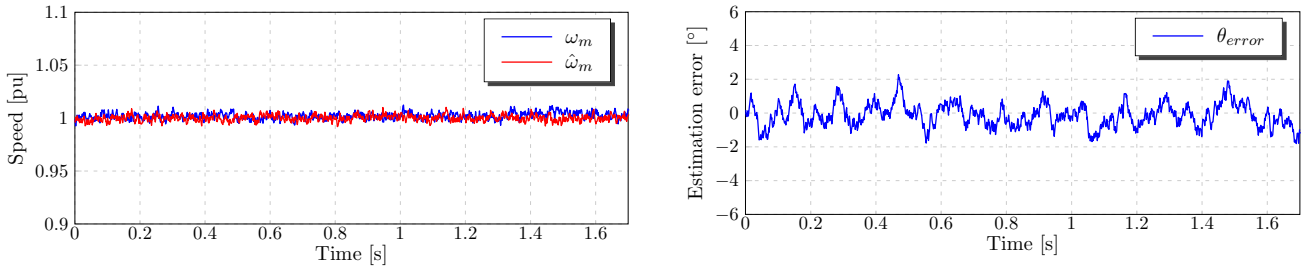

(a) Measured and estimated rotor speeds.

(b) Measured position estimation error.

Figure 11.16: FS-PSC: Measured results at rated speed without load.

changeover between estimation schemes is however the focus. The RSM is controlled position sensorless with a cascaded speed controller. The speed is ramped up from standstill to rated speed while controlled with the HFI assisted hybrid PSC method, as shown in Fig. 11.17a. It is shown in Fig. 11.17a that the measured- and estimated rotor speeds are almost identical. The position estimation error, as shown in Fig. 11.17a, shows no transients. The changeover between the two stand alone PSC methods is thus seamless.

The second test is a no load speed reversal test. The measured speed and reference current of the speed reversal test are shown in Fig. 11.17b. The measured speed is smooth during the entire test and no effect of the changeover is noticeable. There is a transient in the reference current however, but this effect is not visible in the measured speed or position estimation error. A large position estimation error is present at 24 s. This estimation error is only momentarily and does not cause PLL desynchronisation.

11.4.5 AI assisted hybrid PSC method.

The final method to be evaluated in the laboratory environment is the AI assisted hybrid PSC method. The RSM is controlled with a position sensorless cascaded speed controller. The results of a no load rated speed ramp are shown in Fig. 11.18a. There is a good correlation between the measured- and the estimated machine speeds. The position estimation error as shown in Fig. 11.18a, never exceeds $|10°|$ and settles at $\pm 0°$ at steady state.

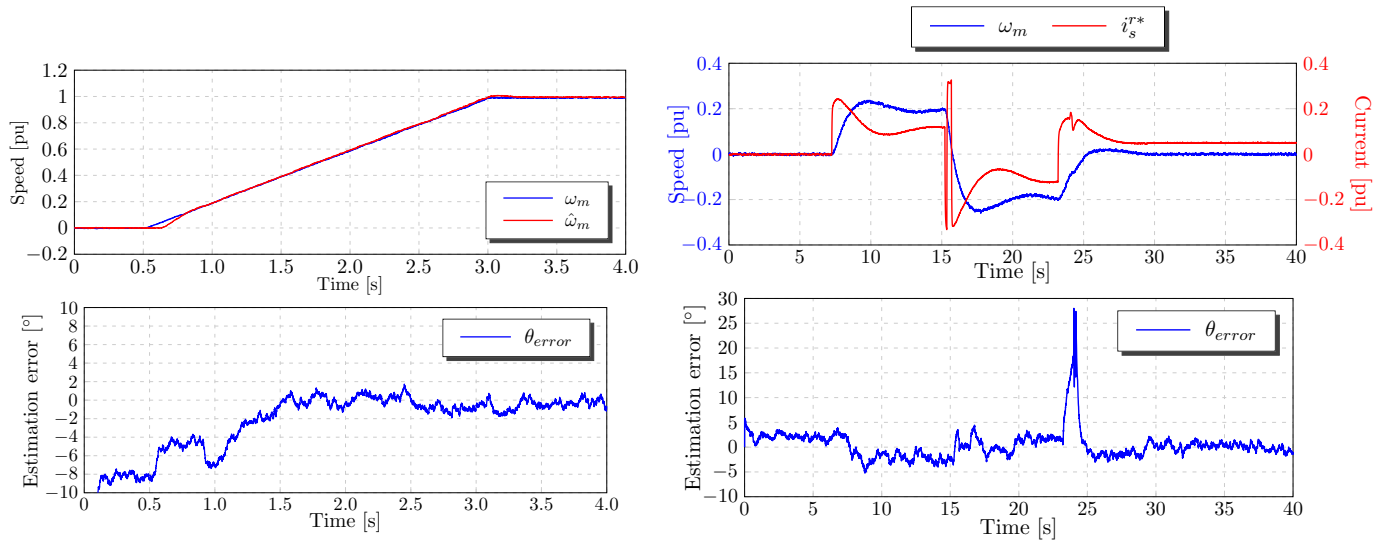

(a) No load speed step ramp from standstill to rated speed.

(b) No load speed reversal test.

Figure 11.17: HFI assisted Hybrid PSC: Measured dynamic results.

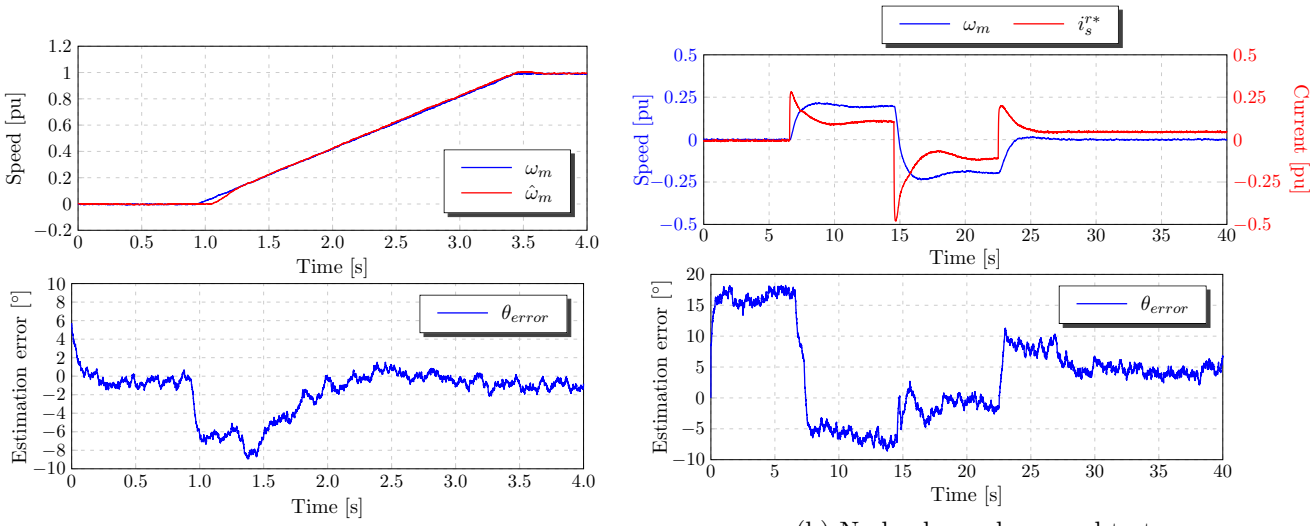

(a) No load speed step ramp from standstill to rated speed.

(b) No load speed reversal test.

Figure 11.18: AI assisted Hybrid PSC: Measured dynamic results.

The final test is a no load speed reversal test. The results of this test are shown in Fig. 11.18b. It is shown in Fig. 11.18b that there are no transients in the position estimation error. The sign of θ_{error} does change however, at the changeover between estimation schemes. This effect is not reflected in the reference current or measured speed of the RSM as shown in Fig. 11.18b.

11.5 Summary

The position sensorless control (PSC) capabilities of a RSM, designed for a variable gear (VG) electric vehicle (EV) drivetrain, are investigated in this chapter. The two core parts of this investigation are the pull-away torque capabilities of the proposed RSM with two proposed saliency-based position sensorless control (SB-PSC) methods and the effectiveness of the fundamental saliency position sensorless control (FS-PSC) method at the rated speed of 4800 rev/min.

It shown through Simulink simulations that a combination of the higher current rating, larger current angle and the simplification of the high frequency injection position sensorless control (HFI-PSC) method prevents proper spectral separation of the HF carrier component from the fundamental current component in the demodulation process. This problem is rectified by subtracting the low pass filtered q-axis current from the unfiltered current to remove the fundamental q-axis current component. This decouples the HF carrier components from the fundamental component. No additional filters are added to implement this process, although this is in effect a band stop filter.

Rated continuous startup torque might not be required from an electric motor with a VG EV drivetrain. Nevertheless, this is still set as a requirement for the research described in this chapter. Test bench limitations do not allow the proposed machine to be tested at rated continuous conditions due to the VSDs not being able to deliver the rated current for the proposed EV RSM. However, a combination of simulation- and measured results are used to show that it is possible to deliver rated continuous torque with the proposed RSM at startup and in the low speed region with the two proposed SB-PSC methods. It is shown in simulation that the low DC bus voltage, provided by the battery pack, does not prove to be problematic for either of the two SB-PSC methods, at standstill and in the low speed region.

It is shown by simulation and measured results that accurate PSC is possible with the FS-SPC method at the high rated speed of the proposed RSM. Only no load tests are possible at rated speed due to the test bench limitations. Simulations are used however, to show that the RSM has good torque performance at rated conditions when controlled with the FS-PSC method.

Both hybrid PSC methods are also implemented and evaluated in the laboratory environment. The focus of the hybrid test are the dynamics of the machine and the changeover between the estimation schemes. Measured results show that the changeovers of both hybrid PSC methods are smooth and effective. It is also shown that the changeover between estimation methods is not visible in the machine's speed response. It can thus be concluded from the work described in this chapter that the position sensorless controlled RSM VG EV is a viable option.

Chapter 12

Position Sensorless Controlled Mine Scraper Winch

Scraper winches have been the primary component of underground cleaning system of ore-bearing rocks in South African mines for the last couple of decades. Scraper winches are used to move these rocks from the blast site to the ore pass. The mining scraper winch is discussed in this section. Some issues regarding the operation and design of the scraper winch are also addressed. Finally, a revised scraper winch design is proposed. The proposed scraper winch is tested and evaluated in this chapter.

12.0.1 The mine scraper winch

A typical scraper winch consists of two drums as shown in Fig. 12.1a. A single line start induction machine (IM) is used to drive a central rotating shaft via a multi-stage gearbox. Force is transferred from the central rotating shaft to each individual drum via a mechanical clutch system. The clutch system allows each individual drum to "grip" on the central rotating shaft as shown in Fig. 12.1b. Being a line start machine, the IM runs at rated electric frequency during the entire scraping operation even when the drum clutches are not engaged. The central rotating shaft thus turns freely without force transfer if the drum clutches are disengaged. The first important aspect to thus point out is that the scraper winch does not operate at optimum efficiency due to the inefficient force transfer of the clutch system and the IM's inability to vary its speed when torque is not required.

Not only is the scraper winch not energy efficient, but its reliability is also brought into question. Up to a 1000 scraper winches are used daily in a typical South African gold mine [197]. These scraper winches require maintenance every 4 to 6 months [197]. Maintenance includes rewinding of the stator, replacement of bearings and/or welding of the cage rotor. It is shown in [197] that high cage rotor currents of the winch IM cause excessive heat which contributes to early bearing failure. A significant amount of production time is lost during the repair of the scraper winches.

12.0.2 Operation of the scraper winch

A typical diagram of how the scraper winch is used underground is shown in Fig. 12.2a. The two drums are named pull- and retrieval drums. A scraper, as shown in Fig. 12.2b, is connected to the pull drum via a steel cable. The scraper is pulled towards the pull drum while the steel cable rolls up on the drum. A winch operator sets the pull process in motion by pressing down on the clutch of the pull drum.

Another steel cable connects the scraper via pulleys in the rock face to the retrieve drum. The steel cable rolls off the retrieval drum during the scraper pull process. The operator lightly clutches the retrieval drum to prevent the cable from dragging on the ground and tethering. This process is referred to as feathering of the retrieval drum. The pull process is halted when the scraper reaches the destination

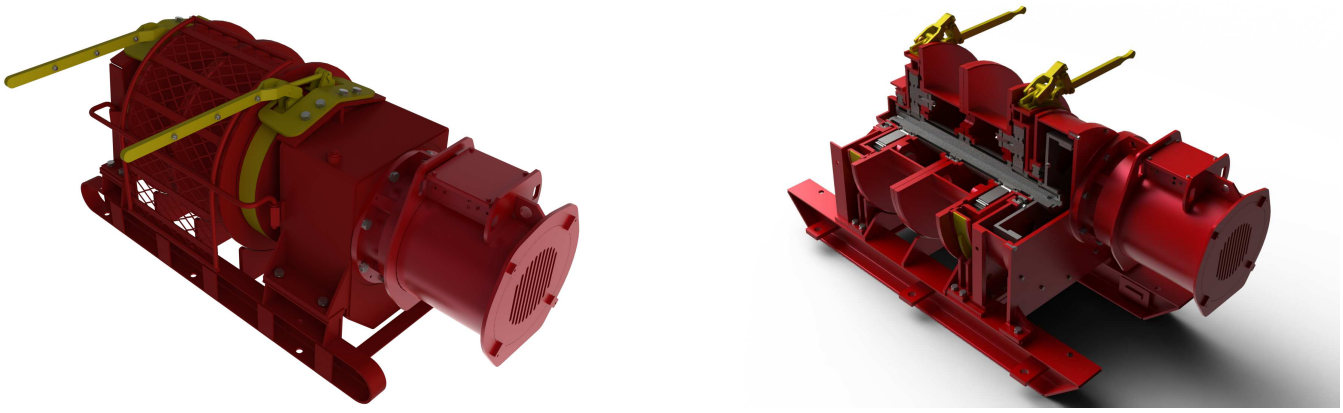

(a) (b)

Figure 12.1: Diagrams of the conventional scraper winch, courtesy of Oceantech.

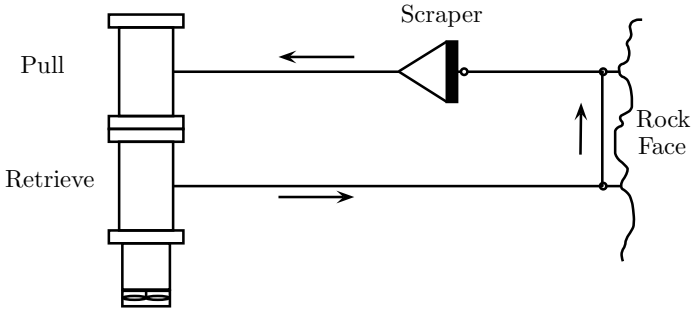

(a) Scraper winch operation as viewed from top.

(b) Typical scraper used with the winch [198].

Figure 12.2: The scraper winch operation.

ore pass. The scraper is returned to the blast site by reversing the IM direction allowing the retrieval drum to pull the scraper back to the ore site. This is known as the retrieval process. The pull drum is feathered during the retrieval process. After this the pull process is initiated again.

12.0.3 Dangers associated with the operation of the scraper winch

It is stated in the safety, health & environmental bulletin of Anglo American in 2003 [199] that the scraper winch operation qualifies as one of the higher risk areas of mining. The conditions are especially dangerous for the winch operators. It is shown in Fig. 12.3 that the winch operators have to work very close to the scraper winches in order to operate the clutch system. Injuries and even fatalities often occur during scraping due to cables and/or pulley failure. The reason behind this failure rate is investigated in [200]. It is found in [200] that the IMs used in the scraper winches are designed with very large slip ratings. This results in the IM delivering up to 3.5 times its rated torque when the scraper is overloaded or hits an immovable object [200]. The winch operator interprets this as the winch having sufficient power to pull the scoop [200]. The force on the cables and pulleys exceed its rated conditions thus causing it to fail.

12.0.4 Proposed RSM winch setup

It is proposed in [200] that a variable speed drive (VSD) be added to the conventional scraper winch to limit the current drawn by the machine and therefore the torque of the machine. This will improve the

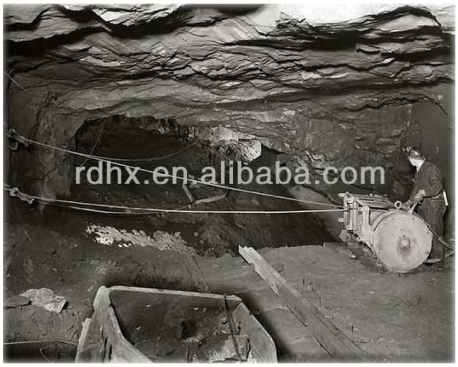

(a) [201]

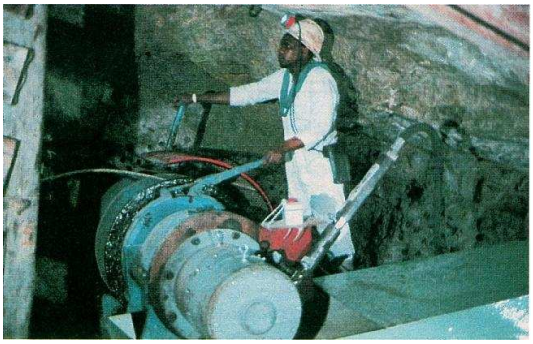

(b) [202]

Figure 12.3: Scraper winch operation conditions.

safety of the winch during operation and its durability. A similar solution to this problem is proposed in this chapter. The IM is replaced with two RSMs in the proposed scraper winch configuration. Each RSM fits inside a drum of the winch. A planetary gearbox connects the machine directly to the drum allowing each drum to be driven by its own machine without a clutch system. A diagram of the winch with the gears, as seen from the side, are shown in Fig. 12.4a, courtesy of Oceantech (PTY) Ltd. A diagram of the proposed RSM winch is shown in Fig. 12.4b.

The RSM will operate in its generating quadrant during the feathering process due to torque being applied in the opposite direction of rotation. It is proposed to connect the DC buses of the two VSDs together to circulate the regenerative power. Feathering can also easily be incorporated in the control system of the machine, automating this process. The efficiency of the winch will thus be improved by the following:

1. Use of a RSM with a comparable or even higher efficiency than the IM.
2. Connection of the RSM directly to the drum via a planetary gearbox. The inefficient clutch system is thus omitted.
3. The VSD can be used to vary the speed of the drum or even stop it when not in use, unlike the line start IM.
4. Power is generated by the RSM during the feathering process and circulated between the VSDs.

The introduction of power electronics and DSPs to the scraper winch system allows for an automation process. The aim of the automation process is to have the winch automatically detect when it is overloaded, or shut down and initiate retrieval. The overload detection will ensure that the drum pull force stays within the designed specification ensuring that the cable force does not exceed the design limits of the cables and pulleys. Finally a remote control device can allow the winch operator to start and stop the winch operation, if needed, while standing at a safe distance.

It is essential that the proposed scraper winch system be robust to outlast the harsh environment of the mines. The environment that the scraper winch operates in makes it non-negotiable for the system to be position sensorless. The big challenge with this application is the high startup torque required from the position sensorless controlled RSM. Up to rated torque can be required from the scraper winch at standstill. It is shown in previous chapters that saliency based position sensorless control (SB-PSC) methods can fail at high loads if the machine's inductance saliency is too small. This application will thus prove to be a good challenge for the two SB-PSC methods.

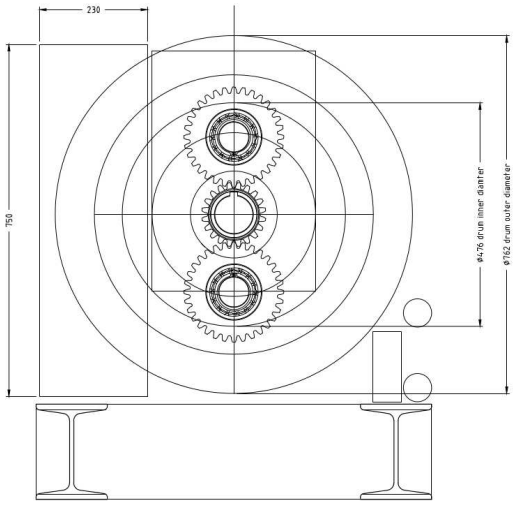

(a) Planetary gearbox viewed from the side.

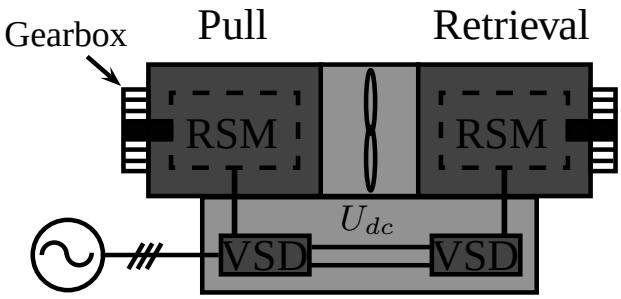

(b) Proposed RSM winch setup.

Figure 12.4: Scraper winch operation conditions.

To conclude, the proposed scraper winch should be more efficient than the standard design. The vector control structure will limit the torque produced by motors, thus reducing the risk of cable and pulley failure. The safety of the winch operator is improved drastically by automating the entire pull and retrieval process with remote control access from a safe distance. The RSM winch design is proposed and supported by scraper winch manufacturer Oceantech (PTY LTD). The mechanical layout, drawings and first prototype are provided by Oceantech.

12.1 The RSM Scraper Winch

Deriving specifications for the RSM designs is not an easy task as there is limited information available regarding the torque required from the machines and their duty cycles. Field test results of a 37 kW Scraper winch are provided in [200]. These results are used as a guideline to draw up specifications for the winch RSMs. The pull drum forces, measured in [200] with the 37 kW scraper winch during face cleaning, peaked just below 20 kN with an average force of 17.5 kN. The force on the retrieval drum, during retrieval of the empty scraper, ranged between 1.5 kN and 3.5 kN. The RSM scraper winch specifications are thus chosen as in Table 12.1.

The torque requirements of both machines are more or less the same, thus it is decided to use two identical machines. This will not only simplify laboratory tests but is also attractive from a manufacturing and production point of view. Two six pole RSMs, which are listed as machine 13 in Table 3.1, are designed for the scraper winch tests. The design of these machines is not within the scope of this thesis. The RSM specifications are listed in Table 12.2.

The design constraints of the RSM are not only determined by the torque and speed specifications of the winch, but also by the available envelope. The outer diameter of the RSM stator is a fixed constraint to fit into the drum as shown in Fig. 12.4a. The large fixed stator outer diameter however, results in a RSM design with a very short active stack length. The winch RSM thus has very large end-windings as shown in Fig. 12.5. The end-windings on both sides of the stator add up to more than double the active length of the machine. Both winch RSMs thus have very large end-winding inductances.

It is found during testing that the voltage drop over the end-windings of the RSM is significant. The voltage drop over the end-windings is so severe that rated current cannot be induced at rated speed in

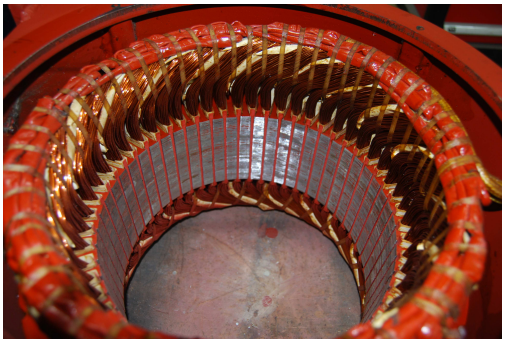

Figure 12.5: Stator of one of the winch RSMs with the end-windings visible.

Table 12.1: Design specifications for the proposed scraper winch.

Pull drum	
Pull Force	21.36 kN
Drum Speed	37.03 rev/min
Drum Torque	8.199 kNm
Reduction Gear	27:1
Machine speed	1000 rev/min
Machine torque	303.67 Nm

Retrieve Drum	
Pull Force	4.144 kN
Drum Speed	75 rev/min
Drum Torque	1.579 kNm
Reduction Gear	5.2:1
Machine speed	390 rev/min
Machine torque	303.65 Nm

Table 12.2: Winch RSM parameters.

Machine Parameters	
Stator resistance R_s	0.135 Ω
Direct-axis inductance L_d	25.5 mH
Quadrature-axis inductance L_q	3.6 mH
Pole pairs N_p	3
Rated speed	1000 rev/min
Continues current (rms)	62.4 A
Continuous torque	303.67 Nm
Continuous power	31.8 kW
Constant current angle ϕ	64^o
Rated saliency ratio γ	0.48
Rated saliency shift ζ	18^o
Drive Parameters	
Switching frequency F_s	6.1 kHz
Sampling frequency f_s	12.2 kHz
DC bus voltage u_{dc}	540 V

the laboratory environment where the VSD supply voltage is 400 V. The full load steady state speed of the RSM is reduced to 750 rev/min in the laboratory environment. The typical supply voltage in the mines is 525 V. Hence, the VSD will have a much larger DC bus voltage when used in a mine allowing it to apply larger voltages and thus achieve rated load at rated speed. Laboratory testing will still however prove to be valuable.

Not much literature exists regarding six pole RSM designs. An efficiency comparison is made in [12]

between a six pole IM and a six pole RSM with a standard field oriented control structure and position feedback. A six pole RSM is proposed and evaluated in [195] for a lathe application where good results for torque ripple suppression and field weakening performance are reported. No literature could however be found, showing experimental results of the performance of a six pole RSM when controlled position sensorless. Literature on position sensorless controlled RSM traction drives, regardless of their number of pole pairs, barely exist, as shown in Table A.1. In this chapter the novel implementation and evaluation of the simplified HF injection PSC (HFI-PSC), arbitrary injection PSC (AI-PSC) and the fundamental saliency PSC (FS-PSC) methods on a six pole traction RSM for a scraper winch application will be investigated. Also the two investigated hybrid PSC methods will be implemented and evaluated.

12.2 Measured And Simulated Results

Tests performed during this research are part of a first implementation and evaluation phase and are limited to the laboratory environment. The test bench used is shown in Fig. 12.6a. There are a few important aspects to note regarding this test bench. The shafts of both winch RSMs are connected. This allows the retrieve drum RSM to load the pull drum RSM, simulating the scraper filling up with rock and ore. This also tests the feathering of the retrieve drum. A fan is connected on the shaft in the middle of the two machines for cooling purposes.

The second important aspect of this test bed is the disc brake fixed to the shaft of the RSM on the right of Fig. 12.6a. This disc brake works with a switch and is able to lock the RSM rotor at 310 Nm. The disc brake is used to test the startup torque of the RSM while controlled with the SB-PSC methods. Also the disc brake can be locked during operation to simulate the effect of the scraper being overloaded or hitting an immovable object. A photo of the shaft connected motors and the disc brake are shown in Fig. 12.6b.

Finally a position sensor is only measured by one rapid prototype system (RPS) as shown in Fig. 12.6a. This signal is used to determine the quality of the PSC methods and to measure the saliency shift for the compensation curves. This signal is made available to the second RPS via a D/A and A/D bus. Also, this bus creates the "master-slave" system needed for the automation process. The pull drum RSM RPS acts as the master giving commands to the slave RPS on when the pull or retrieval process is active.

No torque sensor is used with this winch test bed. Not only is there not enough space for a torque

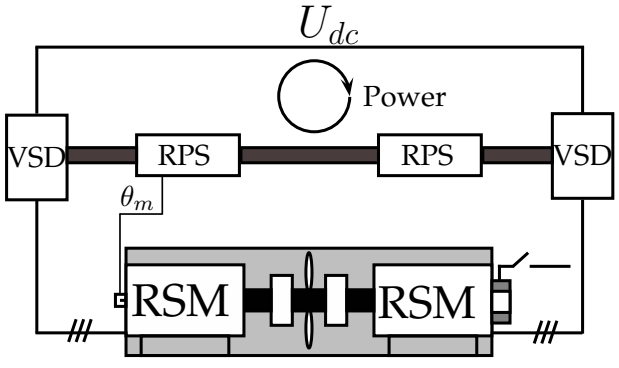

(a) Schematic of the winch test bed.

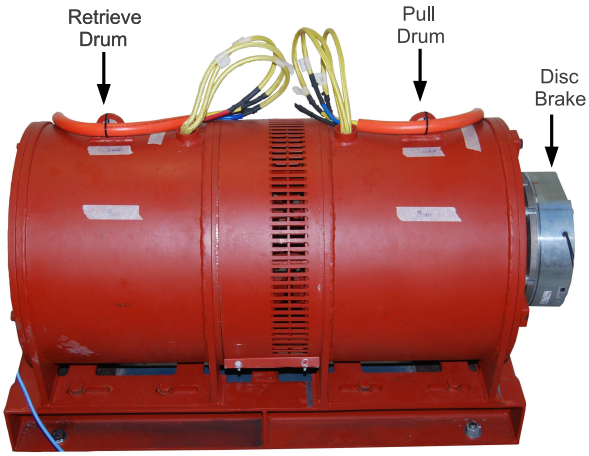

(b) Picture of the test bed with the pull- and retrieve drum motors as well as the disc brake.

Figure 12.6: Laboratory winch test bed.

sensor between the two RSMs, but instantaneous braking applied by the disc brake can cause device failure. The torque is calculated offline with a torque lookup table. The torque lookup table and flux linkage maps of the winch RSM are created with the JMAG FE package. The current vector in the actual rotor reference frame is calculated with the measured electrical angle and stored. This current vector is not used in the feedback loop, but rather the current in the estimated rotor reference frame which is calculated with the estimated electrical angle. The stored current vector values are used offline with the torque lookup table to calculate the machine torque.

It is shown in this thesis that accurate results are achieved with the FE- and flux mapping methods developed in this thesis, hence the offline calculated machine torque will give a good indication of the machine performance. The FE lookup table as a function of i_d and i_q is shown in Fig. 12.7. The torque calculated offline with the FE lookup table and measured current will be referred to as the measured torque in the rest of this section.

Speed voltage decoupling, as shown in Figs. 2.5 and 2.6, is added to the RSM winch control structure to reduce the effect of the large end-winding inductance. The flux linkage curves are extracted from the flux maps of this machine. MATLAB is used to derive exponential equations for these curves to use for the speed voltage decoupling in the RPS.

12.2.1 Locked rotor test

The startup torque capabilities of the position sensorless controlled winch RSM are evaluated with a locked rotor test. A method of adapting the simplified HFI-PSC method to decouple the fundamental q-axis current component from the HF current component in the demodulation process is described in the previous chapter. This adapted method is also implemented for the winch RSM. The Simulink simulated and measured locked rotor test results of the HFI-PSC method are shown in Fig. 12.8. Measured torque results are calculated offline with the torque lookup table and the measured current as described earlier in this section.

The Simulink simulation and RPS control parameters are listed in Table 12.3. The machine current is ramped up from 0.08 $p.u$ to 1 $p.u$ in 60 ms in the locked rotor test performed in Fig. 12.8. The minimum current needed to saturate the q-axis flux linkage for position estimation 0.08 $p.u$. It is shown in Fig. 12.8a that rated torque is delivered successfully by the RSM when controlled with the HFI-PSC method.

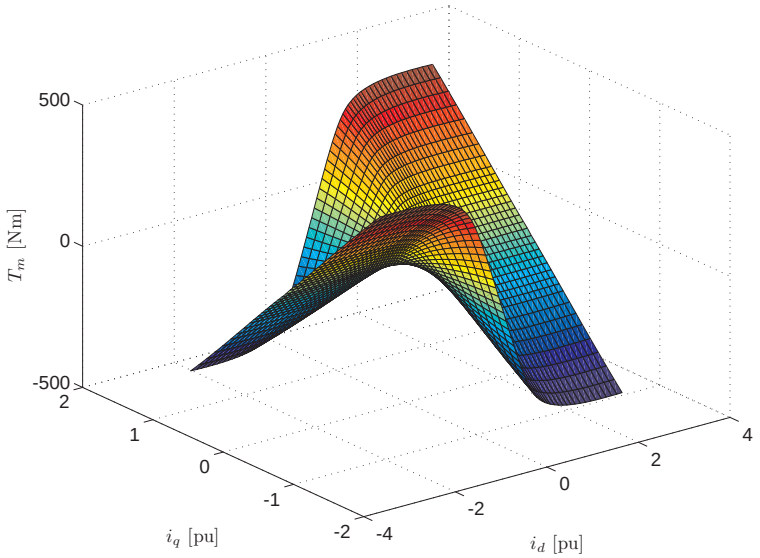

Figure 12.7: FE 3D torque lookup table.

It is also shown that the simulated and measured torque correlates well.

The measured torque makes a dip at 0.8 s as shown in Fig. 12.8a. The current overshoot causes torque overshoot which exceeds the maximum braking torque of the disc brake, causing it to slip. This result is very important. The position estimation error varies as a function of the rotor position, thus results may vary if the saliency shift compensation curve is measured wrongly. The rotor slip shown in Fig. 12.8a thus shows that the HFI-PSC method works well at more than one different rotor position. It is shown in Fig. 12.8b that both the simulated and measured position estimation errors are $\pm 0^\circ$ at steady state. Also no transients are visible indicating that the PSC scheme is stable.

The second locked rotor test is done with the AI-PSC method. The simulation and RPS control parameters are listed in Table 12.4. It is found that the response of the winch RSM, when controlled with the AI-PSC method, is much slower than when controlled with the HFI-PSC method. A minimum current ramp time of 1.25 s could be applied with the machine rotor locked. The simulated and measured results of this test are shown in Fig. 12.9. The measured results show that there are large position estimation errors at startup, as shown in Fig. 12.9b. This affects the measured torque as shown in Fig. 12.9a. The simulated and measured torque does not match in the low load region due to the large position estimation errors. Nevertheless rated torque is applied by the position sensorless controlled RSM.

Torque overshoot is present in the measured result, as with the HFI-PSC method, which results in the disc brake slipping at 2.8 s, as shown in Fig. 12.9a. The disc brake slip shows that the AI-PSC method is stable at various different rotor positions. To conclude, it is shown with simulation and measured results that both evaluated SB-PSC methods are able to control the RSM at standstill up to rated torque. The dynamic response of the two methods however, differ but are satisfactory for the application.

Table 12.3: HFI-PSC: Simulation and rapid prototype system controller parameters for position sensorless current controlled machine 13.

Parameter	Symbol	Simulation	RPS	
Current proportional gain	k_p	8	4	V/A
Current time constant	T_i	238.78	238.78	ms
PLL proportional gain	k_{pPLL}	20	20	rad/s
PLL time constant	T_{PLL}	41.84	41.84	ms
Current LPF	LPF_i	1260	1260	rad/s
PLL LPF	LPF_{PLL}	7540	7540	rad/s
Injection voltage	u_c	100	100	V
Injection frequency	ω_c	6.5×10^3	6.5×10^3	rad/s

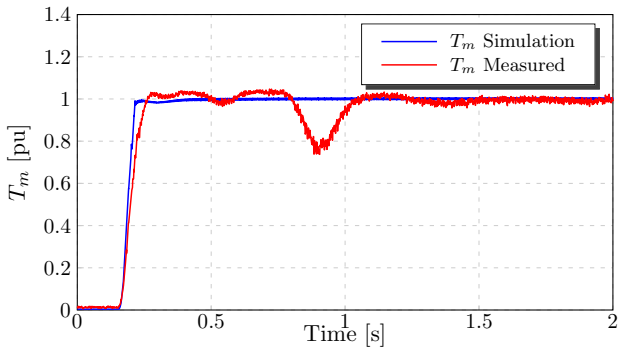

(a) Simulated and measured torque.

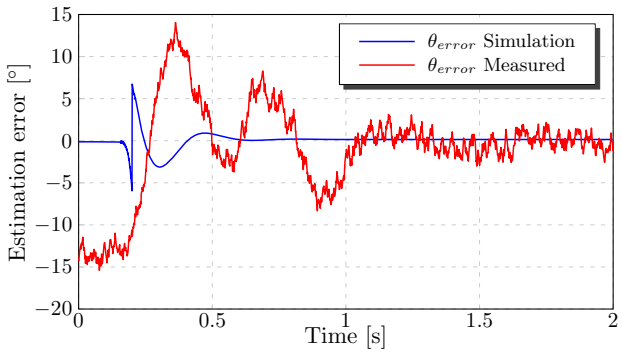

(b) Simulated and measured position estimation error.

Figure 12.8: HFI-PSC: Simulated and measured locked rotor test with a current ramp of 60 ms.

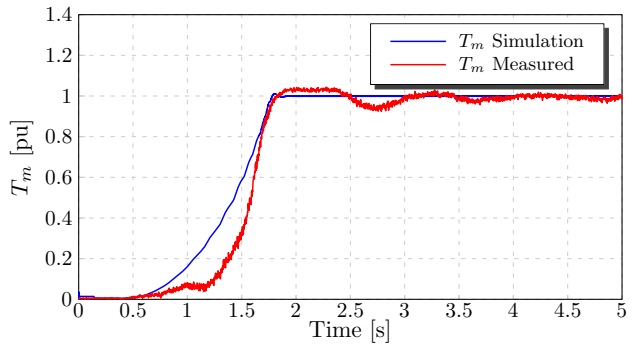

(a) Simulated and measured torque.

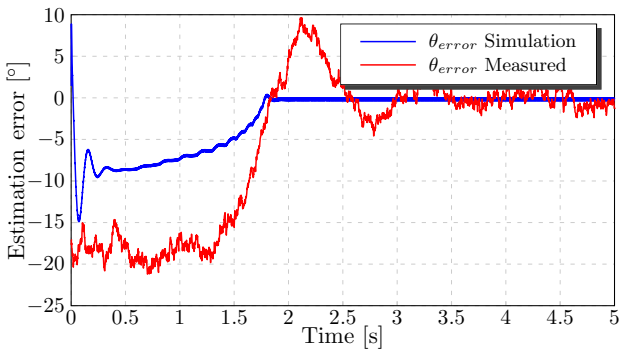

(b) Simulated and measured position estimation error.

Figure 12.9: AI-PSC: Simulated and measured locked rotor test with a current ramp of 1.25 s.

Table 12.4: AI-PSC: Simulation and rapid prototype system controller parameters for position sensorless current controlled machine 13.

Parameter	Symbol	Simulation	RPS	
Current proportional gain	k_p	15.7	6.28	V/A
Current time constant	T_i	238.78	238.78	ms
PLL proportional gain	k_{pPLL}	3	4	rad/s
PLL time constant	T_{PLL}	33.33	33.33	ms
Current LPF	LPF_i	-	-	rad/s
Injection voltage	u_{inj}	70	70	V

12.2.2 Effect of the end-winding inductance on the AI-PSC method

It is shown in the previous subsection that the AI-PSC method suffers from large position estimation errors. The end-winding inductance is modelled in the Simulink simulations to explain its effect on the AI-PSC method. The end-winding inductance voltage drop, $\boldsymbol{u}_{ew}$ is modelled in the stator voltage equation as in (12.1). The end-winding inductance voltage drop is calculated with (12.2), where L_{ew} is the end-winding inductance. The effect of the end-winding inductance can thus be incorporated into the simulation as in (12.3) and Fig. 12.10.

$$\boldsymbol{u}_s^s = \frac{d\boldsymbol{\psi}_s^s}{dt} + r_s \boldsymbol{i}_s^s - \boldsymbol{u}_{ew} \tag{12.1}$$

$$\boldsymbol{u}_{ew} = L_{ew} \frac{d\boldsymbol{i}_s^s}{dt} \tag{12.2}$$

$$\boldsymbol{\psi}_s^s = \int (\boldsymbol{u}_s^s - r_s \boldsymbol{i}_s^s) dt + L_{ew} \boldsymbol{i}_s^s \tag{12.3}$$

The isotropic voltage term, as derived in Chapter 5, thus changes to (12.4). The wrong voltage vector is thus used to predict the isotropic current response and to calculate the isotropic impedance of the RSM.

$$\boldsymbol{u}_L = \boldsymbol{u}_s^s - r_s \boldsymbol{i}_s^s + \boldsymbol{u}_{ew} \tag{12.4}$$

Open loop AI-PSC simulations are used to investigate the effect of the end-winding inductance on the accuracy of the AI-PSC method. The AI-PSC method only observes the states of the machine to estimate the electrical angle without a compensation curve while the machine is controlled with the measured electrical angle. An arbitrary value of 0.9 mH is chosen as the end-winding inductance for simulation

purposes. The simulated position estimation error over current is shown in Fig. 12.11 with, and without the end-winding inductance term. The results in Fig. 12.11 show that the end-winding inductance adds a constant offset to the position estimation error. This constant offset can cause PLL desynchronisation. The HFI-PSC method does not use the machine voltage vector to estimate the electrical angle, thus is not affected by the end-winding inductance. It is thus suggested that the end-winding inductance of the winch RSM be measured to compensate for in the AI-PSC method.

12.2.3 Low speed steady state tests

It is required that the speed of the pull drum be kept constant during the pull process, hence the speed of the RSM must be controlled with a speed controller. A cascaded speed control structure, as shown in Fig. 2.8, is implemented on the pull drum RSM while the retrieve drum RSM applies rated load. The applied load on the pull drum RSM simulates the load on the scraper. The torque applied by the retrieve RSM simulates the feathering process, although the torque required for feathering is probably much less. No information is currently available regarding the torque requirements for the feathering process.

The two SB-PSC methods are tested and evaluated on the pull drum RSM with the cascaded speed control structure. Measurements are limited to the low speed region as this is where the SB-PSC methods are used for PSC. The HFI-PSC method is evaluated first at a pull drum RSM speed of 85 rev/min. The measured results of this test are shown in Fig. 12.12. It is shown in Fig. 12.12a that the measured torque oscillates around 1 $p.u.$ This can be explained by a mechanical imbalance at the shaft connection of the two machines. It is shown in Fig. 2.8 that the outer loop of the cascaded speed control structure is the speed controller and the torque controller, or in this case current controller, the inner loop. The speed controller thus varies the applied torque to keep the speed fixed and i.e. filter out the imbalance on rotor shaft speed. The torque ripple also cause a ripple in the position estimation error, shown in Fig. 12.12b. The position estimation error averages out at around $\pm 0°$ however.

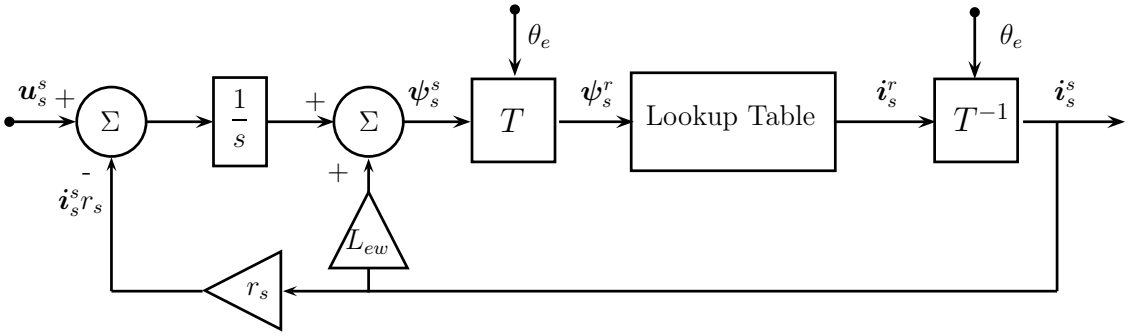

Figure 12.10: Simulation with end-winding inductance.

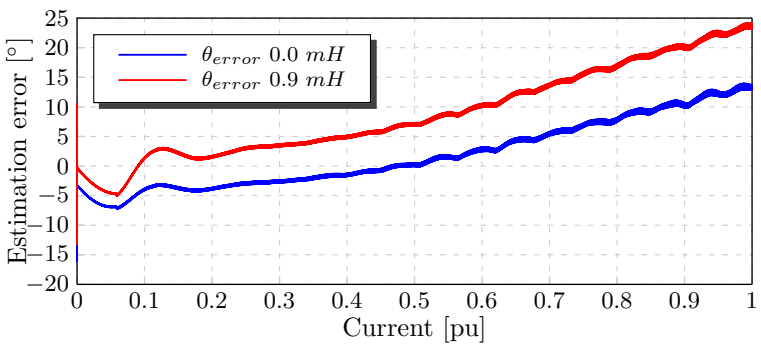

Figure 12.11: Simulated comparison of the end-winding inductance effect on the AI-PSC method.

The AI-PSC method is evaluated in Fig. 12.13 at a speed of 70 rev/min. The mechanical imbalance is not as prominent at this speed hence the measured torque, as shown in Fig. 12.13a, is more or less constant at ± 1 $p.u$. The position estimation error shown in Fig. 12.13b also averages out at around $\pm 0°$. It is shown in this subsection, with measured results, that both evaluated SB-PSC methods are stable in the low speed region with a cascaded speed control structure under full load conditions.

12.2.4 Medium speed steady state torque

The next test is a steady state full load test at a constant medium speed. Speed control is implemented on the pull drum RSM while controlled with the FS-PSC method with the reference speed set to 750 rev/min. This test is performed at a speed of 0.75 $p.u$ as it is explained earlier in this chapter that rated torque cannot be applied by the winch RSM at rated speed due to the large end-winding inductance. The pull drum RSM is loaded to 1 $p.u$ by the retrieve drum RSM as shown by the measured torque in Fig. 12.14a. The average of the position estimation error, as shown in Fig. 12.14b, is $\pm 0°$. This measured result thus show that the winch RSM has good torque capabilities in the medium speed region when controlled with the FS-PSC method.

12.2.5 Hybrid PSC startup

The two hybrid PSC methods developed in this thesis are tested on the pull drum RSM. A cascaded speed control structure is used to control the speed of the pull drum RSM. The retrieve drum RSM is programmed to simulate an inertia type load. This inertia load represents the scraper bucket filling up with rocks and ore at startup as the pull drum starts to roll up the cable. The load applied by the retrieve

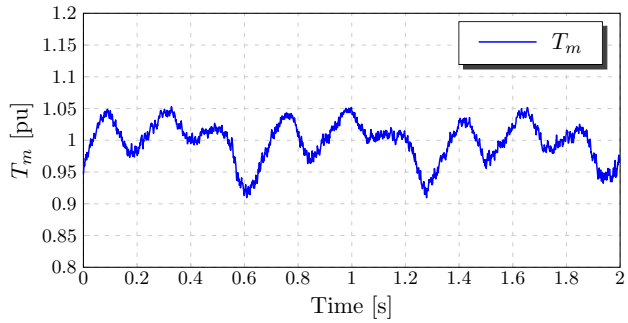

(a) Measured torque.

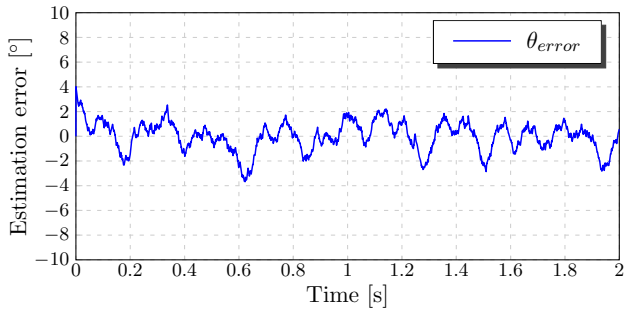

(b) Measured position estimation error.

Figure 12.12: HFI-PSC: Measured full load results at 85 rev/min.

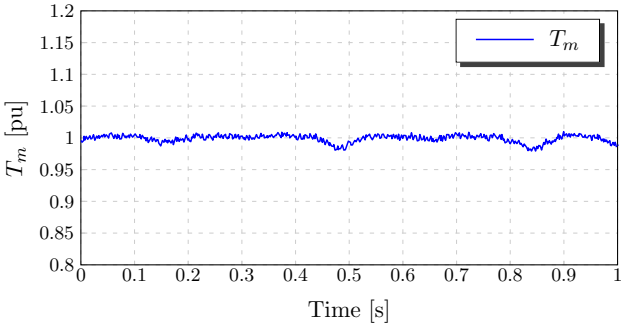

(a) Measured torque.

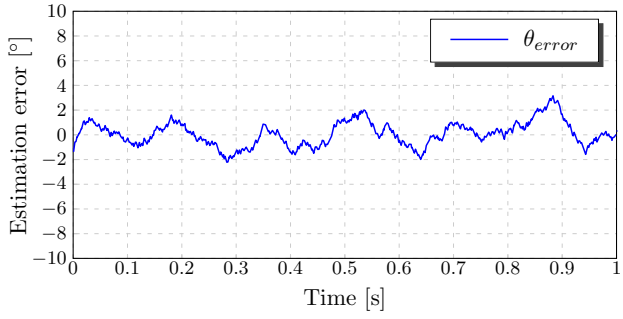

(b) Measured position estimation error.

Figure 12.13: AI-PSC: Measured full load results at 70 rev/min.

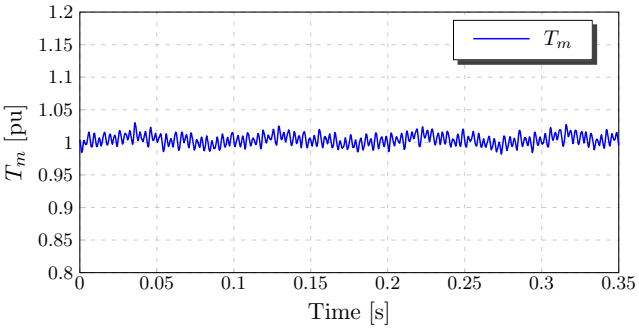

(a) Measured torque.

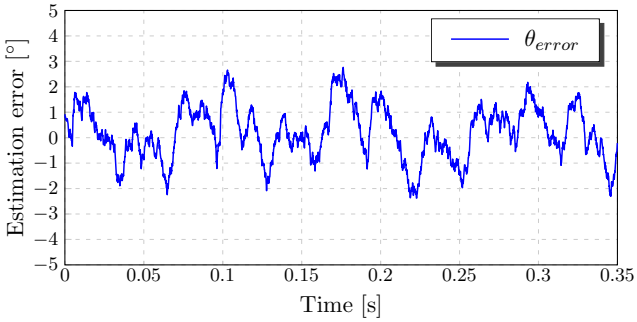

(b) Measured position estimation error.

Figure 12.14: FS-PSC: Measured full load results at 750 rev/min.

drum RSM is ± 0.8 $p.u$. Again this is also a good simulation of the feathering process.

It is shown in [200] that the average pull drum force is 17.5 kN. The applied load of ± 0.8 $p.u$ thus correlates well with the average torque required from the pull drum RSM. Larger torques, which does not exceed the RSM rating can still be applied by the RSM to get the pull drum up to its reference speed.

The results of the HFI assisted hybrid PSC method are shown in Fig. 12.15. The measured pull drum RSM torque and speed are shown on the same graph in Fig. 12.15a. The red line, representing the measured machine torque, shows that the machine is loaded at ± 0.8 $p.u$ at 10 s after which a speed ramp is applied by the position sensorless controlled pull drum RSM. It is shown in 12.15a that the applied torque surpasses ± 0.8 $p.u$ to reach the reference speed of 750 rev/min before settling at $20s$. A slight change in gradient of the measured speed is visible during changeover, but this does not raise any concern. Some transients are present in the position estimation error, shown in Fig. 12.15b, during startup but never exceeds $|6°|$ and averages out at $\pm 0°$ during steady state.

The results of the AI assisted hybrid PSC method are shown in Fig. 12.16. The performance of this method does not compare well with that of the HFI assisted hybrid method. This is mainly due to the large position estimation errors of the AI-PSC method between 0-6 s as shown in in Fig. 12.16b. The large position estimation errors are caused by the large end-winding inductance, as explained earlier in this section. The changeover between the estimation methods is clearly visible in the speed response, as shown in Fig. 12.16a. The reference speed of 750 rev/min is still reached however.

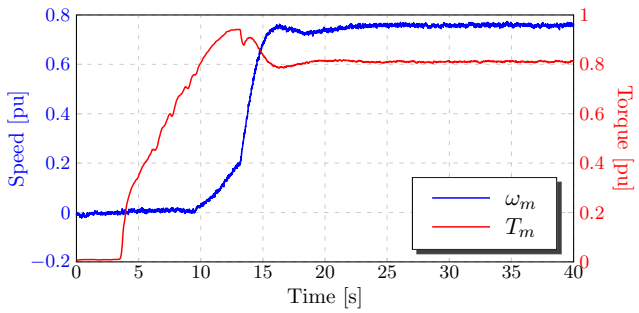

(a) Measured torque and speed.

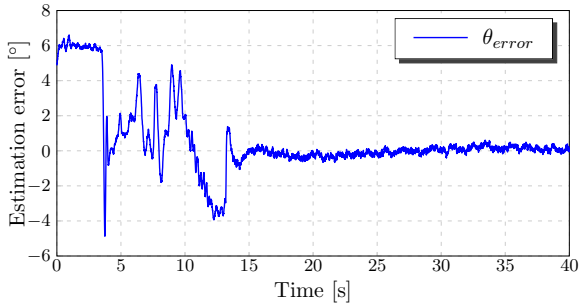

(b) Measured position estimation error.

Figure 12.15: HFI assisted hybrid PSC: Startup with load.

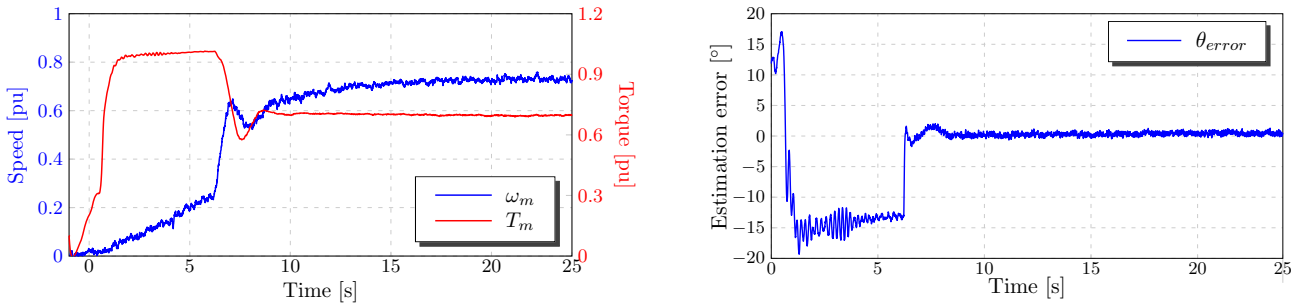

(a) Measured torque and speed.

(b) Measured position estimation error.

Figure 12.16: AI assisted hybrid PSC: Startup with load.

12.2.6 Automation process

The automation process of the two winch motors are tested. This process simulates an event where the scraper hits an immovable or large object during the pull process. Instead of applying more torque to move the object, as with the conventional winches, it is required that the scraper winch shuts off and the retrieval motor retrieves the scraper. The disc brake is locked during operation to simulate the scraper colliding with an immovable object. The rotor is locked instantaneously. This test is much harsher than the actual event of the scraper hitting an immovable object, hence this is a very good evaluation of the stability of the PSC methods.

It is shown earlier in this section that the performance of the AI assisted hybrid PSC method does not compare well to that of the HFI assisted hybrid PSC method. The AI assisted hybrid PSC method is unstable when the disc brake is locked while the pull proses is active. It is believed that this is due to the low pass filtering of the estimated speed. The machine locks instantaneously, hence the low pass filtered estimated speed is very slow to react to this large variation in speed causing the PLL to desynchronise.

The measured results of the pull drum RSM during the automation test are shown in Fig. 12.17. It is shown in Fig. 12.17a that the pull drum RSM is loaded by the retrieve drum RSM at startup as with the tests in the previous subsection. The machine speed increases and settles at 750 rev/min while loaded. The disc brake is locked at 35 s. The measure speed in Fig. 12.17a clearly shows that the machine rotor is locked almost instantaneously. Large transients occur momentarily in the position estimation error as shown in Fig. 12.17b, but the PLL stays synchronised. It is shown in Fig. 12.17a that rated torque is applied by the RSM at standstill after the rotor is locked.

The RPS of the pull drum RSM shuts down the winch after rated torque is applied for a couple of seconds and the torque drops to zero, as shown in Fig. 12.17a. This shut down time is predefined and can be modified easily. The disc brake is released manually as the scraper winch is now inactive. After a couple of seconds (allowing enough time for the brake to be released), the RPS of the pull drum RSM signals the RPS of the retrieve drum RSM to initiate the retrieve procedure. This is shown in Fig. 12.17a as the negative speed measurement. After a predefined number of machine revolutions (again this can easily be modified) the RPS of the pull drum RSM signals the second RPS to halt the retrieve process. The pull process is now ready to restart.

It is clear that the HFI assisted hybrid PSC method is very successful in controlling the RSM during these harsh tests. Also it is shown that, unlike the current winches, the applied torque does not exceed rated torque. Finally it is shown that an overload automation process is successfully implemented.

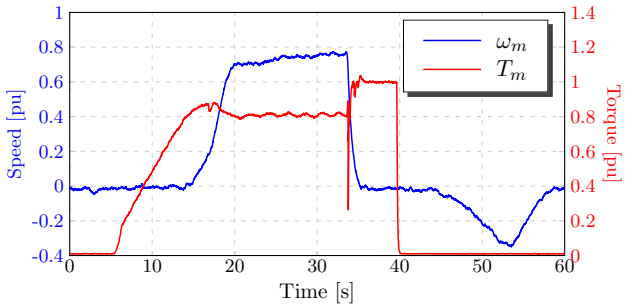

(a) Measured torque and speed.

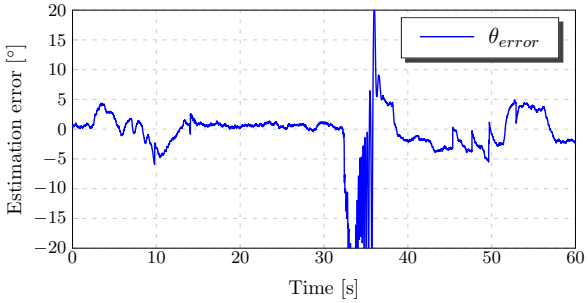

(b) Measured position estimation error.

Figure 12.17: HFI assisted hybrid PSC: Automation test.

12.3 Summary

A new scraper winch concept is proposed in this chapter for a mining application. The aim of the proposed design is to improve on the safety, durability and energy efficiency of the existing scraper winches used in gold mines in South Africa. A single line start induction machine connected to a central rotating clutch system is replaced by two six pole RSMs fitted inside the two drums of the winch.

It is important that the entire winch system operate without position sensors to endure the harsh environment of the mines. The challenge with this implementation is the large startup torque required from the RSMs while controlled with the saliency based position sensorless control (SB-PSC) methods. In this chapter results of the novel implementation of the simplified HFI-, AI- and the FS-PSC methods on a six pole RSMs are shown. Also the two hybrid PSC methods are evaluated on the six pole RSM for the first time.

It is found that performance of the AI-PSC method is affected by the large end-winding inductance of the winch RSM. This also affects the AI assisted hybrid PSC method. Nevertheless it is shown that both RSMs can deliver rated torque when controlled with both SB-PSC methods. At 300 Nm this is, as far as could be determined, one of the largest documented torque delivered by a position sensorless controlled RSM at standstill.

It is shown that the HFI assisted hybrid PSC method works very well with the winch RSM with good torque capabilities. Finally an automation process test shows that the proposed winch design improves on the current design by limiting the applied torque, when overloaded. An overload automation process also shows that the winch is able to shut off and retrieve the scraper when an immovable object is hit or overload occurs, allowing the winch operator to stand clear of the scraper winch. This improves the safety conditions of the winch operator.

Chapter 13

Conclusion

In this thesis the possibility of using position sensorless controlled reluctance synchronous machines in industry applications where variable- and dynamic torque is required, is investigated. The work in this thesis shows that the RSM is overall well suited for position sensorless control (PSC). It is shown that the RSM's saliency ratio is large compared to that of permanent magnet machines. This allows the position sensorless controlled RSM to deliver high startup torque. The following key aspects stem from the work done in this thesis:

Hybrid position sensorless control scheme for reluctance synchronous machines

A hybrid PSC method with a hysteresis changeover scheme is proposed and implemented. The proposed method allows each individual method to operate with its own optimum controller parameters. Also, speed ripples in the changeover region do not cause variable switching between the low- and high speed estimation methods. Finally, phase locked loop (PLL) synchronisation allows for seamless changeover between position estimation methods. The proposed hybrid PSC method allows for a new low speed and standstill extension of the fundamental saliency PSC (FS-PSC) method. Novel extensions of the simplified high frequency injection- (HFI-PSC) and the arbitrary injection PSC (AI-PSC) methods are made with the FS-PSC method to operate in the entire rated speed region.

Design and construction of a zero current position sensorless controlled reluctance synchronous machine

It is shown through finite element (FE) simulations that the ideal rotor RSM configuration has favourable saliency-based PSC (SB-PSC) characteristics at zero reference current. A novel epoxy resin cast design is proposed and implemented to create an ideal rotor RSM to improve on the SB-PSC performance of the lateral rib rotor RSM at zero reference current. Also it is shown that the efficiency of the ideal rotor RSM is superior to that of the lateral rib rotor RSM due to it always operating on the maximum torque per ampere curve.

Saliency-based position sensorless control performance evaluation and comparison of synchronous machines

Established saliency ratio and saliency shift equations are used for a novel SB-PSC comparison of three different types of synchronous machines on a per unit scale. It is shown that, although the saliency characteristics of the investigated field intensified permanent magnet (FI-PM) machines are superior to that of the field weakening interior permanent magnet machine at full load, they do not compare to that of the investigated RSMs. It is shown through FE simulations that the surface mounted FI-PM machine

does not have sufficient saliency ratio at zero to $\pm 0.5\ p.u$ current for SB-PSC. It is also shown through FE simulations that the FI-PM machine with flux barriers suffers from significantly less saliency shift than the the FI-PM machine without flux barriers.

Industry application 1: Reluctance synchronous wind generator with an inverter output LC filter

A robust high speed position sensorless controlled reluctance synchronous wind generator with a inverter output filter is proposed, tested and evaluated. The proposed generator setup allows the power electronics converter to be stationed in the turbine tower instead of the nacelle, reducing the nacelle weight. A new stator quantity estimation method is derived to estimate the stator quantities of the generator to avoid using additional sensors on the machine side of the LC filter. It is shown that the injection frequency of the HFI-PSC method can be chosen in the vicinity of the resonance frequency of the inverter output filter to boost the HF current response which allows the magnitude of the injection voltage to be reduced. In this thesis results of a novel implementation and testing of the HFI-assisted hybrid PSC method with an inverter output filter and a RSG with the derived stator quantity estimation method are shown. Good measured maximum power point tracking results of the position sensorless controlled generator are shown.

Industry application 2: Variable gear electric vehicle

A RSM is proposed for a variable gear (VG) electric vehicle (EV) drivetrain. A combination of simulation- and measured results are used to show that the proposed RSM can deliver rated continues startup torque with the two proposed SB-PSC methods. It is also shown through simulations that the low battery pack voltage does not prohibit SB-PSC in the low speed region. Both developed hybrid PSC methods are implemented and tested successfully.

Industry application 3: Mine scraper winch

A novel scraper winch design is proposed for the mining industry. This design improves on the operating safety, durability and energy efficiency of the conventional scraper winch design. The traction RSM used in the proposed winch design is able to operate position sensorless with rated startup torque capabilities. Also a overload automation proses is implemented. The 304 Nm position sensorless controlled startup torque of the winch RSM is one of the largest documented, as shown in Table A.1.

Effect of medium power range machines on the position sensorless contol methods

A 1.1 kW machine is used in literature to derive and test the AI-PSC and the FS-PSC methods on RSMs. It is shown in this thesis that these methods do not exhibit adverse effects when used with RSMs with higher power ratings. It is shown however, that the simplified HFI-PSC method does suffer from adverse effects when implemented on machines with higher current ratings. A method is derived in this thesis to reduce the effect of the fundamental current harmonic in the demodulation scheme without adding any additional filters to the control or estimation scheme to allow successful position estimation with the simplified HFI-SPC method on machines with higher current ratings.

The following contributions also stem from the work done in this thesis:

- A simplified HFI-PSC method is introduced in Chapter 4. The main advantages are reduced time delay, reduced phase shift, less signal magnitude decrease and improved control structure dynamics. It is also shown that the current LPF's, which already form part of the control structure, can be used to decouple the fundamental current component from the HF component to provide spectral

separation in machines with high current ratings. No delay or filters are added by the decoupling process.

- A new measured maximum torque as a function of speed comparison of the HFI-, AI- and the FS-PSC is shown in this thesis.
- An investigation in this thesis regarding the effect of rotor skewing on the SB-PSC performance of the RSM shows that a full slot pitch skew has little to no effect.
- It is shown through FE simulation results that the saliency shift of the RSM can be reduced by increasing the number of flux barriers per pole and increasing the width of the stator slot opening.
- It is shown through simulations that the AI-PSC method is quite sensitive to the size of the end-winding inductance.
- New implementation and testing of the simplified HF-, AI- and the FS-PSC methods on a six pole RSM. Also a new evaluation of the hybrid PSC methods on a 6 pole RSM.

Recommendations for future work

The following recommendations are made regarding future work that is to stem from this thesis:

- It is recommended that the position sensorless controllability of the EV RSM be measured at full power with a larger variable speed drive. Also this drive should be used to measure its saliency ratio as well as that of the field intensified permanent magnet machines to confirm measured results.
- Each of the investigated industry applications should be subjected to field tests outside the laboratory. The reluctance synchronous generator should be tested on a wind site, the EV RSM should be tested in the electric Opel Corsa and the scraper winch should be tested underground in the mines.
- The active flux method is not considered in this thesis. The active flux method should also be investigated and compared to the FS-PSC method. This method should also be extended to operate in the entire rated speed range by flux linkage stabilisation methods.

References

[1] Q. Ren, D.A. Crolla, and A. Morris. Effect of transmission design on electric vehicle (EV) performance. In *Vehicle Power and Propulsion Conference, 2009. VPPC '09. IEEE*, pages 1260 –1265, Sept. 2009.

[2] P. Landsmann, D. Paulus, P. Stolze, and R. Kennel. Reducing the parameter dependency of encoderless predictive torque control for reluctance machines. In *Sensorless Control for Electrical Drives (SLED), 2010 First Symposium on*, pages 93–99, 2010.

[3] P. Landsmann, R. Kennel, H.W. de Kock, and M.J. Kamper. Fundamental saliency based encoderless control for reluctance synchronous machines. In *Electrical Machines (ICEM), 2010 XIX International Conference on*, pages 1 –7, sept. 2010.

[4] DiesleNet. Emission Test Cycles. `http://www.dieselnet.com/standards/cycles/ftp72.php`.

[5] WinWind. WinWind3. `http://www.winwind.com/the-new-winwind3.aspx`.

[6] S. Morimoto, H. Nakayama, M. Sanada, and Y. Takeda. Sensorless output maximization control for variable-speed wind generation system using ipmsg. *IEEE Transactions on Industry Applications*, 41(1):60–67, 2005.

[7] T.J.E. Miller, A. Hutton, C. Cossar, and D.A. Staton. Design of a synchronous reluctance motor drive. *IEEE Transactions on Industry Applications*, 27(4):741–749, 1991.

[8] A. Vagati A. Fratta. Synchronous reluctance vs induction motor: a comparison. In *Proceedings Intelligent Motion*, pages pp.179–186, April 1992.

[9] A. Vagati. The synchronous reluctance solution: a new alternative in ac drives. In *Industrial Electronics, Control and Instrumentation, 1994. IECON '94., 20th International Conference on*, volume 1, pages 1–13 vol.1, 1994.

[10] M.J Kamper. *Design optimisation of cageless flux barrier rotor reluctance synchronous machines*. PhD thesis, University of Stellenbosch, 1996.

[11] A. Vagati, A. Fratta, G. Franceschini, and P. Rosso. Ac motors for high-performance drives: a design-based comparison. *IEEE Transactions on Industry Applications*, 32(5):1211–1219, 1996.

[12] J.J. Germishuizen, F.S. Van der Merwe, K. Van der Westhuizen, and M.J. Kamper. Performance comparison of reluctance synchronous and induction traction drives for electrical multiple units. In *Industry Applications Conference, 2000. Conference Record of the 2000 IEEE*, volume 1, pages 316–323 vol.1, 2000.

[13] A. Boglietti, A. Cavagnino, M. Pastorelli, and A. Vagati. Experimental comparison of induction and synchronous reluctance motors performance. In *Industry Applications Conference, 2005. Fourtieth IAS Annual Meeting. Conference Record of the 2005*, volume 1, pages 474–479 Vol. 1, 2005.

[14] A. Boglietti, A. Cavagnino, M. Pastorelli, D. Staton, and A. Vagati. Thermal analysis of induction and synchronous reluctance motors. *IEEE Transactions on Industry Applications*, 42(3):675–680, 2006.

[15] A. Boglietti and M. Pastorelli. Induction and synchronous reluctance motors comparison. In *Industrial Electronics, 2008. IECON 2008. 34th Annual Conference of IEEE*, pages 2041–2044, 2008.

[16] R.R. Moghaddam, F. Magnussen, and C. Sadarangani. Theoretical and experimental reevaluation of synchronous reluctance machine. *IEEE Transactions on Industrial Electronics*, 57(1):6–13, 2010.

[17] Hugo W. de Kock. *Position sensorless and optimal torque control of reluctance and permanent magnet synchronous machines*. PhD thesis, Electric and Electronic Department, University of Stellenbosch, 2009.

[18] W.L. Soong and N. Ertugrul. Field-weakening performance of interior permanent-magnet motors. *IEEE Transactions on Industry Applications*, 38(5):1251–1258, 2002.

[19] S. Bolognani. A torque angle calculator for sensorless reluctance motor drives. In *4th European Conference on Power Electronics and Applications*, pages 4–013–0.17, 1991.

[20] P. C. Krause. *Analysis of Electric Machinery*. Mcgraw-Hill Book Company Inc, New York, USA, 1986.

[21] A.E. Fitzgerald, C. Kingsley, and S.D. Umans. *Electric Machinery*. Number v. 2. McGraw-Hill Book Company, 1993.

[22] Pieter D. Fick. Evaluation of the constant current angle controlled reluctance synchronous machine drive. Master's thesis, University of Stellenbosch, 2002.

[23] Hugo W. de Kock. Dynamic control of the permanent magnet assisted reluctance synchronous machine with constant current angle. Master's thesis, University of Stellenbosch, 2006.

[24] J. Stewart. *Calculus*. Stewart's Calculus Series. Thomson Brooks/Cole, 2007.

[25] Rhicard A. Trubenbach. Vector control of a reluctance synchronous machine. Master's thesis, University of Stellenbosch, 1993.

[26] P. Vas. *Sensorless vector and direct torque control*. Monographs in electrical and electronic engineering. Oxford University Press, 1998.

[27] N. Mohan, T.M. Undeland, and W.P. Robbins. *Power electronics: converters, applications, and design*. Number v. 1 in Power Electronics: Converters, Applications, and Design. John Wiley & Sons, 2003.

[28] P. Landsmann, D. Paulus, P. Stolze, and R. Kennel. Saliency based encoderless predictive torque control without signal injection for a reluctance synchronous machine. In *Power Electronics and Motion Control Conference (EPE/PEMC), 2010 14th International*, pages S1–10 –S1–17, sept. 2010.

[29] A. Ravikumar Setty, S. Wekhande, and K. Chatterjee. Comparison of high frequency signal injection techniques for rotor position estimation at low speed to standstill of pmsm. In *Power Electronics (IICPE), 2012 IEEE 5th India International Conference on*, pages 1–6, 2012.

[30] M. Linke, R. Kennel, and J. Holtz. Sensorless position control of permanent magnet synchronous machines without limitation at zero speed. In *IECON 02 [Industrial Electronics Society, IEEE 2002 28th Annual Conference of the]*, volume 1, pages 674–679 vol.1, 2002.

[31] Ji-Hoon Jang, Seung-Ki Sul, Jung-Ik Ha, K. Ide, and M. Sawamura. Sensorless drive of smpm motor by high frequency signal injection. In *Applied Power Electronics Conference and Exposition, 2002. APEC 2002. Seventeenth Annual IEEE*, volume 1, pages 279–285 vol.1, 2002.

[32] M. Linke, R. Kennel, and J. Holtz. Sensorless speed and position control of synchronous machines using alternating carrier injection. In *Electric Machines and Drives Conference, 2003. IEMDC'03. IEEE International*, volume 2, pages 1211–1217 vol.2, 2003.

[33] Ji-Hoon Jang, Jung-Ik Ha, M. Ohto, K. Ide, and Seung-Ki Sul. Analysis of permanent-magnet machine for sensorless control based on high-frequency signal injection. *IEEE Transactions on Industry Applications*, 40(6):1595–1604, 2004.

[34] H.W. de Kock, M.J. Kamper, O.C. Ferreira, and R.M. Kennel. Position sensorless control of the reluctance synchronous machine considering high frequency inductances. In *Power Electronics and Drive Systems, 2007. PEDS '07. 7th International Conference on*, pages 812–821, 2007.

[35] R. Leidhold and P. Mutschler. Interaction between the current controller and the injection of alternating carriers in sensorless drives. In *International Symposium on Power Electronics, Electrical Drives, Automation and Motion, 2008. SPEEDAM 2008.*, pages 262–267, 2008.

[36] R. Leidhold and P. Mutschler. Injection of a carrier with higher than the pwm frequency for sensorless position detection in pm synchronous motors. In *Power Electronics and Motion Control Conference, 2008. EPE-PEMC 2008. 13th*, pages 1353–1358, 2008.

[37] R. Leidhold and P. Mutschler. Improved method for higher dynamics in sensorless position detection. In *Industrial Electronics, 2008. IECON 2008. 34th Annual Conference of IEEE*, pages 1240–1245, 2008.

[38] D. Raca, P. Garcia, D. Reigosa, F. Briz, and R. Lorenz. A comparative analysis of pulsating vs. rotating vector carrier signal injection-based sensorless control. In *Applied Power Electronics Conference and Exposition, 2008. APEC 2008. Twenty-Third Annual IEEE*, pages 879–885, 2008.

[39] Qi Xin, Zhou Xiao-min, Wang Chang-song, Zhong Li-ping, and Wang Hui. Sensorless control of permanent-magnet synchronous motor based on high-frequency signal injection and kalman filter. In *2nd International Symposium on Systems and Control in Aerospace and Astronautics, 2008. ISSCAA 2008.*, pages 1–5, 2008.

[40] W. Hammel and R.M. Kennel. Integration of alternating carrier injection in position sensorless control without any filtering. In *Energy Conversion Congress and Exposition, 2009. ECCE 2009. IEEE*, pages 3830–3836, 2009.

[41] Hao Zhu, Xi Xiao, and Yongdong Li. A simplified high frequency injection method for pmsm sensorless control. In *Power Electronics and Motion Control Conference, 2009. IPEMC '09. IEEE 6th International*, pages 401–405, 2009.

[42] W. Hammel and R.M. Kennel. Position sensorless control of pmsm by synchronous injection and demodulation of alternating carrier voltage. In *Sensorless Control for Electrical Drives (SLED), 2010 First Symposium on*, pages 56–63, 2010.

[43] Y. Kano, T. Kosaka, N. Matsui, T. Takahashi, and M. Fujitsuna. Signal-injection-based sensorless ipm traction drive for wide-torque range operation at low speed. In *Energy Conversion Congress and Exposition (ECCE), 2012 IEEE*, pages 2284–2291, 2012.

[44] M.J. Corley and R.D. Lorenz. Rotor position and velocity estimation for a salient-pole permanent magnet synchronous machine at standstill and high speeds. *IEEE Transactions on Industry Applications*, 34(4):784–789, 1998.

[45] A. Consoli, G. Scarcella, and A. Testa. Industry application of zero-speed sensorless control techniques for pm synchronous motors. *IEEE Transactions on Industry Applications*, 37(2):513–521, 2001.

[46] F. Parasiliti, R. Petrella, and M. Tursini. Sensorless speed control of salient rotor pm synchronous motor based on high frequency signal injection and kalman filter. In *Proceedings of the 2002 IEEE International Symposium on Industrial Electronics, 2002. ISIE 2002.*, volume 2, pages 623–628 vol.2, 2002.

[47] O. Mansouri-Toudert, H. Zeroug, F. Auger, and A. Chibah. Improved rotor position estimation of salient-pole pmsm using high frequency carrier signal injection. In *2012 International Conference on Electrical Machines (ICEM).*, 2012.

[48] B.P. Lathi. *Modern Digital and Analog Communications Systems*. The Oxford Series in Electrical and Computer Engineering Series. Oxford University Press, Incorporated, 1998.

[49] N. Bianchi and S. Bolognani. Influence of rotor geometry of an ipm motor on sensorless control feasibility. *IEEE Transactions on Industry Applications*, 43(1):87–96, 2007.

[50] N. Bianchi, S. Bolognani, Ji-Hoon Jang, and Seung-Ki Sul. Comparison of pm motor structures and sensorless control techniques for zero-speed rotor position detection. *IEEE Transactions on Power Electronics*, 22(6):2466–2475, 2007.

[51] John G. Proakis and Dimitris K. Manolakis. *Digital Signal Processing (4th Edition)*. Prentice Hall, 4th edition, April 2006.

[52] N. Bianchi, S. Bolognani, Ji-Hoon Jang, and Seung-Ki Sul. Comparison of pm motor structures and sensorless control techniques for zero-speed rotor position detection. *IEEE Transactions on Power Electronics*, 22(6):2466–2475, 2007.

[53] J. L. Smuts. Critical evaluation of a position sensorless control technique for the reluctance synchronous machine drive. Master's thesis, University of Stellenbosch, 2001.

[54] D. Paulus, P. Landsmann, and R. Kennel. Sensorless field-oriented control for permanent magnet synchronous machines with an arbitrary injection scheme and direct angle calculation. In *Sensorless Control for Electrical Drives (SLED), 2011 Symposium on*, pages 41–46, 2011.

[55] D. Paulus, P. Landsmann, and R. Kennel. Saliency based sensorless field-oriented control for permanent magnet synchronous machines in the whole speed range. In *Sensorless Control for Electrical Drives (SLED), 2012 IEEE Symposium on*, pages 1–6, 2012.

[56] P. Landsmann, D. Paulus, P. Stolze, and R. Kennel. Saliency based encoderless predictive torque control without signal injection. In *Power Electronics Conference (IPEC), 2010 International*, pages 3029–3034, 2010.

[57] D.G. Zill and M.R. Cullen. *Advanced Engineering Mathematics*. Jones and Bartlett Publishers, 2006.

[58] P. Landsmann, C.M. Hackl, and R. Kennel. Eliminating all machine parameters in encoderless predictive torque control without signal injection. In *Electric Machines Drives Conference (IEMDC), 2011 IEEE International*, pages 1259–1264, 2011.

[59] F. Genduso, R. Miceli, C. Rando, and G.R. Galluzzo. Back emf sensorless-control algorithm for high-dynamic performance pmsm. *IEEE Transactions on Industrial Electronics*, 57(6):2092–2100, 2010.

[60] I. Boldea, M.C. Paicu, and G. Andreescu. Active flux concept for motion-sensorless unified ac drives. *IEEE Transactions on Power Electronics*, 23(5):2612–2618, 2008.

[61] Jung-Ik Ha, Seog-Joo Kang, and Seung-Ki Sul. Position-controlled synchronous reluctance motor without rotational transducer. *IEEE Transactions on Industry Applications*, 35(6):1393–1398, 1999.

[62] H.F. Hofmann, S.R. Sanders, and A. El-Antably. Stator-flux-oriented vector control of synchronous reluctance machines with maximized efficiency. *IEEE Transactions on Industrial Electronics*, 51(5):1066–1072, 2004.

[63] J.-F. Stumper, D. Paulus, P. Landsmann, and R. Kennel. Encoderless field-oriented control of a synchronous reluctance machine with a direct estimator. In *First Symposium on Sensorless Control for Electrical Drives (SLED), 2010.*, pages 18–23, 2010.

[64] K. Ide, H. Iura, and M. Inazumi. Hybrid sensorless control of ipmsm combining high frequency injection method and back emf method. In *IECON 2010 - 36th Annual Conference on IEEE Industrial Electronics Society*, pages 2236–2241, 2010.

[65] Y. Yamamoto, H. Funato, and S. Ogasawara. Hybrid sensor-less control of permanent magnet synchronous motor in low-speed region. In *7th Internatonal Conference on Power Electronics, 2007. ICPE '07.*, pages 823–828, 2007.

[66] C. Silva, G.M. Asher, and M. Sumner. Hybrid rotor position observer for wide speed-range sensorless pm motor drives including zero speed. *IEEE Transactions on Industrial Electronics*, 53(2):373–378, 2006.

[67] Jung-Hyo Lee, Tae-Woong Kong, Won cheol Lee, Chung-Yuen Won, and Jae-Sung Yu. A new hybrid sensorless method using a back emf estimator and a current model of permanent magnet synchronous motor. In *Power Electronics Specialists Conference, 2008. PESC 2008. IEEE*, pages 4256–4262, 2008.

[68] A. Piippo, J. Salomaki, and J. Luomi. Signal injection in sensorless pmsm drives equipped with inverter output filter. *IEEE Transactions on Industry Applications*, 44(5):1614–1620, 2008.

[69] A. Piippo and J. Luomi. Adaptive observer combined with hf signal injection for sensorless control of pmsm drives. In *Electric Machines and Drives, 2005 IEEE International Conference on*, pages 674–681, 2005.

[70] O. Wallmark and Lennart Harnefors. Sensorless control of salient pmsm drives in the transition region. *IEEE Transactions on Industrial Electronics*, 53(4):1179–1187, 2006.

[71] Lennart Harnefors and H-P Nee. A general algorithm for speed and position estimation of ac motors. *IEEE Transactions on Industrial Electronics*, 47(1):77–83, 2000.

[72] M. Tursini, R. Petrella, and F. Parasiliti. Sensorless control of an ipm synchronous motor for city-scooter applications. In *Industry Applications Conference, 2003. 38th IAS Annual Meeting. Conference Record of the*, volume 3, pages 1472–1479 vol.3, 2003.

[73] Manfred Schrodl, M. Hofer, and W. Staffler. Sensorless control of pm synchronous motors in the whole speed range including standstill using a combined inform/emf model. In *Power Electronics and Motion Control Conference, 2006. EPE-PEMC 2006. 12th International*, pages 1943–1949, 2006.

[74] H. Iura, M. Inazumi, T. Kamei, and K. Ide. Hybrid sensorless control of ipmsm for direct drive applications. In *Power Electronics Conference (IPEC), 2010 International*, pages 2761–2767, 2010.

[75] E. Robeischl, M. Schroedl, and M. Krammer. Position-sensorless biaxial position control with industrial pm motor drives based on inform- and back emf model. In *IECON 02 [Industrial Electronics Society, IEEE 2002 28th Annual Conference of the]*, volume 1, pages 668–673 vol.1, 2002.

[76] S. Bolognani, A. Faggion, E. Fornasiero, and L. Sgarbossa. Full speed range sensorless ipm motor drives. In *Electrical Machines (ICEM), 2012 XXth International Conference on*, pages 2209–2215, 2012.

[77] G. Bisheimer, M.O. Sonnaillon, C.H. De Angelo, I.A. Solsona, and G.O. Garcia. Full speed range permanent magnet synchronous motor control without mechanical sensors. *Electric Power Applications, IET*, 4(1):35–44, 2010.

[78] A. Piippo, M. Hinkkanen, and J. Luomi. Sensorless control of pmsm drives using a combination of voltage model and hf signal injection. In *Conference Record of the 2004 IEEE Industry Applications Conference, 2004. 39th IAS Annual Meeting.*, volume 2, pages 964–970 vol.2, 2004.

[79] S.-C. Agarlita, M. Fatu, L.N. Tutelea, F. Blaabjerg, and I. Boldea. I-f starting and active flux based sensorless vector control of reluctance synchronous motors, with experiments. In *Optimization of Electrical and Electronic Equipment (OPTIM), 2010 12th International Conference on*, pages 337–342, 2010.

[80] S.-C. Agarlita, I. Boldea, and F. Blaabjerg. High frequency injection assisted active flux based sensorless vector control of reluctance synchronous motors, with experiments from zero speed. In *2011 IEEE Energy Conversion Congress and Exposition (ECCE).*, pages 2725–2732, 2011.

[81] M. Schroedl and P. Weinmeier. Sensorless control of reluctance machines at arbitrary operating conditions including standstill. *IEEE Transactions on Power Electronics*, 9(2):225–231, 1994.

[82] W.T. Villet, M.J. Kamper, P. Landsmann, and R. Kennel. Hybrid position sensorless vector control of a reluctance synchronous machine through the entire speed range. In *Power Electronics and Motion Control Conference (EPE/PEMC), 2012 15th International*, pages LS4b–1.1–1–LS4b–1.1–7, Sept 2012.

[83] S.-C. Agarlita, I. Boldea, and F. Blaabjerg. High-frequency-injection-assisted active-flux-based sensorless vector control of reluctance synchronous motors, with experiments from zero speed. *IEEE Transactions on Industry Applications*, 48(6):1931–1939, Nov. 2012.

[84] N. Bianchi and S. Bolognani. Influence of rotor geometry of an interior pm motor on sensorless control feasibility. In *Industry Applications Conference, 2005. Fourtieth IAS Annual Meeting. Conference Record of the 2005*, volume 4, pages 2553–2560 Vol. 4, 2005.

[85] N. Bianchi, S. Bolognani, and M. Zigliotto. Design hints of an ipm synchronous motor for an effective position sensorless control. In *Power Electronics Specialists Conference, 2005. PESC '05. IEEE 36th*, pages 1560–1566, 2005.

[86] J. Arellano-Padilla, C. Gerada, G. Asher, and M. Sumner. Inductance characteristics of pmsms and their impact on saliency-based sensorless control. In *Power Electronics and Motion Control Conference (EPE/PEMC), 2010 14th International*, pages S1–1–S1–9, 2010.

[87] C. Gerada, J. A. Padilla, M. Sumner, and T. Raminosoa. Loading effects on saliency based sensorless control of pmsms. In *Electrical Machines and Systems, 2009. ICEMS 2009. International Conference on*, pages 1–6, 2009.

[88] N. Bianchi and S. Bolognani. Sensorless-oriented-design of PM motors. In *Industry Applications Conference, 2007. 42nd IAS Annual Meeting. Conference Record of the 2007 IEEE*, pages 668 –675, Sept. 2007.

[89] N. Bianchi and S. Bolognani. Sensorless-oriented design of pm motors. *IEEE Transactions on Industry Applications*, 45(4):1249–1257, 2009.

[90] Jung-Ik Ha, M. Ohto, Ji-Hoon Jang, and Seung-Ki Sul. Design and selection of ac machines for saliency-based sensorless control. In *Industry Applications Conference, 2002. 37th IAS Annual Meeting. Conference Record of the*, volume 2, pages 1155–1162 vol.2, 2002.

[91] N. Bianchi, S. Bolognani, Ji-Hoon Jang, and S.K. Sul. Advantages of inset pm machines for zero-speed sensorless position detection. In *Industry Applications Conference, 2006. 41st IAS Annual Meeting. Conference Record of the 2006 IEEE*, volume 1, pages 495–502, 2006.

[92] N. Bianchi, S. Bolognani, Ji-Hoon Jang, and Seung-Ki Sul. Advantages of inset pm machines for zero-speed sensorless position detection. *IEEE Transactions on Industry Applications*, 44(4):1190–1198, 2008.

[93] S. Murakami, T. Shiota, M. Ohto, K. Ide, and M. Hisatsune. Encoderless servo drive with adequately designed ipmsm for pulse-voltage-injection-based position detection. *IEEE Transactions on Industry Applications*, 48(6):1922–1930, 2012.

[94] M. Caner, C. Gerada, and G. Asher. Permanent magnet motor design optimisation for sensorless control. In *2011 International Aegean Conference on Electrical Machines and Power Electronics and 2011 Electromotion Joint Conference (ACEMP).*, pages 670–675, 2011.

[95] N. Bianchi, E. Fornasiero, and S. Bolognani. Effect of stator and rotor saturation on sensorless rotor position detection. *IEEE Transactions on Industry Applications*, 49(3):1333–1342, 2013.

[96] Adriano Faggion, N. Bianchi, and S. Bolognani. Ringed-pole permanent-magnet synchronous motor for position sensorless drives. *IEEE Transactions on Industry Applications*, 47(4):1759–1766, 2011.

[97] N. Bianchi, S. Bolognani, and Adriano Faggion. A ringed-pole spm motor for sensorless drives - electromagnetic analysis, prototyping and tests. In *Industrial Electronics (ISIE), 2010 IEEE International Symposium on*, pages 1193–1198, 2010.

[98] L. Alberti, N. Bianchi, M. Morandin, and J. Gyselinck. Finite-element analysis of electrical machines for sensorless drives with signal injection. In *Energy Conversion Congress and Exposition (ECCE), 2012 IEEE*, pages 861–868, 2012.

[99] T. Frenzke. Impacts of cross-saturation on sensorless control of surface permanent magnet synchronous motors. In *Power Electronics and Applications, 2005 European Conference on*, pages 10 pp.–P.10, 2005.

[100] Shih-Chin Yang, T. Suzuki, R.D. Lorenz, and T.M. Jahns. Surface-permanent-magnet synchronous machine design for saliency-tracking self-sensing position estimation at zero and low speeds. *IEEE Transactions on Industry Applications*, 47(5):2103–2116, 2011.

[101] P. Guglielmi, M. Pastorelli, and A. Vagati. Cross-saturation effects in ipm motors and related impact on sensorless control. *IEEE Transactions on Industry Applications*, 42(6):1516–1522, 2006.

[102] B. Stumberger, G. Stumberger, D. Dolinar, A. Hamler, and M. Trlep. Evaluation of saturation and cross-magnetization effects in interior permanent-magnet synchronous motor. *IEEE Transactions on Industry Applications*, 39(5):1264–1271, 2003.

[103] A. Faggion, E. Fornasiero, N. Bianchi, and S. Bolognani. Sensorless capability of fractional-slot surface-mounted pm motors. *IEEE Transactions on Industry Applications*, 49(3):1325–1332, 2013.

[104] N. Bianchi, S. Bolognani, and Adriano Faggion. Predicted and measured errors in estimating rotor position by signal injection for salient-pole pm synchronous motors. In *Electric Machines and Drives Conference, 2009. IEMDC '09. IEEE International*, pages 1565–1572, 2009.

[105] M. Morandin, S. Bolognani, and Adriano Faggion. Outer-rotor ringed-pole spm starter-alternator suited for sensorless drives. In *Sensorless Control for Electrical Drives (SLED), 2011 Symposium on*, pages 96–101, 2011.

[106] R. Wrobel, A. S. Budden, D. Salt, D. Holliday, P.H. Mellor, A. Dinu, P. Sangha, and M. Holme. Rotor design for sensorless position estimation in permanent-magnet machines. *IEEE Transactions on Industrial Electronics*, 58(9):3815–3824, 2011.

[107] P. Sergeant, F. De Belie, and J. Melkebeek. Rotor geometry design of interior PMSMs with and without flux barriers for more accurate sensorless control. *IEEE Transactions on Industrial Electronics*, 59(6):2457–2465, 2012.

[108] P. Guglielmi, M. Pastorelli, and A. Vagati. Impact of cross-saturation in sensorless control of transverse-laminated synchronous reluctance motors. *IEEE Transactions on Industrial Electronics*, 53(2):429–439, 2006.

[109] N. Bianchi, S. Bolognani, and B.J. Chalmers. Salient-rotor pm synchronous motors for an extended flux-weakening operation range. *IEEE Transactions on Industry Applications*, 36(4):1118–1125, 2000.

[110] N. Limsuwan, T. Kato, and R.D. Lorenz. Concurrent design of interior-permanent-magnet machines for self-sensing and power conversion. *IEEE Transactions on Industry Applications*, 48(6):2157–2164, 2012.

[111] Shanshan Wu, D.D. Reigosa, Y. Shibukawa, M.A. Leetmaa, R.D. Lorenz, and Yongdong Li. Interior permanent-magnet synchronous motor design for improving self-sensing performance at very low speed. *IEEE Transactions on Industry Applications*, 45(6):1939–1946, 2009.

[112] T. Kato, N. Limsuwan, ChenYen Yu, K. Akatsu, and R.D. Lorenz. Rare earth reduction using a novel variable magnetomotive force, flux intensified ipm machine. In *Energy Conversion Congress and Exposition (ECCE), 2012 IEEE*, pages 4346–4353, 2012.

[113] N. Limsuwan, T. Kato, K. Akatsu, and R.D. Lorenz. Design and evaluation of a variable-flux flux-intensifying interior permanent magnet machine. In *Energy Conversion Congress and Exposition (ECCE), 2012 IEEE*, pages 3670–3677, 2012.

[114] N. Limsuwan, Y. Shibukawa, D.D. Reigosa, and R.D. Lorenz. Novel design of flux-intensifying interior permanent magnet synchronous machine suitable for self-sensing control at very low speed and power conversion. *IEEE Transactions on Industry Applications*, 47(5):2004–2012, 2011.

[115] Chen-Yen Yu, J. Tamura, D.D. Reigosa, and R.D. Lorenz. Position self-sensing evaluation of a fi-ipmsm based on high-frequency signal injection methods. *IEEE Transactions on Industry Applications*, 49(2):880–888, 2013.

[116] N. Bianchi, S. Bolognani, D. Bon, and M.D. Pre. Rotor flux-barrier design for torque ripple reduction in synchronous reluctance and pm-assisted synchronous reluctance motors. *IEEE Transactions on Industry Applications*, 45(3):921–928, 2009.

[117] M. Sanada, K. Hiramoto, S. Morimoto, and Y. Takeda. Torque ripple improvement for synchronous reluctance motor using an asymmetric flux barrier arrangement. *IEEE Transactions on Industry Applications*, 40(4):1076–1082, 2004.

[118] Jung-Min Park, Sung-Il Kim, Jung-Pyo Hong, and Jung-Ho Lee. Rotor design on torque ripple reduction for a synchronous reluctance motor with concentrated winding using response surface methodology. *Magnetics, IEEE Transactions on*, 42(10):3479–3481, 2006.

[119] L. Alberti, M. Barcaro, and N. Bianchi. Design of a low torque ripple fractional-slot interior permanent magnet motor. In *Energy Conversion Congress and Exposition (ECCE), 2012 IEEE*, pages 509–516, 2012.

[120] M. Barcaro, Adriano Faggion, N. Bianchi, and S. Bolognani. Predicted and experimental anisotropy of a dual three-phase interior permanent magnet motor for sensorless rotor position control. In *6th IET International Conference on Power Electronics, Machines and Drives (PEMD 2012).*, pages 1–6, 2012.

[121] N. Bianchi, S. Bolognani, Adriano Faggion, E. Fornasiero, and Alessandro Sartorello. Zero-speed sensorless drive capability of fractional-slot inset pm machine. In *6th IET International Conference on Power Electronics, Machines and Drives (PEMD 2012).*, pages 1–6, 2012.

[122] J. Malan and M.J. Kamper. Performance of a hybrid electric vehicle using reluctance synchronous machine technology. *IEEE Transactions on Industry Applications*, 37(5):1319–1324, Sep/Oct.

[123] C.W. Vorster, M.H.A Prins, and M.J. Kamper. Reluctance synchronous and field intensified-PM motors for variable-gear electric vehicle drives. In *Energy Conversion Congress and Exposition (ECCE), 2012 IEEE.*

[124] H. Polinder, J.A. Ferreira, B.B. Jensen, A.B. Abrahamsen, K. Atallah, and R.A. McMahon. Trends in wind turbine generator systems. *Emerging and Selected Topics in Power Electronics, IEEE Journal of*, 1(3):174–185, 2013.

[125] M. Lydia, A.I. Selvakumar, S.S. Kumar, and G.E.P. Kumar. Advanced algorithms for wind turbine power curve modeling. *Sustainable Energy, IEEE Transactions on*, 4(3):827–835, 2013.

[126] H. Li and Z. Chen. Overview of different wind generator systems and their comparisons. *Renewable Power Generation, IET*, 2(2):123–138, 2008.

[127] F. Blaabjerg and K. Ma. Future on power electronics for wind turbine systems. *Emerging and Selected Topics in Power Electronics, IEEE Journal of*, 1(3):139–152, 2013.

[128] F. Blaabjerg, Z. Chen, R. Teodorescu, and F. Iov. Power electronics in wind turbine systems. In *Power Electronics and Motion Control Conference, 2006. IPEMC 2006. CES/IEEE 5th International*, volume 1, pages 1–11, 2006.

[129] F. Blaabjerg, F. Iov, Z. Chen, and K. Ma. Power electronics and controls for wind turbine systems. In *Energy Conference and Exhibition (EnergyCon), 2010 IEEE International*, pages 333–344, 2010.

[130] B. Backlund and S. Ebner. The wind power converter for tomorrow is already here. Technical report, ABB Switzerland Ltd, Semiconductors.

[131] ABB. Pcs 6000 for large wind turbines medium voltage, full power converters up to 9 mva. Technical report, ABB.

[132] ABB. Abb wind turbine converters increased turbine output for creating the perfect wind economy. Technical report, ABB, 2013.

[133] N.A. Orlando, M. Liserre, R.A. Mastromauro, and A. Dell'Aquila. A survey of control issues in pmsg-based small wind-turbine systems. *IEEE Transactions on Industrial Informatics.*, 9(3):1211–1221, 2013.

[134] C. Busca, A.-I. Stan, T. Stanciu, and D.-I. Stroe. Control of permanent magnet synchronous generator for large wind turbines. In *2010 IEEE International Symposium on Industrial Electronics (ISIE).*, pages 3871–3876, 2010.

[135] Gilbert Foo Hock Beng. *Sensorless direct torque and flux control of interior permanent magnet synchronous motors at very low speeds including standstill.* PhD thesis, School of Electrical Engineering and Telecommunications, 2010.

[136] Zhe Zhang, Yue Zhao, Wei Qiao, and Liyan Qu. A space-vector modulated sensorless direct-torque control for direct-drive pmsg wind turbines. In *Industry Applications Society Annual Meeting (IAS), 2012 IEEE*, pages 1–7, 2012.

[137] J. Pontt, J. Rodriguez, S. Kouro, C. Silva, H. Farias, and M. Rotella. Output sinus filter for medium voltage drive with direct torque control. In *Industry Applications Conference, 2005. Fourtieth IAS Annual Meeting. Conference Record of the 2005*, volume 1, pages 204–209 Vol. 1, 2005.

[138] J.K. Steinke. Use of an lc filter to achieve a motor-friendly performance of the pwm voltage source inverter. *Energy Conversion, IEEE Transactions on*, 14(3):649–654, 1999.

[139] B. Wu, Y. Lang, N. Zargari, and S. Kouro. *Power Conversion and Control of Wind Energy Systems.* IEEE Press Series on Power Engineering. Wiley, 2011.

[140] A.H. Bonnett. Analysis of the impact of pulse-width modulated inverter voltage waveforms on ac induction motors. *IEEE Transactions on Industry Applications*, 32(2):386–392, 1996.

[141] A. Von Jouanne and P.N. Enjeti. Design considerations for an inverter output filter to mitigate the effects of long motor leads in asd applications. *IEEE Transactions on Industry Applications*, 33(5):1138–1145, 1997.

[142] Nidecon. Wind power applications. `http://www.nidecon.com/applications/renewable-energy.html`.

[143] Schaffner. Wind energy grid compatibility and reliability of wind energy systems. Technical report, Schaffner Group.

[144] S. Tokunaga and K. Kesamaru. Fem simulation of novel small wind turbine generation system with synchronous reluctance generator. In *Electrical Machines and Systems (ICEMS), 2011 International Conference on*, pages 1–6, 2011.

[145] T. Fukao, Z. Yang, and M. Matsui. Voltage control of super high-speed reluctance generator system with a pwm voltage source converter. *IEEE Transactions on Industry Applications*, 28(4):880–886, 1992.

[146] T. Fukao. Principles and output characteristics of super high-speed reluctance generator system. *IEEE Transactions on Industry Applications*, IA-22(4):702–707, 1986.

[147] I. Boldea, Z. X. Fu, and S.A. Nasar. High-performance reluctance generator. *Electric Power Applications, IEE Proceedings B*, 140(2):124–130, 1993.

[148] I. Boldea, L. Tutelea, and C.I. Pitic. Pm-assisted reluctance synchronous motor/generator (pm-rsm) for mild hybrid vehicles: electromagnetic design. *IEEE Transactions on Industry Applications*, 40(2):492–498, 2004.

[149] I. Boldea, Z. Fu, and S.A. Nasar. Sensorless dc output control of a high performance reluctance generator system. In *Industry Applications Society Annual Meeting, 1994., Conference Record of the 1994 IEEE*, pages 16–22 vol.1, 1994.

[150] Z. Xu, T. Pang, and Dianguo Xu. Instantaneous torque control of a permanent magnet wind power generator without a position sensor. In *Electrical Machines and Systems, 2008. ICEMS 2008. International Conference on*, pages 1343–1347, 2008.

[151] J.S. Thongam, P. Bouchard, V. Giurgiu, H. T. Bui, and M. Ouhrouche. Sensorless vector control of pmsg for variable speed wind energy applications. In *Electrical and Computer Engineering (CCECE), 2010 23rd Canadian Conference on*, pages 1–5, 2010.

[152] Keyuan Huang, Lei Zheng, Shoudao Huang, Lei Xiao, and Wenqiang Li. Sensorless control for direct-drive pmsg wind turbines based on sliding mode observer. In *2011 International Conference on Electrical Machines and Systems (ICEMS).*, pages 1–5, 2011.

[153] Shuying Yang, Xing Zhang, Chongwei Zhang, Zhen Xie, and Fei Li. Sensorless control for pmsg in direct-drive wind turbines. In *2010 2nd IEEE International Symposium on Power Electronics for Distributed Generation Systems (PEDG).*, pages 81–84, 2010.

[154] Shengwen Fan, Peng Wang, and Chunxue Wen. A new sensorless control strategy used in direct-drive pmsg wind power system. In *2010 2nd IEEE International Symposium on Power Electronics for Distributed Generation Systems (PEDG).*, pages 611–615, 2010.

[155] M. Braun, O. Lehmann, and J. Roth-Stielow. Sensorless rotor position estimation at standstill of high speed pmsm drive with lc inverter output filter. In *Industrial Technology (ICIT), 2010 IEEE International Conference on*, pages 410 –415, March 2010.

[156] T.D. Batzel and K.Y. Lee. Electric propulsion with sensorless permanent magnet synchronous motor: Implementation and performance. *Energy Conversion, IEEE Transactions on*, 20(3):575 – 583, Sept. 2005.

[157] T.D. Batzel and K.Y. Lee. Electric propulsion with sensorless permanent magnet synchronous motor: Implementation and performance. *Energy Conversion, IEEE Transactions on*, 20(3):575–583, 2005.

[158] Jae-Do Park, C. Khalizadeh, and H. Hofmann. Design and control of high-speed solid-rotor synchronous reluctance drive with three-phase lc filter. In *Industry Applications Conference, 2005. Fourtieth IAS Annual Meeting. Conference Record of the 2005*, volume 1, pages 715–722 Vol. 1, 2005.

[159] Jeihoon Baek, M.M. Rahimian, and H.A. Toliyat. Optimal design and comparison of stator winding configurations in permanent magnet assisted synchronous reluctance generator. In *IEMDC '09. IEEE International Electric Machines and Drives Conference, 2009.*, pages 732–737, 2009.

[160] Jeihoon Baek, M.M. Rahimian, and H.A. Toliyat. Maximum output power control of permanent magnet-assisted synchronous reluctance generator. In *Electrical Machines, 2008. ICEM 2008. 18th International Conference on*, pages 1–5, 2008.

[161] Zhongqing Yang and T. Fukao. Direct output power control for pwm converter-based super-high-speed reluctance generator. *IEEE Transactions on Industry Applications*, 28(1):57–63, 1992.

[162] A. Rolan, A. Luna, G. Vazquez, D. Aguilar, and G. Azevedo. Modeling of a variable speed wind turbine with a permanent magnet synchronous generator. In *Industrial Electronics, 2009. ISIE 2009. IEEE International Symposium on*, pages 734–739, 2009.

[163] Qi Huang and Zaiping Pan. Sensorless control of permanent magnet synchronous generator in direct-drive wind power system. In *Electrical Machines and Systems (ICEMS), 2011 International Conference on*, pages 1–5, 2011.

[164] K Fischer, T Stalin, H Ramberg, T Thiringer, J Wenske, and R Karlsson. Investigation of converter failure in wind turbines. Technical report, Elforsk, 2012.

[165] LORC Knowledge. Alpha ventus offshore wind farm . `http://www.lorc.dk/offshore-wind-farms-map/alpha-ventus?lat=54.0202&lon=6.6062`.

[166] J Lettl, J Bauer, and L Linhart. Comparison of different filter types for grid connected inverter. In *PIERS*, March 2011.

[167] T.D. Batzel and K.Y. Lee. Electric propulsion with sensorless permanent magnet synchronous motor: Implementation and performance. *Energy Conversion, IEEE Transactions on*, 20(3):575–583, 2005.

[168] J. Salomaki, A. Piippo, M. Hinkkanen, and J. Luomi. Sensorless vector control of pmsm drives equipped with inverter output filter. In *IEEE Industrial Electronics, IECON 2006 - 32nd Annual Conference on*, pages 1059–1064, 2006.

[169] B Neammanee, S Sirisumrannukul, and S Chatratana. *Control Strategies for Variable-speed Fixed-pitch Wind Turbines, Wind Power.*

[170] P. Bouwer and M.J. Kamper. Sensorless small-scale variable speed wind energy conversion system incorporating dtc-svm of direct-drive pmsg with rlc filter. In *Energy Conversion Congress and Exposition (ECCE), 2012 IEEE*, pages 3756–3763, 2012.

[171] J. de Santiago, H. Bernhoff, B. Ekergrd, S. Eriksson, S. Ferhatovic, R. Waters, and M. Leijon. Electrical motor drivelines in commercial all-electric vehicles: A review. *IEEE Transactions on Vehicular Technology.*, 61(2):475–484, 2012.

[172] X.-D. Xue, K. W E Cheng, and N.C. Cheung. Selection of electric motor drives for electric vehicles. In *Power Engineering Conference, 2008. AUPEC '08. Australasian Universities*, pages 1–6, 2008.

[173] L. Chang. Comparison of ac drives for electric vehicles-a report on experts' opinion survey. *Aerospace and Electronic Systems Magazine, IEEE*, 9(8):7–11, 1994.

[174] D.G. Dorrell. Are wound-rotor synchronous motors suitable for use in high efficiency torque-dense automotive drives? In *IECON 2012 - 38th Annual Conference on IEEE Industrial Electronics Society*, pages 4880–4885, 2012.

[175] J. Nerg, M. Rilla, V. Ruuskanen, J. Pyrhonen, and S. Ruotsalainen. Direct-driven interior magnet permanent magnet synchronous motors for a full electric sports car. *IEEE Transactions on Industrial Electronics*, PP(99):1–1, 2013.

[176] M. Barcaro, N. Bianchi, and F. Magnussen. Pm motors for hybrid electric vehicles. In *Universities Power Engineering Conference, 2008. UPEC 2008. 43rd International*, pages 1–5, 2008.

[177] C.S. Namuduri and B.V. Murty. High power density electric drive for an hybrid electric vehicle. In *Applied Power Electronics Conference and Exposition, 1998. APEC '98. Conference Proceedings 1998., Thirteenth Annual*, volume 1, pages 34–40, 1998.

[178] Aimeng Wang, Yihua Jia, and W.L. Soong. Comparison of five topologies for an interior permanent-magnet machine for a hybrid electric vehicle. *Magnetics, IEEE Transactions on*, 47(10):3606–3609, 2011.

[179] K. Rajashekara. Present status and future trends in electric vehicle propulsion technologies. *IEEE Journal of Emerging and Selected Topics in Power Electronics.*, 1(1):3–10, 2013.

[180] P. Guglielmi, N.G. Giraudo, G.-M. Pellegrino, and A. Vagati. P.m. assisted synchronous reluctance drive for minimal hybrid application. In *Industry Applications Conference, 2004. 39th IAS Annual Meeting. Conference Record of the 2004 IEEE*, volume 1, pages –306, 2004.

[181] S. Ooi, S. Morimoto, M. Sanada, and Y. Inoue. Performance evaluation of a high-power-density pmasynrm with ferrite magnets. *IEEE Transactions on Industry Applications*, 49(3):1308–1315, 2013.

[182] M. Paradkar and J. Boecker. Design of a high performance ferrite magnet-assisted synchronous reluctance motor for an electric vehicle. In *IECON 2012 - 38th Annual Conference on IEEE Industrial Electronics Society*, pages 4099–4103, 2012.

[183] Shuang Zhao, O. Wallmark, and M. Leksell. Analysis of a deeply saturated sensorless pmsynrel drive for an automotive application. In *Power Electronics and Applications (EPE 2011), Proceedings of the 2011-14th European Conference on*, pages 1–10, 2011.

[184] D.G. Dorrell, A.M. Knight, M. Popescu, L. Evans, and D.A. Staton. Comparison of different motor design drives for hybrid electric vehicles. In *Energy Conversion Congress and Exposition (ECCE), 2010 IEEE*, pages 3352–3359, 2010.

[185] Sung-Joo Kim, Yong-Kyun Lee, Ju-Suk Lee, Kwang-Woon Lee, Taesuk Kwon, and Hyungsoo Mok. Sensorless control method in ipmsm position sensor fault for hev. *Journal of Electrical Engineering and Technology*, 2013.

[186] N. Patel, T. O'Meara, J. Nagashima, and R. Lorenz. Encoderless ipm traction drive for ev/hev's. In *Industry Applications Conference, 2001. Thirty-Sixth IAS Annual Meeting. Conference Record of the 2001 IEEE*, volume 3, pages 1703–1707 vol.3, 2001.

[187] J. Lara, A. Chandra, and J. Xu. Integration of hfsi and extended-emf based techniques for pmsm sensorless control in hev/ev applications. In *IECON 2012 - 38th Annual Conference on IEEE Industrial Electronics Society*, pages 3688–3693, 2012.

[188] R. Masaki, S. Kaneko, M. Hombu, T. Sawada, and S. Yoshihara. Development of a position sensorless control system on an electric vehicle driven by a permanent magnet synchronous motor. In *Power Conversion Conference, 2002. PCC-Osaka 2002. Proceedings of the*, volume 2, pages 571–576 vol.2, 2002.

[189] M. Kajino, N. Hoshi, and Meifen Cao. Comparison of driving characteristics in two kind of control schemes for permanent magnet synchronous motor mounted on electric vehicle. In *Power Electronics and ECCE Asia (ICPE ECCE), 2011 IEEE 8th International Conference on*, pages 1969–1975, 2011.

[190] Xu Jiaqun, Ouyang Minggao, and Tang Renyuan. Study on direct torque control of permanent magnet synchronous motor in electric vehicle drive. In *Advanced Motion Control, 2006. 9th IEEE International Workshop on*, pages 774–777, 2006.

[191] T. Holdstock, A. Sorniotti, M. Everitt, M. Fracchia, S. Bologna, and S. Bertolotto. Energy consumption analysis of a novel four-speed dual motor drivetrain for electric vehicles. In *Vehicle Power and Propulsion Conference (VPPC), 2012 IEEE*, pages 295–300, 2012.

[192] Lin Lai and M. Ehsani. Sensitivity analysis of vehicle performance to transmission parameters in parallel hevs with dynamic programming optimization. In *Transportation Electrification Conference and Expo (ITEC), 2012 IEEE*, pages 1–5, 2012.

[193] T. Hofman and C. H. Dai. Energy efficiency analysis and comparison of transmission technologies for an electric vehicle. In *Vehicle Power and Propulsion Conference (VPPC), 2010 IEEE*, pages 1–6, 2010.

[194] A. Sorniotti, M. Boscolo, A. Turner, and C. Cavallino. Optimization of a multi-speed electric axle as a function of the electric motor properties. In *Vehicle Power and Propulsion Conference (VPPC), 2010 IEEE*, pages 1–6, 2010.

[195] M. Nashiki, A. Satake, Y. Kawai, T. Yokochi, and S. Okuma. A new flux-barrier-type reluctance motor with a slit rotor. *IEEE Transactions on Industrial Electronics*, 46(6):1199–1206, 1999.

[196] P. D. Chandana Perera. *Sensorless Control of Permanent-Magnet Synchronous Motor Drives*. PhD thesis, Institute of energy technology Aalborg university., 2002.

[197] J.F. Pritchard and C.F. Landy. Scraper winch motors on South African gold mines-an investigation into their failure. In *AFRICON, 1996., IEEE AFRICON 4th*, volume 1, pages 435–440 vol.1, 1996.

[198] `http://lcwinch.com/wp/en/78`.

[199] Anglo American. Scraper winch operations and rigging. In *Safety, health & environment bulletin*, volume S122/2003, June 2003.

[200] D. Janicijevic. Scraper winch operations and rigging. In *Third platinum conference 'Platinum in Transformation', the Southern African institute of mining and metallurgy*, 2008.

[201] `http://www.gs-harper.com/Mining_Research/Power/hydropower.asp`.

[202] `http://www.globalmarket.com/product-info/air-scraper-winch-with-scraper-pan-1328852.html`.

[203] A. Ghaderi and T. Hanamoto. Wide-speed-range sensorless vector control of synchronous reluctance motors based on extended programmable cascaded low-pass filters. *IEEE Transactions on Industrial Electronics*, 58(6):2322–2333, 2011.

[204] Ghaderi Ahmad, Hanamoto Tsuyoshi, and T. Teruo. A novel implementation of low speed sensorless vector control of synchronous reluctance motors with a new online parameter identification approach. In *Applied Power Electronics Conference and Exposition, 2006. APEC '06. Twenty-First Annual IEEE*, pages 7 pp.–, 2006.

[205] R. Lagerquist, I. Boldea, and T.J.E. Miller. Sensorless-control of the synchronous reluctance motor. *IEEE Transactions on Industry Applications*, 30(3):673–682, 1994.

[206] Ming-Yen Wei and Tian-Hua Liu. A high-performance sensorless position control system of a synchronous reluctance motor using dual current-slope estimating technique. *IEEE Transactions on Industrial Electronics*, 59(9):3411–3426, 2012.

[207] S. Ichikawa, M. Tomita, S. Doki, and S. Okuma. Sensorless control of synchronous reluctance motors based on extended emf models considering magnetic saturation with online parameter identification. *IEEE Transactions on Industry Applications*, 42(5):1264–1274, 2006.

[208] A. Consoli, F. Russo, G. Scarcella, and A. Testa. Low- and zero-speed sensorless control of synchronous reluctance motors. *IEEE Transactions on Industry Applications*, 35(5):1050–1057, 1999.

[209] Seog-Joo Kang, Jang-Mok Kim, and Seung-Ki Sul. Position sensorless control of synchronous reluctance motor using high frequency current injection. *Energy Conversion, IEEE Transactions on*, 14(4):1271–1275, 1999.

[210] E. Capecchi, P. Guglielmi, M. Pastorelli, and A. Vagati. Position-sensorless control of the transverse-laminated synchronous reluctance motor. *IEEE Transactions on Industry Applications*, 37(6):1768–1776, 2001.

[211] M.G. Jovanovic, R.E. Betz, and D. Platt. Sensorless vector controller for a synchronous reluctance motor. *IEEE Transactions on Industry Applications*, 34(2):346–354, 1998.

[212] M.G. Jovanovic and R.E. Betz. Maximum torque control of a sensorless synchronous reluctance motor drive. In *Industry Applications Conference, 1997. Thirty-Second IAS Annual Meeting, IAS '97., Conference Record of the 1997 IEEE*, volume 1, pages 637–644, 1997.

[213] T. Tuovinen, M. Hinkkanen, and J. Luomi. Analysis and design of a position observer with resistance adaptation for synchronous reluctance motor drives. *IEEE Transactions on Industry Applications*, 49(1):66–73, 2013.

Appendix A

Data Collection of Types and Sizes of Position Sensorless Control Synchronous Machines as Portrayed in Literature

Summarised in Table A.1 are the type and size of machines used in literature to evaluate PSC methods.

Table A.1: Data summary of literature.

Machine type	Power (kW)	Reference
RSM	0.086	[203]
RSM	0.086	[204]
PMSM	0.1	[39]
RSM	0.15	[205]
ALA RSM	0.3	[83]
IPMSM	0.4	[38]
IPMSM	0.5	[6]
RSM	0.56	[206]
IPMSM	0.7	[59]
IPMSM	0.7	[58]
PMSM	0.7	[55]
IPMSM	0.75	[45]
RSM	1	[207]
ALA RSM	1	[149]
RSM	1	[81]
PMSM	1	[46]
RSM	1.1	[28]
PMSM	1.1	[151]
RSM	1.1	[2]

Machine type	Power (kW)	Reference
RSM	1.1	[3]
ALA RSM	1.5	[80]
SMPSM	1.2	[30]
SMPSM	1.2	[32]
RSM	1.5	[208]
PMSM	1.57	[54]
PMSM	1.7	[44]
IPMSM	1.8	[72]
PMSM	2	[41]
PMSM	2.2	[78]
PMSM	2.2	[35]
PMSM	2.2	[68]
PMSM	2.2	[37]
PMSM	2.2	[168]
PMSM	2.2	[69]
PMSM	2.3	[36]
PMSM	3	[136]
SMPMSM	3.4	[40]
PMSM	3.4	[42]
ALA RSM	3.75	[61]
ALA RSM	3.75	[209]
SMPMSM	4	[66]
IPMSM	4	[76]
SMPMSM	4.4	[47]
PMSM	5	[163]
RSM	5	[210]
ALA RSM	5.8	[211]
RSM	5.8	[212]
IPMSM	6	[74]
IPMSM	6	[64]
RSM	6.7	[213]
PMSM	7.5	[152]
PMSM	10	[150]
SMPMSM	11	[31]
SMPMSM	11	[33]
PMSM	15	[153]
PMSM	12	[56]
PMSM	13.3	[67]
IPMSM	15	[185]
PMSM	34.6	[188]
IPMSM	36	[43]
PMSM	37	[65]
PMSM	50	[70]
PMSM	52	[157]
IPM	70 & 15	[186]

Appendix B

Data Collection of Commercially Available HEVs and EVs

A summary of the different machines used in HEV and EVs is shown in Table B.1 [171, 176].

Table B.1: Data summary of commercially available EVs and selected HEV's.

Model	Power (kW)	Motor type
Tesla Model S	225: Rear mounted	IM
Tesla Roadster	215: Rear mounted	IM
Lightning GT	150 X 2: Rear mounted	PM
Mercedes-Benz SLS AMG Electric Drive	138 X 4	PM
Venturi Ftish	220: Central rear mounted	PM
BWM Mini E	150	IM
BYD e6	160 + 40: 4 Wheel drive	PM
Mitsubishi i-MiEV	47: Rear mounted	PM
Ford Focus Electric	100	PM
Ford transit connect EV	50	IM
Nissan Leaf	80: Front mounted	PM
Renault Fluence Z.E.	70	Wound rotor synchronous
Renault ZOE	65: Front mounted	Wound rotor synchronous
Smart electric drive	30: Rear mounted	PM
Think City	34	IM
Hyundai blue on	61	PM
Tata indica	55	PM
Kangoo express Z.E	44	Wound rotor synchronous
Fiat Doblo	43	IM
Peugeot iOn	25	PM
REVAi	13	IM

Model	Power (kW)	Motor type
Citroen C zero	49	PM
Gordon Murray T-27	49	PM
Wheego whip life	15	IM
Citroen C1	30	IM
Micro-Vett Fiat Panda	15	IM
Micro-Vett Fiat 500	15	IM
Tazzario Zero	15	IM
Lumeneo SMERA	30	PM
Stevens Zecar	13 x 2	IM
AC Propulsion eBox	150	IM
ZAP! Obvio 828E	120	IM
Kewet Buddy	13	DC
ZAP Xebra	5	DC
NICE Mega City	4	DC
Commuter Cars Tango	21 X 2	DC
Cree SAM	11.6	PM
G-Wiz	4.8	DC
General Motors EV1	102: Front mounted	IM
Ford Ranger EV	45	IM
Peugeot Partner	28	DC
Nissan Hypermini	24: Rear wheel mounted	PM
Myers Motor NmG	20	DC
Peugeot 106	20	DC
Toyota RAV4 EV	115	IM
GEM Car	9	DC
CitiCom Mini-EI	9	PM
GM S-10	85	IM
Nissan Altera	62	PM
Honda EV Plus	49: Front mounted	DC
Citroen Berlingo	28	DC
Citroen Saxo	28	DC
Subaru minivan 200	14	DC
Solectria Sunrise	50	IM
Chrysler TEVan	27	DC
Citroen AX	20	DC
VW Golf CityStromer	17.5	PM
Ford Ecostar	56	IM
Bertone Blitz	52	DC
Chevrolet Spark EV	97	PM
Fiat 500e	83	PM
Honda Fit	92	PM
Toyota Prius	28 + 50: Hybrid	PM
Toyota Highlander is a SportUtility vehicle	123: Front Wheel + 50: Rear wheel Hybrid	PM
Honda Civic Hybrid	85: Hybrid	PM
Peugeout 307	16: Hybrid	PM

Appendix C

Pictures

Construction of the ideal rotor RSM

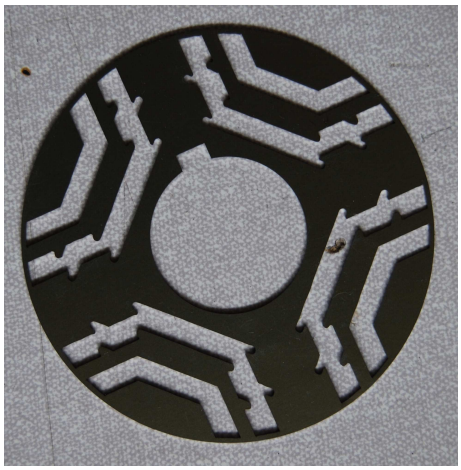

(a) Lamination used for ideal rotor RSM.

(b) Laminations being stacked on the end-cap.

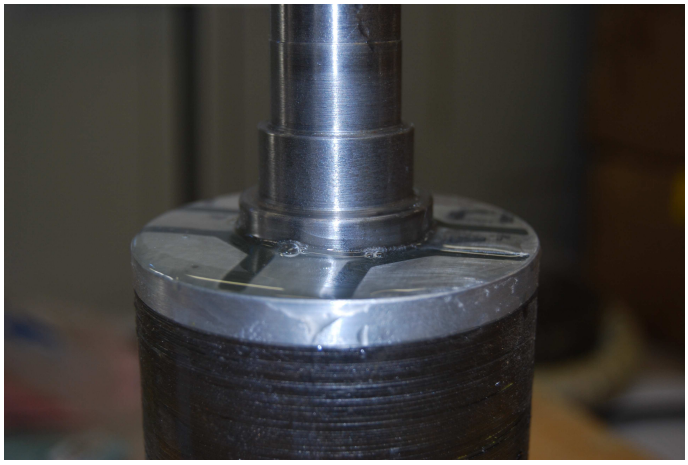

(c) Finished rotor filled with epoxy.

Figure C.1

Winch RSM

(a) One of the winch RSMs disconnected.

(b) Rotor of the winch RSM lifted into the stator with a crane.

(c) Disc brake on the side of the RSM.

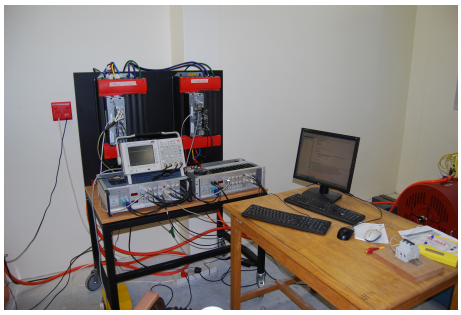

(d) Laboratory testing space with drives and RPSs.

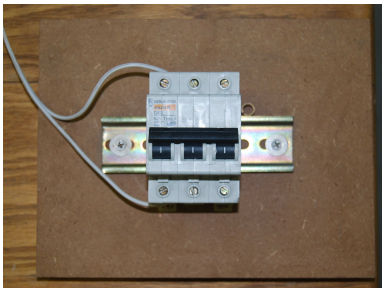

(e) Switch used to activate the disc brake.

Figure C.2